SPECTRAL STUDIES OF GAMMA-RAY BURST PROMPT EMISSION

by

YUKI KANEKO

A DISSERTATION

Submitted in partial fulfillment of the requirements
for the degree of Doctor of Philosophy
in
The Department of Physics
to
The School of Graduate Studies
of
The University of Alabama in Huntsville

HUNTSVILLE, ALABAMA

2005

In presenting this dissertation in partial fulfillment of the requirements for a doctoral degree from The University of Alabama in Huntsville, I agree that the Library of this University shall make it freely available for inspection. I further agree that permission for extensive copying for scholarly purposes may be granted by my advisor or, in his absence, by the Chair of the Department or the Dean of the School of Graduate Studies. It is also understood that due recognition shall be given to me and to The University of Alabama in Huntsville in any scholarly use which may be made of any material in this dissertation.

_____ _____

(student signature) (date)

DISSERTATION APPROVAL FORM

Submitted by Yuki Kaneko in partial fulfillment of the requirements for the degree of Doctor of Philosophy in Physics and accepted on behalf of the Faculty of the School of Graduate Studies by the dissertation committee.

We, the undersigned members of the Graduate Faculty of The University of Alabama in Huntsville, certify that we have advised and/or supervised the candidate on the work described in this dissertation. We further certify that we have reviewed the dissertation manuscript and approve it in partial fulfillment of the requirements of the degree of Doctor of Philosophy in Physics.

_____ Committee Chair

(Date)

_____

_____

_____

_____

_____

_____ Department Chair

_____ College Dean

_____ Graduate Dean

ABSTRACT

School of Graduate Studies
The University of Alabama in Huntsville

Degree Doctor of Philosophy College/Dept. Science/Physics

Name of Candidate Yuki Kaneko

Title Spectral Studies of Gamma-Ray Burst Prompt Emission

Gamma-Ray Burst (GRB) prompt emission spectra contain a wealth of information about the unresolved creation mechanism and source environment. A detailed spectral study of GRBs is, therefore, crucial to unveiling their nature. Previous spectral studies have shown compelling evidence that the Synchrotron Shock Model (SSM) cannot entirely account for observed spectra in terms of the spectral parameters. However, spectral parameters often depend on photon models employed and integration timescales of the spectra. The primary purpose of this dissertation is to explore model-unbiased spectral properties of GRB prompt emission in great detail with the best available statistics.

First, I present a systematic spectral analysis of 350 bright BATSE GRBs (30 keV – 2 MeV) with high energy and time resolution. To obtain unbiased spectral parameters, various photon models were used to fit each spectrum, and internal characteristics of each model were also investigated. A thorough analysis was performed on 342 time-integrated and 8459 time-resolved burst spectra, and the effects of integration times in determining the spectral parameters were explored. Typical spectra are described as a broken power law with various break curvatures: very sharp to very smooth. The analysis was then extended to broadband spectra of high-energy GRBs observed with BATSE and EGRET (30 keV – 200 MeV). One event was identified to have a very high peak energy in the power density spectrum, $E_{\rm peak} > 167$ MeV, and two events indicated high-energy excess.

Finally, the well-constrained, model-unbiased spectral parameters were used to examine some of the existing GRB emission models. I show, with good statistical confidence, that a considerable number of spectra are inconsistent with the SSM, while the jitter–synchrotron model can account for the spectral behavior of most GRBs in our sample.

The analysis of GRB prompt emission spectra presented in this dissertation is derived from the most sensitive and largest database to date. Therefore, these results provide exceptional statistics to set a standard for spectral properties of GRB prompt emission, and will be a pivotal reference for both theorists and observers, for the upcoming *GLAST* era and for defining science criteria for future missions.

Abstract Approval: Committee Chair _____

Department Chair _____

Graduate Dean _____

ACKNOWLEDGMENTS

I am extremely fortunate to have had the support from so many people during the course of my study, and to have been a part of such a wonderful group, the gamma-ray astronomy group at NSSTC. First and foremost, I would like to thank my advisor and committee chair, Rob Preece. He introduced me to the field of gamma-ray bursts and guided me so patiently through the research projects. I deeply appreciate all he has taught me and the fact that he always puts his students first. I am also very grateful to the rest of my committee: Bill Paciesas, for his academic and scientific guidance; Yoshi Takahashi, for giving me insight into broader range of physics; Chip Meegan, for all his help and guidance; and Michael Briggs, for always being available for my questions and explaining things very clearly and patiently. Everybody in the gamma-ray astronomy group has helped me so much over the past four years. I am very thankful to them all, and especially to Jerry Fishman and Chryssa Kouveliotou for providing me so many opportunities.

Over the years, I had the privilege of working with many wonderful scientists. I especially thank Brenda Dingus, Magda González, and Lorraine Hanlon for their collaborations, numerous useful discussions, and their hospitality during my visit to Madison and to Dublin. Also, I thank Misha Medvedev and David Band for very helpful discussions and suggestions on my work, on many occasions.

I am also grateful to the late Lloyd Hillman, the Physics Department Chair, for bringing me to UAH. I would also like to thank professors at Youngstown State University for their exceptional support even during my graduate years.

All my friends here in Huntsville and all over the world have been a great support for me all this years. I thank every one of them, for all their endless help, encouragement, and for believing in me. You all mean so much to me.

Finally, one person I really could not have done all this without, is Ersin Göğüş. From the very beginning of my graduate career, he has helped me clear the hurdles, understand physics concepts, and made me believe in myself. I thank him so much for his patience and encouragement, and all he has done for me.

TABLE OF CONTENTS

Page

LIST OF FIGURES . . . . . **xiii**

LIST OF TABLES . . . . . **xxii**

LIST OF SYMBOLS . . . . . **xxiv**

LIST OF ACRONYMS . . . . . **xxvii**

CHAPTER

1. INTRODUCTION **1**

1.1 Dissertation Outline 4

2. INSTRUMENTS **6**

2.1 Gamma-Ray Detectors 7

2.1.1 NaI Scintillation Detectors 7

2.1.1.1 Photoelectric Absorption 8

2.1.1.2 Compton Scattering 9

2.1.1.3 Pair Production 11

2.2 Burst And Transient Source Experiment 12
2.2.1 Large Area Detector 12
2.2.2 Spectroscopy Detector 16
2.2.3 BATSE Science Datatypes 16
2.3 The Energetic Gamma-Ray Experiment Telescope 22
2.3.1 Total Absorption Shower Counter 23
2.4 The Imaging Compton Telescope 26
2.5 Detector Response Matrix 28
2.5.1 Problems with BATSE Spectroscopy Detector DRM . . 29
2.5.2 Summary of SD DRM Problems 37

3. GAMMA-RAY BURSTS: OBSERVATIONS AND THEORIES 38

3.1 Observational Milestones 38
3.1.1 Pre-BATSE Era 39
3.1.2 BATSE Era 41
3.1.3 Afterglow Era 47
3.1.3.1 X-Ray Afterglow 49
3.1.3.2 Optical Afterglow 49
3.1.3.3 GRB-SN Connection 53
3.1.3.4 Radio Afterglow 55
3.1.4 X-Ray Flashes and X-Ray Rich GRBs 56
3.2 Theoretical Models of GRBs 57
3.2.1 Expanding Fireball 57
3.2.2 Fireball-Shock Model: Internal and External 59
3.2.3 Acceleration and Emission Mechanisms in Shocks 61

3.2.4 Progenitors ("Central Engines") 63
3.2.5 Short GRB Models 65
3.2.6 XRF Models 65
3.2.7 Alternative Physical Models of GRBs 66

4. SPECTRAL ANALYSIS OF BRIGHT BATSE GRBs 68

4.1 Selection Methodology 70
4.1.1 Event Selection 71
4.1.2 The Detector 79
4.1.3 Data Type Selection 79
4.1.4 Time Interval Selection 82
4.1.5 Energy Interval Selection 85
4.2 Spectral Analysis 85
4.2.1 Spectral Fitting Software 85
4.2.2 Photon Models 86
4.2.2.1 Power Law Model (PWRL) 86
4.2.2.2 The GRB Model (BAND) 87
4.2.2.3 The GRB Model with fixed β (BETA) 88
4.2.2.4 Comptonized Model (COMP) 88
4.2.2.5 Smoothly-Broken Power Law (SBPL) 89
4.3 Spectral Simulations 91
4.3.1 BAND vs. COMP 92
4.3.2 SBPL Break Scales 97
4.3.2.1 Finding the Break Scale 97
4.3.2.2 Comparison with BAND & COMP 102
4.4 Spectral Analysis Results 105

4.4.1 Spectral Parameter Distributions . . . 106
4.4.2 Model Comparison within Each Spectrum . . . 122
4.4.3 Time-Integrated and Time-Resolved Spectra . . . 138
4.4.4 Correlations Among Spectral Parameters . . . 150
4.4.5 BETA Model Fit Results . . . 158
4.4.6 Short GRBs . . . 162
4.5 Summary and Discussion . . . 165

5. BROADBAND SPECTRAL STUDY OF HIGH-ENERGY GRBs . . . 168

5.1 Selection Methodology . . . 170
5.2 Spectral Analysis . . . 172
5.3 Analysis Results . . . 174
5.3.1 Effective Area Correction Issue . . . 181
5.4 GRB 941017: A Distinct MeV Spectral Component . . . 184
5.4.1 COMPTEL Observation of GRB 941017 . . . 186
5.5 Summary and Discussion . . . 190

6. EXAMINING GRB PROMPT EMISSION MODELS . . . 192

6.1 Alternative Emission Models . . . 194
6.2 Low-Energy Spectral Index . . . 198
6.2.1 Constant Low-Energy Index Case . . . 205
6.3 High-Energy Spectral Index . . . 207
6.3.1 Varying High-Energy Index Case . . . 207

7. CONCLUSIONS 211

7.1 Prospects for Future Work 218

APPENDIX A: SBPL MODEL E_{peak} 221

A.1 Finding E_{peak} 221

A.2 Error Propagation ($\sigma_{E_{\mathrm{peak}}}$) 222

APPENDIX B: BAND MODEL E_{b} 225

B.1 Finding E_{b} 225

B.2 Error Propagation ($\sigma_{E_{\mathrm{b}}}$) 226

APPENDIX C: EFFECTIVE α 229

C.1 Error Propagation ($\sigma_{\alpha_{\mathrm{eff}}}$) 231

REFERENCES 233

LIST OF FIGURES

Figure **Page**

2.1 Cross sections for gamma-ray photon interaction processes in NaI crystal. 8

2.2 [*Top*] Response function for an input photon energy of 800 keV. Contributions from photoelectric absorption and Compton scattering are seen. [*Bottom*] Response function for an input photon energy of 2 MeV. Contribution from pair production is seen. 10

2.3 The *Compton Gamma-Ray Observatory*. The spacecraft's x, y, and z axes are shown. 13

2.4 BATSE detector module (one of eight). 14

2.5 Effective areas of BATSE LAD and SD as a function of energy, for normal incident angle (from Fishman et al. 1989). 15

2.6 EGRET module (from Thompson et al. 1993). The vertical center line represents the spacecraft z-axis. TASC is located below the spark chamber. 22

2.7 Typical energy spectrum of TASC. ^{40}K line, Fe line, the instrumental artifact, and the cosmic-ray proton features are evident. 24

2.8 Calculated effective area of TASC for azimuth angle of 168° (from Thompson et al. 1993). Zenith angle of 0° points to the spark chamber upwards and 90° is the x-y plane of the spacecraft. 25

2.9 COMPTEL module (from Schönfelder et al. 1993). 26

2.10 Contour maps of a detector response matrix, for LAD (*top*) and SD (*bottom*). Input photon energies are plotted against output channel energies, and off-diagonal components are clearly shown. 30

2.11 Response function of the SD for input photon energies of 10 MeV (*top*) and 20 MeV (*bottom*). 33

2.12 Projected geometric area of the SD NaI crystal for various incident angles. 34

2.13 The detection efficiency of an SD for different input photon energies. It diverges at energies above 3 MeV. 35

2.14 The detection efficiency of a LAD for different input photon energies, corresponding to Figure 2.13 for the SD. 36

3.1 The angular distribution of 2704 BATSE GRBs in galactic coordinates. The distribution is consistent with isotropy. 42

3.2 Cumulative peak flux distribution of >2000 BATSE GRBs. Dashed line shows $-3/2$ power law expected for a homogeneous distribution in Euclidean space. The peak flux integration time is 64 ms in $50 - 300$ keV. The deviation from the power law is seen at the lower peak flux. 42

3.3 Duration (T_{90}) distribution of 2041 BATSE GRBs. The values were taken from the "current" BATSE catalog. 43

3.4 Example lightcurves of BATSE GRBs, each showing different broad category of burst profiles: multi-episode (a, c), single peak (b), FRED (d), erratic (e), and short (f). 45

3.5 Example non-thermal spectrum of a BATSE GRB. 46

3.6 The achromatic break in optical afterglow lightcurves of GRB 990510 (from Harrison et al. 1999). 50

3.7 Schematics of various jet structures (from Rossi et al. 2004). The homogeneous jet has a uniform energy density independent of angle, whereas the Gaussian and power-law structured jets provide the energy density as a function of viewing angles. 52

3.8 Spectral evolution of SN2003dh compared with SN1998bw. (from Hjorth et al. 2003). 54

3.9 Optical afterglow lightcurve of GRB 021211 showing the SN bump at $\sim$ 20 days. The dashed line shows a "template" SN curve at similar redshift, and the dotted line shows the afterglow component. The horizontal line indicates the host galaxy magnitude (from Della Valle et al. 2003). 55

3.10 Schematic of the fireball shock scenario. 59

3.11 Theoretical energy flux spectra resulting from synchrotron emission by electrons with a power-law energy distribution with index p (from Sari et al. 1998). 62

4.1 Example count spectra of bright HERB (*top*) and MER (*bottom*) events in which systematic deviations between the data (crosses) and the model (solid lines) are evident below $\sim$ 100 keV. 81

4.2 S/N per detector for 15 MER events that produced the equivalent number of spectra to HERB binned by S/N $\geq$ 45 case. The dotted line marks 45σ. 83

4.3 Comparison of BAND and COMP models for $A = 0.1$, $\alpha = -1.2$, $E_{\rm peak} =$ 300 keV, and $\beta = -2.3$. $E_{\rm c}$ is where the high-energy power law of BAND begins. 93

4.4 Two simulated COMP spectra with S/N $\sim$ 80. Low-$E_{\rm peak}$ spectrum (solid curve) can be fitted with the BAND model much more frequently than the high-$E_{\rm peak}$ spectrum (dashed curve). 96

4.5 The simulated SBPL model spectra with $\Lambda = 0.01$, 0.1, 0.2, 0.3, 0.4, 0.5, 0.6, 0.7, 0.8, 0.9, and 1.0, from top to bottom at 300 keV. The other parameters are fixed at $A = 0.05$, $E_{\rm b} = 300$, $\lambda_1 = -1.0$, and $\lambda_2 = -2.5$. . 98

4.6 The break scale Λ found by 5-parameter SBPL fits to 11 simulated spectra for bright (*top*) and faint (*bottom*) cases. Horizontal axis shows the simulated Λ values and vertical axis shows the fitted Λ values. The dotted line corresponds to the correct Λ. 99

4.7 Median χ^2 map of 4-parameter SBPL fits to 11 simulated spectra (with Λ = 0.01 to 1.0, from top to bottom; dof = 113). Horizontal axis is the fixed Λ values of the 4-parameter model. The diamonds indicate the median χ^2 from the BAND fits to 11 simulated spectra (dof = 112). 101

4.8 Example BAND fits (dashed lines) to the simulated SBPL spectra (solid lines) with $\Lambda = 0.01$ (*top*) and with $\Lambda = 0.7$ (*bottom*). 104

4.9 Low-energy index distribution of 342 time-integrated spectra. [*Top Left*] *Good* parameters of all models. Numbers of parameters included are 38 PWRL, 235 COMP, 271 BAND, and 241 SBPL. The other plots show all (solid line) and *good* (dotted line) parameters of COMP (green), BAND (blue), and SBPL (red). The lowest (highest) bin includes values lower (higher) than the edge values. 111

4.10 High-energy index distribution of 342 time-integrated spectra. [*Top*] *Good* parameters of all models. Numbers of parameters included are 38 PWRL, 233 BAND, and 259 SBPL. The other plots show all (solid line) and *good* (dotted line) parameters of BAND (blue) and SBPL (red). The lowest (highest) bin includes values lower (higher) than the edge values. 112

4.11 $E_{\rm peak}$ distribution of 342 time-integrated spectra. [*Top Left*] *Good* parameters of all models. Numbers of parameters included are 219 COMP, 237 BAND, and 172 SBPL. The other plots show all (solid line) and *good* (dotted line) parameters of COMP (green), BAND (blue), and SBPL (red). The lowest (highest) bin includes values lower (higher) than the edge values. 113

4.12 Break Energy distribution of 342 time-integrated spectra. [*Top*] *Good* parameters of all models. Numbers of parameters included are 233 BAND and 272 SBPL. The other plots show all (solid line) and *good* (dotted line) parameters of BAND (blue) and SBPL (red). The lowest (highest) bin includes values lower (higher) than the edge values. 114

4.13 ΔS distribution of 342 time-integrated spectra. ΔS is the difference between low-energy and high-energy indices. [*Top*] *Good* parameters of all models. Numbers of parameters included are 217 BAND and 209 SBPL. The other plots show all (solid line) and *good* (dotted line) parameters of BAND (blue) and SBPL (red). The lowest (highest) bin includes values lower (higher) than the edge values. 115

4.14 Low-energy spectral index distribution of 8459 time-resolved spectra. [*Top Left*] *Good* parameters of all models. Numbers of parameters included are 1971 PWRL, 8050 COMP, 5510 BAND, and 6533 SBPL. The other plots show all (solid line) and *good* (dotted line) parameters of COMP (green), BAND (blue), and SBPL (red). The lowest (highest) bin includes values lower (higher) than the edge values. 116

4.15 High-energy spectral index distribution of 8459 time-resolved spectra. [*Top*] *Good* parameters of all models. Numbers of parameters included are 1971 PWRL, 4810 BAND, and 7003 SBPL. The other plots show all (solid line) and *good* (dotted line) parameters of BAND (blue) and SBPL (red). The lowest (highest) bin includes values lower (higher) than the edge values. 117

4.16 $E_{\rm peak}$ distribution of 8459 time-resolved spectra. [*Top Left*] *Good* parameters of all models. Numbers of parameters included are 7702 COMP, 4677 BAND, and 3291 SBPL. The other plots show all (solid line) and *good* (dotted line) parameters of COMP (green), BAND (blue), and SBPL (red). The lowest (highest) bin includes values lower (higher) than the edge values. 118

4.17 Break energy distribution of 8459 time-resolved spectra. [*Top*] *Good* parameters of all models. Numbers of parameters included are 4825 BAND and 7207 SBPL. The other plots show all (solid line) and *good* (dotted line) parameters of BAND (blue) and SBPL (red). The lowest (highest) bin includes values lower (higher) than the edge values. 119

4.18 ΔS distribution of 8459 time-resolved spectra. ΔS is the difference between low-energy and high-energy indices. [*Top*] *Good* parameters of all models. Numbers of parameters included are 5322 BAND and 4441 SBPL. The other plots show all (solid line) and *good* (dotted line) parameters of BAND (blue) and SBPL (red). The lowest (highest) bin includes values lower (higher) than the edge values. 120

4.19 Count spectra of GRB 000429 (trigger number 8087). Data points are shown as crosses and the color lines are convolved model counts. COMP, BAND, and SBPL all fit statistically as good as each other. The BEST model determined by parameter constraints in this case is SBPL. 125

4.20 BEST model parameter distributions of the time-integrated spectra. The black lines show the total distributions, and the constituents are shown in colors. The lowest (highest) bin includes values lower (higher) than the edge values. 132

4.21 BEST model parameter distributions of the time-integrated spectra. The black lines show the total distributions, and the constituents are shown in colors. The lowest (highest) bin includes values lower (higher) than the edge values. 133

4.22 BEST model parameter distributions of the time-resolved spectra. The black lines show the total distributions, and the constituents are shown in colors. The lowest (highest) bin includes values lower (higher) than the edge values. 134

4.23 BEST model parameter distributions of the time-resolved spectra. The black lines show the total distributions, and the constituents are shown in colors. The lowest (highest) bin includes values lower (higher) than the edge values. 135

4.24 [*Top*] BEST model history of GRB 950403 (BATSE trigger number 3491). The BEST model of the time-integrated for this burst is SBPL. [*Bottom*] Evolutions of the low-energy index (effective) and $E_{\rm peak}$ for the same event. The arrowheads in $E_{\rm peak}$ plot indicate where the $E_{\rm peak}$ values cannot be determined. 139

4.25 [*Top*] BEST model history of GRB 950403 (BATSE trigger number 3492). The BEST model of the time-integrated for this burst is SBPL. [*Bottom*] Evolutions of the low-energy index (effective) and $E_{\rm peak}$ for the same event. The arrowheads in $E_{\rm peak}$ plot indicate where the $E_{\rm peak}$ values cannot be determined. 140

4.26 Comparisons of the BEST model parameter distributions of time-integrated (dotted; right axis) and time-resolved spectra (solid; left axis). The lowest (highest) bin includes values lower (higher) than the edge values. 141

4.27 Comparisons of the BEST model break scale and ΔS distributions of time-integrated (dotted; right axis) and time-resolved spectra (solid; left axis). The break scale values are for spectra fitted with SBPL only, while ΔS values are for those fitted with BAND and SBPL. 143

4.28 Spectral evolution of GRB 911109 (BATSE trigger number 1025). Time-resolved BEST models are color-coded by time from yellow to red, earlier to later. Time-integrated BEST model is plotted in black solid curve. The blue-dashed curve shows the $\bar{\mathcal{F}}_{flnc}$ spectrum, which is consistent with the BEST model. 146

4.29 Distribution of peak (maximum) photon flux (*top*) and total photon fluence values (*bottom*) of 325 bursts. The bursts with $P_{\chi^2} > 1\%$ (solid line) have lower peak flux than those with $P_{\chi^2} < 1\%$ (dotted line). 147

4.30 [*Top*] The actual deconvolved time-integrated photon data and model of GRB 980306. [*Bottom*] The spectral evolution of GRB 980306 (yellow to red, earlier to later) blue dashed curve is the constructed photon flux $\bar{\mathcal{F}}$. In both plots, the best-fitted model (SBPL with $\Lambda = 0.2$) is plotted with black solid curves. 149

4.31 Example scatter plots of $E_{\rm peak} - \alpha$ of GRB 931204 (trigger number 2676; *top*) and $E_{\rm b} - \alpha$ of GRB 941017 (3245; *bottom*). Both show strong correlations. 154

4.32 Example scatter plots of $E_{\rm peak} - \beta$ of GRB 911118 (trigger number 1085; *top*) and $E_{\rm b} - \beta$ of GRB 980203 (6587; *bottom*). Positive (*top*) and negative (*bottom*) correlations are seen. 155

4.33 Example scatter plot of $\alpha - \beta$ of GRB 920824 (trigger number 1872). Negative correlation is evident. 156

4.34 [*Top*]Energy fluence in 20 – 2000 keV vs. $E_{\rm peak}$ plot. The Amati relation limit is shown as a solid line and Ghirlanda 3σ limit is shown as a dashed line. Bursts below these lines are inconsistent with the relation. The uncertainties are 1σ. [*bottom*]$E_{\rm peak}$ distributions of three different intensity groups. 159

4.35 The distributions of the BAND fit β values of time-resolved spectra within varying-β (solid line) and constant-β (dotted line) GRBs. The lowest bin includes values lower than –4. 161

4.36 Parameter evolution of a short event, GRB 000326 (trigger number 8053). The photon flux histories are over-plotted with dotted lines (top panel, right axis). $E_{\rm peak}$ tracks the photon flux while the indices evolve from hard to soft. 164

5.1 LAD and TASC lightcurves of GRBs 950425 and 990104. The dotted lines show background models and the vertical solid lines indicate the selected integration time intervals. 173

5.2 Parameter distribution comparisons of 15 joint events with 342 bright BATSE GRBs. The crosses represent photon fluence (*top*) and spectral indices (*bottom*) of jointly analyzed events, and histogram shows the distribution of LAD events. 176

5.3 Parameter distribution comparisons of 15 joint events with 342 bright BATSE GRBs. The crosses represent $E_{\rm peak}$ (*top*) and break energy (*bottom*) values of jointly analyzed events, and histogram shows the distribution of LAD events. 177

5.4 Effective low-energy indices (*top*) and high-energy indices (*bottom*) determined by joint analysis and individual analysis of LAD and TASC. Left axis shows the event trigger numbers. 179

5.5 $E_{\rm peak}$ (*top*) and break energy (*bottom*) values determined by joint analysis and individual analysis of LAD and TASC. Left axis shows the event trigger numbers. For 2329, $E_{\rm peak} > 167$ MeV. 180

5.6 Lightcurves (*top*) and time-integrated νF_ν spectrum (*bottom*) of LAD and TASC of GRB 941017 (trigger number 3245). Dotted lines in the lightcurves are background models. The spectra were fitted with the BEST model shown in solid line in the spectrum (Table 5.2). The normalization 182

5.7 Effective area correction values of 15 events as a function of incident zenith angle. 183

5.8 Spectral evolution of GRB 941017, shown in νF_ν spectra. LAD data (plus sign) and TASC data (filled circle) are fitted with BAND and additional power law with index ~ -1. 185

5.9 νF_ν spectra corresponding to the second and third time intervals of Figure 5.8, with the data from LAD, TASC, and COMPTEL. The BAND model and the additional high-energy PWRL model are shown separately with dashed lines. 188

6.1 (a) Regular synchrotron emission case where only parts of trajectory is observed and (b) jitter radiation case where the entire trajectory is observed (from Medvedev 2000). 196

6.2 A composite F_ν spectrum of jitter (short dashed) + synchrotron (long dashed; from Medvedev 2000). 197

6.3 *Good* time-resolved low-energy index distribution (same as Figure 4.22, top left panel), with three critical values indicated. 199

6.4 Distribution of deviations (in units of σ) of time-resolved low-energy indices from values predicted by the emission models; 0 (solid line), –2/3 (dashed line), and –3/2 (dash-dot line). Positive 3σ deviation is marked by the dotted line. 200

6.5 Examples of hard low-energy index events. Clockwise from top left: GRB 910807 (trigger number 647), GRB 930214 (2193), GRB 980306 (6630), and GRB 970111 (5773). The photon flux histories are over-plotted with dotted lines (right axes) and index = 0 is indicated by dashed lines. . . . 202

6.6 Examples of hard low-energy index events; GRB 921009 (trigger number 1983; *top*) and GRB 000221 (7994; *bottom*). The photon flux histories are over-plotted with dotted lines (right axes) and index = –2/3 is indicated by dashed lines. 204

6.7 Examples of constant low-energy index events: GRB 000511 (trigger number 8101, *top*) and GRB 910614 (351, *bottom*). The photon flux histories are over-plotted with dotted lines (right axes). 206

6.8 Examples of variable high-energy index events, GRB 941023 (trigger number 3255, *top*) and GRB 970201 (5989, *bottom*). The photon flux histories are over-plotted with dotted lines (right axes). Arrows indicate COMP model fits where no high-energy component is evident. 209

C.1 The BAND model (dashed curve) and the SBPL model (solid curve) with the same low-energy index values of $\alpha = \lambda_1 = -1$. The other parameters are also kept the same ($E_{\rm peak} = 300$ keV and $\beta = \lambda_2 = -2.5$). A dotted line is a power law with index of –1. The difference in the low-energy behavior is evident. 230

C.2 The comparison of the effective α distribution (solid line) and the fitted α distribution (dashed line) of the BAND model fits to the 7861 time-resolved spectra. 231

LIST OF TABLES

Table **Page**

2.1 BATSE trigger criteria history. Only the changes are noted. 18

2.2 BATSE data types. 21

4.1 Basic properties of 350 GRBs included in the catalog. 73

4.2 Example fit results to simulated BAND spectra. The parameters are median values and the standard deviations are shown in parentheses. . . . 94

4.3 Results of BAND fits to simulated SBPL spectra with various Λ. The simulated Parameters are $A = 0.05$, $E_{\rm b} = 300$ keV, $\lambda_1 = -1.0$, and $\lambda_2 = -2.5$. "$E_{\rm peak}$" is the calculated νF_ν peak energy in the SBPL model. The parameters are median values and the standard deviations are shown in parentheses. 103

4.4 The percentage of fits resulted in χ^2 with confidence level within 3σ (99.7%) out of the total number of 342 time-integrated spectra and 8459 time-resolved spectra. 105

4.5 Spectral parameters fitted in each model. 107

4.6 The most probable *good* parameter values and the widths of the distributions determined by fitting all spectra, both time-integrated and time-resolved, separately with four models. 110

4.7 Model comparison summary. The best-fit models were first determined statistically by χ^2 probabilities (Column 1) and finalized by fitted parameter constraints (Columns 3 – 6, 8 – 11). 123

4.8 Summary of time-integrated spectral fit results of 342 GRBs. 1σ uncertainties are shown in parentheses. 126

4.9 Most probable parameter values and HWHM determined by the BEST model fits. The BEST model set consists of 17 (374) PWRL, 70 (3164) COMP, 118 (2828) BAND, and 137 (2093) SBPL time-integrated (time-resolved) spectra. The constituent parameter distribution values are also shown. 136

4.10 Comparison of the most probable values for time-integrated and time-resolved spectra. HWHM of each distribution is shown in parentheses. K-S probabilities and the corresponding parameters for two distributions are also shown. 142

4.11 Summary of total numbers of events considered for each correlation and percentages of events with high significance. 151

4.12 Events with strong spectral parameter correlations. Spearman rank correlation coefficients (r_s) and associated significance probabilities (P_{rs}) are listed. α and β denote low-energy and high-energy indices. 152

4.13 Summary of time-integrated spectral fit results for 17 short GRBs. 1σ uncertainties are shown in parentheses. 162

4.14 Median values of the BEST spectral parameters for short and long GRBs. K-S probabilities and the corresponding K-S parameters for two distributions are also shown. 163

5.1 General properties of GRBs included in the LAD–TASC joint spectral analysis. 171

5.2 Summary of LAD–TASC joint fit results for time-integrated spectra. 1σ uncertainties are shown in parentheses. 175

5.3 Best fit parameters for the two time intervals, with only LAD and TASC data ("**LAD+TASC**"), and with data from all three instruments ("**+COMPTEL**"). The uncertainties are 1σ. 189

6.1 Numbers and percentages of 8459 time-resolved spectra providing low-energy indices inconsistent with 1, 0, –2/3, and –3/2 (by 1σ and 3σ). . . . 201

LIST OF SYMBOLS

Symbol	Definition
A	Amplitude
α	BAND Low-Energy Spectral Index; Electron Deflection Angle
$\bar{\alpha}$	Afterglow Time Index
$\alpha_{\rm eff}$	Effective α
B	Magnetic Field
$B_{\rm LS}$	Large-Scale Magnetic Field Strength
$B_{\rm SS}$	Small-Scale Magnetic Field Strength
β	BAND High-Energy Spectral Index
$\bar{\beta}$	Afterglow Spectral Index
c	Speed of Light
$D_{\rm KS}$	The Kolmogorov-Smirnov Parameter
ΔS	Spectral Index Difference
δ	Ratio of Electron Deflection Angle to Beaming Angle
δt	Variability timescale
$\Delta\theta$	Synchrotron Emission Beaming Angle
e	Electron Charge
E_0	e-folding Energy of BAND and COMP Models
$E_{\rm b}$	Break Energy of SBPL Photon Spectrum
$E_{\rm c}$	BAND Characteristic Energy

E_e	Electron Energy
$E_{\rm peak}$	Peak Energy of Power Spectrum
$E_{\rm piv}$	Pivot Energy
f	Photon Flux
$\mathcal{F}$	Time-Integrated Photon Flux
$\bar{\mathcal{F}}$	Constructed Time-Integrated Photon Flux
ϕ	Compton Scattering Angle
Γ	Bulk Lorentz Factor
γ, γ_e	Electron Lorentz Factor
γ_m	Lorentz Factor of Electron with Energy ν_m
$\mathcal{L}$	Luminosity
Λ	SBPL Break Scale
λ	PWRL Spectral Index
λ_1	SBPL Low-Energy Spectral Index
λ_2	SBPL High-Energy Spectral Index
$M_\odot$	Solar Mass
m_e	Electron Mass
m_o	Electron Rest Mass
M_o	Baryon Rest Mass
N	Number
n	Electron Number Density
ν	Photon Energy
ν_a	Synchrotron Self-Absorption Energy
ν_c	Synchrotron Cooling Energy
$\nu_{\rm jm}$	Jitter Radiation Characteristic Energy
ν_m	Minimum Energy of Accelerated Electrons
P	Peak Photon Flux

$P(\gamma_e)$	Synchrotron Emission Power
$P_{\rm KS}$	The Kolmogorov-Smirnov Probability
P_{rs}	Rank-Order Correlation Significance Probability
P_{χ^2}	χ^2 Significance Probability
p	Electron Energy Distribution Index
R	Emission Radius
r	Radius; Distance
R_{jk}	Correlation Coefficient
r_s	Spearman Rank-Order Correlation Coefficient
S	Energy Fluence
T_{50}	Time to Accumulate 50 % of Total Counts
T_{90}	Time to Accumulate 90 % of Total Counts
θ	Jet Half-Opening Angle
V	Volume
$\omega_{\rm pe}$	Electron Plasma Frequency
z	Cosmological Redshift

LIST OF ACRONYMS

Acronym	**Definition**
BAND	GRB Model (§4.2.2.2)
BATSE	Burst and Transient Source Experiment
BEST	Best-Fitted Model
BETA	GRB Model with Fixed β (§4.2.2.3)
BSA	Burst Spectrum Analyzer
CEU	Central Electronics Unit
CGRO	*Compton Gamma-Ray Observatory*
COMP	Comptonized Model (§4.2.2.4)
COMPTEL	Imaging Compton Telescope
CONT	Continuous Data
CPD	Charged Particle Detector
dof	Degrees of Freedom
DRM	Detector Response Matrix
EAC	Effective Area Correction
EGRET	Energetic Gamma-Ray Experiment Telescope
FWHM	Full-Width at Half Maximum
GBM	GLAST Burst Monitor
GRB	Gamma-Ray Burst
HERB	High-Energy Resolution Burst Data

HWHM	Half-Width at Half Maximum
LAD	Large Area Detector
LAT	Large Area Telescope
MER	Medium-Energy Resolution Data
PHA	Pulse Height Analyzer
PWRL	Power Law Model (§4.2.2.1)
PMT	Photo Multiplier Tube
SBPL	Smoothly-Broken Power Law Model (§4.2.2.5)
S/N	Signal-to-Noise Ratio
SD	Spectroscopy Detector
SMM	*Solar Maximum Mission*
SSM	Synchrotron Shock Model
TASC	Total Absorption Shower Counter

CHAPTER 1

INTRODUCTION

Sudden flashes of gamma-ray photons, known as gamma-ray bursts (GRBs), occur randomly in the sky and outshine all other gamma-ray sources for a short period of time. Despite extensive studies during the past few decades, the creation mechanism of GRBs and their progenitors still remains uncertain. Durations of GRBs vary from milliseconds to a few minutes, and their time profiles are extremely diverse, often very complex with very high variability (Fishman & Meegan 1995). Based on their durations, GRBs are broadly classified into two groups: short GRBs and long GRBs, with ~ 2 second as a dividing line (Kouveliotou et al. 1993). Long GRBs are usually followed by afterglow emission observable in the longer wavebands, lasting much longer than the bursts themselves, for hours to months after the bursts. Multi-wavelength observations of afterglow emission have provided advancement in our knowledge of the energetic events in recent years (van Paradijs et al. 2000). The total energy released is estimated to be about $10^{50} - 10^{51}$ ergs, and the emission is believed to be collimated in a jet with an opening angle of ~ 3 – 30 degrees (Frail et al. 2001; Ghirlanda et al. 2004). Many of them are known to originate in distant star-forming galaxies, and sometimes accompanied by a supernova (Zhang & Mészáros 2004; Piran 2005).

The current theoretical picture of long GRBs is that they are associated with a massive star collapsing into a black hole at the end of its life (Woosley 1993; MacFadyen & Woosley 1999). When this catastrophic event occurs, a series of

relativistically expanding shells is ejected. GRB prompt emission is believed to be emitted by relativistic electrons that have been accelerated in a shock formed when two expanding shells (with different velocities) collide with one another, dissipating some of their kinetic energy. As the shells keep traveling outward, they encounter interstellar medium and go through another series of shocks. Radiation from electrons accelerated in these external shocks is thought to be responsible for afterglow emission. It has been widely believed that the shock-accelerated electrons emit their energy via synchrotron radiation due to a magnetic field behind the shock (Katz 1994; Tavani 1996a,b). Afterglow observations seem to be consistent with this picture; however, observations of prompt GRB emission have shown inconsistency with this model.

The bulk amount of the total energy budget of GRBs is contained in prompt gamma-ray emission. Therefore, understanding GRB prompt emission spectra is crucial to revealing their nature. GRB spectra are non-thermal, generally well described by two power laws joined smoothly at a break energy (Band et al. 1993; Preece et al. 2000). They are usually characterized by their power law indices and the peak energy in power density spectrum, $E_{\rm peak}$, where the most energy is emitted. The low-energy power law indices have been extensively studied and a substantial fraction of spectra was found to be inconsistent with the values expected from the synchrotron shock model (Preece et al. 1998b, 2000; Ghirlanda et al. 2002; Preece et al. 2002; Lloyd-Ronning & Petrosian 2002). Some alternative emission models have been proposed to account for such spectra, including the anisotropic pitch-angle model (Lloyd-Ronning & Petrosian 2002), the fireball photospheric model (Mészáros & Rees 2000), the saturated Comptonization model (Liang et al. 1997), and the jitter radiation model (Medvedev 2000). Strong spectral evolutions have also been observed in many events (e.g., Ford et al. 1995; Liang & Kargatis 1996; Band 1997; Crider et al. 1997; Preece et al. 1998a; Ryde 1999; Crider et al. 1999;

Lloyd-Ronning & Petrosian 2002; Ghirlanda et al. 2003). In addition, previous analysis of GRBs observed with the Burst and Transient Source Experiment (BATSE) found a very narrow distribution of $E_{\rm peak}$ and spectral break energy, centered about 220 keV with a width of less than a decade of energy (Preece et al. 2000). Given that spectra are shifted due to the cosmological redshift, by a factor of $(1+z)$ from their source spectra, the narrowness of the distribution implies even narrower intrinsic distribution. This poses a challenge to the current internal shock model or any other existing model of GRB prompt emission. Although redshift values of most BATSE GRBs are unknown, their redshift range is assumed to extend up to $z \gtrsim 5$ (e.g., Bromm & Loeb 2002). A possible instrumental sensitivity limitation has also been suggested to explain the narrowness of $E_{\rm peak}$ distribution (e.g., Piran 2005). There are also some correlations found observationally, such as ones between $E_{\rm peak}$ & low-energy index (Crider et al. 1997; Lloyd-Ronning & Petrosian 2002), $E_{\rm peak}$ & isotropic-equivalent total energy (Amati et al. 2002), $E_{\rm peak}$ & collimation-corrected total energy (Ghirlanda et al. 2004), and $E_{\rm peak}$ & peak flux or energy fluence (Lloyd et al. 2000).

GRB spectra are very commonly fitted with an empirical function found by Band et al. (1993). The model seems to well describe most GRB spectra; however, some spectra have been found to be better (or as adequately well) described by other photon models (Preece et al. 2000; Ghirlanda et al. 2002). Spectral parameters obtained from a GRB analysis often depend greatly on photon models employed and integration timescales of the spectra; therefore, in order to correctly understand spectral behavior of GRBs, any systematic biases must be removed. The primary goal of the work presented in this dissertation is to study model-unbiased spectral properties of GRB prompt emission with well-determined spectral parameters. A systematic analysis of bright GRB prompt emission spectra obtained with BATSE is performed, using various photon models often used in GRB spectral analyses. Our

sample size is much larger than the ones previously used, and will provide the most comprehensive resource of GRB spectral properties. Using the model-unbiased parameters, we study overall distributions, evolutions, correlations, and also examine some GRB emission models.

1.1 Dissertation Outline

Chapter 2 first reviews scintillation detector physics, and describes characteristics and data types of each instrument involved in this work: BATSE, the Energetic Gamma-Ray Experiment Telescope (EGRET), and the Imaging Compton Telescope (COMPTEL) all aboard the *Compton Gamma-Ray Observatory*. Detector response matrices (DRMs), which are indispensable to gamma-ray spectroscopy, are also reviewed, and problems with the BATSE Spectroscopy Detector DRMs are investigated. GRB observations and theoretical advancements marked by some key events are summarized in Chapter 3 including a review of current GRB models.

Chapter 4 presents a high-energy resolution spectral analysis of 350 bright GRBs observed with BATSE. A total of 342 time-integrated spectra and 8459 time-resolved spectra is analyzed with various photon models. The models employed are also explored in order to understand their characteristics possibly affecting the spectral fit results. We obtain best-fitted spectral parameters that are unbiased by photon models and study the overall parameter distributions, correlations, and evolution within bursts. We also show the relation between time-integrated spectra and time-resolved ones and identify some cases in which the time-integrated spectra deviate from a simple broken power law. The narrow distribution of $E_{\rm peak}$ is confirmed with much better statistics.

In Chapter 5, we study high-energy broadband spectral properties of 15 GRBs by combining BATSE and EGRET observations. Continuum spectra of GRBs extend

up to $\sim$ 200 MeV without a cutoff, and are usually described by an extension of a BATSE component. Indication of possible high-energy excess is found in two events, including GRB 941017, for which a delayed distinct MeV spectral component was previously identified with time-resolved analysis. We also confirm the high-energy component of GRB 941017 using the COMPTEL observation.

Chapter 6 examines the existing GRB emission models with the use of the well-constrained, model-unbiased spectral parameters obtained in Chapters 4 and 5. We find a significant number of GRB spectra that violate the low-energy index limit predicted by the synchrotron shock model, although they are a smaller fraction of sample than previously reported. Some interesting cases are also studied in the context of several emission models. Finally, Chapter 7 summarizes the results obtained, and the prospects for future work are discussed.

We note that the naming of GRB is traditionally done by the date of the detection in UT, in the form of "GRB *yymmdd*." For example, a burst that occurred on January 23, 1999 is referred to as GRB 990123. Additionally, for BATSE-triggered GRBs, there are also BATSE trigger numbers associated with them. Both the GRB name and BATSE trigger numbers are used when introducing individual events throughout this dissertation.

CHAPTER 2

INSTRUMENTS

Gamma-rays can only be detected in space due to the atmospheric absorption of the high-energy photons. Starting from the *Vela* satellite, which discovered the phenomenon of GRB, a few dozen space-based gamma-ray detectors have observed GRBs. The GRB data used in this dissertation work were collected with three different experiments, all on board the *Compton Gamma-Ray Observatory* (*CGRO*), namely, the Burst and Transient Source Experiment (BATSE), the Energetic Gamma-Ray Experiment Telescope (EGRET), and the Imaging Compton Telescope (COMPTEL). The *CGRO* was launched in April 1991, as one of NASA's Great Observatories: a series of four space-based observatories to study astronomical objects or phenomena in visible, gamma-ray, X-ray, and infrared energy bands. The *CGRO* observed the sky in high-energy gamma-rays and detected thousands of GRBs as well as many other high-energy transient phenomena in its nine-year lifetime that ended in June 2000.

In this chapter, detailed descriptions of the gamma-ray detectors involved in this work are presented, and detector response matrices used in the spectral analysis are discussed. The sections are organized as follows. First, a general discussion of the scintillation detector physics is presented in §2.1. Then the BATSE, EGRET, and COMPTEL detectors are described in §2.2 through §2.4. Finally, some problems associated with the BATSE Spectroscopy Detector response matrices are identified and discussed in detail in §2.5.

2.1 Gamma-Ray Detectors

Detecting gamma-ray photons is possible only when high-energy photons interact within absorbing material, to which their energies are transferred. Although photon interaction processes in the absorbing material, such as sodium iodide (NaI) crystals are well known, understanding and calculating detector's behavior can be extremely complicated. Detector Response Matrices (DRMs) are usually generated to represent the detector behavior (or response) and used when observed spectra are analyzed so as to correct the detector dependency of observed count spectra. Therefore, accurate DRMs are crucial to perform spectral analysis and tremendous effort is usually put into generating DRMs as accurately as possible (see §2.5 for detailed discussions of DRMs). All data involved in this dissertation work were collected with NaI scintillation detectors. Therefore, in this section, the scintillation mechanism of NaI detectors is reviewed.

2.1.1 NaI Scintillation Detectors

A typical NaI scintillation detector consists of a NaI scintillator crystal that is coupled to a photomultiplier tube (PMT), which converts scintillation photons to photoelectrons. It is the most commonly used high-energy photon detector, due to its excellent light yield as well as its relatively high atomic number (effective Z = 50). The principle mechanism of the scintillation detector is that an incident photon interacts with the crystal, and some or all of its energy is transferred to electrons in the scintillator, which in turn is converted to visible scintillation light. The PMT transforms the scintillation photon into photoelectrons that are measurable by electronic devices. For efficient yielding of the scintillation light, NaI crystals are

usually "doped" with thallium (Tl). The Tl is called an activator in this case and thallium-doped (or -activated) NaI is noted as NaI(Tl).

There are several mechanisms for gamma-ray photons to interact in the scintillation crystal, the most significant ones being photoelectric absorption, Compton scattering, and pair production. The interaction cross sections for these three processes in the NaI crystal are energy dependent, as shown in Figure 2.1. The details of the each gamma-ray interaction process and the resulting energy depositions are described below.

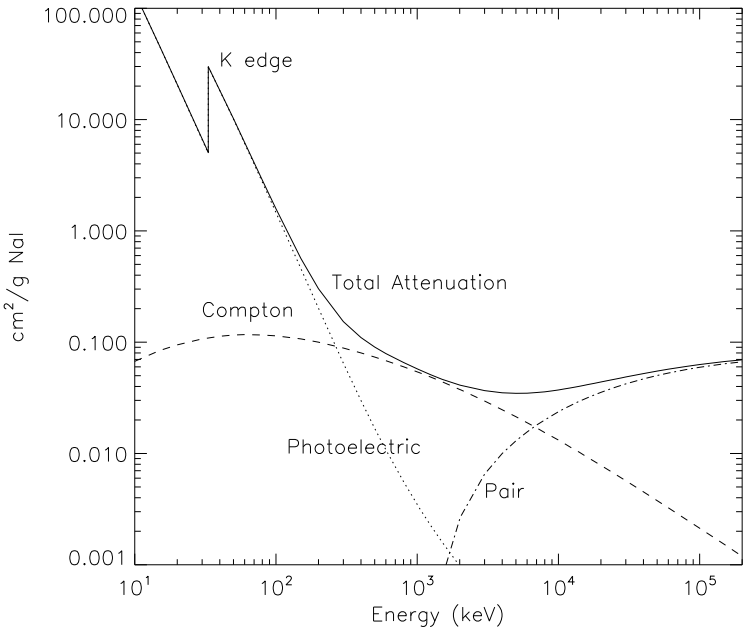

Figure 2.1 Cross sections for gamma-ray photon interaction processes in NaI crystal.

2.1.1.1 Photoelectric Absorption

The photoelectric absorption process is dominant at relatively lower energies, below a few hundred keV (Figure 2.1). In photoelectric absorption, almost all of

the incident photon energy is transferred to bound electrons in the crystal through photoelectric effect. This is followed by fluorescent X-ray emission that is usually also fully absorbed. Therefore, in the measured spectrum, photons that undergo this process contribute to *photopeak* (or *full energy peak*) at $E \sim h\nu$ (see Figure 2.2). Ideally, this peak would simply be a delta function if incident photons were monoenergetic. Practically, it is broadened, and the width of the peak depends on the efficiency of the detector. The sudden increase of the cross section at ~ 30 keV is called the *K-edge*. This edge is the result of the incident photon energy being sufficiently high to overcome the inner K-shell electron binding energy of iodide atoms, and hence the inner shell electrons become accessible for the interaction as well as the outer shell electrons.

2.1.1.2 Compton Scattering

If the incident photon energy is between a few hundred keV and several MeV (see Figure 2.1), Compton scattering becomes the dominant photon interaction process. When an incident photon is Compton scattered by an electron in the crystal to some angle ϕ, a part of its energy is transferred to the electron. The amount of energy transferred is the difference between the incident photon energy and the scattered photon energy ($E_e = h\nu - h\nu'$), where the scattered photon energy ($h\nu'$) can be derived using conservation of energy and momentum;

$$h\nu' = \frac{h\nu}{1 + \frac{h\nu}{m_o c^2}(1 - cos\phi)}. \tag{2.1}$$

Here, $h\nu$ is the incident photon energy, $m_o c^2$ is the electron rest energy, and ϕ is the scattering angle with respect to the original direction of the incident photon. Evidently, the electron energy (E_e) is maximum when $\phi = \pi$ (scatter backwards), and minimum when $\phi = 0$ ($E_{e,\min} = 0$; $h\nu' = h\nu$, no scattering). The maximum

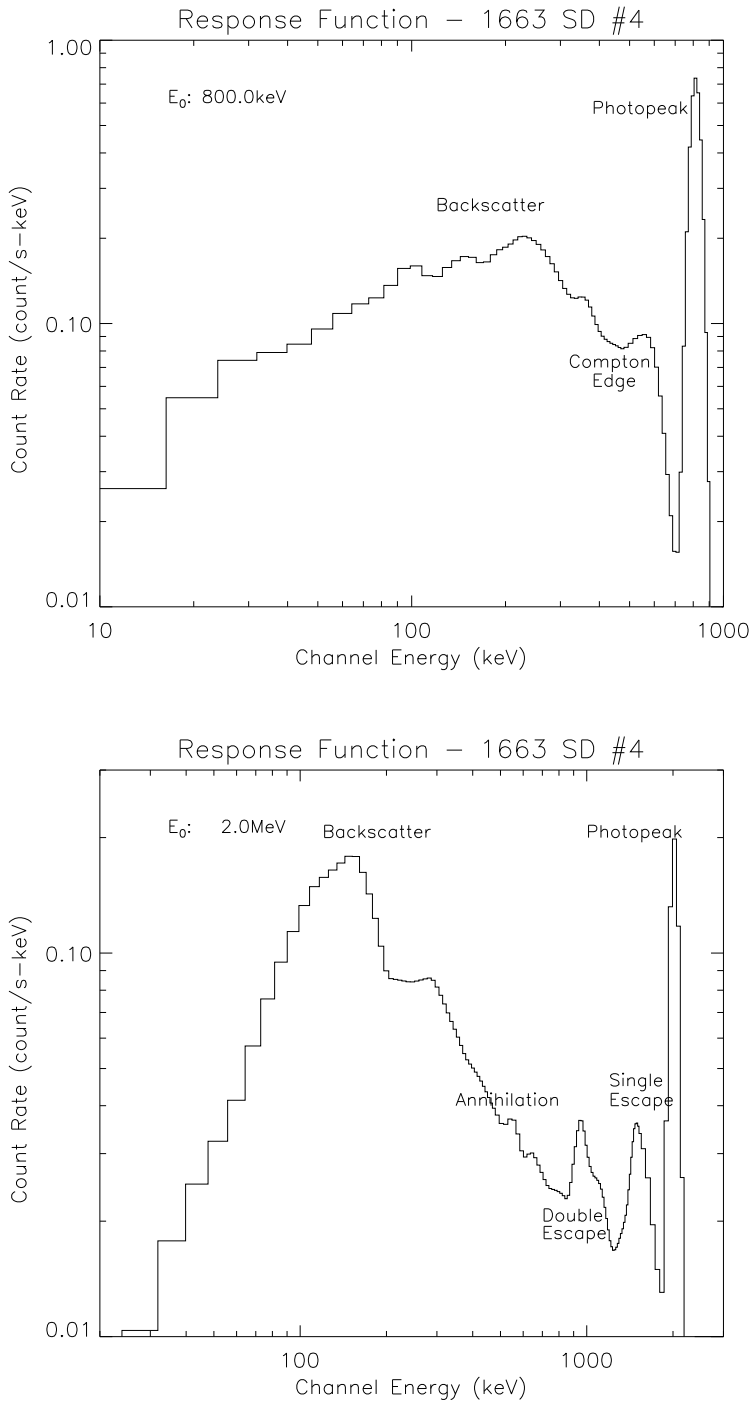

Figure 2.2 [*Top*] Response function for an input photon energy of 800 keV. Contributions from photoelectric absorption and Compton scattering are seen. [*Bottom*] Response function for an input photon energy of 2 MeV. Contribution from pair production is seen.

electron energy can be written as

$$E_{e,\max} = h\nu \left(1 - \frac{1}{1 + \frac{2h\nu}{m_o c^2}} \right) < h\nu. \tag{2.2}$$

Since any scattering angle is possible, the distribution of the electron energy is continuous from 0 to $E_{e,\max}$, and its shape can be predicted by the Klein-Nishina cross section for a given incident photon energy. The upper edge of this distribution (*Compton continuum*), corresponding to $E_{e,\max}$, is called the *Compton edge*, as seen in Figure 2.2.

2.1.1.3 Pair Production

For incident photons with even higher energy ($\gtrsim$ 7 MeV, see Figure 2.1), pair production becomes the most important photon interaction process. This process can occur in the vicinity of heavy nuclei in the crystal, and it converts the photon energy to an electron-positron pair. In order for the process to take place, the incident photon energy must be at least the rest energy of electron-positron pair ($2m_o c^2 = 1.022$ MeV). Any excess energy is shared by the produced pair as their kinetic energies. If all of their kinetic energies are absorbed in the material, it results in producing a peak at an energy $h\nu - 2m_o c^2$. However, this is not the case most of the time since the positron quickly annihilates with an available electron, producing two photons with energy $m_o c^2$. Depending on where in the crystal this event occurs, one or both of these annihilation photons may escape the detector. If only one such photon escapes the detector without interaction and the other one is totally absorbed, this contributes to a peak at an energy $h\nu - m_o c^2$, and is known as the *single escape peak*. On the other hand, if both such photons escape the detection, its contribution is to another peak at an energy $h\nu - 2m_o c^2$, and is known as the *double escape peak*. If neither one of them escapes, it contributes to the photopeak.

2.2 Burst And Transient Source Experiment

The Burst And Transient Source Experiment (BATSE) was specifically designed to detect GRBs and study their temporal and spectral characteristics in much greater resolution than the previous experiments. In order to increase the GRB detection probability, BATSE consisted of eight detector modules that were located at the corners of the spacecraft so as to cover the entire 4π steradian of sky (Figure 2.3). Each module was oriented at an angle of 54.7° with respect to the spacecraft's z-axis so that all eight modules together would form an octahedron. This allowed any given burst to be observed with four BATSE detectors, which enabled subsequent localizations of the events to a few degrees. The eight modules were numbered 0 to 7. They were arranged aboard the spacecraft such that a sum of the module numbers on opposite faces of the octahedron was always 7. Even number modules (0, 2, 4, and 6) were placed on +z side of the spacecraft (Figure 2.3). In the spacecraft x-y plane, module 0 was located in (+x, +y), module 2 in (+x, –y), module 4 in (–x, +y), and module 6 in (–x, –y). The detector numbers that are used later in this dissertation correspond to these module numbers. Each module comprised two types of detectors, a Large Area Detector (LAD) and a Spectroscopy Detector (SD) (Figure 2.4). They were both NaI(Tl) scintillation detectors of different dimensions designed to achieve different scientific goals.

2.2.1 Large Area Detector

The LAD was the primary detector of BATSE. It was made of a disc-shaped NaI(Tl) crystal of 50.8-cm diameter and 1.27-cm thick, un-collimated for a large field of view. The crystal was mounted on a 1.91-cm layer of fused quartz, as an optical window, which was attached to a light collection cone. The scintillation light was collected by three 12.7-cm diameter PMTs, coupled to the cone. The interior

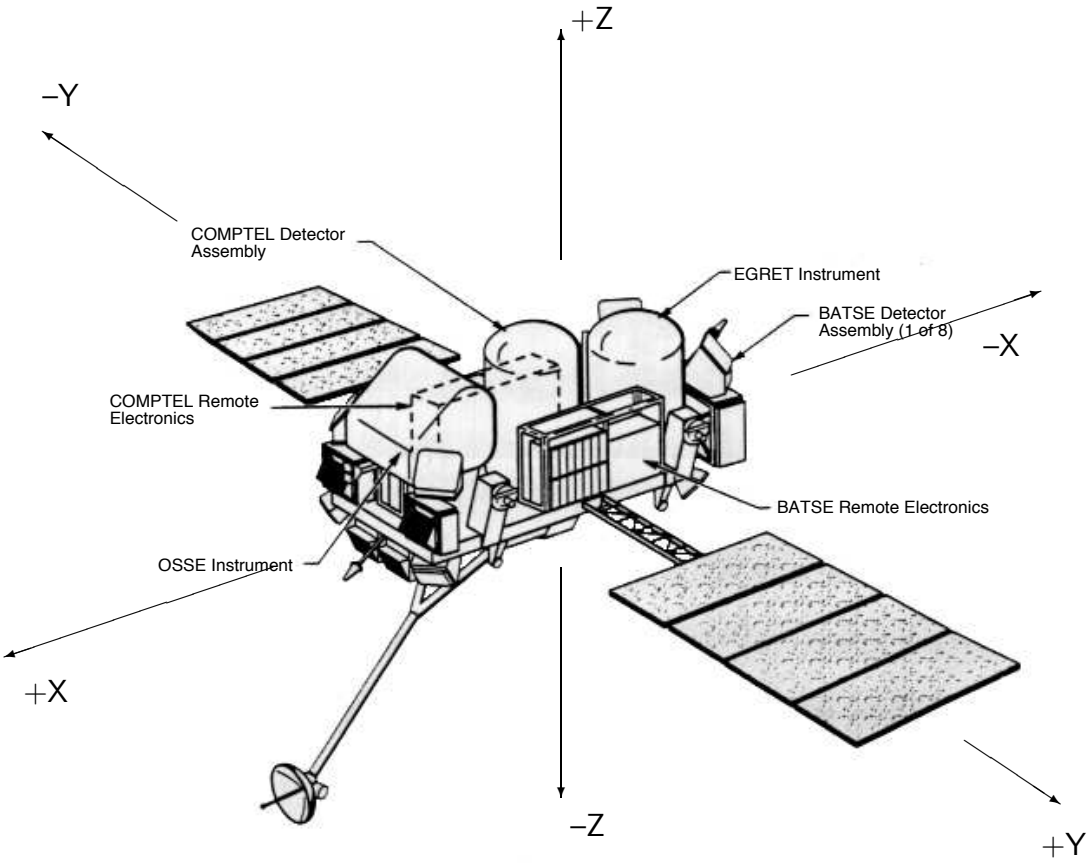

Figure 2.3 The *Compton Gamma-Ray Observatory.* The spacecraft's x, y, and z axes are shown.

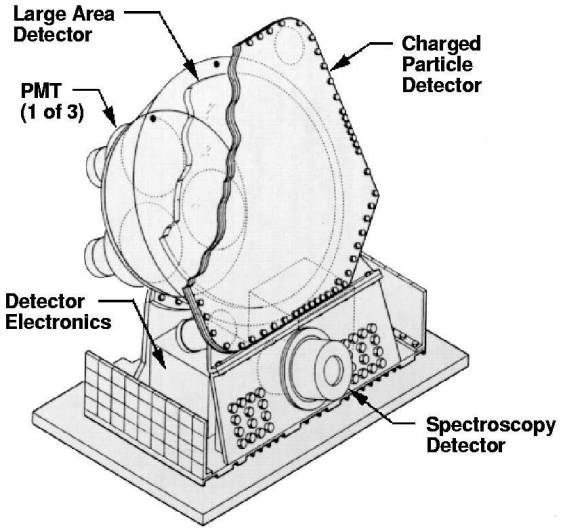

Figure 2.4 BATSE detector module (one of eight).

wall of the collection cone was coated with barium sulfate ($BaSO_4$), which is highly reflective to the scintillation light, and the outer layers were made of tin and lead, which acted as a passive shield from gamma-rays coming from the backside of the detector. The passive shielding was effective up to $\sim$ 300 – 400 keV.

Located in front of the LAD, the charged-particle detector (CPD) was a plastic scintillator of 0.64-cm thickness and used as an active shield against charged particles. The scintillator was an octagon of 55.9-cm width, enclosed between two aluminum honeycomb support layers. The scintillation light was collected by two 5.08-cm PMTs coupled to the plastic. The LAD and the CPD worked in anti-coincidence mode; namely, events registered in both detectors were rejected. The coincidence gating time was set to 2 μs and the energy threshold was $\sim$ 500 keV (Fishman et al. 1989).

The large detection area of the LAD provided much higher sensitivity than the SD (Figure 2.5), and thus offered a fine temporal resolution with a sufficiently high

energy resolution. The Full-Width at Half-Maximum (FWHM) energy resolutions of the LAD at 88, 511, 662, and 1275 keV are, on average, 27%, 17%, 16% and 19%, respectively (Horack 1991). The LAD used automatic gain control to stabilize the energy gain by adjusting the high voltage applied to the PMTs so that the 511 keV electron annihilation line position in the detector's channel space stays constant. Therefore, the energy ranges of all eight LADs were nearly fixed to 30 – 2000 keV throughout the mission.

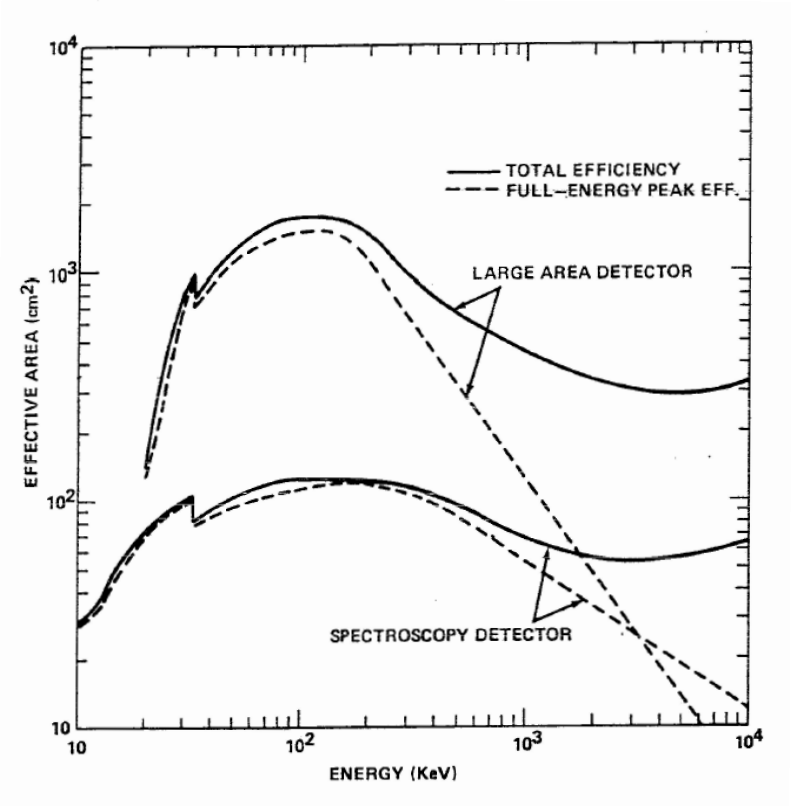

Figure 2.5 Effective areas of BATSE LAD and SD as a function of energy, for normal incident angle (from Fishman et al. 1989).

2.2.2 Spectroscopy Detector

The SD was also an un-collimated NaI(Tl) scintillation detector, but with a cylindrical shape of 12.7-cm diameter and 7.62-cm thick. It was directly coupled to a single PMT, identical to those used for the LADs. The housing of the PMT provided a passive shielding of tin and lead similar to that of the light collection cone of the LAD. On the BATSE module, the SD was mounted below the LAD (Figure 2.4), and its normal axis was offset by 18.5° from the LAD normal due to mechanical envelope constraints. Because of its geometry, the SD provided much finer energy resolution than the LAD. The FWHM energy resolutions of the SD at 88, 511, 662, and 1275 keV are, on average, 15%, 8%, 7% and 6%, respectively (Horack 1991). Unlike the LADs, the gains of the SDs were commandable from ground to allow broader energy coverage of as low as $\sim$ 5 keV, with high gain, to as high as $\sim$ 20 MeV, with low gain.

2.2.3 BATSE Science Datatypes

Both the LADs and the SDs provided various types of data products to be used for various purposes. Each detector module was equipped with a detector electronics unit, in which scintillation pulses were first processed. The signals from all detector modules were sent to the Central Electronics Unit (CEU). In the CEU, pulses were processed two ways: a fast, 4-channel discriminator circuit and a pulse-height analyzer (PHA) system. The lower- and upper-level discriminator thresholds were typically set so that the energy range of the four discriminator channels were $\sim 25-50$, $50-100$, $100-300$, and > 300 keV for the LADs, whereas for the SDs, they were gain dependent. The PHA produced a logic-level output pulse with duration proportional to the charge contained in the output pulse of the PMT. The PHA signals were converted to 128-channel quasi-logarithmic spectra for the LADs

and 256-channel quasi-logarithmic spectra for the SDs. The LAD PHA signals were also utilized to construct 16-channel spectra, based on programmable look-up tables. The discriminator data were accumulated every 64 ms, and were used for monitoring a bursting event. The CEU normally operated in the non-burst mode, and initiated the burst mode when a burst was triggered. The burst trigger was declared when count rates of at least two LADs exceed a certain signal-to-noise level on timescales of 64, 256, and 1024 ms, in ground commandable discriminator energy channels. The average background rate for each detector was determined over a programmable time interval (nominally ~ 17 s). The burst triggering criteria were ground commandable and changed throughout the mission, although mostly they were set to 5.5 σ above background in all time scales in energy range of 50 – 300 keV (discriminator energy channels 2 and 3). Table 2.1 lists the entire history of the BATSE trigger criteria.

In non-burst mode, the data were usually continuous, except for possible telemetry gaps. The data types available in this mode are Discriminator from the LADs and the SDs (DISCLA and DISCSP), Continuous (CONT), High Energy Resolution (HER), and Spectroscopy High Energy Resolution (SHER) data. The 4-channel DISCLA and DISCSP were read out every 1.024 s, while 16-channel CONT data (for the LADs only) provided 2.048 s time resolution. For higher spectral resolution, 128-channel HER data and 256-channel SHER data were made available for the LADs and SDs, respectively. They provided coarse time resolution to serve as background data. These non-burst mode data are available for all detectors.

In burst mode, the time coverage of each burst data types vary greatly, depending on their time and energy resolutions. The triggered detectors (i.e., the detectors that satisfied the triggering criteria) were identified on-board as DSELB detectors (two to four detectors), while the four brightest detectors, determined at the time of trigger, were identified as DSELH detectors. Burst data were generated for the

Table 2.1 BATSE trigger criteria history. Only the changes are noted.

Date	TJD/SOD	Disc. Channels	Thresholds (σ) 64ms	256ms	1024ms	Trig #	Number of GRBs
19-Apr-91		2+3	5.5	5.25	5.0		
28-Apr-91	8367/5632			5.5	5.5	105	16
10-May-91	8386/75036				7.0	179	19
04-Jun-91	8411/68201				5.5	268	392
18-Aug-92	8852/56078				10.0	1852	1
24-Aug-92	8858/81762			8.0	8.0	1874	0
26-Aug-92	8860/78199				10.0	1881	9
14-Sep-92	8879/70852			5.5	5.5	1928	683
19-Sep-94	9614/57154	3+4				3175	99
31-Jan-95	9748/55085	1+2	6.0	6.0	6.0	3386	1
06-Feb-95	9754/69000				10.0	3405	9
17-Feb-95	9765/62185	3+4	4.5	4.5	4.5	3434	35
12-Apr-95	9819/56745	1+2	6.0	6.0	6.0	3504	19
10-May-95	9847/74116				10.0	3570	35
20-Jul-95	9918/73523		20.0	10.0		3672	0
21-Jul-95	9919/62439		10.			3679[1]	0
24-Jul-95	9922/54971	1+2+3+4	26.0	6.0	6.0	3704	2
28-Jul-95	9926/66825		10.0			3713	27
05-Sep-95	9965/60364		5.5	5.5	5.5	3778	25
02-Oct-95	9992/77028	1+2			7.0	3843	15
23-Oct-95	10013/73672	2+3			5.5	3883	46
11-Dec-95	10062/77542	1			3.5	3942[2]	1
18-Dec-95	10069/64796				4.0	4027	8
07-Jan-96	10089/62939	1+2+3			5.5	4263	50
05-Apr-96	10178/85399	2+3				5413	88
25-Jun-96	10259/53576	3+4	4.5	4.5	4.5	5520	55
29-Aug-96	10324/77818	2+3	5.5	5.5	5.5	5589	54
05-Nov-96	10392/70428	1+2			7.0	5657[3]	53
25-Feb-97	10504/80816	2+3			5.5	6102	399
19-May-98	10952/52786	3+4				6765	10
31-May-98	10964/67660	1+2			7.0	6801	58
25-Aug-98	11050/71130	3+4			5.5	7019	3
30-Aug-98	11055/54346	1+2			7.0	7034	17
28-Sep-98	11084/69980	3+4			5.5	7132	72
27-Jan-99	11205/75731	2+3				7356	216
16-Sep-99	11437/72219	1+2				7768	2
20-Sep-99	11441/72476	2+3				7771	101
04-Feb-00	11578/51480	4				7981	5
14-Feb-00	11588/73920	3+4				7989	77

[1] Trigger requires that only one detector be above threshold.

[2] Trigger uses detector modules 2 and 3 only.

[3] Flight software crash on TJD/SOD 10416/16897 which was fixed TJD/SOD 10418/73555.

DSELB and DSELH detectors. In burst mode, the discriminator data produced are Discriminator Science (DISCSC), Time-Tagged Event (TTE), and Time-To-Spill (TTS) data. The DISCSC data were summed over all DSELB detectors with 64-ms time resolution, and were the outputs while the other data types were stored at a high rate for several minutes. The TTE provided a time resolution of 2 μs and recorded the time of occurrence, discriminator channel, and detector number up to 32,768 LAD photons individually. The data were recorded from a continually running ring buffer when the burst trigger occurred. On the other hand, the TTS data recorded the time it took to accumulate a certain number of events that were commandable (64 nominally), with a minimum time resolution of 2 μs. The TTE and TTS data are available only for DSELB detectors. In addition, Preburst (PREB) data were also made available when a trigger occurred, with 64-ms time resolution. The data were always read in a buffer memory which was kept updated until a trigger occurred, at which time the data were stored for readout. The PREB data are available for all LADs.

Finally, the higher energy resolution data products of the burst mode are Medium Energy Resolution (MER), High Energy Resolution Burst (HERB), Spectroscopy High Energy Resolution Burst (SHERB), and Spectroscopy Time-Tagged Event (STTE) data. The MER data provide 16 energy channels, with 16 ms time resolution for the first 32.768 s (2048 spectra) and 64 ms up to 163.84 s (2048 spectra) after the trigger. The data are summed over the DSELB detectors. The accumulation times of both HERB and SHERB data are rate dependent. The 128-energy channel HERB consists of 128 spectra with minimum time-to-spill of 128 ms (with a 64 ms increment). As for the SHERB, it provides 256 energy channels and accumulates 192 spectra, with the same time resolutions as the HERB. Both HERB and SHERB data are available for four DSELH detectors, with the brightest detector (DSELH1) having the finest time resolution. The STTE data recorded up

to 16,384 SD individual events with 128 μs resolution in 256 energy channels, for DSELB detectors. Similar to the TTE data for the LAD, the STTE data were recorded from a continually running ring buffer. The summary of the data types provided by the CEU is shown in Table 2.2. In our spectral analysis presented in this dissertation, we use high-energy and medium-energy resolution data from LAD: HERB, MER, and CONT. The data type selection methodology is described in §4.1.3.

Table 2.2 BATSE data types.

	Detector		Number of	Time	Number of	
Name	Type	Subset[1]	Energy Chan	Resolution	Spectra/Events[2]	Description
HERB	LAD	DSELH	128	$\geq$ 128 ms	128	High resolution spectra
HER	LAD	All	128	$\geq$16.384 s[4]	—	High resolution spectra
MER	LAD	DSELB	16	16 ms, 64 ms[5]	2048, 2048	Medium resolution spectra
CONT	LAD	All	16	2.048 s	—	Medium resolution spectra
DISCSC	LAD	DSELB	4	64 ms	$\geq$ 2816[6]	Discriminators after trigger
PREB	LAD	All	4	64 ms	32	Discriminators prior to trigger
TTE	LAD	DSELB[3]	4	2 ms	32,768	Time-tagged events
TTS	LAD	DSELB	4	2 ms	64	Time-to-Spill data
DISCLA	LAD	All	4	1.024 s	—	Discriminators
DISCLB	LAD	All	4	1.024 s	—	Discriminators during telemetry gap
SHERB	SD	DSELH	256	128 ms	192	High resolution spectra
SHER	SD	All	256	$\geq$ 32.768 s[4]	—	High resolution spectra
STTE	SD	DSELB	256	128 ms	16,384	Time tagged events
DISCSP	SD	All	4	2.048 s	—	Discriminators

[1] DSELH: 4 detectors with highest count rates determined at trigger.
DSELB: 2-4 triggered detectors. MER and DISCSC are summed over these detectors.
[2] Continuous for non-burst mode data.
[3] Pre-burst data are from all detectors.
[4] Normally set to $\sim$ 300 seconds.
[5] 64 ms begins at 32.768 seconds after trigger.
[6] Accumulated during the commandable burst acquisition period of $\sim 180 - 573$ s.

2.3 The Energetic Gamma-Ray Experiment Telescope

Another experiment aboard the *CGRO* was the Energetic Gamma-Ray Experiment Telescope (EGRET). The location of EGRET on the spacecraft is seen in Figure 2.3. It was designed to observe high-energy gamma rays much above the BATSE energy band, between $\sim$ 20 MeV – 30GeV. It was a spark chamber equipped with an anti-coincidence counter and a calorimeter, Total Absorption Shower Counter (TASC), located at the bottom of the module. Figure 2.6 shows the schematic of the EGRET module configuration. In the spark chamber, incoming gamma-ray photons are converted to electron-positron pairs which move downward. If the time-of-flight coincidence system detects a downward-moving electron or positron and if

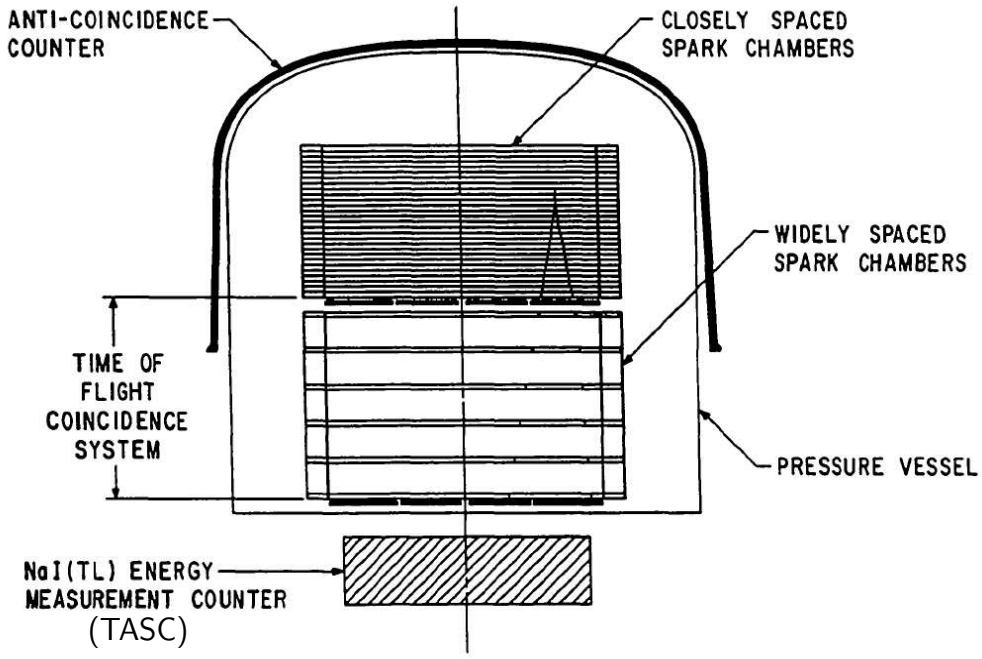

Figure 2.6 EGRET module (from Thompson et al. 1993). The vertical center line represents the spacecraft z-axis. TASC is located below the spark chamber.

there is no anti-coincidence counter signal, the track imaging system is triggered and energy is measured with the TASC. The original photon energy and the incident direction are subsequently determined. The sensitivity of the EGRET spark chamber was the best at the zenith angle 0°, and the efficiency drops by a half at 18° and factor of 6 at 30° (Dingus et al. 1998). Although the field of view of the EGRET spark chamber was very limited, the TASC was capable of accumulating data for BATSE-triggered GRBs from all directions, independently from the spark chamber events.

2.3.1 Total Absorption Shower Counter

Like the BATSE detectors, the TASC was also a NaI(Tl) scintillation detector with much larger dimension of 76 cm × 76 cm and 20 cm thickness (corresponding to 8 radiation lengths). In its low-energy mode in the energy range of $\sim 1 - 200$ MeV, the TASC continuously accumulated the non-burst Solar spectra (SOLAR), every 32.768 seconds. In addition, it collected Burst spectra (BURST) initiated by BATSE triggers, in four commandable time intervals of 1, 2, 4, and 16 (or 32) seconds. Both the SOLAR and BURST data provided spectra with 256 energy channels. An example of the TASC spectrum is seen in Figure 2.7, in which the ^{40}K line at 1.46 MeV and the Fe neutron capture line at 7.64 MeV are always present for on-board calibration purposes. The instrumental artifact at $\sim$ 1.2 MeV is due to an error in the electronics design (Thompson et al. 1993). There is also a bump around 100 – 200 MeV caused by cosmic-ray protons that pass through the TASC along the z-axis that deposit energy of $\sim$ 105 MeV in the TASC. The proton spectral feature was also used to monitor the gain of the TASC. The FWHM energy resolution of the TASC is about 20% over the entire energy range. The response is highly dependent on the incident direction of the event photons, because of the block

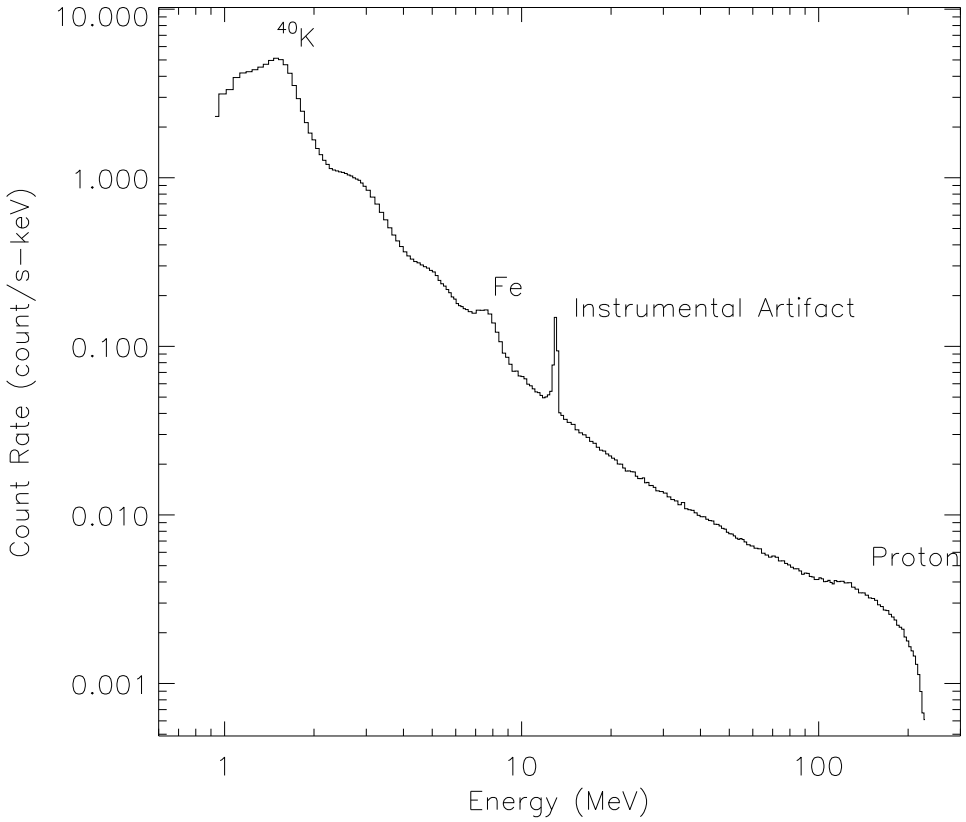

Figure 2.7 Typical energy spectrum of TASC. ^{40}K line, Fe line, the instrumental artifact, and the cosmic-ray proton features are evident.

shape of the TASC NaI crystal, as well as the presence of intervening spacecraft materials surrounding the detector. The TASC was not capable of localizing events; therefore, for GRB observations, the locations determined by BATSE were used to obtain detector response for each event. The response was calculated using EGS4 Monte Carlo code (Nelson et al. 1985) with the complete *CGRO* mass model. The calculated effective area as a function of zenith angles is shown in Figure 2.8, for incident photon energy of 1.2 and 60 MeV. It should be noted that the deadtime of the TASC is extremely high, $\sim 60\%$ on average.

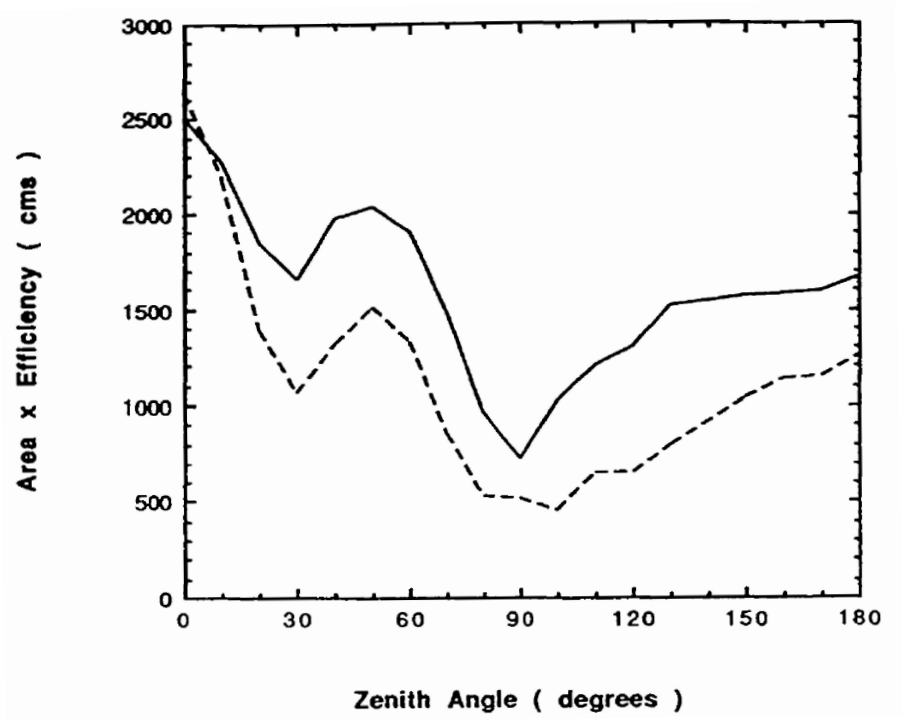

Figure 2.8 Calculated effective area of TASC for azimuth angle of 168° (from Thompson et al. 1993). Zenith angle of 0° points to the spark chamber upwards and 90° is the x-y plane of the spacecraft.

2.4 The Imaging Compton Telescope

The third experiment aboard the *CGRO* was the Imaging Compton Telescope (COMPTEL), installed at the center of the spacecraft (see Figure 2.3). COMPTEL primarily operated as a double-scatter telescope and was designed to observe the gamma-ray sky in an energy range of 0.8 to 30 MeV, as well as to search for linear polarization from gamma-ray sources. Figure 2.9 shows the schematic of the COMPTEL module. The telescope consisted of two sets of detectors in two layers;

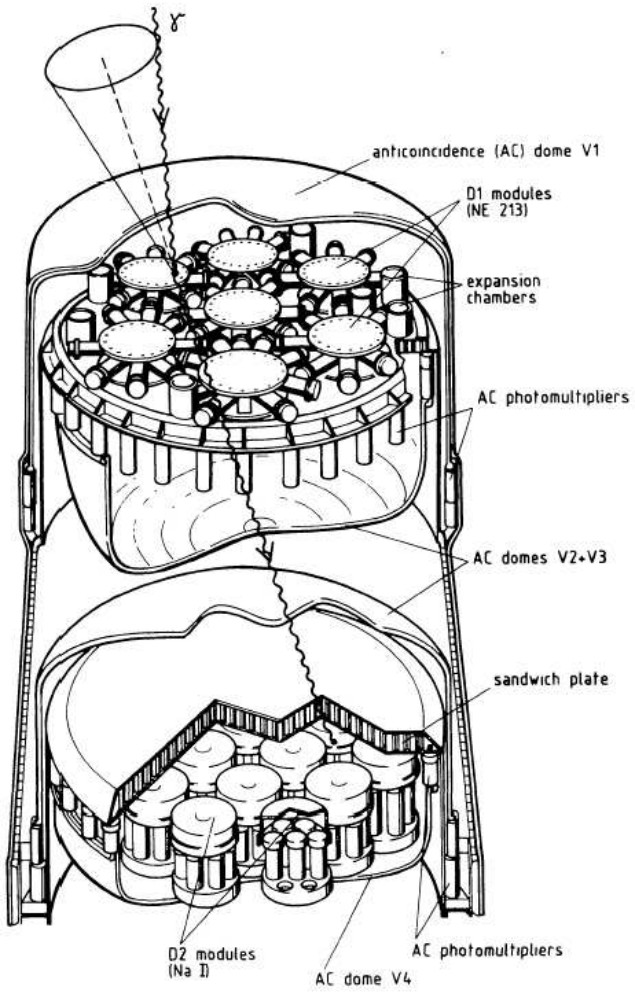

Figure 2.9 COMPTEL module (from Schönfelder et al. 1993).

D1 and D2 (separated by 1.5 m), covered by the anti-coincidence (AC) domes. The upper layer D1 consists of 7 cylindrical modules filled with NE213A liquid organic scintillator. The low atomic number and low density of the liquid allow for single Compton scattering within each D1 module. The total area of D1 is ~ 4200 cm^2, and the detectors were coupled to 8 PMTs. The lower layer D2, on the other hand, consists of 14 NaI(Tl) scintillation detectors, 28-cm in diameter and 7.5-cm thick. The high-atomic number NaI was used at the bottom layer so that the energy of the photons that are first Compton scattered by D1 would be totally absorbed in D2. They were coupled to 7 PMTs. Each AC dome was made of plastic scintillator 1.5-cm thick that were viewed by 24 PMTs.

In the double-scatter telescope mode, the field of view was limited to $\lesssim 1$ sr; however, two of the 14 D2 detectors also simultaneously operated as burst mode detectors, sensitive to all directions. The burst mode detectors were equipped with the Burst Spectrum Analyzer (BSA), an electronic subsystem dedicated for this purpose. The burst module consisted of two NaI detectors (D2-7 and D2-14) that provided spectra in the energy range of 300 keV – 1.3 MeV ("Low") and 800 keV – 10.6 MeV ("High"). The BSA normally accumulated data in its background mode every 100 seconds, and began data acquisition in the burst mode when activated by a BATSE trigger. In the burst mode, it provided 6 spectra with 1 second resolution (B1 – B6), followed by 12 "tail mode" spectra with 6 second resolution (T1 – T12). The number of energy channels was 122 for Low and 128 for High spectra, and the FWHM energy resolution was 9.6% at 0.5 MeV and 7% at 1.5 MeV (Hanlon et al. 1994). A more detailed COMPTEL instrument description can be found in Schönfelder et al. (1993).

2.5 Detector Response Matrix

A DRM is a matrix that maps input energies of gamma-ray photons onto the energies measured by a detector. Given an incident photon, a DRM basically redistributes the input photon energy to output channel energies with corresponding counts according to the calculated detector behavior. How much of incident photon energy is deposited in a detector depends on the incident energy, angle of incidence, type of interactions that the photons undergo, the geometry of the detector and many more factors. Consequently, it varies from detector to detector, event to event, and all of these detector response characteristics need to be taken into account when converting measured count spectra into incident photon spectra. Physical units of the DRM are cm^2, and the DRM should convert an input photon flux spectrum in photons s^{-1} cm^{-2} keV^{-1} to an output count rate spectrum in counts s^{-1} keV^{-1}. Employing dimensional analysis, [input photon] $\times$ [DRM] = [output counts] can be viewed as

$$\left[\frac{photon}{s-cm^2-bin}\right] \times \left[\frac{cm^2-bin-counts}{photon-channel}\right] = \left[\frac{counts}{s-channel}\right], \qquad (2.3)$$

where *bin* is input photon bin (total number varies case by case) and *channel* is output energy channel (128 for a BATSE LAD and 252 for a BATSE SD). The DRM is a two-dimensional matrix with dimensions photon bins $\times$ number of channels. However, the output count rate is discontinuous since the channel width is not constant throughout. In order to correct this, the output must be divided by the channel width in keV. The output units will then be counts s^{-1} keV^{-1}.

Usually, DRMs are generated from actual calibrations with radioactive sources as well as Monte Carlo simulations which include the materials of the detector, spacecraft, and the Earth's atmosphere, as accurately as possible. The DRM is essential to spectral analysis since the deduced photon spectrum must not be detector

dependent. Not having an accurate DRM would result in deducing a wrong source spectrum and any analysis that followed would not be correct.

2.5.1 Problems with BATSE Spectroscopy Detector DRM

It has been noticed that spectral analysis using the BATSE SD data does not yield consistent results with the analysis results using other high-energy detectors also on board the *CGRO* (such as COMPTEL and EGRET) that share portions of the energy range (M.S. Briggs 2002, private communication). The discrepancy occurs at energies higher than $\sim$ 2 MeV or so, and it is possible that this results from an inaccurate DRM at these higher energies. We investigate the SD DRM in detail here.

The energy coverage of the SD extends from $\sim$ 5 keV to $\sim$ 20 MeV, depending on its gain (see §2.2.2). The SD DRMs were generated using the Monte Carlo simulation and calibrated with several radioactive sources whose highest photon energy was 1.33 MeV from ^{60}Co (Horack 1991). The simulated spectra are stored in compressed form and retrieved when a DRM for a specific detector and event is generated. Photon energies higher than a few MeV cannot easily be calibrated using radioactive sources, and therefore the DRM for energies above 1.33 MeV relies solely on the simulations in case of the SDs. The simulations were run for 71 energies between 3 keV and 100 MeV for the SDs (Pendleton et al. 1995). COMPTEL has been calibrated up to 200 MeV with a neutron beam and EGRET up to 10 GeV using SLAC (Schönfelder et al. 1993; Thompson et al. 1993); therefore, their responses above 1 MeV do not rely solely on simulations, unlike the SD case.

As an example, DRMs for LAD (HERB) and SD (SHERB) module 4, for GRB 920622 (BATSE trigger number 1663) are shown as a contour map in Figure 2.10. These plots show the output count rates per energy as a function of input photon

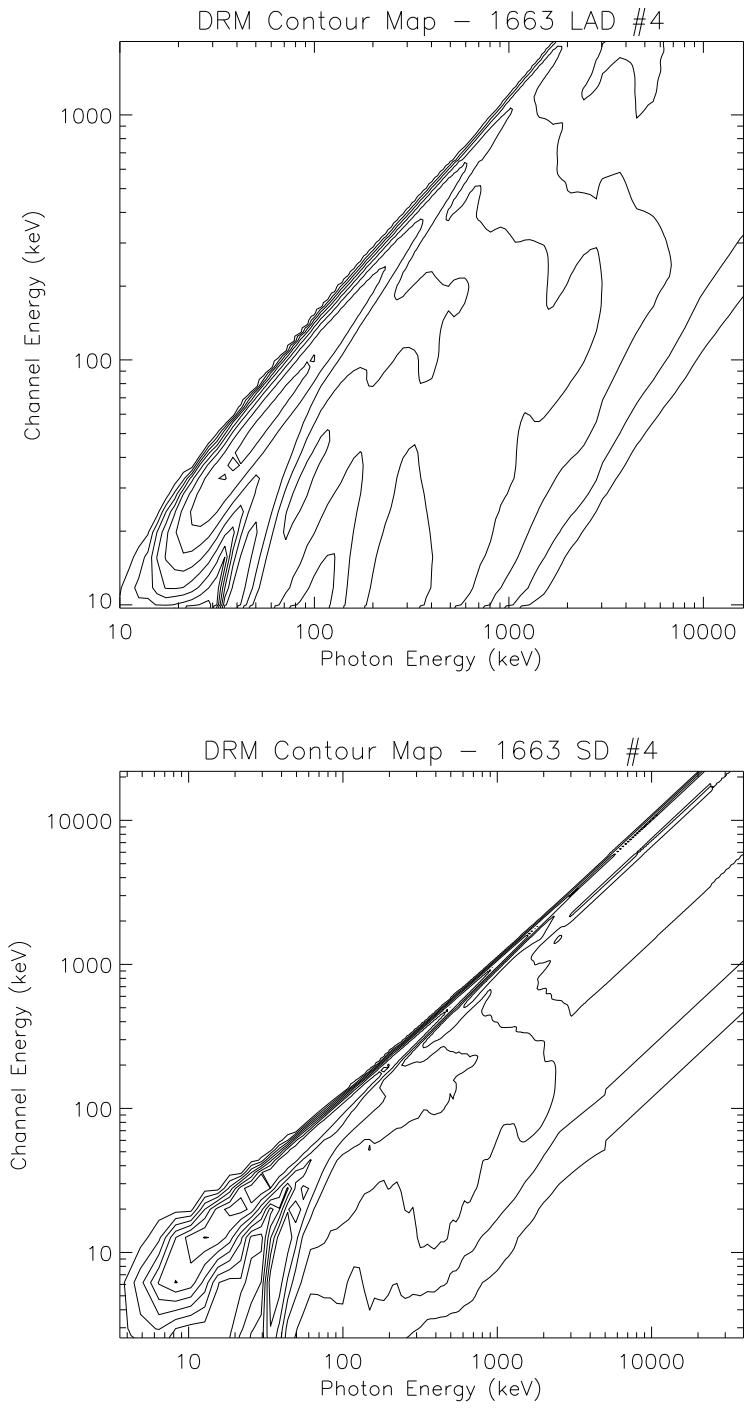

Figure 2.10 Contour maps of a detector response matrix, for LAD (*top*) and SD (*bottom*). Input photon energies are plotted against output channel energies, and off-diagonal components are clearly shown.

energy (see Equation 2.3). We note that the DRMs for this event will be used hereafter within this chapter as examples. This particular burst and set of detectors were chosen as examples due to the relatively small incident angles (14.8° from LAD normal and 30.0° from SD normal), the SD's low gain (i.e., higher energy coverage), and the brightness of the event. The contours represent detector response. If the detector were ideal, the DRM would only have diagonal terms corresponding to a series of photopeaks. In reality, however, the photon interactions with a detector described in §2.1 contribute to the off-diagonal components of the DRM. The components are clearly seen in the contour map. We note that the SD DRM contours indicate a strange behavior at energies above $\sim$ 3 MeV, shown by the straight lines. In comparison with the LAD DRM, it is evident that the SD DRM does not change its shape above this energy but only shifts. This flat feature is clearly seen in every SD DRM that was investigated, always starting at the same energy.

In order to better illustrate the detector behavior, monoenergetic photon input is assumed and the resulting output count spectra for some given energies are plotted in Figure 2.2 shown in an earlier section. These figures can be thought as taking "slices" of the contour map (Figure 2.10) at each input photon energy. For the incident photon energy of 800 keV (Figure 2.2, top panel), photopeak at 800 keV and the Compton edge (see §2.1.1.2) at $\sim$ 600 keV can be identified. This energy, at which the Compton edge is located, agrees well with the theoretical maximum energy of the Compton electron of 609.5 keV, for a 800 keV incident photon. The counts existing between the Compton edge and the photopeak may arise from multiple Compton scattering, in which case the energy deposited can exceed the Compton edge for a single Compton scattering. A peak at $\sim$ 250 keV can be accounted for by *backscatter* from materials surrounding the detector; i.e., photons that miss the detector encounter the surrounding material outside the detector and get Compton scattered by electrons in the material. When the scattered photons come back into

the detector and get absorbed, they contribute to this backscatter peak. In order for these photons to backscatter into the detector, the scattering angle must be relatively large, and the scattered photon energies ($h\nu'$) at large scattering angles ($\phi \gtrsim 120^{\circ}$) for all incident photon energy are nearly identical. This results in the peak that appears in the count spectrum and the peak energy corresponds to

$$h\nu' \,|_{\phi=\pi} = \frac{h\nu}{1 + \frac{2h\nu}{m_o c^2}}. \tag{2.4}$$

In the limit of high incident photon energy, namely, $h\nu \gg m_o c^2$, this reduces to

$$h\nu' \,|_{\phi=\pi} \approx \frac{m_o c^2}{2} \approx 250\text{keV}, \tag{2.5}$$

and therefore, the backscatter peak is observed always less than $\sim$ 250 keV, and depends on the angle of incidence.

On the other hand, in the case of the incident photon energy of 2 MeV (Figure 2.2, bottom panel), signatures of pair production (see §2.1.1.3) are evident, as expected. The annihilation peak at $\sim m_o c^2 = 511$ keV comes from photons interacting within the surrounding material. Just like the backscatter case, an incident photon misses the detector, hits the surrounding material and interacts via pair production. One of the resulting annihilation photon comes back to the detector and gets absorbed. The backscatter peak is also present at $\sim$ 150 keV, and the photopeak at 2 MeV is much lower compared to the case of 800 keV photon. At this high incident energy, the Compton edge is not clearly visible since it blends into the lower edge of the photopeak. Similarly, we show the response functions of the SD for the incident photon energies of 10 MeV and 20 MeV in Figure 2.11. As indicated by the parallel lines in the DRM contour map (Figure 2.10, bottom panel), the shapes of these two functions are almost identical in logarithmic scale.

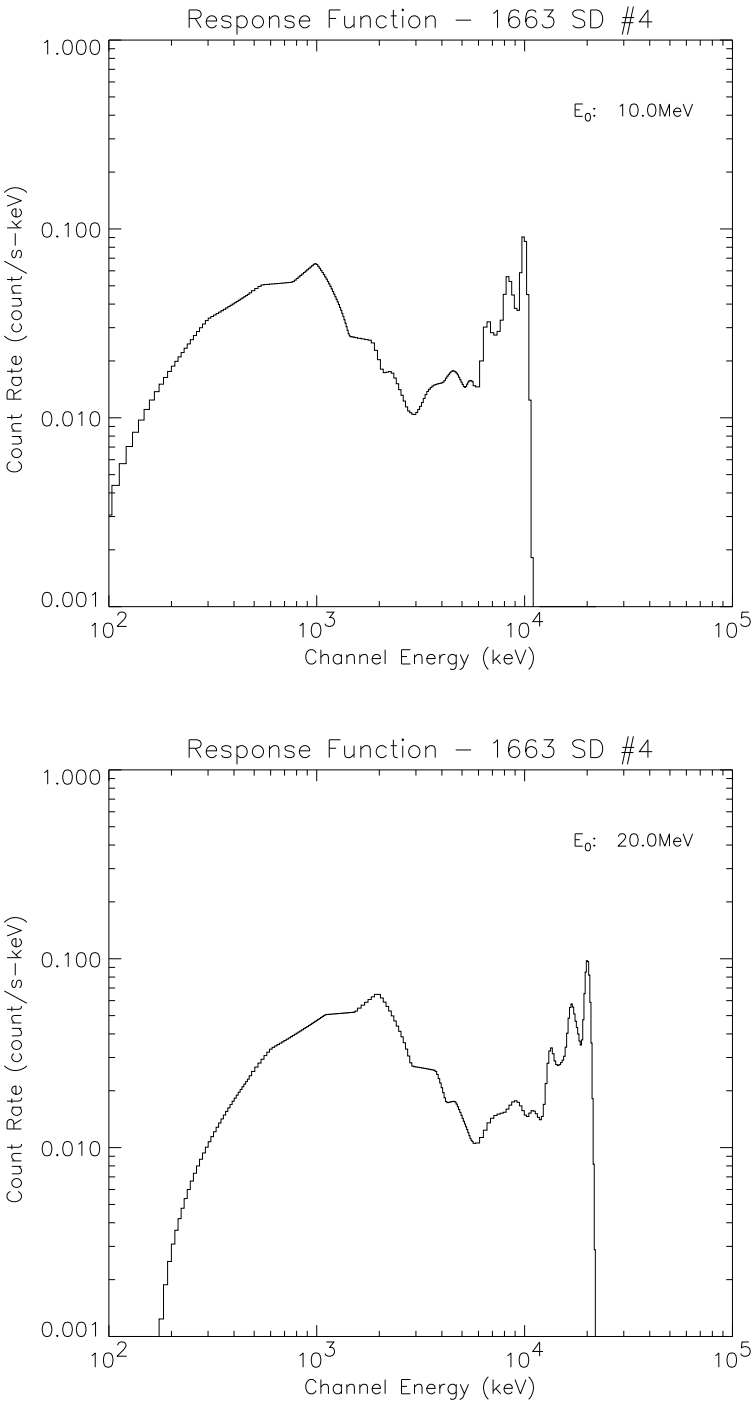

Figure 2.11 Response function of the SD for input photon energies of 10 MeV (*top*) and 20 MeV (*bottom*).

If only one input photon of a single energy is assumed and multiplied by the DRM, the resulting output counts should add up to ≤ 1 because the input photon was one. In other words, the DRM should only redistribute the single input photon to at most a single count in broader energy range, but not create more than one count. If a single input photon produces one count as an output, regardless of output energy distribution, the detection efficiency is said to be 100%, where the effective area of the detector equals the geometric area. It must be noted that for SDs, the effective area could be larger than the geometric area of the detector at energies around 200 keV, due to the backscatter from surrounding material (Pendleton et al. 1995). Integrating the output count rate spectrum over all energy should correspond to the detection efficiency for a specific input photon. In fact, the actual total efficiency should be the integrated count rate divided by the detector's geometric area, so as to make the output rate consistent with the input flux (rate per area; Equation 2.3). The geometric area of an SD varies with incident angle as shown in Figure 2.12.

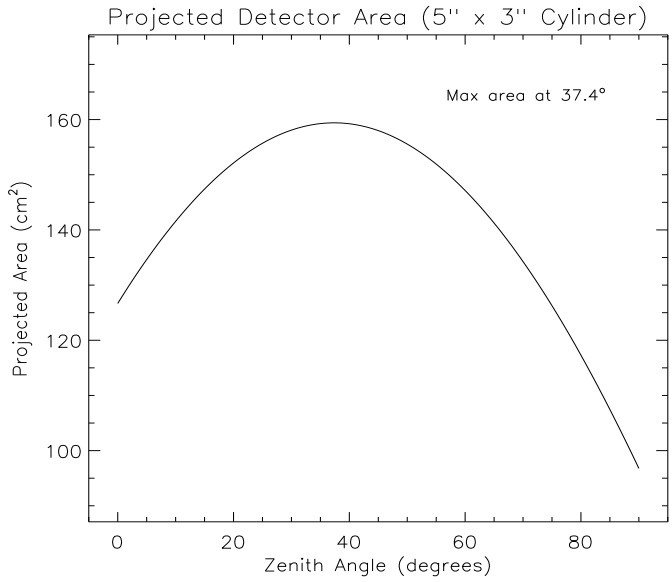

Figure 2.12 Projected geometric area of the SD NaI crystal for various incident angles.

The efficiency (i.e., the ratio of the effective area to the geometric area) calculated for various input photon energies is shown in Figure 2.13. It goes beyond 1.0 at $\sim$ 70 keV up to $\sim$ 500 keV due to the backscatter photons, as mentioned earlier. Although the units seem to be correct, the efficiency diverge at energies $\sim$ 2.9 MeV and above, which is not physical. This diverging feature is found in every DRM that has been investigated, always starts at the same input photon energy of 2.9 MeV. Interestingly, this is the energy around which the DRM contour plot in Figure 2.10 starts to show the straight line contours. The exact reason is unknown at this point.

For the purpose of testing this method of determining the efficiency more in detail, we used the LAD DRM for the same event instead of the SD DRM, and calculated the detection efficiency by the same method applied in the SD case. The

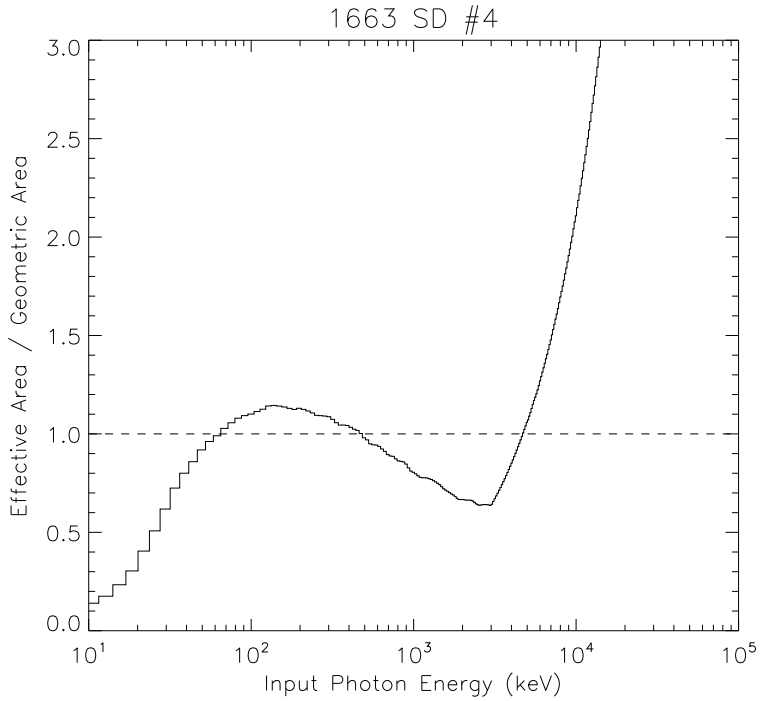

Figure 2.13 The detection efficiency of an SD for different input photon energies. It diverges at energies above 3 MeV.

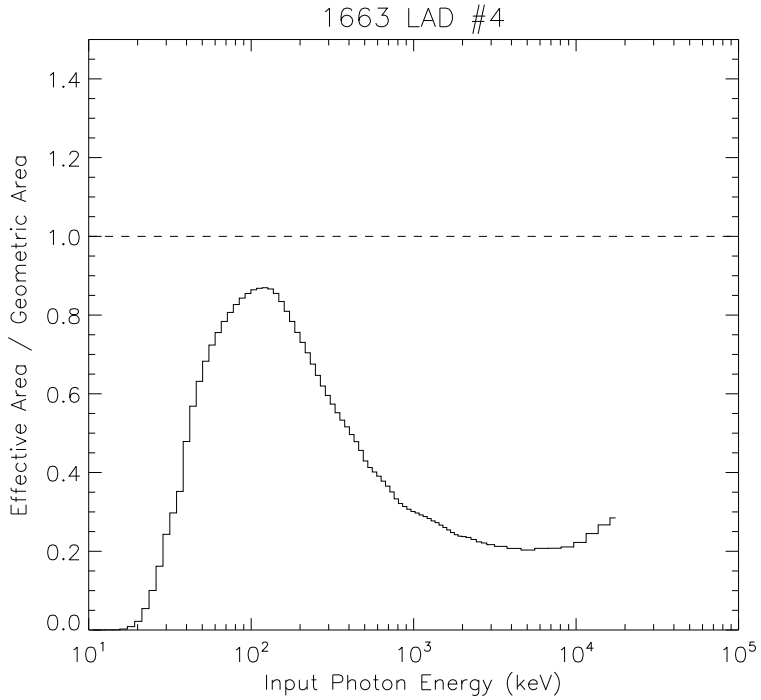

Figure 2.14 The detection efficiency of a LAD for different input photon energies, corresponding to Figure 2.13 for the SD.

results are shown in Figure 2.14. The plot shows a very good efficiency distribution unlike the SD DRM case. A slight increase at the higher end (> 10 MeV) is likely to be a result of being out of the LAD energy range, which ends at lower energy than that of SD. Below 10 MeV, there is no sign of any sudden increase. The method seems to produce the correct detection efficiency for the LAD DRM at all energies while the same method results the unphysical efficiency for the SD DRM at higher incident photon energies.

2.5.2 Summary of SD DRM Problems

The method for calculating the detection efficiency was reviewed a number of times, yet the causes for the problems still cannot be identified. One possible cause of the diverging at 2.9 MeV may be a change in channel width or photon bin width around this energy. However, we found that both the channel width and photon bin width stay the same near 2.9 MeV and thus, this is not likely to be the cause. In addition, the fact that the LAD detection efficiency does not diverge seems to rule out this possibility as well, since the LAD DRM channel width and photon bin width also change in the same manner as those of the SD DRMs. Conceivably and perhaps the most likely cause is that the SD DRMs are not correctly generated for energies higher than 2.9 MeV. Given the fact that the LAD DRMs at higher energies are generated based only on simulations, just as was done for the SD DRMs, it is more likely that problems exist in the DRM generating codes and not within the simulated data. This is strongly supported by the unusual straight lines seen in the contour plot (Figure 2.10, bottom panel) that begin at $\sim$ 3 MeV, which are only seen in SD DRMs. These problems identified here urge that the SD DRM generating codes to be reviewed and corrected if necessary. Until the correct DRMs are obtained, spectral analysis using the SHERB data above a few MeV should not be taken to be reliable, while limiting the analysis to lower energies may still prove to be valid.

CHAPTER 3

GAMMA-RAY BURSTS: OBSERVATIONS AND THEORIES

During the past several decades, thousands of GRBs have been observed and new bursts are being detected daily with experiments currently in orbit, such as *Swift*, *HETE-II*, and *INTEGRAL*. Numerous theoretical models have been suggested in attempts to explain this mysterious phenomenon, and many have been eliminated as they were confronted with new observational evidence. In this chapter, the observational milestones and global properties of GRBs are first reviewed in §3.1, while the physical models of GRB creation mechanisms and progenitors that are widely accepted in the GRB community are discussed in §3.2.

3.1 Observational Milestones

The very first serendipitous observations of cosmic gamma-ray bursts in the energy range of 0.2 – 1.5 MeV by the *Vela* satellites were reported in 1973 (Klebesadel et al. 1973). Since then, both instrumentation and our understanding of the phenomenon have improved immensely, marked by several key events. The most significant of all was perhaps the launch of the *CGRO* (with BATSE on board) in 1991, and the discovery of multi-wavelength afterglows of GRBs in 1997. These two events had tremendous impact on advancing our ability to explore gamma-ray bursts and in turn, improving our knowledge of what they might be. Therefore, I

divide the time line into three periods; the pre-BATSE era, the BATSE era, and the afterglow era, and give an overview of significant observational findings and implications in each period in the following sections.

3.1.1 Pre-BATSE Era

The primary gamma-ray missions in this period that observed significant numbers of GRBs were *Vela* (Strong et al. 1974), *Venera 11 & 12* (Mazets & Golenetskii 1981), *Venera 13 & 14* (Mazets et al. 1983), *Solar Maximum Mission* (Share et al. 1993), *Pioneer Venus Orbiter* (Fenimore et al. 1993b), and *Ginga* (Ogasaka et al. 1991). The detectors covered mainly ~ 30 – 1000 keV energy range, similar to that of BATSE (see Chapter 2), and observed a total of ~ 700 GRBs.

The *Vela* observations of 23 bursts by the start of 1970s, including the ones reported by Klebesadel et al. (1973), already hinted at the diverse duration property of GRBs (Strong et al. 1974). The origin and distance scale to the source, however, remained unknown. In the years following that, the observation of 85 GRBs by the KONUS experiment on board the *Venera* satellites confirmed the diversity and variability in the burst time profiles with millisecond resolution, including several short events lasting less than a second (Mazets & Golenetskii 1981). These observations also revealed power-law like spectral properties (often with a high-energy cut-off) of GRBs and the indication of gradual spectral softening within a burst. In addition, bursts were found to be inhomogeneously distributed in space, as indicated by cumulative intensity distributions; $LogN(>S) - LogS$ and $LogN(>P) - LogP$ plots, where $N(>S, P)$ are the number of bursts with energy fluence or peak flux greater than a certain energy fluence S or peak flux P (e.g., Figure 3.2). The plot is used as an indicator of spatial distribution as $N \propto S^{-3/2}, P^{-3/2}$ would be expected from a homogeneous distribution in Euclidean space, given that $N \propto V \propto r^3$

and $S, P = \mathcal{L}/4\pi r^2$, where $\mathcal{L}$ is luminosity. The KONUS observations showed significantly fewer dim events compared to a homogeneous distribution, which was attributed to a disk-like nature for the source distribution. Additionally, the angular distribution of 37 localized bursts indicated (though without sufficient statistics) a slight concentration towards the galactic plane. These results were interpreted as an indication of a galactic halo origin for GRBs (Mazets & Golenetskii 1981), and was widely believed at the time. Another intriguing report from the KONUS observations was the appearance of absorption features at 20 – 60 keV in many of their spectra (Mazets et al. 1981). These were interpreted as cyclotron absorption lines, and thus indicated that bursts originated from nearby strongly magnetized neutron stars. This was further evidence to sustain a galactic origin for GRBs. However, the line detection was to remain controversial for a long time, mainly due to systematics that were not made clear at the time of the report (Briggs 1999).

Meanwhile, the Gamma-Ray Spectrometer on the *Solar Maximum Mission* (*SMM*) observed 177 GRBs (Matz et al. 1985; Harris & Share 1998) in the energy range extending to $\sim$ 10 MeV, and found that the GRB spectra were usually continuous up to $\sim$ 6 MeV with no cutoff (Matz et al. 1985). The finding conflicted with the cut-off power law spectra commonly observed in the sub-MeV energy, and urged revisions to existing thermal models. At that time, it was customary to fit GRB spectra with an optically-thin thermal bremsstrahlung model; $f(E) \propto E^{-1}\exp(-E/kT)$, where kT is the electron temperature. The hard-to-soft spectral evolution was also found in the majority of the 48 strong bursts observed during the *SMM* mission with an analysis performed much later (Share & Matz 1998).

Finally, in the late 1980s, the Gamma-Ray Burst Detector on the *Ginga* satellite observed about 120 GRBs in 4.5 years of its operation in the energy range 1 – 400 keV (Ogasaka et al. 1991; Strohmayer et al. 1998). The *Ginga* observations of GRBs revealed many interesting X-ray spectral features, including the still-controversial

confirmation of absorption lines (Murakami et al. 1988), thermal precursor, and soft tails of GRBs (Murakami et al. 1991). In particular, the absorption lines were found at energies corresponding to the first and second harmonics of the resonant cyclotron scattering of electrons in tera-gauss magnetic fields, and offered more solid evidence that these cyclotron absorption features were real. Moreover, the X-ray thermal precursor was consistent with the radiation from a neutron star surface. Although there were some cosmological models that had been proposed, including a supernova model (Colgate 1974) as well as compact object mergers (see Nemiroff 1994, for a list), the galactic neutron star model of GRBs seemed to be strongly supported by the early observations.

3.1.2 BATSE Era

After the launch of *CGRO* in 1991, BATSE began detecting one GRB a day, on average. Soon, the observations revealed an isotropic angular distribution (Figure 3.1) and inhomogeneous spatial distribution (Figure 3.2) for GRBs, with better and better statistics as more numbers of bursts were observed (Meegan et al. 1992; Briggs et al. 1996). The isotropy of GRB locations rejected the galactic disk population hypothesis, and confirmed that we were at the center of the source distribution. Along with the inhomogeneity (i.e., the deficit of dimmer events in $LogN(> P) - LogP$ plot; Figure 3.2), the indicated GRB distribution was a geocentric spherical distribution with decreasing number density at further distance. The distribution was not consistent with any known population of galactic objects. It was, however, consistent with a cosmological origin hypothesis since isotropy is naturally expected from the cosmological distribution and the inhomogeneity could be explained by the non-Euclidean geometry at very far distances.

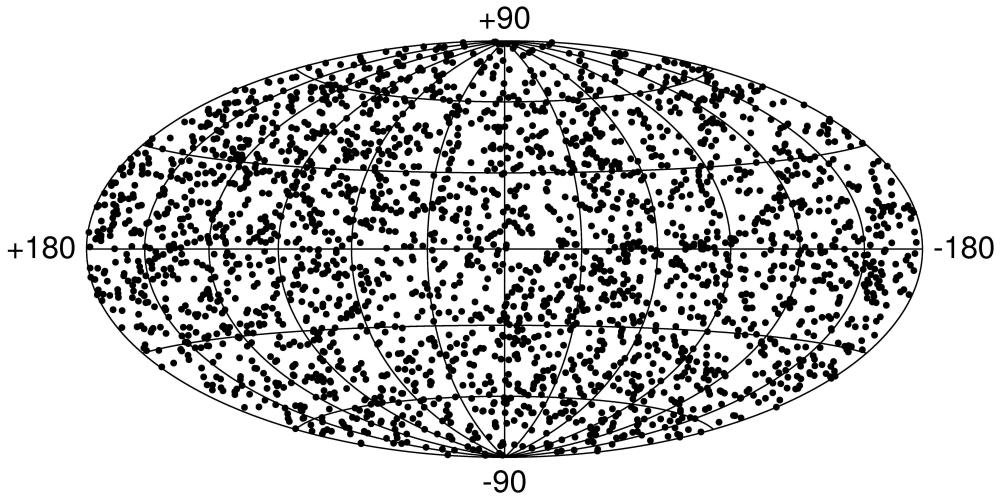

Figure 3.1 The angular distribution of 2704 BATSE GRBs in galactic coordinates. The distribution is consistent with isotropy.

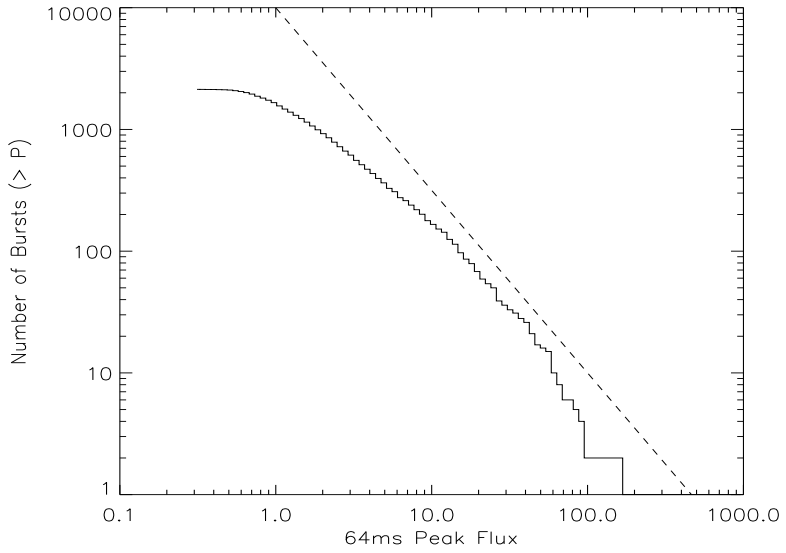

Figure 3.2 Cumulative peak flux distribution of >2000 BATSE GRBs. Dashed line shows $-3/2$ power law expected for a homogeneous distribution in Euclidean space. The peak flux integration time is 64 ms in $50 - 300$ keV. The deviation from the power law is seen at the lower peak flux.

Another cosmological signature was also found by Norris et al. (1994), the possible cosmological time dilation effects in the long GRBs observed by BATSE: dimmer bursts have longer durations.

The BATSE observations also verified the GRB time-profile diversity varying from milliseconds to hundreds of seconds, and successfully identified two classes of GRBs: short and long (Kouveliotou et al. 1993). The burst durations are usually defined by T_{90}, the time during which 90% of the burst's total photon fluence is accumulated. The T_{90} distribution of 2041 BATSE GRBs is shown in Figure 3.3, in which the sum of two distributions, of short events ($T_{90} \lesssim 2$ s) and long events ($T_{90} \gtrsim 2$ s), can be seen. Very interestingly, there is a correlation between the duration and the spectral hardness: short bursts are spectrally harder (Dezalay et al. 1992; Kouveliotou et al. 1993). In general, both short and long bursts can be very complex and exhibit high variability, even down to sub-millisecond scale

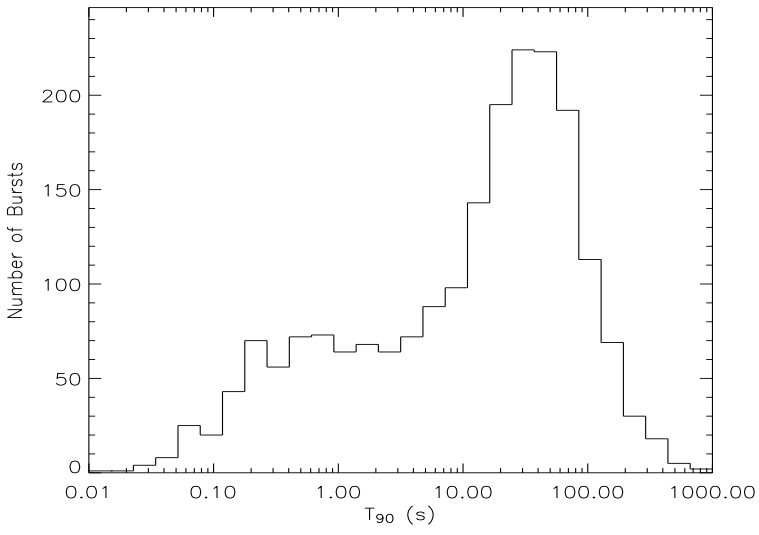

Figure 3.3 Duration (T_{90}) distribution of 2041 BATSE GRBs. The values were taken from the "current" BATSE catalog.

(e.g., Bhat et al. 1992). Some example burst time profiles are shown in Figure 3.4. Because of their extremely wide variety in temporal characteristics, no detailed classification of GRBs by their morphology has been successful. Nonetheless, GRBs can be very broadly (and vaguely) sorted into several categories such as: single pulse, smooth, well-defined peak, multi-episode, and very erratic, chaotic events (Fishman & Meegan 1995). A burst with a single smooth episode (e.g., Figure 3.4d) is usually called a FRED – Fast Rise Exponential Decay, in which the rise time is much shorter than the fall time. The FRED is also the general description of each pulse within a burst, in case of multi-peak and/or multi-episodic bursts.

On the other hand, GRB spectra are found to be fairly uniform and non-thermal. The empirical model developed by Band et al. (1993), based on the BATSE SD burst data, seems to fit adequately well most GRBs to date (Figure 3.5). The mathematical form and the detailed description of the model can be found in §4.2.2.2. Basically, the model consists of two power laws that are joined smoothly at a break energy typically well within the BATSE energy band (Preece et al. 2000). For the time-resolved spectra of long, bright GRBs, the typical value for the low-energy spectral index α is ~ -1.0 and for the high-energy spectral index β is ~ -2.3. The hard-to-soft spectral evolution was also confirmed with time-resolved spectral analysis of BATSE GRBs and found to be very common among bursts (Ford et al. 1995; Band 1997; Crider et al. 1997; Preece et al. 1998a; Crider et al. 1999). Also, the dimmer bursts were found to have lower peak energy in energy flux spectra ($E_{\rm peak}$, uniquely related to the break energy and the spectral indices), another possible cosmological implication (Mallozzi et al. 1995). The spectral properties are discussed in detail in Chapter 4.

Surprisingly, the highly-anticipated cyclotron-like absorption features were not explicitly observed by BATSE, which was sensitive enough to observe such a feature if it existed (Palmer et al. 1994; Band et al. 1994, 1995, 1996, 1997). An automated

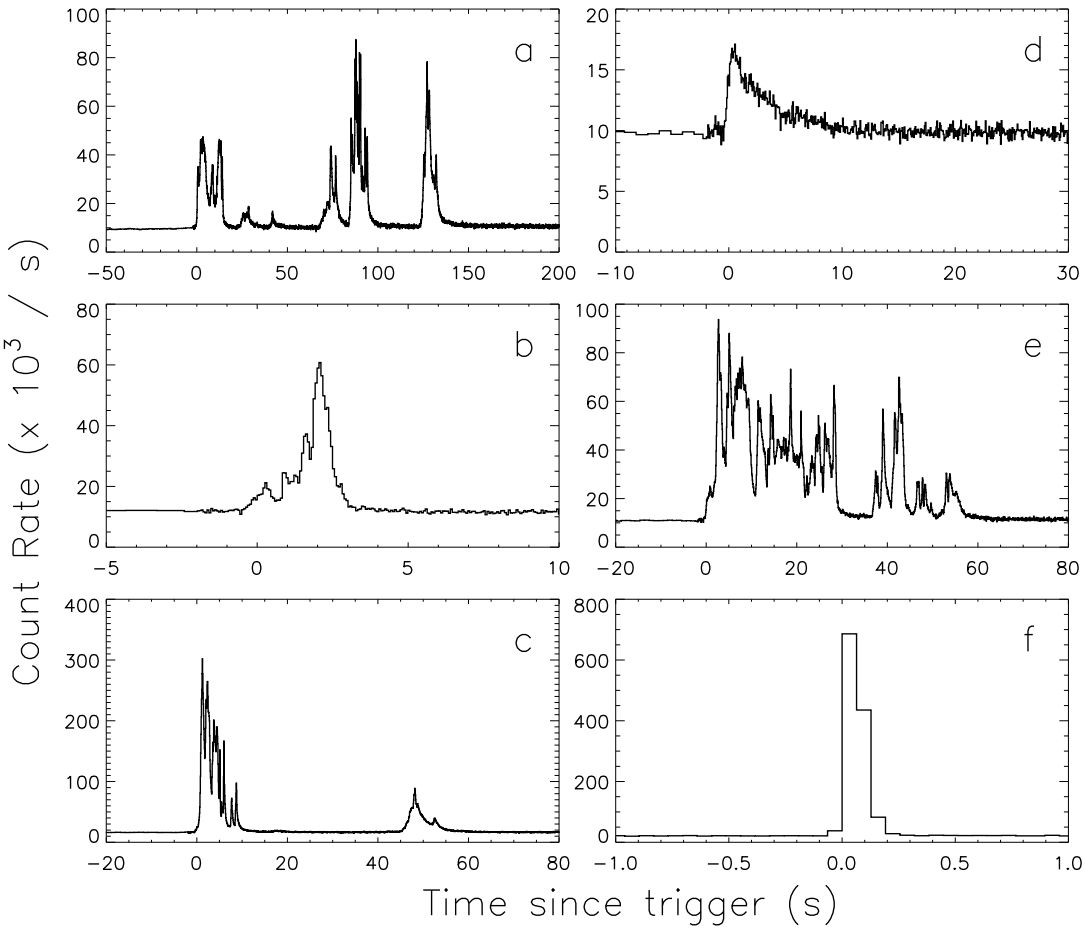

Figure 3.4 Example lightcurves of BATSE GRBs, each showing different broad category of burst profiles: multi-episode (a, c), single peak (b), FRED (d), erratic (e), and short (f).

search for such spectral features identified only a handful of candidate bursts. The search, however, did not yield conclusive results due to lack of consistency between several detectors (Briggs 1996, 1999).

The other experiments on board the *CGRO*, in particular EGRET and COMPTEL, also observed some BATSE-triggered GRBs at higher energies, and verified that GRB spectra could extend up to MeV – GeV (Hanlon et al. 1994; Dingus et al. 1998). One remarkable observation was made with EGRET of GRB 940217 (Hurley et al. 1994), where an 18-GeV photon was detected at 1.5 hours after the BATSE trigger, long after the emission in the sub-MeV energy range ceased. This photon still remains the highest-energy photon detected from a GRB to date. Another type of delayed high-energy emission was also observed with EGRET during GRB 941017, but the data were not analyzed until much later (González et al. 2003). More discussion of high-energy emission from GRBs is to follow (Chapter 5).

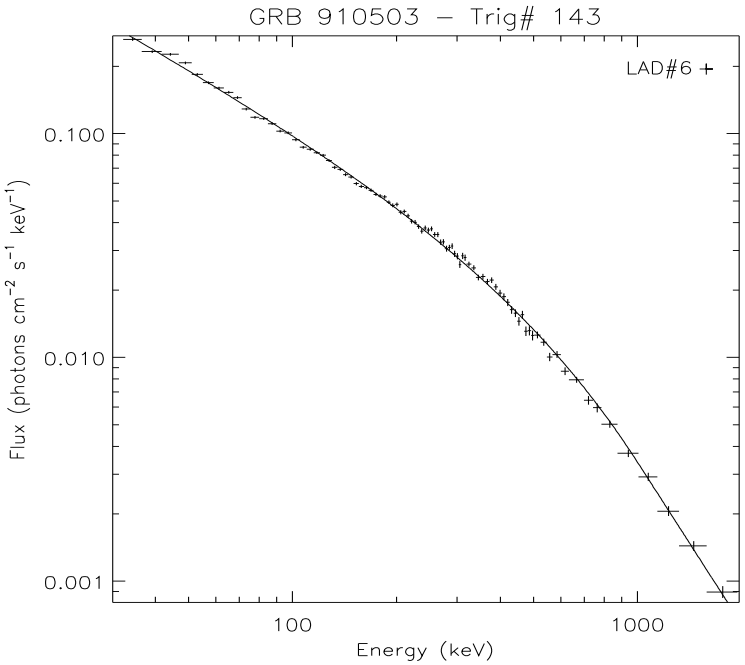

Figure 3.5 Example non-thermal spectrum of a BATSE GRB.

3.1.3 Afterglow Era

With growing evidence of a cosmological origin for GRBs emerging from the BATSE observations, the detection of GRB counterparts was crucial to settle the distance scale from which they originate, and to possibly learn about the GRB source environment. The archival counterpart searches had not been fruitful (van Paradijs et al. 2000, and references therein), and the near-simultaneous detection of such counterparts was extremely difficult, due to the insufficient position resolution and promptness in localizing bursts with the gamma-ray detectors as well as the lack of fast response time of follow-up telescopes on the ground.

The long-awaited success came in 1997 when the Wide Field Camera (2 – 26 keV energy range) on *BeppoSAX* quickly localized a burst (GRB 970228) triggered by the Gamma-Ray Burst Monitor (40 – 700 keV), also on board the satellite, with sufficient accuracy. It prompted the Narrow Field Instruments (0.1 – 10 keV), another set of X-ray instruments on board, to be slewed onto the source location, and an X-ray transient was discovered 8 hours after the burst trigger (Costa et al. 1997). Subsequently, the burst location was communicated quickly to a ground-based optical telescope, and an optical transient was also detected in a position consistent with the GRB, just 21 hours after the burst trigger (van Paradijs et al. 1997). However, an actual redshift measurement for this burst was not confirmed until a few years later (Bloom et al 2001).

The first "real time" measurement of redshift was made a few months after the first afterglow detection, with the observation of an optical afterglow of GRB 970508, localized also with *BeppoSAX* (Djorgovski et al. 1997). The immediate analysis of the optical spectrum revealed a few absorption lines which, along with the lack of Lyman α forest features, indicated the redshift of $0.835 \leq z \lesssim 2.3$ (Metzger et al. 1997). The solid evidence for cosmological distance to GRB source was finally found.

The burst was also the first for which an afterglow in the radio band was detected (Frail et al. 1997).

A cosmological distance to the source meant that the total energy budget of a typical GRB must be at least on the order of 10^{53} ergs, if emitted isotropically, and made GRBs the most energetic events in the Universe. Moreover, the optical monitoring of the fading sources revealed an underlying host galaxy in most of the bursts, for which the optical transients were detected, and these were identified to be star-forming galaxies. Fueled by these exciting results, the global burst alert system as well as automated GRB follow-up techniques improved dramatically in the following few years, and the number of ground-based telescopes involved in the search of GRB counterparts grew. The localization capabilities of the space-based gamma-ray and X-ray telescopes have also advanced.

Owing to technological progress, there have been reports of more than 100 GRB afterglow observations with X-ray, optical, infrared, or radio wave bands at the time of this writing. In addition, redshifts have been measured for ~ 50 GRBs with values $0.1 \lesssim z \lesssim 4.5$ since the report of the first afterglow detection (see Greiner 2005, for an up-to-date list of GRB follow-up observation results). It must be noted that the afterglows of short GRBs have yet to be detected, perhaps due to the current limitation of our observational capabilities. It should also be remarked, however, that a recently-detected *HETE-II* burst, GRB 040924 (H3564, $T_{50} = 0.6$ s, in 30 – 400 keV) was followed by detections of optical afterglow (Fan et al. 2005), and a redshift of $z = 0.859$ was subsequently measured (Wiersema et al. 2004). This may be the first short burst for which an afterglow has been observed, although the burst was spectrally very soft, unlike the BATSE short-hard GRBs. Consequently, all the afterglow arguments in this dissertation apply only to long GRBs.

The multi-wavelength observations of GRB counterparts have provided us many important clues with which to answer the ultimate question of what GRBs are and

how they (and their afterglows) are created. Right after the gamma-ray prompt burst emission, the afterglow is first observed in X-ray, followed by longer wavelength in optical and radio, on timescales of minutes, hours, days, and even months. In general, the X-ray afterglow is the shortest and brightest, and the radio afterglow is the longest and faintest. The transitions from one wave band to another seem to be very smooth, and in fact, the transition from GRB to afterglow has also been observed in the BATSE data as a soft gamma-ray tail (Connaughton 2002; Giblin et al. 2002). In the following sections, some of the most significant improvements in our current understanding of GRBs that came from the follow-up observations in the past several years are briefly reviewed, starting from the summary of the general characteristics of the afterglows in X-ray, optical, and radio.

3.1.3.1 X-Ray Afterglow

X-ray afterglows have been detected for most ($\sim 90\%$) recent GRBs. A typical afterglow decays monotonically, following a power law both in time and energy, namely, $F(t,\nu) \propto t^{\bar{\alpha}}\nu^{\bar{\beta}}$, where $\bar{\alpha} \sim -0.9$ and $\bar{\beta} \sim -1.4$ (Zhang & Mészáros 2004). There have been several reported detections of X-ray emission lines in the afterglow spectra, which can be attributed to the Fe Kα emission from the host galaxies; however, the statistical significance of the detections are still a subject of debate, and therefore the features are not established at present (Piran 2005).

3.1.3.2 Optical Afterglow

Similar to the X-ray case, the optical afterglow tends to decay with a power law of $F(t,\nu) \propto t^{-1}\nu^{-0.7}$, during the early portion, just after the GRB (Zhang & Mészáros 2004). In many cases, however, the lightcurves are found to steepen over a matter

of days in all optical bands. An example of such break can be seen in Figure 3.6. This achromatic break is now believed to be a "jet break," which is caused by the jet geometry of GRBs. The jet break was initially predicted by Rhoads (1999) in the context of the fireball-shock model (see §3.2.2 for detailed discussion of the model). GRBs are relativistically beamed within a half-angle of $1/\Gamma$, where Γ is the bulk Lorentz factor of the blastwave. If they are geometrically collimated to a half-angle θ, apart from the relativistic beaming, we would first observe emission from a beamed region of angle $1/\Gamma$ and as the blastwave decelerates (and Γ decreases), the emission region eventually would be equal to θ when $\Gamma \approx 1/\theta$. After this point, the observed flux decays quicker, because there is no longer lateral inclusion of the emission surface to compensate for the decreasing brightness. After the jet break, the steeper decay in the observed optical afterglow lightcurve continues until it

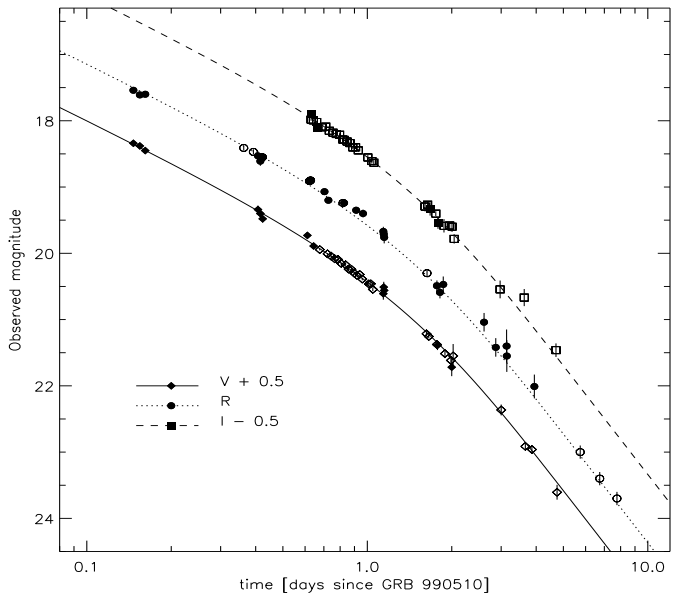

Figure 3.6 The achromatic break in optical afterglow lightcurves of GRB 990510 (from Harrison et al. 1999).

reaches the constant luminosity of the host galaxy. It has been found that, when corrected for the jet angles (estimated from the time of jet break), the total emitted energies of most GRBs are of the order of 10^{51} ergs (Frail et al. 2001).

One striking observational achievement was the detection of an optical flash from at least one burst, GRB 990123 (Akerlof et al. 1999). The very bright prompt optical flash was observed while the prompt gamma-ray emission ($T_{90} = 63$ s) was still in progress. Interestingly, the optical flux did not match the extrapolated gamma-ray flux observed at the same time, suggesting that the optical flash was produced by a different mechanism than the prompt gamma-ray emission (Briggs et al. 1999). In fact, such early flashes are expected from the reverse shock of the external shock, and therefore, the observation strongly supports the fireball-shock model of GRB (Sari & Piran 1999; Nakar & Piran 2005a, see §3.2.2). This remarkably bright optical flash, combined with the redshift of $z \geq 1.6$ measured from the afterglow observations for this event (Kulkarni et al. 1999), resulted in a total isotropic emitted energy estimated to be $> 10^{54}$ ergs (Briggs et al. 1999). This enormous energy raised some concerns, and contributed to the recognition of the idea that GRBs may be collimated.

I note that very recent observations of optical and infrared (IR) flashes from a long burst, GRB 041219a (detected by *INTEGRAL*, duration ~ 520 s), revealed behavior dissimilar to the optical flash of GRB 990123 (Vestrand et al. 2005; Blake et al. 2005). In this case, the flux of the optical flash followed the prompt gamma-ray emission lightcurve, which may indicate that the flash was a low-energy tail from the internal, forward shock emission. In addition, the IR observation showed an indication of delayed, weak emission possibly from the reverse shock. These observations reinforce the fireball-shock model more strongly than ever.

Another remarkable finding from optical follow-up observations is the detection of polarization. The amount of polarization is found to be very small, of a few

percent, and in a few cases the evolution of polarization has been observed (Rol et al. 2003; Greiner et al. 2003). Polarization is expected if the emission is due to synchrotron radiation, although the very small degree of polarization observed must be justified. One theory is that an entangled magnetic field behind the shock may exist at least at the radius where the afterglow is emitted (Greiner et al. 2003). When a larger number of observational datasets with sufficient quality become available, it may be possible to use such polarization curves to reveal the jet structure of GRBs (Figure 3.7). Currently, modeling of the jet structure using the polarization curve is still premature to explain the best-sampled polarization curve so far (of GRB

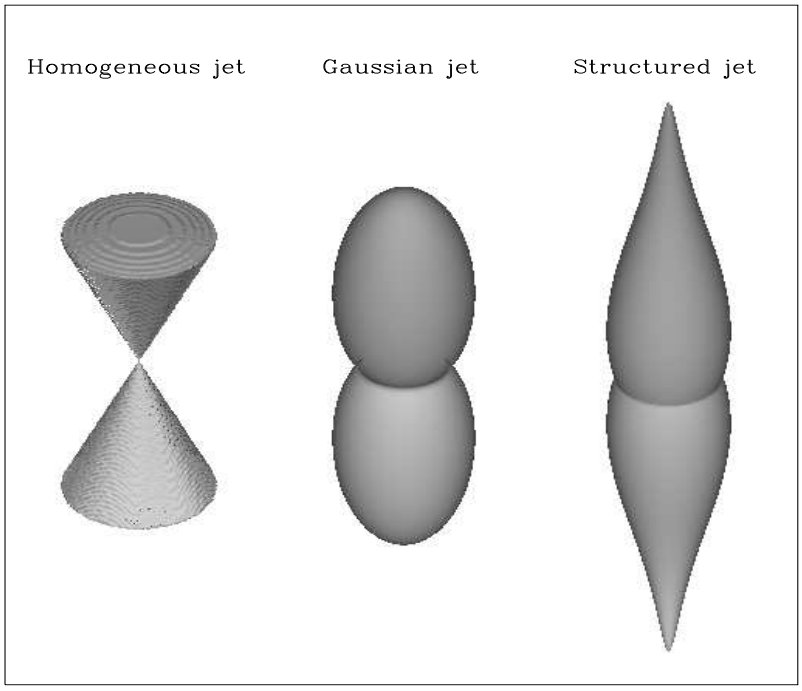

Figure 3.7 Schematics of various jet structures (from Rossi et al. 2004). The homogeneous jet has a uniform energy density independent of angle, whereas the Gaussian and power-law structured jets provide the energy density as a function of viewing angles.

030329 associated with a very complex lightcurve). Complications in the modeling might arise from the existence of an external magnetic field or dust within our own galaxy or the GRB host galaxies (e.g., Rossi et al. 2004; Lazzati et al. 2004).

Interestingly, an optical afterglow is not detected for all GRBs: about a half of these whose X-ray afterglows were detected did not show any optical signals, despite observational attempts early enough for such detections to be possible. The bursts with no associated optical transients are dubbed "dark bursts." Two possible explanations of the dark bursts are that they are intrinsically faint bursts or that there is extinction by dust. Recently, Rol et al. (2005) studied a sample of 20 dark bursts and extrapolated the observed X-ray flux down to the optical range, according to the physical models of afterglows. They found that only three bursts are truly "dark," and the others were merely due to the detection sensitivity limitations. To draw any conclusion, it is clear that more observational evidence is needed.

3.1.3.3 GRB-SN Connection

The signatures of a GRB-supernova (SN) association are also detected in the optical afterglow of some bursts: GRBs 980425, 030329, and 031203, in particular. These three bursts are strongly believed to be associated with type Ic SNe; SN1998bw, 2003dh, and 2003lw, respectively (Galama et al. 1998; Hjorth et al. 2003; Price et al. 2003; Uemura et al. 2003; Stanek et al. 2003; Thomsen et al. 2004; Cobb et al. 2004; Malesani et al. 2004). All of the associated SNe were bright, core-collapse SNe relatively nearby ($z \lesssim 0.2$), with strikingly similar spectral characteristics (see Figure 3.8), and their lightcurves showed significant deviations from the regular power-law like afterglow. According to the core-collapse supernova model of GRBs an underlying SN component should appear in the afterglow lightcurve as a "bump," about a week or two after the GRB (Figure 3.9; see §3.2.4 for detailed

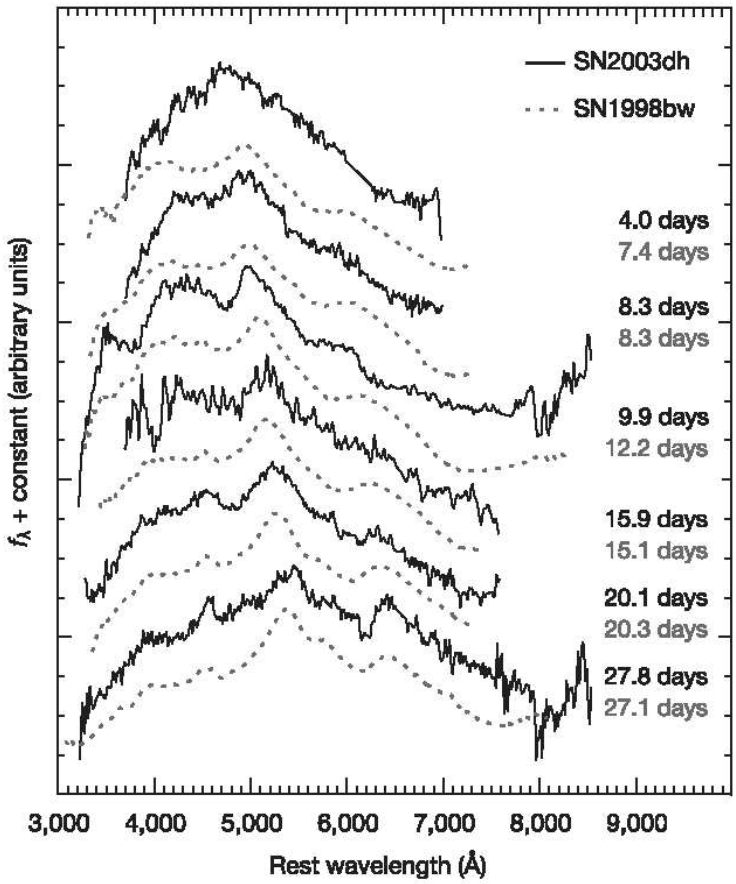

Figure 3.8 Spectral evolution of SN2003dh compared with SN1998bw. (from Hjorth et al. 2003).

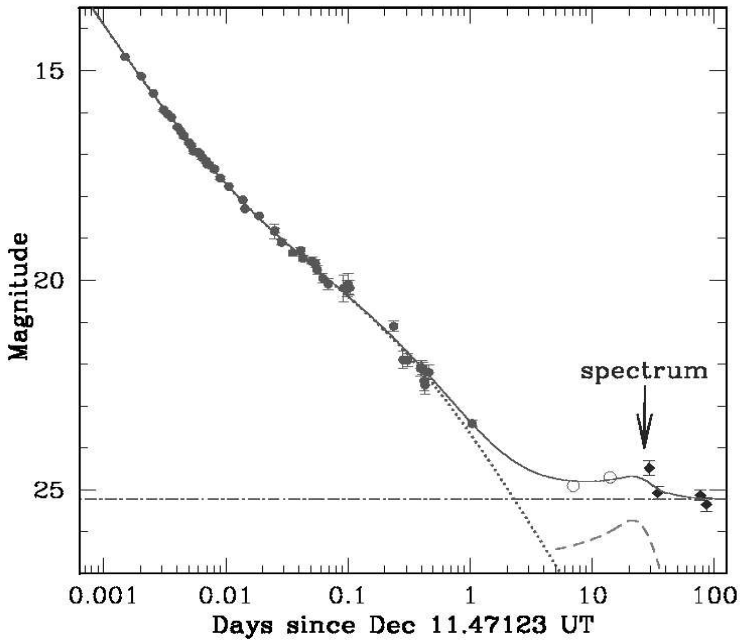

Figure 3.9 Optical afterglow lightcurve of GRB 021211 showing the SN bump at $\sim$ 20 days. The dashed line shows a "template" SN curve at similar redshift, and the dotted line shows the afterglow component. The horizontal line indicates the host galaxy magnitude (from Della Valle et al. 2003).

discussion of the model). Unfortunately, unless the SN is extremely bright and/or occurs nearby, this bump is not clearly detected. Nevertheless, several other bursts have been found to exhibit the bump features in their lightcurves that could be attributed to underlying SNe (Zhang & Mészáros 2004; Piran 2005).

3.1.3.4 Radio Afterglow

The radio afterglow can be detectable for a much longer period, lasting for months to even years. Unlike the X-ray and optical afterglows, it usually does not decay as a power law but varies for days or weeks (Frail et al. 2003). Especially large fluctuations at the beginning of the radio afterglow observation have been

seen and it has been suggested that this "twinkle" may be due to the diffractive scintillation by the nearby interstellar medium (Goodman 1997). If such is the case, the diffractive angle can constrain the emitting region of the radio afterglow. In the case of GRB 970508, the large observed fluctuation indicated the emitting region at a few weeks after the GRB could be estimated to be $R \sim 10^{17}$ cm, if it were indeed due to interstellar scattering (Frail et al. 1997). Therefore, the observations at various times could be used as a direct confirmation of the relativistic expansion. Similar to the optical afterglow case, the radio afterglow is also expected to show the signature of jet geometry as an early decline in its lightcurve, which has been observed for some GRBs (e.g., Harrison et al. 1999).

3.1.4 X-Ray Flashes and X-Ray Rich GRBs

BeppoSAX also discovered X-ray flashes (XRFs), a very rare (4 – 5 per year) transient detectable only in hard X-rays less than 100 keV (Heise et al. 2001). Their peak spectral energies ($E_{\rm peak}$) were found to be less than 40 keV. The XRFs were first thought to be a new type of phenomenon, different from GRBs; however, their temporal and spectral characteristics were noticeably similar to X-ray rich, soft GRBs (XRGRBs) that had been observed by BATSE and *Ginga*. As more numbers of XRFs and XRGRBs were observed by *BeppoSAX*, as well as by *HETE-II*, the evidence emerged that GRBs, XRFs, and XRGRBs all belong to one family of GRBs, namely, their agreement with the correlation between $E_{\rm peak}$ and luminosity (Kippen et al. 2004; Sakamoto et al. 2004b). This has been confirmed by the detection of afterglows from several XRFs in recent years (e.g., Soderberg et al. 2004; Fynbo et al. 2004), a few of which yielded redshift measurements ($z \sim 0.2$; Soderberg et al. 2004). In addition, a possible association of XRFs with SNe was recently reported (Soderberg et al. 2005), which strengthens the claim that the XRFs are indeed the

same phenomenon as GRBs. As of yet, the reason why their emission energies are low remains an open question. Some of the proposed models for XRFs are discussed in §3.2.6.

3.2 Theoretical Models of GRBs

As discussed so far, the number of acceptable physical models has been substantially narrowed down by multi-wavelength observations of GRBs, at least for the long GRBs. Physical models attempt to explain two main aspects of GRBs: what creates the prompt gamma-ray and afterglow emission, and what is the source of the energy (progenitor). As far as the former is concerned, the most widely currently accepted model of long GRBs is the fireball-shock model, in which two types of shocks are involved: internal and external. The model seems to explain most of the observational signatures of GRBs fairly well, especially the afterglow. As for the latter, namely the GRB progenitors, the leading model is a collapsing massive star forming an accreting black hole (for long GRBs), and a binary neutron star merger or neutron star – black hole merger (for short GRBs). In this section, the development of the fireball-shock model along the observational time line presented above is discussed in detail, followed by progenitor model discussions. Some alternative models are also briefly discussed at the end of this section.

3.2.1 Expanding Fireball

Shortly after the discovery of GRBs, a so-called "compactness problem" was realized in the context of cosmological models. The observed sub-second variability implies that the radius of the emitting region must be fairly small ($R \lesssim c\delta t \approx 10^{10}$ cm). This, combined with the observed non-thermal photon spectra and the

cosmological distance to the source, indicates that the high-energy photon density at the source must be extremely high. Such a condition would give rise to a large optical depth to pair production and the creation of a $\gamma - e^{\pm}$ "fireball," which in turn, would trigger the super-Eddington outflow of the fireball material (Goodman 1986; Paczyński 1986). As described in the previous section, observed GRB spectra can extend to well above MeV; however, with such a high optical depth, the gamma-rays above the pair-production threshold energy ($\gtrsim 0.5$ MeV) should not be observed at all. This was the compactness problem.

This contradiction can be overcome by invoking the idea that the fireball expands ultra-relativistically toward the observer (Fenimore et al. 1993a). The relativistic motion, with a bulk Lorentz factor Γ, reduces the pair-production optical depth by a factor of $\Gamma^{2|\beta|+2}$ (Lithwick & Sari 2001), where β is high-energy photon index of the observed spectrum. The reduction is due to two reasons: first, the observed photon energy is blue-shifted by a factor of Γ and therefore the photon energy in the comoving frame is lower, greatly decreasing the number of photons above the pair-production threshold energy. Second, the emission radius can now be estimated by $R \sim \Gamma^2 c\delta t$, relaxing the emission region constraints. Therefore, for the source to be optically thin, $\Gamma \gtrsim 100$ is required for typical GRBs with $|\beta| \gtrsim 2$ (Lithwick & Sari 2001).

An ultra-relativistic expansion of the fireball could indeed account for the optically-thin spectra observed; however, the emission directly from the expanding fireball would not be very efficient and the emitted spectra would still not be guaranteed to be non-thermal as observed. Also, the transition timescale from optically-thick to optically-thin would be too short to explain the long-lasting bursts. Therefore, a model that can somehow sustain the energy ejection as well as provide an efficient non-thermal radiation mechanism was needed.

3.2.2 Fireball-Shock Model: Internal and External

The fireball-shock model seems to address these issues well. Figure 3.10 shows the fireball shock picture. The model incorporates the idea that shocks are very likely to occur in such a scenario and are capable of converting the bulk kinetic energy of the outflow into internal energy of non-thermal particles, which subsequently radiate as non-thermal photon emission. The expanding fireball must eventually encounter the interstellar media (ISM) that causes it to decelerate, producing an *external shock* (Rees & Mészáros 1992; Mészáros & Rees 1993). The energy conversions at the shocks should be very efficient and such a model is capable of producing bursts with durations of the order of seconds.

The model seems to account for the cases of single-bump, smooth GRBs well (Fenimore et al. 1996; Sari & Piran 1997; Panaitescu & Mészáros 1998); however,

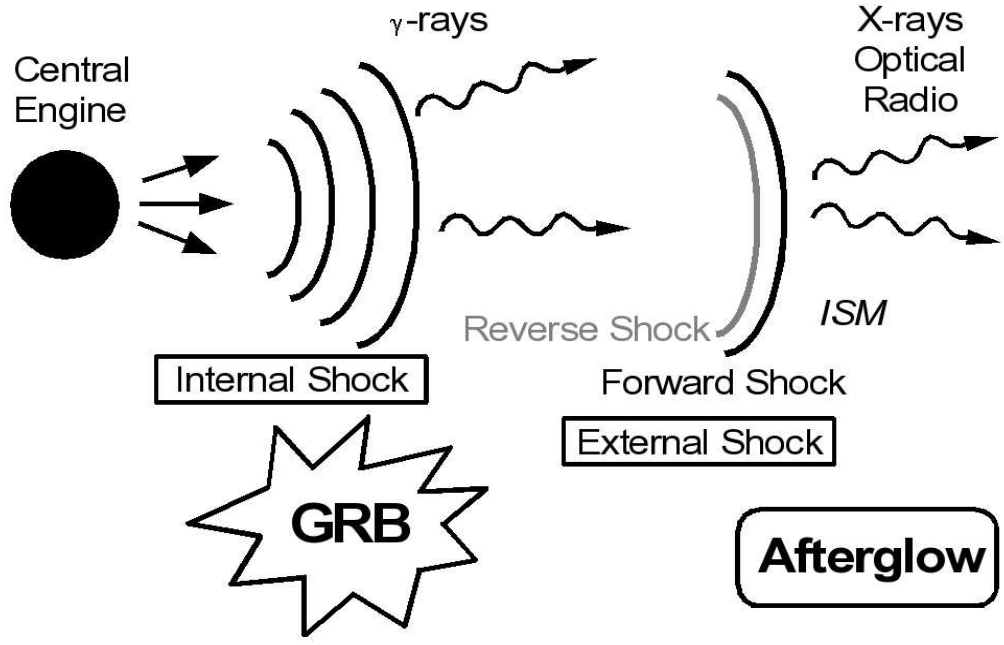

Figure 3.10 Schematic of the fireball shock scenario.

the majority of the observed GRBs exhibit very complex, highly variable lightcurves that last for 10 –100 seconds. Some difficulties arise to explain such lightcurves only with an external-shock scenario. It should be noted, however, that Dermer & Mittman (1999) have shown it may still be possible to produce such short-timescale variability, if there exist small dense clouds of certain size scales in the ISM.

In order to resolve the fine variability timescale issue, the *internal shock* model was suggested (Rees & Mészáros 1994). In the internal shock model, the energy of the fireball is ejected in a series of relativistically-expanding shells, and as the name suggests, the shocks occur internally between the shells themselves. When shells are ejected with various values of Γ, fast-moving shells can overtake the slowly moving ones and form shocks. This requires that the relative speed of the two shells in the comoving frame be relativistic (i.e., $\Gamma_2/\Gamma_1 > 2$), and that the upper limit on Γ is determined by the ratio of internal radiation energy to baryon rest energy ($\eta = E_0/M_0c^2$), which is variable from ejecta to ejecta due to a "central engine" (Fenimore et al. 1996). When the shells collide with each other, the bulk kinetic energy of the shells is converted into the internal energy that is to be radiated as gamma-rays. As the shells continue to travel outwards, they are still expected to subsequently go through the external shocks; therefore, the model is called internal-external shock model.

The internal shock model successfully explains both the observed duration and variability of the prompt emission, whereas the external shock model satisfactorily explains the low-energy afterglow observations. Therefore, the prevailing theory is that the internal shocks are responsible for the GRB prompt emission while the external shocks produce the broadband afterglows.

3.2.3 Acceleration and Emission Mechanisms in Shocks

In the shock scenario, the particles must be accelerated in the shock and most of the converted internal energy of the particles must somehow be radiated away as the GRB or afterglow that we observe. The mechanisms for acceleration and emission at the ultra-relativistic shocks are still subject to detailed studies that largely rely on sophisticated computer simulations. However, in the fireball-shock model, the general assumption is that both the prompt emission and the afterglow emission are due to the synchrotron radiation by Fermi-shock accelerated electrons. If electrons are accelerated by the Fermi mechanism at the shock, the resulting electron distribution is expected to be a power law; $N(\gamma_e) \propto \gamma_e^{-p}$ for $\gamma_e > \gamma_m$. Furthermore, another general assumption of the shock acceleration mechanism is the equipartition between the particle energy density and magnetic energy density. The accelerated electrons interact with this magnetic field and emit most of their energy as synchrotron radiation, which is an extremely efficient radiative process. This scenario is the synchrotron shock model (SSM; Tavani 1996a,b).

The predicted broadband spectra of the cooling synchrotron emission from power-law distributed electrons are shown in Figure 3.11. In the figure, "fast cooling" corresponds to the case in which all the accelerated electrons ($> \nu_m$) cool by radiating synchrotron to an energy ν_c, and "slow cooling" is the case in which only the higher energy electrons cool to ν_c. Since the synchrotron emission power of a single electron is

$$P(\gamma_e) = \frac{4}{3}\sigma_T c {\gamma_e}^2 \frac{B^2}{8\pi}, \tag{3.1}$$

where σ_T is the Thomson cross section, c is the speed of light, and $B^2/8\pi$ is the magnetic energy density, the more energetic electrons cool faster than the less energetic ones (e.g., Rybicki & Lightman 1979). Therefore, the cooling energy ν_c is the

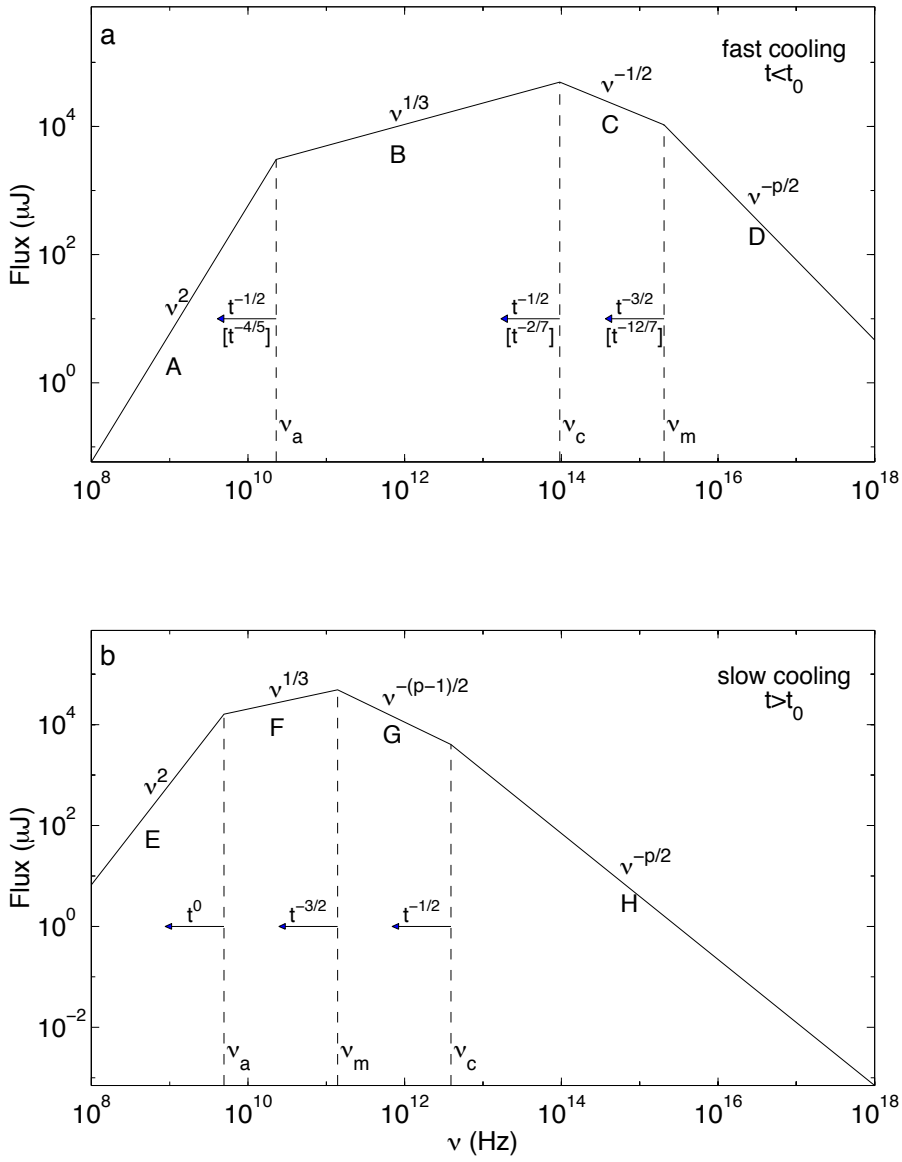

Figure 3.11 Theoretical energy flux spectra resulting from synchrotron emission by electrons with a power-law energy distribution with index p (from Sari et al. 1998).

energy at which the synchrotron cooling timescale balances the cooling timescale due to the adiabatic expansion of the shell. In the GRB prompt emission, the synchrotron cooling time is extremely short, and the resulting spectra are more likely to be the fast cooling ones. On the other hand, in the afterglow, the cooling timescale becomes longer and the emerging spectra are expected to be the slow cooling ones. In the SSM, radiation from synchrotron self-Compton that may arise in the scenario is excluded, and no re-acceleration of the electrons is assumed.

The observed afterglow spectra are generally found to be consistent with the SSM, which requires $p = 2.2 - 2.3$ in the ultra-relativistic Fermi acceleration case (Waxman 1997; Gallant 2002). Also, the small degree of polarization observed in the afterglow discussed in §3.1.3.2 is also consistent with the model, due to the likely existence of highly random magnetic field behind the shocks. Therefore, the afterglow external-shock scenario seems to be consistent with the observations.

However, that is not the case for the prompt emission. Although the majority of the observed GRB spectra are found to be consistent with the SSM, there are significant fractions of spectra that are not explainable within the simple SSM. Also, it has recently been reported that the post-shock particle distribution presumed in the SSM may be inconsistent with observed spectra (Baring & Braby 2004). This issue is further discussed in a later chapter (Chapter 6).

3.2.4 Progenitors ("Central Engines")

The fireball-shock model discussed above does not predict what the central engine or the progenitor is. Since the progenitor lies well inside the optically-thick region, it is not possible to observe any signal from it directly (except perhaps in the form of neutrino emission or gravitational waves, if strong enough). Nonetheless,

the central engine is required to posses at least an observed total energy of $\sim 10^{51}$ erg to launch the narrowly collimated ultra-relativistic outflows.

The current leading model for progenitors of long GRBs is the collapsar model (Woosley 1993; Woosley & MacFadyen 1999; MacFadyen & Woosley 1999). The collapsar is a rotating massive star with no hydrogen envelope, whose iron core collapses into a black hole with an accretion disk. A star with an initial mass $> 35 - 40 M_{\odot}$, where $M_{\odot}$ is the mass of the Sun, would evolve into a helium star of mass $\sim 10 - 15 M_{\odot}$. Such a star would have an iron core of typically $\sim 1.5 - 2.3 M_{\odot}$. At the end of its life, the core collapses into a black hole, as well as forming an accretion disk. The accretion rate at this point is of the order of 0.1 $M_{\odot}$ s^{-1}, and the black hole grows to a few solar masses in a matter of seconds. Subsequently, relativistic outflow jets form along the rotational axis, driven possibly by neutrino emission from the disk, with the total energy deposited along the rotational axis by neutrino annihilation that is found to be $\sim 10^{51}$ ergs. Initially, when the model was first proposed, such a star would be too massive to successfully eject materials in the envelope as a SN, and therefore, the model was called a "failed SN" (Woosley 1993). Later, detailed simulation studies found that not only could they produce successful SNe, but also the consequences can be diverse, being very sensitive to the physical parameters of the system, such as the accretion rate, angular momentum, and disk viscosity (MacFadyen & Woosley 1999; Zhang, Woosley & Heger 2004). The collapsar model seems to be able to account for many observational signatures of the prompt emission and the afterglow of long GRBs successfully, such as the SN bump observations, total energy budget estimated, the star-forming host galaxy observations, and jet geometry.

3.2.5 Short GRB Models

As seen in the duration distribution (Figure 3.3), about 25% of the BATSE GRBs are classified as being short. Since the afterglow of short GRB has not been observed, the nature of the short events remains an open question. Since the collapsar model cannot produce a burst with very short duration (MacFadyen & Woosley 1999), it is widely believed that the short bursts may be produced by a different type of catastrophic event. The most popular idea is that they are created in the merger of neutron stars (Goodman 1986; Paczyński 1986; Eichler et al. 1989) that form a rotating black hole with remnant torus around it (Mészáros & Rees 1997). The merger occurs on a very short time scale (determined by the amount of accreting material) and therefore, should be able to produce bursts < 2 s with adequate energetics. Observations of counterparts for short GRBs are needed to constrain the existing physical models.

3.2.6 XRF Models

In order to explain the very soft nature of XRFs and XRGRBs, the suggested models involve higher redshift, more baryonic load, or off-axis viewing angles in comparison with GRB cases. Based on the recent observational findings described in §3.1.4, currently the most favored and perhaps most likely model is the off-axis one. The jet geometry of GRBs has been almost completely established; however, the structure and other properties of the jets have not been confirmed. Therefore, the off-axis models vary depending on the type of jet assumed, such as the Gaussian jet (Zhang et al. 2004, Figure 3.7 center), the power-law shaped jet (Lamb et al. 2005, Figure 3.7 right), or uniform jet (Yamazaki et al. 2004; Lamb et al. 2005, Figure 3.7 left). In addition, the jet structure can either be assumed to vary from

GRB to GRB, or assumed to be universal. Some of the off-axis jet models seem to successfully explain the empirical properties of GRB and XRFs.

A model within the context of the collapsar scenario has also been suggested, in which the XRF may be the result of off-axis collapsar jet in a cocoon that is mildly relativistic and extends to larger angles (Zhang, Woosley & Heger 2004). In this case, there should always be an underlying XRF in every GRB, which may manifest itself as a soft precursor or soft tail in GRBs. In fact, such precursors or tails have been observed in some GRBs (e.g., in't Zand et al. 1999; Vanderspek et al. 2004). Nevertheless, the observed XRF sample is very small compared to the GRB sample, and more observational evidence is required to better understand the soft nature of XRFs and the relation between XRFs and GRBs.

3.2.7 Alternative Physical Models of GRBs

Although the models discussed above are the leading candidates for the GRB creation mechanism and progenitor, there exist many other models that may account for the observed phenomenon. One alternative model to the internal-external shock scenario of GRB creation mechanism is the electromagnetically-dominated model (Lyutikov & Blandford 2003). In this model, the relativistic outflow is the Poynting flux extracted from an accreting magnetized black hole (Blandford & Znajek 1977), and the particles are accelerated through electromagnetic instabilities rather than shocks. A rotating, strongly-magnetized black hole is very likely to be a natural consequence of a collapsing star. Currently, the major disadvantage of this model is that the particle acceleration and the energy dissipation in magnetically-dominated media in the relativistic regime have not been well modeled (Lyutikov & Blandford 2003).

As for the progenitor for long GRBs, another competing model is the Supranova model (Vietri & Stella 1998). The model involves a very massive ("supramassive") neutron star collapsing into a black hole. Unlike the collapsar model, the SN in this case happens weeks or months before the catastrophic event that produces the GRB occurs due to the loss of angular momentum supporting the neutron star. This model, therefore, is not consistent with the SN bumps observed soon after GRBs. The advantage of the model, however, is that the outflow from the progenitor can be very clean (i.e., baryon free). The baryon purity constraint arises from the inferred high Lorentz factor ($\Gamma \sim 100$), implying that the total mass present in the emission region must be much less than a stellar mass.

Finally, for short GRBs, the very recent giant flare from the soft gamma repeater SGR 1806-20 that occurred on December 27, 2004, has invoked the theory that some short GRBs may be the same type of magnetic flare from far distances (Hurley et al. 2005). The giant flare consisted of an initial bright-hard spike of ~ 0.2 s, followed by a softer pulsating tail lasting for ~ 400 s. The first short spike may be what is observed as a short GRB. According to Hurley et al. (2005), BATSE would not have been sensitive enough to detect the soft pulsating tail in a single short GRB. The theory might be supported by the possible existence of X-ray tails in short GRBs, revealed by co-adding 76 spectra of short BATSE GRBs (Lazzati et al. 2001). However, the lack of concentration of BATSE short GRBs in the direction of Virgo cluster suggests that only a very small fraction of short GRBs can be associated with such an SGR flare nearby (Palmer et al. 2005). There are only three such giant flares observed in the past 25 years, and the model could be tested with more observations of such events in the future.

CHAPTER 4

SPECTRAL ANALYSIS OF BRIGHT BATSE GRBs

In the context of GRB prompt emission, the simple emission scenario by optically-thin synchrotron radiation that is most widely favored has been challenged by the observations (Preece et al. 1998a, 2000; Ghirlanda et al. 2002; Lloyd-Ronning & Petrosian 2002). While this emission model can account for many of the observed spectra, a considerable number of spectra exhibit behavior inconsistent with what the model predicts. The energy spectra of GRB prompt emission observed with BATSE are generally well described by smoothly-broken power laws. GRB spectral analysis attempts to empirically characterize the spectra, usually parameterized by spectral indices and a peak energy in the power density spectrum. The parameters are then used to infer the GRB emission and acceleration mechanism.

BATSE GRB spectra are most commonly fitted with an empirical smoothly-broken power law model (Band et al. 1993), and often with a power law with high-energy cut-off or a sharply-broken power law. However, it has been pointed out that spectral parameters are highly dependent on spectral model choices (Preece et al. 2002; Ghirlanda et al. 2002). Thus, a consistent, model-independent spectral analysis should be carried out with sufficiently large database, in order for spectral parameters to meaningfully constrain the existing physical emission models.

Additionally, to deduce the emission mechanism from observations, spectra with fine time resolution are necessary because of the short timescales involved in typical emission processes (i.e., the radiative cooling time, dynamical time, or acceleration

time), which are also indicated by the extremely short timescale variability observed in GRB lightcurves (e.g., Bhat et al. 1992). The integration times of spectra certainly depend on the capabilities of detectors as well as the brightness of events and photon flux evolution. GRB spectral analyses, therefore, have been performed on various timescales, yet a comprehensive study of the relations between time-averaged and time-resolved spectra, and effects of various integration times on spectral properties has not been done.

Among all the gamma-ray experiments that have detected GRBs, BATSE provides the largest GRB database from a single experiment, consisting of observational data for 2704 GRBs. For many of the BATSE GRBs, high time and energy resolution data are available. The BATSE data, therefore, are the most suitable for detailed spectral studies, both in quantity and quality. The previous BATSE GRB spectral catalog (Preece et al. 2000, SP1 hereafter) consisted of 5500 time-resolved spectra from 156 bright GRBs that occurred before October 1998. The SP1 burst sample was selected from a set of 1771 GRBs, nearly 1000 bursts less than what is currently available in the complete database. The sample was also limited to the events that provided more than 8 spectra and therefore, excluded relatively shorter and weaker events. In addition, a combination of LAD and SD data was used, no time-integrated spectral fit results were presented, and only one photon model (out of four models available) was fitted to each spectrum. Finally, the mathematical differences in parameterization of each model were not taken into account to obtain corrected overall statistics of the analysis results.

We present in this chapter the high-energy resolution spectral analysis of 350 bright BATSE GRBs. The main objective of this work is to obtain model-independent spectral properties of GRB prompt emission with sufficiently good statistics. This is done by a systematic analysis of the large sample of GRB spectra, using a set of various photon models, all fitted to each and every one of the

spectra. We obtain model-unbiased spectral properties by studying characteristics of each photon model, taking into account the parameterization differences, and statistically determining the best-fitted model for each spectrum.

The analysis performed here is much more comprehensive and consistent than that of SP1 in the sense that (i) only LAD data are used, (ii) the burst selections are more objective, (iii) 5 different models are fitted to each spectrum, both time-integrated and time-resolved, and (iv) the best-fitted spectral parameters of each spectrum are independently determined by statistical analysis. The use of multiple models allows us to compare the internal characteristics of different models as well as to obtain unbiased statistics for the spectral parameters. We also note that the BATSE data and the DRMs used here have been regenerated since the publication of SP1, with a refined detector calibration database. This provided more precise LAD energy edges, thus assuring the improved accuracy of the spectral analysis.

The chapter is organized in the following manner. We first describe the event and interval selection methodology in §4.1. The details of the spectral analysis methods are then discussed in §4.2, including descriptions of the photon models used. We also discuss our simulation results in §4.3, which were performed to assist us in interpreting the analysis results correctly. Finally, in §4.4, the analysis results are presented.

4.1 Selection Methodology

The BATSE detectors were sensitive enough to detect relatively weak GRBs down to a peak photon flux of ~ 1 s^{-1} cm^{-2} and a total energy fluence in 25 – 2000 keV of $\sim 10^{-8}$ ergs cm^{-2}. Unfortunately, many dim bursts do not provide enough signal above background for high energy resolution spectral analysis, nor particularly for time-resolved spectroscopy. Therefore, we need to select and limit

our analysis to GRBs with sufficient signal. In addition, the available data types and data ranges vary for each event. In this section, we present the methodology employed for the event selection, the data type selection, and time and energy interval selections.

4.1.1 Event Selection

The primary selection was made based on the peak photon flux and the total energy fluence in the BATSE 4B catalog (Paciesas et al. 1999), as well as the current BATSE GRB catalog[1] for the post-4B events. The catalogs list a total of 2702 GRBs, of which two were later identified as non-GRBs (trigger numbers 5458 and 7523). Additionally, there are four events that were later identified as GRBs (trigger numbers 1505, 2580, 3452, and 3934), bringing the total number of BATSE GRBs to 2704. The number is consistent with the final BATSE 5B catalog (M.S. Briggs et al. in preparation). Our sample was selected from these 2704 events. The burst selection criterion is a peak photon flux in 256 ms greater than 10 photons s^{-1} cm^{-2} or a total energy fluence in the summed energy range (> 20 keV) larger than 2.0×10^{-5} ergs s^{-1}. Having the criteria both in terms of energy fluence and photon flux allows inclusion of short bright events as well as long weaker bursts. The peak photon flux criterion remains the same as SP1, although it was misstated in SP1 as a 1024 ms integration time. The energy fluence criterion has been lowered from the value used in SP1 so as to include more events, while still securing sufficiently good statistics. A total of 298 GRBs satisfied these criteria.

In addition, 573 GRBs out of 2704 do not have flux/fluence values published in any BATSE GRB catalog, mainly due to gaps in the 4-channel discriminator data, used to obtain the flux/fluence values. Nonetheless, for many of these bursts, finer

[1]Available online at http://gammaray.nsstc.nasa.gov/batse/grb/catalog/current/

energy-resolution data are still available for spectral analysis, and some are bright enough to be included in this work. Therefore, we estimated the photon flux and the energy fluence values for the events without published flux/fluence values, using available data. To estimate the peak photon flux and energy fluence for such bursts, we used 16-channel MER data (see §2.2.3 for the description of the data type) binned to a 256-ms integration time and fitted with a smoothly-broken power-law model (§4.2.2.5). There were some cases where MER data were not available but either HERB or CONT data existed. Most of these cases, however, turned out to be noticeably very weak, or else all of the available data were not complete, and therefore did not qualify for inclusion. In this way, 55 GRBs yielded peak photon flux and/or energy fluence values well above our threshold criteria, and are therefore included in this work.

Out of these selected bright bursts, we found two cases (trigger numbers 3366 and 7835) in which the published flux/fluence values were incorrect and the actual flux/fluence values were much lower than the criteria used here. Consequently, these two events were excluded. We also found one case (trigger number 5614, peak photon flux = 182 photons s^{-1} cm^{-2}) in which the burst was so bright that the indication of possible pulse pile-up was seen in the energy spectra of all available detectors and the data were not usable. Thus, this event was also excluded in this work. The resulting total number of GRBs included in this spectral analysis was 350. The events are listed in Table 4.1, along with the data types, time and energy intervals, and numbers of spectra contained.

Table 4.1 Basic properties of 350 GRBs included in the catalog.

GRB Name[1] (1)	BATSE Trig # (2)	Trig SOD (UT,s) (3)	Data Type (4)	LAD # (5)	Time Interval[2] Start (s) (6)	Time Interval[2] End (s) (7)	Energy Interval Start (keV) (8)	Energy Interval End (keV) (9)	# of Spectra (10)
910421	105	33243	HERB	7	0.064	5.184	27.109	1948.4	12
910425	109	2265	MER	04	–14.336	86.815	32.506	1813.5	26
910430	130	61719	CONT	6	–17.408	64.512	36.383	1799.3	22
910503	143	25452	HERB	6	0.000	18.560	32.275	1900.9	46
910522	219	43929	MER	456	105.947	133.147	33.638	1821.8	13
910525	226	69987	CONT	5	–3.072	171.010	32.678	1853.1	19
910601	249	69734	MER	0246	0.107	45.019	34.665	1814.1	68
910602	257	82501	HERB	0	0.000	17.664	33.151	2039.4	7
910609	298	2907	CONT	4	–1.408	0.640	31.936	1817.7	1
910614	351	6864	HERB	6	31.934	61.824	31.934	1878.1	5
910619	394	51272	HERB	1	0.000	43.456	29.058	1823.6	36
910626	444	26113	HERB	2	0.000	0.256	28.126	1953.7	1
910627	451	16157	HERB	4	0.000	13.056	27.166	1951.5	16
910717	543	16384	HERB	4	0.000	6.144	31.837	1946.4	10
910807	647	26432	HERB	2	0.000	27.200	28.141	1909.9	16
910814	676	40180	MER	23	–46.080	69.342	35.485	1829.6	19
910814	678	69273	HERB	2	0.000	31.680	32.468	1900.5	42
910905	761	85735	HERB	0	0.000	54.144	28.947	2043.0	24
911031	973	34580	HERB	3	0.000	33.728	29.899	1795.4	34
911104	999	54281	HERB	2	0.000	4.736	28.099	1906.1	4
911109	1025	12457	HERB	4	0.000	3.264	27.152	1905.3	6
C 911118	1085	68258	HERB	4	0.000	25.408	27.186	1908.0	60
911126	1121	46127	HERB	4	0.000	33.216	27.163	1906.2	33
911127	1122	15728	HERB	1	0.000	22.144	29.037	1821.5	35
C 911202	1141	73729	HERB	7	0.064	23.104	27.110	1903.6	42
911209	1156	58962	MER	45	–110.592	106.910	32.224	1829.7	14
911209	1157	66957	HERB	1	0.128	23.360	29.005	1818.2	18
920110	1288	33478	MER	46	0.030	137.374	34.060	1802.8	28
920210	1385	35623	HERB	5	0.000	43.264	32.585	1985.5	36
920218	1419	67342	MER	01	25.486	132.570	33.231	1846.5	13
920226	1440	29728	HERB	3	0.000	29.120	29.895	1841.2	18
920308	1468	17745	HERB	4	0.000	25.344	27.090	1900.5	3
C 920311	1473	8424	HERB	5	0.000	28.864	27.503	1989.9	55
920314	1480	21747	HERB	2	1.792	16.704	32.574	1863.4	2
920315	1484	15567	HERB	3	0.000	2.944	29.903	1841.8	7
920320	1503	44338	HERB	5	0.000	26.240	27.425	1982.4	30
920325	1519	62255	HERB	1	0.000	39.680	33.185	1822.4	19
920329	1525	59906	MER	0234	0.024	0.568	34.017	1823.0	1
920404	1538	47503	HERB	1	0.000	5.376	29.223	1840.0	9
920406	1541	9853	CONT	3	–1.024	119.808	33.923	1842.6	15
920414	1553	84161	HERB	3	0.064	1.088	29.923	1843.5	3
920429	1571	68372	CONT	6	91.136	113.660	36.297	1794.6	4
920511	1601	23245	HERB	1	0.064	12.672	29.045	1822.3	2
920513	1606	60779	CONT	3	–2.048	102.400	33.964	1845.5	36
920517	1609	11874	CONT	7	–2.048	18.432	27.063	1810.7	5
920524	1623	13902	HERB	3	0.000	42.432	29.911	1842.5	9
920525	1625	12421	HERB	4	0.064	23.616	27.137	1904.2	37
920617	1652	19611	CONT	6	–2.048	81.920	36.410	1800.9	18
920622	1663	25504	HERB	4	0.000	27.584	31.868	1948.5	61
920627	1676	46956	MER	26	0.031	55.647	36.610	1802.2	30
920711	1695	58140	MER	37	0.027	103.260	30.455	1824.0	142
920714	1698	47069	HERB	4	0.000	30.912	27.190	1908.3	32
920718	1709	77563	HERB	7	0.128	6.208	27.100	1902.9	13
920720	1711	11524	CONT	0	–0.448	7.744	33.267	1821.1	4
920720	1712	21172	MER	135	0.031	114.463	33.210	1851.5	11
920723	1721	3634	HERB	3	0.064	30.464	29.969	1847.4	33
920801	1733	4600	CONT	0	–5.120	11.264	33.203	1817.3	4
920824	1872	39183	MER	57	0.024	163.416	29.876	1832.1	110
920902	1886	1736	HERB	5	0.064	14.592	27.510	1990.6	30
921008	1982	76057	HERB	5	0.000	26.240	27.508	1990.4	7

Table 4.1 (continued)

GRB Name[1]	BATSE Trig #	Trig SOD (UT,s)	Data Type	LAD #	Time Interval[2] Start (s)	Time Interval[2] End (s)	Energy Interval Start (keV)	Energy Interval End (keV)	# of Spectra
C 921009	1983	24070	HERB	2	0.064	33.408	28.133	1864.0	54
921015	1989	5792	CONT	4	–8.192	299.008	31.849	1812.3	30
921022	1997	55259	HERB	2	0.000	40.832	32.561	1907.6	21
921118	2061	79904	CONT	4	–60.416	152.580	31.862	1813.1	26
C 921123	2067	22711	HERB	1	12.160	31.744	28.979	1816.1	45
921206	2080	66259	HERB	6	0.000	40.256	32.112	1890.0	22
C 921207	2083	57647	HERB	0	0.000	21.248	33.251	2046.1	45
921209	2090	41738	HERB	1	0.000	41.408	29.092	1827.5	18
921230	2110	32270	MER	57	–2.048	27.214	29.908	1834.4	11
921230	2112	56461	CONT	0	–86.016	169.984	33.186	1816.3	1
930106	2122	71835	HERB	6	0.064	61.184	36.302	1884.0	11
930112	2127	13650	HERB	0	0.000	29.888	28.952	2043.5	27
930120	2138	84700	MER	012	0.027	96.155	34.497	1836.0	39
930131	2151	68231	HERB	3	0.000	2.112	29.941	1798.8	3
930201	2156	60115	MER	137	0.030	173.056	31.252	1838.5	97
930214	2193	65578	HERB	1	0.000	36.160	29.057	1776.6	10
930309	2228	11269	HERB	6	0.064	48.256	36.310	1884.4	12
930331	2276	11476	HERB	1	0.064	44.096	33.226	1826.1	5
930405	2286	32089	HERB	6	0.000	24.000	36.516	1896.4	26
930405	2287	50390	HERB	6	0.000	61.696	32.295	1902.3	13
930425	2316	37049	HERB	1	0.000	29.440	33.224	1826.0	33
930506	2329	53571	MER	37	0.027	29.675	30.590	1883.3	100
930609	2383	36444	HERB	7	0.064	34.112	27.037	1898.5	5
930612	2387	2657	HERB	2	0.000	38.208	32.580	1909.0	19
930612	2389	32037	HERB	0	0.000	57.216	33.182	2041.5	23
930706	2431	18810	MER	1357	0.024	2.088	31.657	1840.1	13
930720	2450	52509	MER	67	0.027	78.875	31.721	1805.0	11
930809	2486	18664	HERB	0	0.000	66.688	28.937	1997.1	15
930905	2514	12390	HERB	6	0.000	0.256	32.269	1855.6	1
930910	2522	43928	HERB	4	0.000	74.752	31.737	1894.9	8
930916	2533	73163	MER	23	0.030	67.102	27.016	1831.2	70
930922	2537	23086	HERB	1	0.064	6.144	29.103	1876.0	26
931008	2571	40150	HERB	2	0.064	54.336	32.569	1908.2	12
931026	2606	41757	CONT	7	–50.176	99.328	27.112	1814.0	20
931031	2611	14795	HERB	5	0.000	2.496	27.502	1989.8	8
931103	2617	59142	HERB	5	0.064	18.688	32.628	1942.4	25
931106	2619	73924	CONT	0	–1.024	125.952	33.235	1819.2	3
931126	2661	70299	HERB	3	0.000	12.928	29.910	1796.3	29
931204	2676	35290	MER	013	0.027	44.763	33.376	1838.5	122
931205	2679	53991	HERB	0	0.000	0.320	28.875	1992.4	1
931221	2700	7790	HERB	3	0.064	56.320	29.932	1844.3	5
931222	2703	76893	HERB	4	0.000	59.456	27.059	1987.9	8
940119	2770	9730	HERB	2	0.064	34.816	32.591	1955.0	3
940128	2790	60665	HERB	0	0.064	47.808	29.024	2003.8	19
940203	2797	56816	HERB	3	0.000	4.160	29.977	1848.1	12
940206	2798	517	MER	13	0.030	64.094	33.534	1855.0	95
940210	2812	69196	HERB	6	0.000	29.056	36.200	1878.0	24
940217	2831	82962	MER	02	0.030	180.220	35.162	1819.4	112
940218	2833	70348	HERB	0	0.000	13.312	33.102	2036.1	35
940228	2852	41340	HERB	5	0.000	36.736	32.567	1984.1	16
940301	2855	72637	HERB	4	0.000	35.648	27.066	1988.5	35
940302	2856	18511	MER	01	0.030	151.840	33.217	1845.4	114
940306	2863	13033	CONT	3	–1.024	27.648	33.876	1839.3	6
940319	2889	86240	HERB	4	0.064	61.184	31.783	1987.8	9
940321	2890	79507	HERB	6	0.064	38.592	31.975	1836.4	6
940323	2891	79478	HERB	4	0.064	40.064	31.838	2036.5	29
940329	2895	20966	HERB	6	0.000	4.032	32.196	1895.7	9
940410	2919	56702	HERB	6	0.000	8.512	36.303	1884.0	10
940414	2929	60385	HERB	4	0.896	42.368	27.120	1993.0	35
940419	2940	69058	MER	23	0.030	58.846	27.002	1829.8	17
C 940429	2953	2633	HERB	3	0.000	16.704	33.938	1843.7	32

Table 4.1 (continued)

GRB Name[1]	BATSE Trig #	Trig SOD (UT,s)	Data Type	LAD #	Time Interval[2] Start (s)	Time Interval[2] End (s)	Energy Interval Start (keV)	Energy Interval End (keV)	# of Spectra
940520	2984	1298	HERB	4	0.000	26.944	27.102	1991,4	10
940526	2993	39326	HERB	3	0.000	22.976	29.908	1842.3	7
940526	2994	73205	HERB	1	2.240	42.240	29.020	1914.8	37
940529	3002	58836	MER	37	0.031	133.410	30.431	1822.4	19
940529	3003	76736	HERB	0	0.000	24.512	28.985	2000.8	12
940619	3035	77480	MER	26	0.030	106.140	36.635	1803.9	28
940623	3042	67583	HERB	1	0.128	56.192	33.217	1967.6	29
940624	3044	52394	HERB	6	0.000	2.944	36.548	1943.1	1
940703	3057	16846	MER	15	0.300	85.790	32.948	1863.4	165
940708	3067	74526	HERB	6	0.000	12.800	32.151	1892.6	29
940710	3071	35729	CONT	3	–6.144	40.960	33.891	1840.4	3
940717	3087	12269	HERB	0	0.000	0.320	28.976	2000.1	1
940806	3110	71000	HERB	0	0.034	9.920	33.175	2041.0	4
940810	3115	8562	HERB	3	0.026	30.656	33.857	1838.0	21
940817	3128	31215	HERB	5	0.033	48.000	32.626	1988.6	44
940826	3138	75320	HERB	6	0.029	14.080	35.919	1861.7	17
940902	3152	52192	HERB	4	0.026	2.560	27.036	1986.1	2
940921	3178	18493	HERB	0	0.033	54.720	33.194	2042.3	37
941008	3227	48772	MER	15	0.030	124.446	32.869	1856.9	50
C 941014	3241	33608	HERB	6	0.030	49.472	36.153	1875.3	44
941017	3245	37173	MER	04	–2.048	86.558	32.483	1812.1	116
941018	3247	21730	CONT	7	–102.400	198.660	26.931	1801.8	9
941020	3253	72327	MER	45	0.024	64.920	32.253	1831.7	94
941023	3255	16472	HERB	6	0.127	37.504	36.325	1885.2	12
941119	3287	70250	HERB	5	0.091	32.256	27.437	1983.5	9
941121	3290	62697	HERB	0	0.026	46.784	28.938	2042.4	19
941126	3298	44521	MER	01	0.030	81.310	33.129	1838.2	20
941126	3301	71798	HERB	5	0.029	22.656	27.455	1985.2	7
941228	3330	27581	HERB	3	0.108	54.528	29.951	1799.7	13
950104	3345	26319	HERB	1	0.033	11.584	29.067	1919.7	17
950111	3352	44310	HERB	2	0.033	58.880	37.012	1905.0	29
950117	3360	5761	HERB	1	0.090	75.840	29.030	1915.9	6
950208	3408	7824	MER	26	1.950	60.062	36.662	1805.3	63
950210	3410	8421	HERB	1	0.034	0.320	29.007	1913.4	1
950211	3412	8697	HERB	6	0.031	0.320	36.256	1836.8	1
950211	3415	72468	HERB	5	0.026	54.592	27.470	1940.2	25
950301	3448	75761	CONT	3	–40.960	296.960	33.862	1838.3	13
950305	3458	54304	MER	45	0.027	22.299	32.169	1826.2	19
950310	3464	78395	HERB	3	0.033	30.272	33.983	1846.8	5
950325	3480	25844	HERB	3	0.033	6.528	29.924	1797.5	10
950325	3481	63391	HERB	2	0.033	47.616	37.055	1953.0	30
950401	3489	74634	HERB	1	0.116	16.512	33.142	1961.0	12
950403	3491	47987	HERB	3	0.090	20.672	33.780	1832.5	53
950403	3492	84826	HERB	5	0.032	43.904	32.637	1989.5	49
950425	3523	919	HERB	6	0.033	28.864	32.037	1929.6	58
950503	3537	66970	HERB	4	0.109	76.288	27.141	1949.5	42
950509	3567	83765	CONT	0	–47.104	514.050	33.202	1817.2	2
950513	3571	81703	HERB	5	0.092	36.352	27.490	1942.1	22
950522	3593	85283	HERB	2	0.026	35.520	28.097	1905.9	15
950608	3634	81272	HERB	3	0.033	130.816	29.989	1849.0	4
950701	3657	12758	HERB	4	0.032	37.952	31.800	1988.9	31
950701	3658	23737	HERB	5	0.026	11.392	27.507	2036.8	30
950706	3662	42735	HERB	5	0.029	29.824	27.388	1978.7	8
950711	3663	13789	HERB	1	0.029	165.376	33.245	1922.6	10
950804	3734	7134	HERB	4	0.147	3.712	31.721	1849.1	15
950805	3736	13454	CONT	2	–0.512	1.536	37.084	1819.3	1
950818	3765	5002	HERB	1	0.184	73.280	29.018	1914.5	33
950822	3767	13749	HERB	3	0.028	6.592	34.007	1802.2	20
950909	3788	85452	HERB	3	0.176	49.408	33.959	1845.2	37
951011	3860	77679	HERB	5	0.033	29.760	32.608	1987.2	17
951016	3870	2481	HERB	5	0.026	11.776	32.636	1989.5	17

Table 4.1 (continued)

GRB Name[1]	BATSE Trig #	Trig SOD (UT,s)	Data Type	LAD #	Time Interval[2] Start (s)	Time Interval[2] End (s)	Energy Interval Start (keV)	Energy Interval End (keV)	# of Spectra
951102	3891	21175	HERB	2	0.090	42.368	32.524	1904.8	13
951123	3917	65405	HERB	4	0.090	8.064	31.739	1895.0	1
951124	3918	21258	HERB	6	0.033	25.600	36.461	1893.2	7
951202	3929	39100	HERB	0	0.091	16.384	33.179	2041.3	11
951203	3930	3987	HERB	0	0.032	46.208	33.394	2010.3	22
951208	3937	42443	HERB	5	0.030	73.728	27.416	1981.4	7
951213	3954	17852	HERB	2	0.031	11.904	32.540	1951.1	16
951219	4039	60679	HERB	6	0.025	45.184	36.499	1895.4	19
960114	4368	44104	CONT	2	–1.408	45.696	32.555	1816.9	16
960124	4556	3385	HERB	5	0.026	6.912	27.495	1989.1	24
960201	4701	78523	HERB	1	0.029	55.360	33.022	1950.5	21
960216	4898	57796	HERB	2	0.027	1.216	36.971	1857.4	6
960321	5299	76280	MER	01	40.923	69.211	33.111	1837.4	50
960322	5304	19641	MER	57	0.024	25.528	29.783	1825.8	48
960523	5470	59521	HERB	6	0.042	3.584	32.014	1883.4	4
960524	5473	72549	HERB	2	0.090	73.024	32.554	1907.0	12
960529	5477	43665	HERB	1	0.091	18.688	33.056	1906.3	15
960605	5486	29392	HERB	2	0.026	75.456	32.567	1908.1	32
960607	5489	78075	HERB	1	0.033	65.536	33.134	1913.0	29
960623	5512	4728	HERB	5	0.033	29.952	27.430	1982.8	13
960703	5526	49373	HERB	4	0.090	79.552	31.841	1901.7	10
960804	5563	84535	HERB	4	0.108	2.944	26.996	1893.2	7
960807	5567	71366	HERB	0	0.090	17.792	28.883	1993.0	31
960808	5568	60123	HERB	6	0.190	5.632	32.081	1843.3	8
960824	5585	6110	CONT	4	–7.168	183.300	31.923	1816.9	5
960831	5591	37710	MER	67	0.030	144.930	31.608	1797.8	18
960917	5606	80552	CONT	5	–69.888	30.464	32.590	1846.6	7
960921	5609	54228	HERB	5	0.026	38.912	27.484	1941.6	39
961001	5621	75185	HERB	2	0.026	10.304	32.574	1908.6	25
961006	5624	32164	HERB	2	0.128	9.344	32.554	1907.0	2
961009	5629	49065	HERB	6	0.033	19.904	31.837	1871.5	28
961015	5632	58123	HERB	2	0.026	19.456	32.562	1907.7	2
961029	5649	24350	MER	15	0.021	81.877	32.877	1857.5	155
961102	5654	41903	HERB	5	0.079	46.464	27.498	1989.5	45
961126	5697	24199	HERB	6	0.028	1.728	36.428	1891.3	7
961130	5701	18832	HERB	0	0.863	9.472	33.227	1999.3	11
961202	5704	66661	HERB	0	0.030	5.184	33.425	2012.3	10
961212	5711	14870	HERB	4	0.102	3.072	26.964	1890.8	6
961228	5731	86318	HERB	3	0.033	45.120	33.879	1839.5	10
970111	5773	35040	HERB	0	0.029	21.824	33.181	1996.2	57
970201	5989	57250	HERB	1	0.026	31.040	29.028	1868.3	26
970202	5995	25844	HERB	1	0.090	22.976	28.898	1901.9	61
970223	6100	30377	HERB	6	0.090	29.440	36.158	1875.6	36
970306	6115	10059	HERB	2	0.150	103.620	32.497	1902.8	15
970315	6124	56454	MER	26	0.024	21.160	36.745	1810.0	60
970404	6157	63011	HERB	0	0.033	12.608	28.886	1993.2	21
970411	6168	35545	MER	01	0.030	59.870	41.336	1834.2	38
970420	6198	72842	HERB	6	0.045	13.312	36.326	1885.3	24
970517	6235	32682	HERB	5	0.090	4.288	27.527	1992.3	8
970523	6240	82890	HERB	3	0.041	7.488	30.054	1854.5	1
970603	6249	35345	HERB	0	0.032	66.624	28.952	2043.5	5
970612	6266	52104	HERB	4	0.033	48.960	27.282	1960.8	18
970616	6274	65390	HERB	1	0.033	121.220	33.559	1949.6	19
970704	6293	4096	HERB	0	0.026	0.256	33.272	2002.3	1
970807	6329	66309	HERB	4	0.045	47.744	27.103	1946.5	31
970816	6336	8264	HERB	7	1.984	14.528	27.030	1898.0	11
970827	6349	35750	HERB	2	0.033	69.056	32.541	1906.0	5
970828	6350	63876	HERB	5	0.032	84.224	27.476	1987.3	44
970831	6353	63570	HERB	0	0.033	115.580	33.176	1995.9	35
970912	6380	78744	HERB	3	0.033	56.128	29.913	1842.6	7
970919	6389	65669	MER	013	–16.064	20.505	33.359	1837.2	16

Table 4.1 (continued)

GRB Name[1]	BATSE Trig #	Trig SOD (UT,s)	Data Type	LAD #	Time Interval[2] Start (s)	Time Interval[2] End (s)	Energy Interval Start (keV)	Energy Interval End (keV)	# of Spectra
970919	6390	79816	HERB	7	0.034	6.464	26.890	1843.6	2
970925	6397	81795	HERB	7	0.092	30.272	26.995	1895.5	18
970930	6404	59	HERB	6	0.058	46.720	35.787	1854.0	21
971006	6414	19017	HERB	3	0.173	24.576	29.952	1799.7	9
971029	6453	5318	HERB	1	0.033	111.740	32.998	1901.3	44
971029	6454	22428	CONT	4	–6.656	728.580	31.864	1813.2	34
971110	6472	68006	MER	13	0.027	225.020	33.374	1841.6	49
971113	6476	58130	HERB	0	0.026	42.752	28.852	2035.6	6
971207	6525	72232	HERB	3	0.084	58.560	30.219	1868.2	23
971208	6526	28092	CONT	6	–11.264	760.830	34.435	1691.4	115
971220	6539	14793	HERB	6	0.026	9.536	31.196	1785.3	2
980105	6560	2681	HERB	7	0.030	37.056	26.908	1889.4	16
980113	6570	14845	HERB	2	0.033	68.160	32.699	1917.9	12
980124	6576	23673	HERB	6	0.095	43.648	31.327	1793.9	21
980125	6581	74368	HERB	0	0.032	64.768	29.317	2026.2	18
980203	6587	82028	HERB	1	0.091	31.680	33.015	1902.8	60
980208	6593	46259	HERB	3	0.033	29.632	30.152	1862.6	32
980219	6609	49963	HERB	2	0.030	31.872	32.552	1906.9	13
980225	6615	30564	HERB	5	0.090	164.100	32.553	1982.9	11
980228	6617	24247	HERB	0	0.026	0.960	28.982	2000.6	3
980228	6618	60841	HERB	4	0.029	61.312	26.973	1936.2	16
980306	6629	34382	HERB	0	0.090	232.130	28.908	1994.9	8
980306	6630	63251	HERB	3	0.042	25.984	29.840	1790.6	17
980315	6642	26640	HERB	7	0.090	90.368	27.046	1899.1	5
980329	6665	13478	HERB	0	0.026	20.736	28.795	1986.3	38
980330	6668	93	HERB	6	0.026	0.640	31.131	1781.0	1
980420	6694	36412	HERB	5	0.030	55.872	27.477	1987.4	8
980508	6744	14848	HERB	2	0.026	2.048	32.478	1946.3	4
980518	6763	35231	HERB	2	0.115	20.864	32.841	1928.7	5
980703	6891	15765	HERB	3	0.090	79.680	29.902	1795.6	14
980703	6892	49708	HERB	6	0.115	94.016	36.211	1878.7	5
980706	6904	57587	HERB	2	0.026	10.816	32.526	1904.9	3
980724	6944	74080	HERB	6	0.090	50.560	31.903	1831.6	23
980803	6963	48980	MER	26	0.031	23.439	32.233	1802.6	31
980810	6985	66929	HERB	3	0.033	42.432	29.867	1792.8	56
980821	7012	62165	HERB	0	0.091	30.784	28.902	1994.5	31
980828	7028	70685	HERB	4	0.026	4.992	31.619	1887.2	4
980923	7113	72647	MER	37	0.024	67.416	31.289	1879.7	243
981021	7170	83292	HERB	6	0.026	102.340	36.529	1852.3	30
981128	7236	69366	HERB	3	0.095	82.112	29.830	1789.8	8
981130	7240	3184	HERB	4	0.041	3.392	32.618	1952.4	3
981203	7247	3552	HERB	1	0.150	130.370	33.207	1919.3	15
981203	7248	26260	HERB	2	0.090	38.656	32.658	1914.9	14
981219	7270	33948	HERB	1	0.185	207.360	28.889	1901.0	3
981223	7277	43875	HERB	2	0.145	31.488	32.566	1907.9	10
981226	7281	38824	HERB	2	0.033	0.896	32.583	1954.4	2
981228	7285	44616	HERB	6	0.032	49.152	32.172	1894.0	3
990102	7295	49918	HERB	3	0.029	26.560	30.076	1856.3	5
990104	7301	57753	MER	357	0.024	200.320	31.906	1881.0	56
990108	7310	30066	HERB	7	0.090	76.544	29.278	2007.4	10
990111	7318	43041	HERB	5	0.087	12.608	32.559	1983.4	11
990123	7343	35216	MER	04	0.030	89.118	32.390	1806.5	134
990129	7360	18950	MER	67	0.030	91.230	42.535	1866.3	32
990304	7446	36936	HERB	0	0.160	3.264	28.889	1993.4	2
990308	7457	18907	HERB	1	0.032	11.776	29.363	1951.0	1
990311	7464	79905	HERB	6	0.033	47.040	36.017	1823.2	25
990316	7475	34839	HERB	5	0.029	31.488	27.441	1937.5	25
990316	7477	44939	HERB	5	0.033	36.032	32.513	1979.9	12
990323	7491	62977	MER	23	0.024	55.128	35.695	1843.5	132
990403	7503	35282	HERB	4	0.029	89.024	27.091	1900.6	16
990411	7515	15931	HERB	7	0.050	25.280	29.881	2048.8	8

Table 4.1 (continued)

GRB	BATSE	Trig SOD	Data	LAD	Time Interval[2]		Energy Interval		# of
Name[1]	Trig #	(UT,s)	Type	#	Start (s)	End (s)	Start (keV)	End (keV)	Spectra
990424	7527	11551	HERB	7	0.034	14.784	29.941	2053.0	21
990425	7530	8366	HERB	2	0.108	1.728	32.738	1920.9	4
990506	7549	41010	MER	57	0.031	136.160	31.200	1920.0	105
990510	7560	31746	HERB	5	0.033	60.160	27.416	1981.4	22
990516	7569	86063	HERB	7	0.033	28.480	30.494	2141.4	3
990518	7575	62325	CONT	1	–1.024	205.820	33.310	1880.5	21
990522	7578	15225	HERB	2	0.109	8.704	32.572	1908.4	7
990527	7586	50215	MER	45	0.030	64.926	32.048	1819.1	7
990531	7592	57384	HERB	5	0.031	32.704	27.393	1933.0	20
990619	7610	46922	HERB	6	0.026	4.864	30.976	1770.9	1
990712	7647	27919	HERB	3	0.026	42.304	29.912	1796.5	4
990718	7660	43611	HERB	6	0.041	89.024	31.754	1821.9	6
990728	7678	39824	HERB	4	0.030	45.568	31.548	1882.6	37
990802	7688	3883	CONT	5	–148.224	21.760	32.588	1846.5	21
990803	7695	23375	MER	267	0.024	21.592	34.334	1869.4	29
990807	7703	78946	HERB	5	0.032	16.192	27.441	1983.9	2
990909	7760	28274	HERB	7	0.099	37.440	30.911	2170.7	23
990915	7766	83722	HERB	0	0.026	23.744	33.362	2053.5	21
991004	7788	47660	HERB	2	0.033	74.624	28.176	1913.1	14
991009	7794	60595	HERB	1	0.090	151.040	28.952	1860.5	14
991018	7810	68561	MER	02	0.026	6.250	35.041	1812.1	2
991113	7854	81660	HERB	4	0.032	73.664	26.713	1871.2	32
991121	7868	40904	HERB	2	0.032	131.010	32.618	1911.8	19
991127	7884	53699	HERB	4	0.026	79.488	31.429	1874.8	17
991210	7898	850	HERB	4	0.026	2.688	27.120	1902.9	5
991216	7906	58021	HERB	5	0.032	31.872	27.353	1929.2	59
991229	7925	54683	HERB	6	0.032	101.180	31.766	1822.6	35
000101	7929	4799	HERB	2	0.033	70.656	32.516	1904.2	29
000103	7932	84908	HERB	1	0.033	45.376	33.082	1861.4	6
000107	7938	78273	HERB	0	0.034	38.784	32.992	1983.9	2
000109	7941	37634	HERB	0	0.033	134.530	33.270	2002.1	39
000113	7948	34202	HERB	1	0.033	77.312	29.180	1884.0	4
000115	7954	53372	HERB	5	0.026	16.128	27.405	1934.1	27
000126	7971	84389	HERB	6	0.033	54.976	31.781	1823.6	24
000131	7975	53877	HERB	2	0.057	102.980	32.536	1905.7	22
000201	7976	10929	HERB	4	0.033	92.736	26.946	1844.7	17
000207	7986	86182	HERB	3	0.090	4.800	33.913	1795.8	7
000221	7994	85150	HERB	5	0.028	27.264	27.339	1974.0	25
000301	8005	9234	HERB	5	0.051	6.144	27.406	1934.2	3
000302	8008	10225	HERB	3	0.026	24.640	33.800	1834.0	27
000326	8053	19136	HERB	4	0.026	1.408	26.903	1886.0	5
000408	8069	9348	HERB	3	0.026	7.744	29.865	1838.6	7
000420	8081	51730	MER	46	0.027	31.579	42.899	1767.8	8
000429	8087	36442	HERB	4	0.211	170.180	26.692	1869.6	14
000508	8098	69050	HERB	5	0.045	20.672	27.443	1984.1	6
000511	8101	4319	HERB	1	0.098	103.680	29.012	1866.6	16

[1] The calibration bursts are noted with C in front of the name.
[2] Time since trigger.

4.1.2 The Detector

In this spectral analysis, only the LAD data are used, mainly to take advantage of its larger effective area (Figure 2.5), and thus higher sensitivity. Another reason that only the LAD data are used is due to the problems in the SD DRMs at high energies, described in §2.5.1. These problems give rise to uncertainties in the SD DRMs and make SD data not favorable for spectral analysis. Moreover, limiting to one type of detector eliminates systematic uncertainties arising from different detector characteristics, and thus keeps the analysis more uniform.

4.1.3 Data Type Selection

The LAD data types were discussed in detail in §2.2.3 and summarized in Table 2.2. The three LAD data types used in this work, in order of priority, are High Energy Resolution Burst data (HERB), Medium Energy Resolution data (MER), and Continuous data (CONT). The HERB and MER data are burst-mode data, whereas CONT was continuous, non-burst mode data. HERB provides the highest energy resolution consisting of 128 energy channels with modest sub-second time resolution, and thus is used as the primary data type. The HERB for the brightest LAD provides the finest time resolution, and was always selected for the analysis. The coarser-time resolution ($\sim$ 300 s) HER data are used as background data for the HERB, $\sim$ 2000 seconds before the trigger and after the HERB accumulation is finished.

However, especially for long, bright bursts, the HERB data can often be incomplete since HERB had a fixed memory space that could fill up before the burst was over. In this work, we consider the HERB data incomplete when the data do not cover most of the burst duration (i.e., T_{90}) or when the data do not include the main peak episodes (this could occur if a burst data accumulation was triggered by

weak precursor). In such cases, or if HERB was not usable, 16-channel MER data were used instead. Although MER provides medium energy resolution, it has much finer time resolution than HERB, making it possible to re-create the time resolution of the missing HERB. In the MER data, the CONT data are used as background; therefore, the spectra accumulated before the trigger time and after 164 seconds (the MER accumulation time) are identical to those of CONT, with 2.048-second integration times. The downside of using MER is that the data are summed over multiple sets of detectors (usually two to four), and, therefore, systematic errors tend to dominate, especially for bright bursts. Systematic errors cannot be modeled into the analysis and can contribute to large χ^2 especially at lower energies where the counts are really high. Examples of HERB and MER spectra that show such systematic fluctuations are seen in Figure 4.1. Possible contributions to the systematics include the uncertainties from the LAD calibration (Preece et al. 1998a) and the DRM (Pendleton et al. 1995; Harmon et al. 2002).

Lastly, in the cases where neither HERB nor MER were available for the analysis, 16-channel CONT data from the brightest LAD were used. Despite the lack of sub-second time resolution, the advantage of CONT is that the data are continuous. Thus, significant precursor activities may be included in the analysis using the CONT data. This was not possible for HERB, because the data accumulations always started at triggers, and the background data (HER) did not provide a sufficient time resolution for pre-trigger data. For each of 350 events, the data type used is listed in column 4 of Table 4.1, and the total number of each data type is 270 (HERB), 52 (MER), and 28 (CONT).

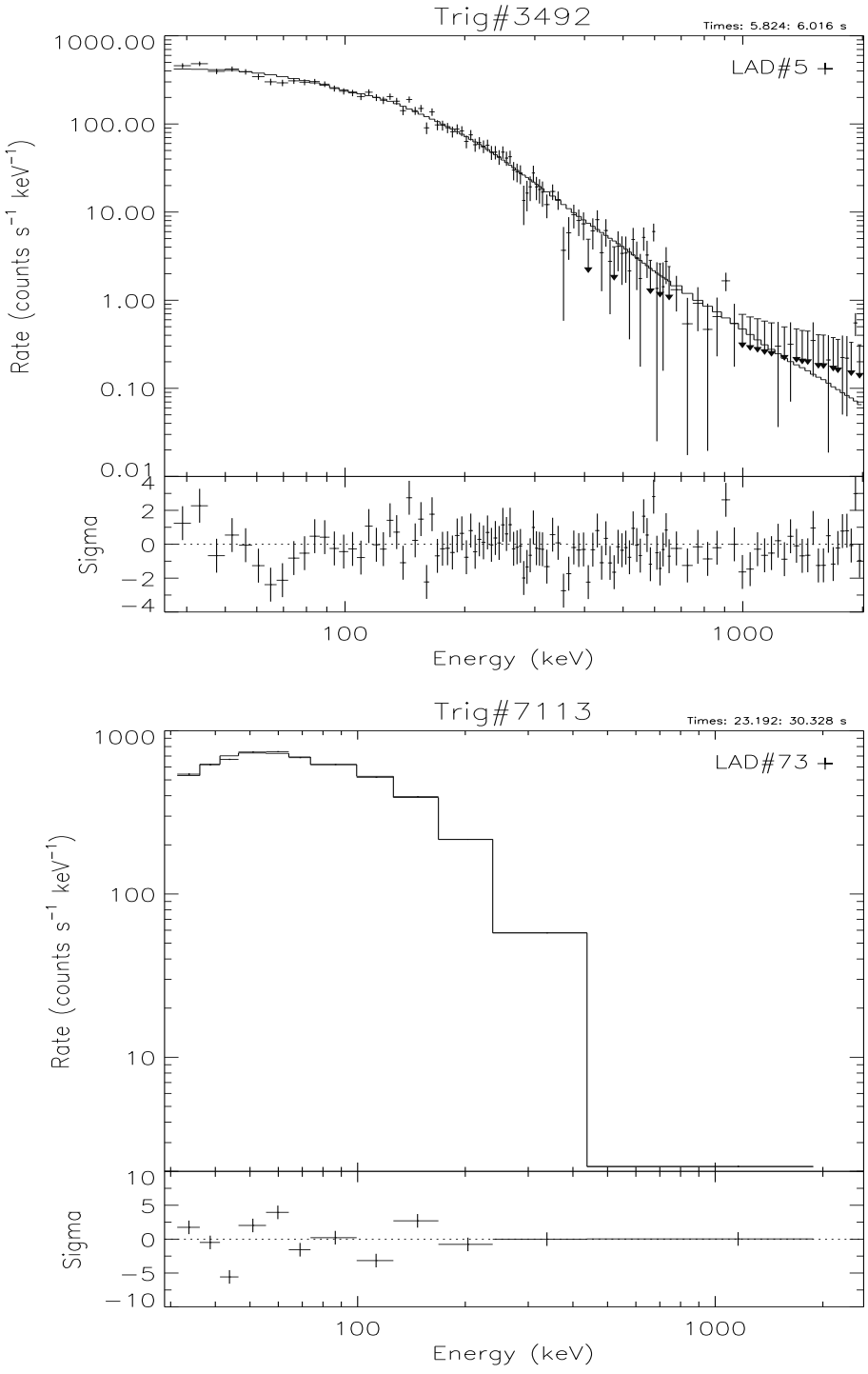

Figure 4.1 Example count spectra of bright HERB (*top*) and MER (*bottom*) events in which systematic deviations between the data (crosses) and the model (solid lines) are evident below $\sim$ 100 keV.

4.1.4 Time Interval Selection

The data are binned in time until each spectrum has a large enough signal-to-noise ratio (S/N) to ensure acceptable statistics for the time-resolved spectral analysis. The S/N is calculated based upon the background model of each event. The background model is determined by fitting a low-order (≤ 4) polynomial function to spectra that cover time intervals before and after each burst, for at least a few hundred seconds. In cases where the background data are not available for a sufficiently long period, the longest available time intervals were used, and the background model was checked against those determined using other LAD data available for the same event. The burst start time is usually the trigger time, unless there is bright pre-trigger activity, containing significant amount of emission for those cases where CONT or MER was used.

In SP1, a minimum S/N of 45 was used for the time binning of spectra regardless of the data type used. The S/N level was chosen so that each resolution element (non-overlapping FWHM resolution elements, of which there are about 16 – 20 in the LAD energy range) has approximately 2σ of the signal on average (SP1). The noise (or σ) defined here is the Poisson error of the observed total counts, including the background counts. Binning by a constant S/N, however, usually yields on average a few times larger number of time-resolved spectra when MER data are used, than the HERB and CONT cases. This is because the MER data are summed over two to four detectors while HERB and CONT are single-detector data, and thus the MER data have higher S/N to begin with, on top of having a finer time resolution. As a result, bursts with MER data were overrepresented in the spectral sample of SP1, which in turn biased the spectral parameter and model statistics presented there. To avoid this problem, we investigated which S/N value for MER would yield comparable numbers of time-resolved spectra compared with HERB

binned by S/N $\geq$ 45, for the same events. Since the MER data are mainly used for bright, long events, and also the oversampling problems are more likely to occur when the photon flux is high, we selected 15 events with high peak photon flux ($\gtrsim$ 50 photons s^{-1} cm^{-2}, determined using HERB data), for which both MER and HERB data were available. We re-binned the HERB data with minimum S/N of 45, and reproduced the same number of spectra for the same time intervals with MER data, by increasing the minimum S/N in steps. We found that a minimum S/N of 45 *per detector* could roughly accomplish this, regardless of the brightness, as shown in Figure 4.2. Therefore, the minimum S/N used for the MER binning is 45 $\times$ number of detectors, with the exception of 10 events (out of 52 total MER events). These 10 events were mostly with three or four detectors and the minimum S/N was found to be too high, for various reasons, when compared with the available portion

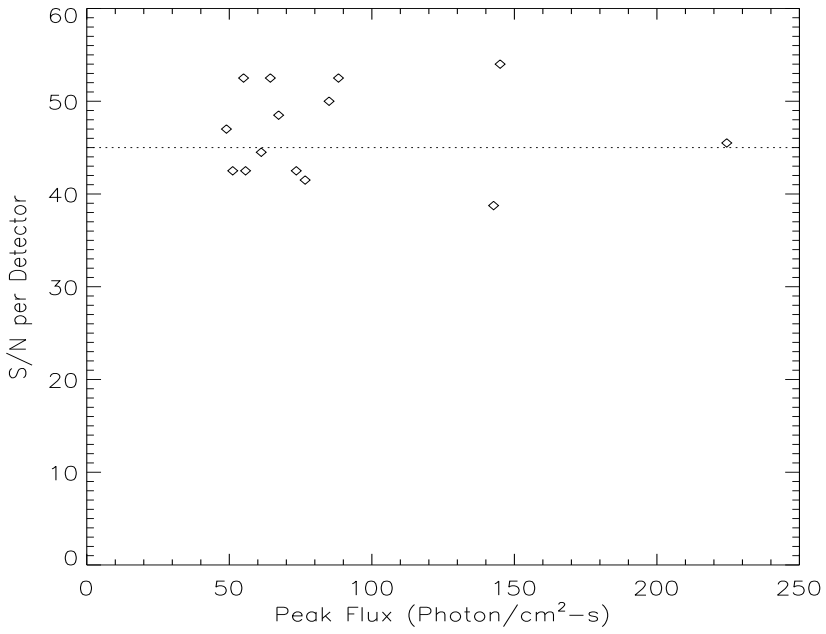

Figure 4.2 S/N per detector for 15 MER events that produced the equivalent number of spectra to HERB binned by S/N $\geq$ 45 case. The dotted line marks 45σ.

of single-detector data (i.e., HERB or CONT) for the same event. Consequently, for these bursts, the minimum S/N was reduced by steps of 45 until satisfactory binning was achieved.

After time-binning by the minimum S/N, the last time interval, with a S/N less than the minimum value, was dropped. Although the last time bin may constitute a significant tail portion of the event, we found that this exclusion of the last time bin does not affect the time-integrated spectral fits. This is true even when the resulting time interval is much shorter than the T_{90} of the burst (e.g., a burst with a very long tail).

Unlike for SP1 where bursts with less than 8 spectra were dropped, no bursts that satisfy the burst selection criteria described above are excluded, regardless of the resulting number of spectra after binning in each burst. This allowed the inclusion of 15 short GRBs ($T_{90} < 2.0$ s) as well as several dimmer events in this work. There are 17 events for which the detection was $\sim 45\sigma$ only in one time interval, because they were either weak or short. These events include 12 short GRBs (trigger numbers 298, 444, 1525, 2514, 2679, 3044, 3087, 3410, 3412, 3736, 6293, and 6668) and 5 of the weakest events in the sample (2112, 3917, 6240, 7457, and 7610). For these events, the same spectra are included with both the time-integrated and time-resolved spectra. It must also be noted that there are 8 events (indicated by "C" in Table 4.1) whose time-integrated spectra were used for calibration of the LADs (Preece et al. 1998a). Therefore, these 8 must be excluded from the time-integrated analysis, while their time-resolved spectra are still independent and usable, and thus included. Columns 6 and 7 of Table 4.1 list the time intervals used for each burst.

4.1.5 Energy Interval Selection

As mentioned in §2.2.1, the LAD was gain-stabilized; therefore, the usable energy range is $\sim$ 30 keV – 2 MeV for all events. The lowest 7 or 8 channels of HERB and 1 or 2 channels of MER and CONT are usually below the electronic lower-energy cutoff and were excluded. Likewise, the highest few channels of HERB and normally the very highest channel of MER and CONT were unbounded energy overflow channels and also not usable. The actual energy range used in the analysis for each event is shown in columns 8 and 9 of Table 4.1.

4.2 Spectral Analysis

Our sample consisted of 350 GRBs, providing 342 time-integrated spectra (8 calibration events excluded) and 8459 time-resolved spectra. We analyzed both time-integrated and time-resolved spectra, each fitted by a set of photon models that are commonly used to fit GRB spectra. Each of the photon models used provides different number of free parameters and, therefore, different degrees of freedom for each fit. This allows statistical comparisons among the model fits. The fitting procedures and the photon models are discussed in this section.

4.2.1 Spectral Fitting Software

For the spectral analysis presented herein, we used the spectral analysis software RMFIT, which was specifically developed for burst data analysis by the BATSE team (Mallozzi, Preece & Briggs 2005). It incorporates a fitting algorithm MFIT that employs the forward-folding method (Briggs 1996), and the goodness of fit is determined by χ^2 minimization. One advantage of MFIT is that it utilizes model variances instead of data variances, which enables more accurate fitting even for

low-count data (Ford et al. 1995). We analyzed both time-integrated and time-resolved spectra for each event, using a set of photon models described in the next section.

4.2.2 Photon Models

We have selected five spectral models of interest to fit the BATSE GRB spectra, three of which (BAND, COMP, and SBPL) are the same models employed in SP1. Having a variety of models in fitting each spectrum eliminates the need for manipulating one model, such as the "constrained" Band function introduced by Sakamoto et al. (2004a), which requires some presumptions of the form for the original photon spectrum. As briefly discussed in §3.1, GRB spectra are usually well-represented by a broken power law in the BATSE energy band. However, it is possible that the break energy lies outside the energy range, or that the spectrum is very soft or dim and the high-energy component is not detected. Therefore, we use a simple power-law and a power-law with exponential cutoff model that may accommodate such spectra, in addition to the more commonly-fitted broken power-law models. We review each model used in the analysis below.

4.2.2.1 Power Law Model (PWRL)

The first model is a single power law,

$$f_{\mathrm{PWRL}}(E) = A \left(\frac{E}{E_{\mathrm{piv}}} \right)^{\lambda}, \tag{4.1}$$

where A is the amplitude in photons s^{-1} cm^{-2} keV^{-1}, λ is a spectral index, and the pivot energy E_{piv} was kept constant at 100 keV for this work. The use of this model was motivated by the fact that the break energy of a broken power law spectrum could lie well outside the LAD passband. There may also be a case where the signal

is weak and the break energy cannot be adequately determined. In such cases, the 2-parameter single power law should be able to fit the spectra better than the other models with more parameters.

4.2.2.2 The GRB Model (BAND)

The next model is the empirical model most widely used to fit GRB spectra (Band et al. 1993):

$$f_{\rm BAND}(E) = \begin{cases} A\left(\frac{E}{100}\right)^{\alpha} \exp\left(-\frac{E(2+\alpha)}{E_{\rm peak}}\right) & \text{if } E < E_{\rm c} \\ A\left[\frac{(\alpha-\beta)E_{\rm peak}}{100(2+\alpha)}\right]^{\alpha-\beta} \exp\left(\beta-\alpha\right)\left(\frac{E}{100}\right)^{\beta} & \text{if } E \geq E_{\rm c}, \end{cases} \tag{4.2}$$

where

$$E_{\rm c} = (\alpha-\beta)\frac{E_{\rm peak}}{2+\alpha} \equiv (\alpha-\beta)E_0.$$

The model consists of 4 parameters: the amplitude A in photons $\rm s^{-1}$ $\rm cm^{-2}$ $\rm keV^{-1}$, a low-energy spectral index α, a high-energy spectral index β, and a νF_ν peak energy $E_{\rm peak}$ in keV. νF_ν is the photon spectrum $f(E)$ integrated twice over all energies ($E^2 f(E)$). Therefore, νF_ν represents the total energy flux per energy band (i.e., power density spectrum). We stress that the α index characterizes an asymptotic power-law (i.e., the tangential slope determined at $E \rightarrow 0$ in a logarithmic scale). This may not characterize the actual low-energy power-law, determined within the data energy range, when the e-folding energy E_0 approaches the lower energy bound. Although the model was originally constructed based on the observed time-integrated BATSE spectra (SD data), it has now become common practice to use the model to fit time-resolved GRB spectra as well. Very frequently, however, we find some time-resolved spectra cannot be adequately fitted with this model. By fitting this model to both time-integrated and time-resolved spectra, we test the validity of the scope of this model.

4.2.2.3 The GRB Model with fixed β (BETA)

The BETA model is a variation of the BAND, with a fixed high-energy index β, and is only applicable to the time-resolved spectral fits. The fixed value of β is determined from the time-integrated spectral fit using the regular BAND model. Since β is fixed in the fit, this is essentially a 3-parameter model with A, α, and $E_{\rm peak}$. Our motivation for using this model is to test the hypothesis that the energy distribution of the shock-accelerated electron remains constant throughout a burst. It has been found that for Fermi-type acceleration, the accelerated particles have a power-law distribution with index $p \sim 2.2 - 2.3$ that is constant in time (Gallant 2002). Because β should be directly related to p ($\beta = -(p+1)/2$), if p remains constant throughout a burst, β should also remain constant in the context of the synchrotron shock model. In fact, it has been found with a smaller sample that the majority of GRBs do not exhibit strong evolution in β (Preece et al. 1998a), so we examine this here with a larger sample.

4.2.2.4 Comptonized Model (COMP)

The next model considered is a low-energy power law with an exponential high-energy cutoff. It is equivalent to the BAND model without a high energy power law, namely $\beta \rightarrow -\infty$, and has the form

$$f_{\rm COMP}(E) = A \left(\frac{E}{E_{\rm piv}} \right)^{\alpha} \exp \left(-\frac{E(2+\alpha)}{E_{\rm peak}} \right). \tag{4.3}$$

Like the PWRL case, $E_{\rm piv}$ was always fixed at 100 keV in this work; therefore, the model consists of 3 parameters: A, α, and $E_{\rm peak}$. There are many BATSE GRB spectra that lack high-energy photons (Pendleton et al. 1997), and these no-high-energy spectra are usually fitted well with this model. Another case where this model

would be a good fit is when the e-folding energy ($E_{\rm peak}/(2+\alpha) \equiv E_0$) approaches $\sim$ 1 MeV, and the high-energy index of the BAND model cannot be determined by the data. The model is so named because in the special case of $\alpha = -1$, it represents the Comptonized spectrum from a thermal medium; however, α is kept as a free parameter here.

4.2.2.5 Smoothly-Broken Power Law (SBPL)

The last model we have selected is a broken power law with flexible curvature at the break energy, and thus the model can accommodate spectra with very sharp breaks, as well as ones with very smooth curvature. This SBPL model is expressed by

$$f_{\rm SBPL}(E) = A \left(\frac{E}{E_{\rm piv}}\right)^b 10^{(a-a_{\rm piv})}, \tag{4.4}$$

where:

$$a = m\Lambda \ln\left(\frac{e^q + e^{-q}}{2}\right), \qquad a_{\rm piv} = m\Lambda \ln\left(\frac{e^{q_{\rm piv}} + e^{-q_{\rm piv}}}{2}\right),$$
$$q = \frac{\log\left(E/E_{\rm b}\right)}{\Lambda}, \qquad q_{\rm piv} = \frac{\log\left(E_{\rm piv}/E_{\rm b}\right)}{\Lambda},$$
$$m = \frac{\lambda_2 - \lambda_1}{2}, \qquad \text{and} \qquad b = \frac{\lambda_1 + \lambda_2}{2}.$$

The parameters are the amplitude A in photons s^{-1} cm^{-2} keV^{-1}, a lower power-law index λ_1, a break energy $E_{\rm b}$ in keV, a break scale Λ, in decades of energy, and an upper power-law index λ_2. The amplitude A represents the photon flux at $E_{\rm piv}$. The model introduces a break scale Λ as the fifth parameter; this is thus a 5-parameter model. Like the COMP model above, the pivot energy $E_{\rm piv}$ is always fixed to 100 keV: it represents a convenient overall energy scale. This model was originally created to be implemented into MFIT. The basic idea in deriving this model was

to have the derivative of the photon flux (in logarithmic scale) to be a continuous function of the hyperbolic tangent (SP1; Ryde 1999). The main difference between this model and the BAND model is that the break scale is not coupled to the power laws; therefore, the low-energy spectral index λ_1 could characterize values that are closer to the *true* power law indices indicated by the actual data points, than is possible with α of the BAND model. Note also that as $\Lambda \rightarrow 0$, the model reduces to a sharply-broken power law.

However, introducing a fifth parameter can be a problem in fitting the LAD spectra. Although the HERB data provides 126 energy channels, the energy range encompasses only about 20 energy resolution elements, as mentioned earlier. Fitting a 4-parameter model to the HERB data can cause the covariance matrix $[C]$ to be ill-determined, resulting in unconstrained parameters. This is indicated by a condition number for $[C]^{-1}$ that is of the order of the reciprocal of the machine precision, meaning that the matrix is nearly singular (e.g., Press et al. 1992). Consequently, having an additional free parameter usually results in highly cross-correlated, unconstrained parameter determinations, and is not favored. For this reason, in SP1, Λ was fixed for each time-resolved spectral fit to the value determined by the time-integrated fit for the corresponding burst; however, there is no reason to presume that Λ remains constant throughout a burst, and also it could be problematic if the initial time-integrated break scale is unconstrained. On the other hand, we may not be able to constrain Λ any better than a particular value, due to the finite energy resolution of the LADs, even if the 5-parameter model fit can be done. To resolve this issue, we have simulated SBPL spectra with various parameters and fitted these spectra with the SBPL model for various values of Λ. The simulation results are discussed in §4.3.2.

We emphasize that the break energy $E_{\rm b}$ of the SBPL model should not be confused with $E_{\rm peak}$ of the BAND and COMP models. The break energy is simply the

energy at which the spectrum changes from the low-energy to high-energy power law, whereas $E_{\rm peak}$ is the energy at which the νF_ν spectrum peaks. The break energy $E_{\rm b}$ is also different from the characteristic energy $E_{\rm c}$ in the BAND model, which is the energy where the low-energy power law with exponential cutoff ends and the pure high-energy power law starts. However, the νF_ν peak energy of the SBPL spectra, as well as the power-law break energy of BAND, can be easily derived (see the Appendices A and B) for comparison among the various models, which we have done here for the first time.

4.3 Spectral Simulations

In order to interpret the quantitative analysis results correctly, we first need to understand the general characteristics and behavior of each photon model when applied to the BATSE LAD GRB spectra. Therefore, we have generated a large set of simulated burst spectra with various spectral shapes and signal strengths, and subjected them to our analysis regime. In the simulations, an actual burst background photon model and DRM are taken as input. Then, Poisson fluctuations are added to the background model, which is assumed to be true. The background model and source photon model (with specific parameters) are multiplied by the DRM to be converted to count rate spectra. The sum of the background and source count rates are multiplied by a given live time, and Poisson noise is again added at the end. It should be noted that the simulated spectra do not include any sources of systematic effects that are present in the real spectra. There are two main objectives in simulating data for this study. One is to investigate the behavior of the BAND and COMP models in the limit of low S/N and the other is to explore the break scale determination of SBPL.

4.3.1 BAND vs. COMP

The broken-power law nature of the GRB spectra indicates that there typically are considerably lower photon fluxes at higher energies. Because of this, there is a good chance that the LADs are not sensitive enough to detect the non-thermal high-energy power law component of spectra in fainter bursts with sufficient significance. In such cases, even if the original source spectra have high-energy components, our data may not be able to identify this component and therefore, the no-high-energy COMP model may statistically fit as well as the BAND model. As an example, we show in Figure 4.3 a comparison between the BAND and the COMP photon spectra with the same A, α, and $E_{\rm peak}$ values. In fact, Band et al. (1993) found that the simulated 4-parameter BAND spectra with low S/N could be adequately fitted with the 3-parameter COMP model, although there were some shifts in the COMP-fitted parameters. In order to validate this for our dataset and using our analysis tool (RMFIT, §4.2.1), we have further explored these two models by creating sets of simulated burst spectra, based on the actual fitted parameters of some of the observed GRB spectra.

To start with, we selected a sample of six bright GRB spectra (three each with HERB and CONT) to which the BAND model fits substantially better than the COMP model, with well-constrained parameters, resulting in large improvements ($\Delta\chi^2 > 20$) for the additional 1 degree-of-freedom (dof). This assures that the spectra have an identifiable high-energy power law component. Based on the spectral parameters provided with the BAND fits to the sample spectra (i.e., spectra with high-energy component), sets of 100 simulated spectra with various amplitudes, and thus various S/N, were created. A total of 19 sets provided $2 \lesssim \langle {\rm S/N} \rangle \lesssim 200$.

The sets of simulated spectra were then fitted with the BAND and the COMP models. Some example results are presented in Table 4.2, where $\langle x \rangle$ indicates a

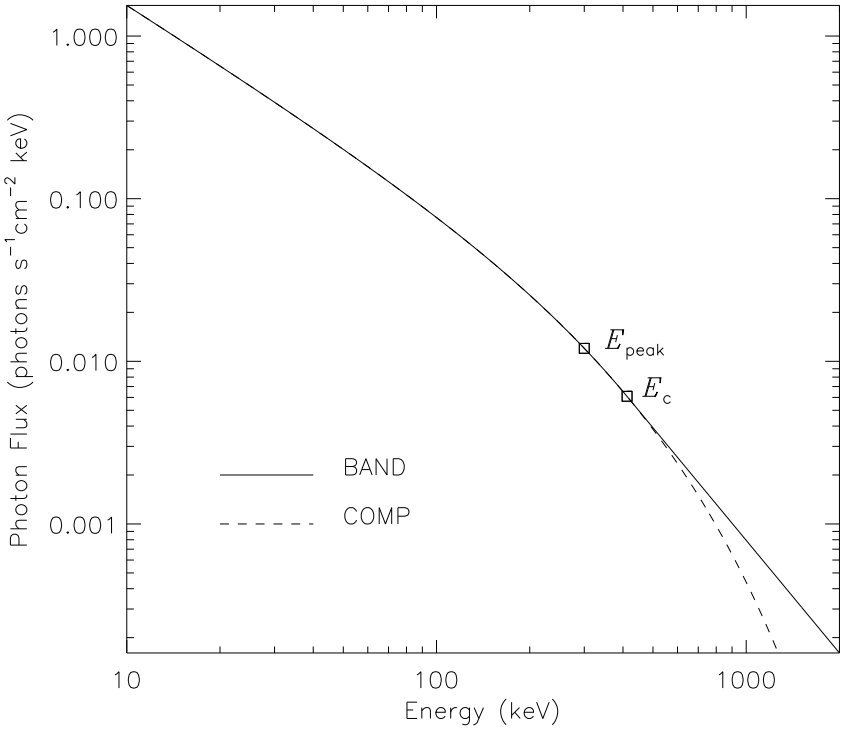

Figure 4.3 Comparison of BAND and COMP models for $A = 0.1$, $\alpha = -1.2$, $E_{\rm peak} = 300$ keV, and $\beta = -2.3$. $E_{\rm c}$ is where the high-energy power law of BAND begins.

Table 4.2 Example fit results to simulated BAND spectra. The parameters are median values and the standard deviations are shown in parentheses.

	Simulated Parameters: $E_{\mathbf{peak}}$ = 559.5 keV, α = –0.52, β = –2.24							
	BAND Fit Parameters				COMP Fit Parameters			
⟨S/N⟩	$\langle E_{\rm peak}\rangle$	$\langle\alpha\rangle$	$\langle\beta\rangle$	$\langle\chi^2\rangle$/dof	$\langle E_{\rm peak}\rangle$	$\langle\alpha\rangle$	$\langle\chi^2\rangle$/dof	$\Delta\chi^2$
285.1	559 (14)	–0.52 (0.02)	–2.23 (0.05)	111.2/112	746 (14)	–0.66 (0.01)	252.3/113	14.1
75.9	585 (60)	–0.53 (0.07)	–2.21 (0.32)	109.4/112	740 (55)	–0.65 (0.05)	118.4/113	9.0
12.3	549 (427)	–0.45 (0.72)	–1.77 (1.78)	108.6/112	1083 (1E4)	–0.74 (0.29)	109.2/113	0.6

	Simulated Parameters: $E_{\mathbf{peak}}$ = 493.5 keV, α = –0.97, β = –2.36							
	BAND Fit Parameters				COMP Fit Parameters			
⟨S/N⟩	$\langle E_{\rm peak}\rangle$	$\langle\alpha\rangle$	$\langle\beta\rangle$	$\langle\chi^2\rangle$/dof	$\langle E_{\rm peak}\rangle$	$\langle\alpha\rangle$	$\langle\chi^2\rangle$/dof	$\Delta\chi^2$
143.6	494 (38)	–0.97 (0.04)	–2.28 (0.34)	110.1/111	593 (36)	–1.03 (0.03)	122.1/112	12.0
27.5	467 (288)	–0.91 (0.25)	–1.97 (1.56)	105.3/111	679 (386)	–1.03 (0.13)	106.2/112	0.9
3.3	299 (517)	–0.53 (2.05)	–1.46 (1.97)	111.4/111	1388 (5E6)	–0.85 (3.19)	111.0/112	–0.4

median value and the standard deviation is $\sigma_x = \sqrt{\langle x^2\rangle - \bar{x}^2}$. The fit results indicated that S/N $\gtrsim$ 80 is needed for the BAND fits to be significantly better than the COMP fits, with $\gtrsim$ 99.9% confidence level (i.e., $\Delta\chi^2 > 10$ for Δdof = 1). For spectra with S/N $\sim$ 40, the confidence level of improvements in BAND over COMP were $< 70\%$. Given that the minimum S/N of our time-resolved spectra in this work was set to 45, for many dimmer spectra we should only be able to determine a better fit between the BAND and COMP by only about 1σ (68.3%), although this may depend on the spectral parameters in each fit.

In accord with the Band et al. (1993) results, the COMP model resulted in higher fitted $E_{\rm peak}$ values and steeper values of α, due to compensating for the lack of high-energy spectral component in the model. Consequently, the difference in the COMP $E_{\rm peak}$ and the actual $E_{\rm peak}$ value tends to be correlated with β. In addition, a strong anti-correlation was always found between $E_{\rm peak}$ and α in both BAND and COMP fits, regardless of S/N or values of other parameters. As a result, the amplitude A is also highly anti-correlated to $E_{\rm peak}$ because the parameter A of BAND and COMP

is the photon flux at 100 keV of the low-energy power-law *without* the exponential cutoff. This is different from A of the SBPL model. We also fitted the 5-parameter SBPL model to the same sets of simulated BAND spectra, to investigate the possible parameterization differences. It was found that the SBPL λ_1 tends to be smaller than α while λ_2 seems to be consistent with β, as we expected.

Similarly, we have also simulated sets of COMP spectra with low and high $E_{\rm peak}$ values (300 and 760 keV, respectively) with different S/N, and fitted them with the BAND model. In the high $E_{\rm peak}$ case, we found that the BAND fits failed nearly half of the time, regardless of the S/N. The fitting failure is caused by a very poorly-constrained parameter. On the other hand, in the low $E_{\rm peak}$ case, the number of failed fits were significantly smaller for the spectra with average S/N < 100. In both cases, the $\langle E_{\rm peak}\rangle$ and $\langle\alpha\rangle$ values fitted by the BAND model were consistent with the simulated COMP parameters, while $\langle\beta\rangle$ only gave upper limits in a range of ~ -2.5 to ~ -4. The simulation results suggest that the BAND model fails when a spectrum has sufficient high-energy photon flux but lacks the high-energy power-law component with finite spectral index. Figure 4.4 shows two simulated spectra both with S/N ~ 80 but with different $E_{\rm peak}$ values. As mentioned above, the BAND model fails to fit the high-$E_{\rm peak}$ spectrum much more frequently than the low-$E_{\rm peak}$ one. From Figure 4.4, it is evident that the high-$E_{\rm peak}$ spectrum has much larger photon flux at about 1 MeV although the overall signal strengths are similar. Therefore, it is very likely that the spectra that the BAND model fails to fit lack a high-energy power law component, yet this does not mean that these are the no-high-energy (NHE) spectra identified by Pendleton et al. (1997), which show no counts above 300 keV.

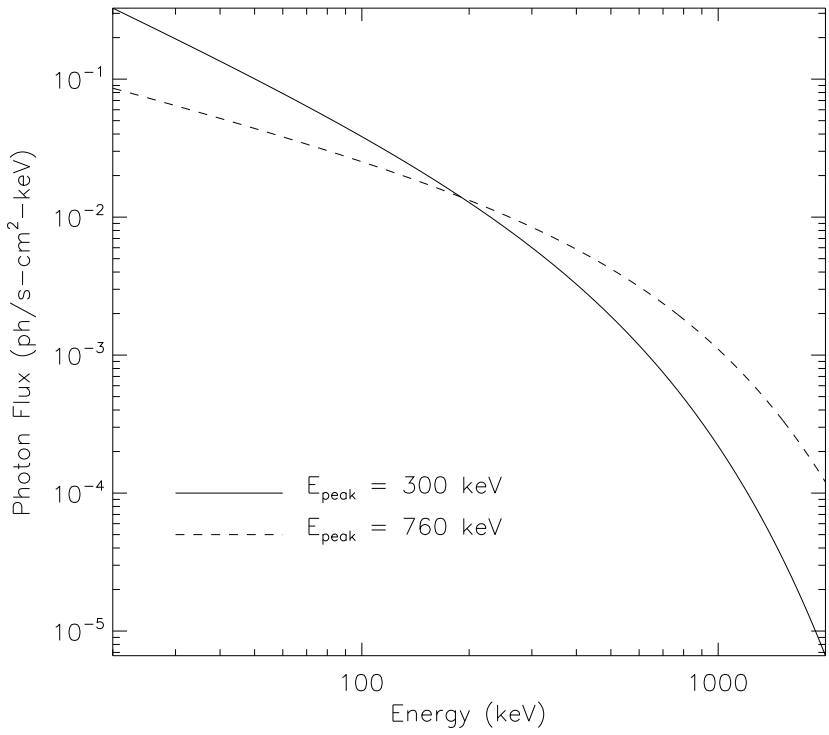

Figure 4.4 Two simulated COMP spectra with S/N $\sim$ 80. Low-$E_{\rm peak}$ spectrum (solid curve) can be fitted with the BAND model much more frequently than the high-$E_{\rm peak}$ spectrum (dashed curve).

4.3.2 SBPL Break Scales

Another topic that needs to be addressed is the break scale (Λ) of the SBPL model, as mentioned in §4.2.2.5. The purpose of this simulation is to test the feasibility of performing the 5-parameter SBPL model fits with Λ as a free parameter, as well as to examine the capability of the determination of Λ by alternatively using a set of 4-parameter SBPL models with fixed Λ.

First, we created sets of 100 simulated SBPL spectra with Λ values 0.01 and between 0.1 and 1.0 with an increment of 0.1 (11 total), while keeping the other parameters fixed at typical fitted values of $E_{\rm b} = 300$ keV, $\lambda_1 = -1.0$, and $\lambda_2 = -2.5$. Figure 4.5 shows the 11 simulated spectra in νF_ν, with $A = 0.05$. The upper limit of $\Lambda = 1.0$ (in decades of energy) is reasonable, considering that the LAD spectra span less than two decades of energy. The spectrum with $\Lambda = 0.01$ represents a sharply-broken power law. To provide variations in the signal strength, the amplitude A was set to a typical value of 0.05 in one group, and was 0.01 in the other group, corresponding to the average S/N of $\sim$ 100 and $\sim$ 30 per spectrum, respectively. Each of the simulated spectra was then fitted with the full 5-parameter SBPL model allowing Λ to vary, with a set of 4-parameter SBPL models, each with Λ fixed to the 11 values mentioned above, as well as with the BAND and the COMP models for comparison.

4.3.2.1 Finding the Break Scale

In Figure 4.6, we show the Λ values found by the 5-parameter SBPL model fits, with Λ varied. For the high S/N case, the correct Λ values were found up to $\Lambda \sim 0.6$, with relatively small dispersions. For the low S/N case, only the very sharp break ($\Lambda = 0.01$) was constrained by the 5-parameter fits. As for the other parameters associated with the fits, we found that even for the bright cases, the 5-parameter

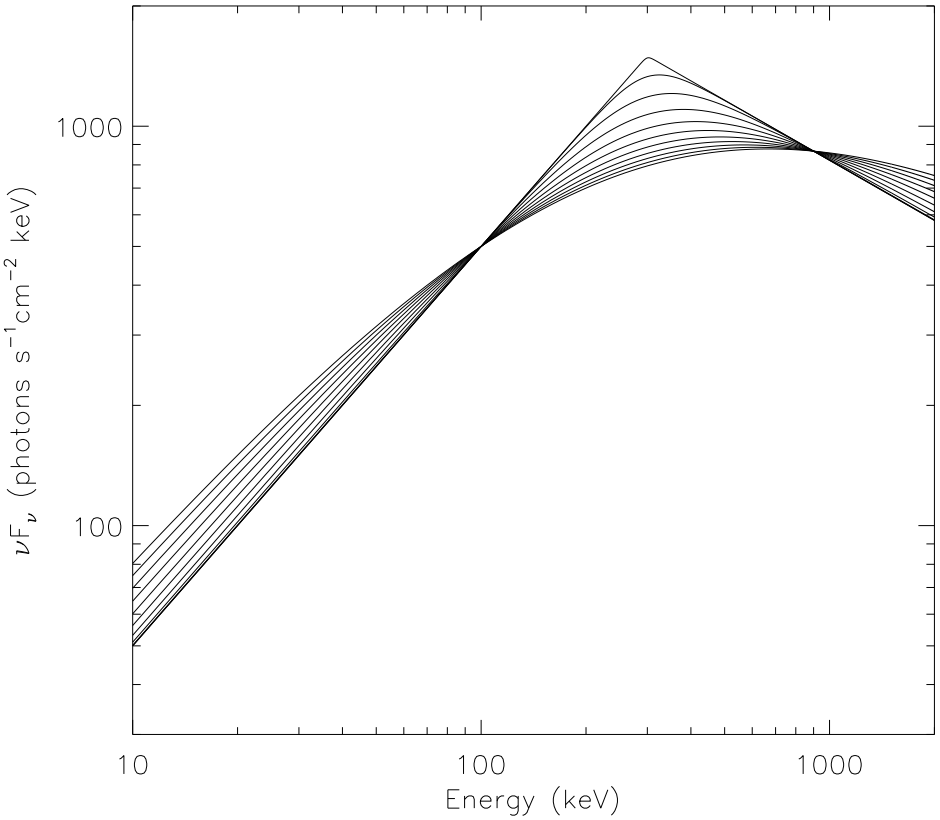

Figure 4.5 The simulated SBPL model spectra with $\Lambda = 0.01$, 0.1, 0.2, 0.3, 0.4, 0.5, 0.6, 0.7, 0.8, 0.9, and 1.0, from top to bottom at 300 keV. The other parameters are fixed at $A = 0.05$, $E_{\rm b} = 300$, $\lambda_1 = -1.0$, and $\lambda_2 = -2.5$.

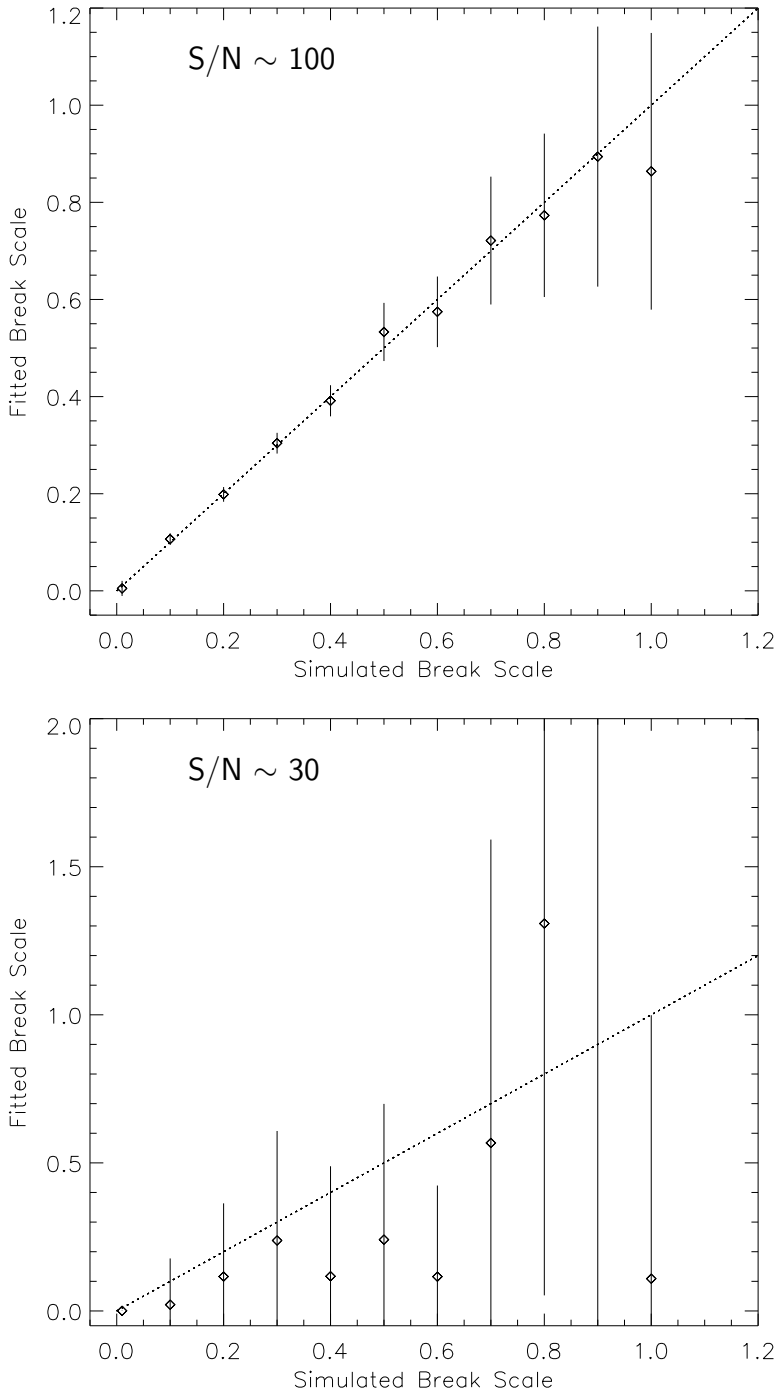

Figure 4.6 The break scale Λ found by 5-parameter SBPL fits to 11 simulated spectra for bright (*top*) and faint (*bottom*) cases. Horizontal axis shows the simulated Λ values and vertical axis shows the fitted Λ values. The dotted line corresponds to the correct Λ.

fits resulted in relatively large uncertainties in all parameters, which worsened as Λ became larger. This was also indicated by the large correlation coefficients among all parameters. This confirms that fitting 5 free parameters at once does not determine the parameter with a good confidence, regardless of the S/N of spectrum, and therefore, the full 5-parameter fit is not favored. It is, however, worth noting that despite the large errors, Λ found by the 5-parameter fits may still provide a rough estimate of the break scale even for faint spectra, as a last resort.

Alternatively, we could employ a subset of 4-parameter SBPL fits with various fixed values of Λ to determine the real Λ. Having such a set of 4-parameter model fits to each spectrum enables us to construct a one-dimensional χ^2 map for Λ, showing the changes in χ^2 for $\Delta\text{dof} = 1$ as a function of Λ. From the χ^2 map, we can determine the most likely value of Λ (where the χ^2 is minimum) as well as the confidence interval, while having the other parameters still constrained.

The $\langle\chi^2\rangle$ map obtained from a 4-parameter model fitting of the bright simulated spectra is seen in Figure 4.7. It is seen that for $\Lambda \leq 0.4$ the set of 4-parameter fits yields a minimum for χ^2 at the correct Λ values with 1σ uncertainties less than 0.01. However, for $\Lambda \geq 0.5$, the Λ value could not be sufficiently constrained, especially at the upper ends, and the BAND model starts to give satisfactory fits that are statistically comparable to the SBPL model fits. This suggests that in the case of $\Lambda \geq 0.5$ we can only determine the lower limit of $\Lambda = 0.5$ with confidence. Furthermore, for $\Lambda > 0.6$, the uncertainties associated with other spectral parameters become large although they are still in agreement within the uncertainties with the simulated values. As for the faint spectra, we found that the total change in χ^2 for the entire set of Λ values was only about 4, which is within the 2σ confidence interval for $\Delta\text{dof} = 1$; therefore, the correct value of Λ cannot be determined even with the use of 4-parameter fits, due to the low S/N. In such cases, however, we also found that the Λ determined from the 5-parameter SBPL fit can be used as an

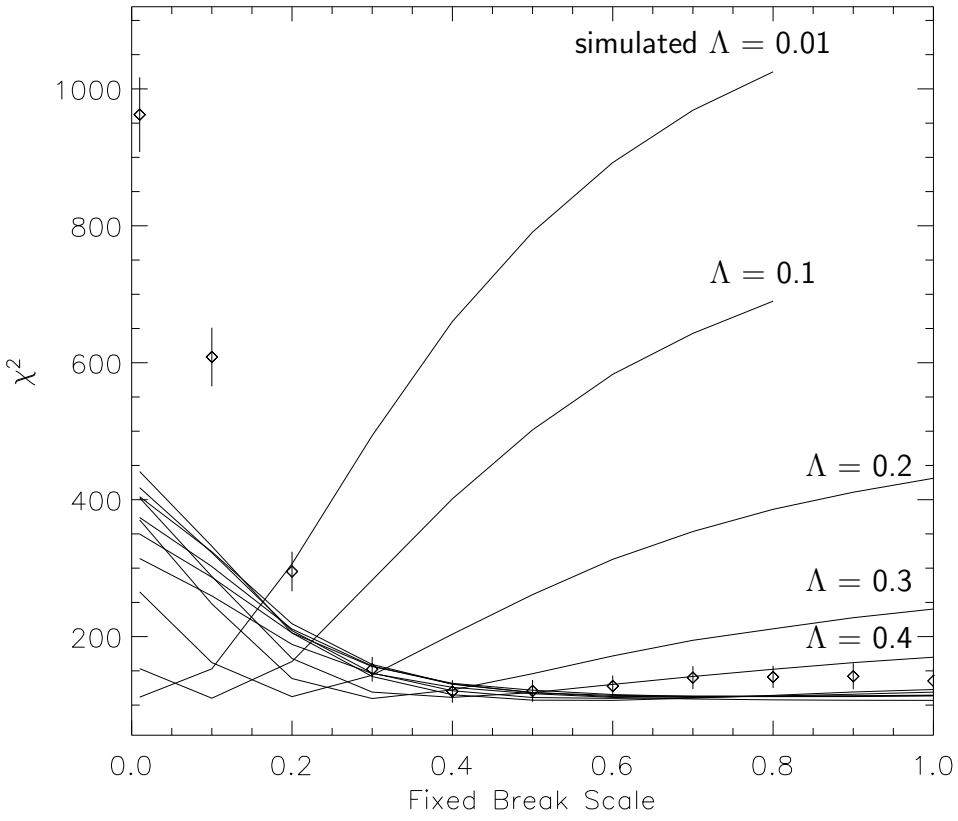

Figure 4.7 Median χ^2 map of 4-parameter SBPL fits to 11 simulated spectra (with $\Lambda = 0.01$ to 1.0, from top to bottom; dof = 113). Horizontal axis is the fixed Λ values of the 4-parameter model. The diamonds indicate the median χ^2 from the BAND fits to 11 simulated spectra (dof = 112).

estimate. In other words, the fit with a 4-parameter model with Λ closest to the 5-parameter-fit Λ could yield parameters that are adequately constrained and still consistent with the actual simulated parameters. The simulation was done both with 128-energy channel data and 16-energy channel data, in order to investigate the possible effects that might arise from the energy resolution issues. We found no differences between the 128-channel data and the 16-channel data in determining the break scales.

Based on these simulation results, we conclude that the 4-parameter SBPL models with $\Lambda > 0.5$ do not contribute much additionally to our analysis; therefore, we decided to use a set of 4-parameter SBPL models with $\Lambda = 0.01$, 0.1, 0.2, 0.3, 0.4, and 0.5, as well as 5-parameter SBPL model with Λ varied, and Λ fixed to the time-integrated fit value (for comparison with SP1). With regard to correlations among the spectral parameters, $E_{\rm b}$ and λ_2 are found to be always strongly anti-correlated in both 4-parameter and 5-parameter fits. Moreover, the 4-parameter fits where Λ is fixed tend to produce higher anti-correlation between $E_{\rm b}$ and λ_1 than the 5-parameter cases, which is expected for the fixed break scale cases. Not surprisingly, in the 5-parameter fits, the λ_1 (λ_2) is more strongly correlated (anti-correlated) with Λ, as Λ becomes larger. There was no difference found in these correlations according to S/N.

4.3.2.2 Comparison with BAND & COMP

To compare other model characteristics, the simulated SBPL spectra were also fitted with the BAND and COMP models. The fit results for the BAND fits are shown in Table 4.3. As seen in the table (also in Figure 4.7), the BAND model is not able to adequately fit the SBPL spectra with relatively sharp break scale ($\Lambda \lesssim 0.4$) because of its rather inflexible, smooth curvature. Generally, for sharply broken

Table 4.3 Results of BAND fits to simulated SBPL spectra with various Λ. The simulated Parameters are $A = 0.05$, $E_{\rm b} = 300$ keV, $\lambda_1 = -1.0$, and $\lambda_2 = -2.5$. "$E_{\rm peak}$" is the calculated νF_ν peak energy in the SBPL model. The parameters are median values and the standard deviations are shown in parentheses.

Simulated		BAND Fit Parameters				
Λ	"$E_{\rm peak}$"	$\langle A\rangle \times 10^3$	$\langle E_{\rm peak}\rangle$	$\langle\alpha\rangle$	$\langle\beta\rangle$	$\langle\chi^2\rangle$/dof
0.01	302	70 (0.3)	457 (4)	–0.68 (0.01)	–2.93 (0.06)	962.3/112
0.10	325	70 (0.4)	448 (4)	–0.69 (0.01)	–2.85 (0.04)	608.4/112
0.20	352	69 (0.4)	434 (4)	–0.74 (0.01)	–2.64 (0.04)	295.1/112
0.30	381	67 (0.5)	419 (5)	–0.80 (0.01)	–2.48 (0.04)	152.4/112
0.40	413	66 (0.6)	406 (6)	–0.86 (0.01)	–2.33 (0.03)	119.9/112
0.50	447	65 (0.5)	402 (7)	–0.94 (0.01)	–2.25 (0.02)	120.7/112
0.60	484	64 (0.7)	396 (8)	–1.00 (0.01)	–2.18 (0.02)	127.8/112
0.70	524	63 (0.5)	396 (7)	–1.06 (0.01)	–2.13 (0.02)	140.2/112
0.80	568	62 (0.6)	394 (9)	–1.11 (0.01)	–2.07 (0.02)	141.1/112
0.90	615	62 (0.7)	397 (12)	–1.15 (0.01)	–2.04 (0.02)	142.1/112
1.00	666	61 (0.6)	404 (12)	–1.20 (0.01)	–2.02 (0.02)	135.3/112

spectra with small Λ, the BAND $E_{\rm peak}$ and α are larger than the SBPL "$E_{\rm peak}$" and λ_1, while the BAND β is smaller than λ_2. The opposite is true for smooth break spectra with large Λ. The tendencies are clearly seen in the example νF_ν spectra in Figure 4.8, in which the BAND fits to the SBPL with $\Lambda = 0.01$ and 0.7 are shown. The BAND model seems to fit the SBPL spectra with $\Lambda \sim 0.4$ the best, at least for these given values of $E_{\rm b}$ and $\lambda_{1,2}$. The BAND fit to this spectrum, in fact, resulted in $E_{\rm peak}$ consistent with the SBPL "$E_{\rm peak}$" and α larger than λ_1, which agrees with what was found from the SBPL fits to the simulated BAND spectra in an earlier section (§4.3.1). We also observe in Table 4.3 that the BAND fits yielded much smaller $E_{\rm peak}$ range ($\sim 390 - 460$ keV) than the simulated "$E_{\rm peak}$" ($\sim 300 - 670$ keV).

For spectra with S/N ~ 100, we find that the SBPL model can fit substantially better than the BAND model (by confidence level $> 99.9\%$) to the simulated SBPL

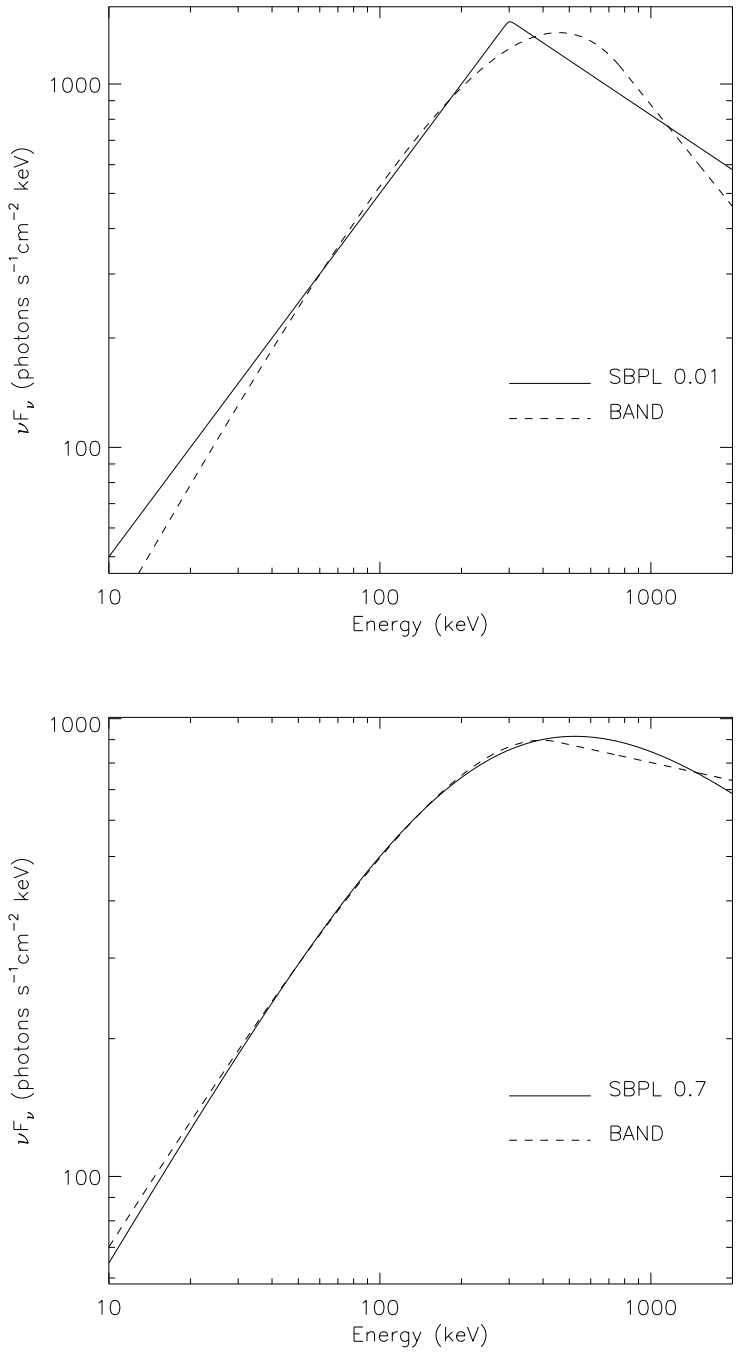

Figure 4.8 Example BAND fits (dashed lines) to the simulated SBPL spectra (solid lines) with $\Lambda = 0.01$ (*top*) and with $\Lambda = 0.7$ (*bottom*).

spectra with $\Lambda \leq 0.3$; however, for the higher value of Λ, BAND begins to fit statistically as well as SBPL fits. The COMP model gave worse fits by far to all Λ, due to the lack of a high-energy component, and thus the SBPL fits were always definitely better. On the other hand, for the spectra with S/N $\sim$ 30, the SBPL fitted better than the BAND or the COMP model for $\Lambda = 0.01$ and 0.1, but only by confidence level of $\sim$ 90%. For the spectra with larger Λ values, we found that the BAND and the COMP fits are statistically as good as the SBPL fit.

4.4 Spectral Analysis Results

The results of the comprehensive spectral analysis performed herein constitute the richest resource of GRB prompt emission spectral properties. Therefore, careful examination of these results enables us to better constrain the proposed physical models for the GRB prompt emission process. This also allows us to explore systematics that are internal to the spectral models employed.

The overall performance of each model in fitting to all spectra is summarized in Table 4.4, in which the percentages of acceptable fits yielded by each model are shown. The BETA model is excluded here because it is a special case of the BAND model and was used only to investigate the constant-β hypothesis in each burst.

Table 4.4 The percentage of fits resulted in χ^2 with confidence level within 3σ (99.7%) out of the total number of 342 time-integrated spectra and 8459 time-resolved spectra.

	PWRL	COMP	BAND	SBPL
Time-Integrated	11.4%	69.3%	84.2%	87.4%
Time-Resolved	23.3%	95.7%	92.3%	99.2%

The BETA model fits are explored in §4.4.5. Also, the SBPL used here is the set of 4-parameter model fits, with the break scale Λ determined according to minimum χ^2 as described in §4.3.2. Therefore, dof -1 was used to obtain the χ^2 confidence levels for these fits, since we are indeed allowing the break scale to vary, making the model equivalent to a 5-parameter model. From Table 4.4, it is clear that many spectra are fitted adequately well with multiple photon models. Solely by the resulting χ^2 of the fits, the SBPL model seems to be able to fit the data better than the other models in general, as seen in the Table 4.4, although the values are only slightly better than those obtained by the BAND model. The time-resolved spectra provide better χ^2 values, due to the lower S/N compared with the time-integrated spectra. This is especially evident in the results for the COMP cases. As expected, the PWRL resulted in poor fits for most of the spectra. In the following sections, we look at the results of our spectral analysis in terms of the parameter distributions, the model statistics, and the comparison between time-integrated and time-resolved spectra.

4.4.1 Spectral Parameter Distributions

The spectral parameters can be compared by two different aspects; namely, a comparison among parameters yielded by different models, and a comparison between time-integrated vs. time-resolved parameters. The comparison among the models reveals the internal characteristics of each model, whereas the comparison between the time-integrated and time-resolved parameters uncovers the differences internal to the spectra.

Before comparing the fitted parameters of various models, there are some issues to be discussed. As mentioned in §4.2.2, the parameterizations are different in each model. For clarity, the free parameters in each model are summarized in Table 4.5. The main concern here is the difference in the low-energy spectral indices: α of

Table 4.5 Spectral parameters fitted in each model.

Model	Amplitude	Low-E Index	High-E Index	Peak Energy	Break Energy	Break Scale
PWRL	A	λ	—	—	—	—
COMP	A	α	—	$E_{\rm peak}$	—	—
BAND	A	α	β	$E_{\rm peak}$	—	—
SBPL	A	λ_1	λ_2	—	$E_{\rm b}$	Λ

BAND and COMP and λ_1 of SBPL, where α is the asymptotic power-law index, while λ_1 is the index of the actual power law fitted to the data. The natural consequence of this is that α tends to be harder than λ_1 (i.e., $\alpha > \lambda_1$), when fitted to the same dataset, which was confirmed in the simulation study presented in §4.3. They are therefore not directly comparable. In order to minimize the discrepancies, an "effective" α ($\alpha_{\rm eff}$) was introduced by Preece et al. (2002). This is the tangential slope at 25 keV in a logarithmic scale, and is found to describe the data more accurately than the fitted asymptotic α value. Therefore, we employ the $\alpha_{\rm eff}$ instead of the fitted-α values for BAND and COMP fits in the following parameter distribution comparisons. The detailed discussion of $\alpha_{\rm eff}$ can be found in Appendix C.

Another issue in comparing and presenting the spectral parameter distributions is the uncertainty associated with each parameter. The parameter distribution in a large sample can be effectively shown in a binned, histogram plot (e.g., Figure 4.9); however, such a plot does not include the uncertainties associated with each value. Consequently, the reliability of the distribution is not evident. One way of treating this problem is to only include well-constrained parameters in the distribution. This certainly results in providing a reliable probability distribution of a given parameter, although it could also introduce some biases depending on how the *good*

class of parameters are determined. To interpret such distributions correctly, the criteria used to determine the *good* parameters are reviewed here. We note that for all parameters, the very first cut was made by the χ^2 confidence level of each fit being less than 3σ (99.7%) for a given dof.

Low-Energy Indices. Since each model handles spectral curvature differently, the condition under which the spectral indices can be determined with good confidence differs for each model. The PWRL indices were found to be almost always constrained extremely well due to the simplicity of the model, so they can all be considered *good*. On the other hand, α (BAND and COMP) is constrained only if the e-folding energy E_0 is sufficiently above the lower energy threshold of the data. In our case, E_0 above 30 keV was considered acceptable. For SBPL λ_1 to be constrained, the lowest energy that determines the break scale must be above 30 keV. Determined from the error distributions of all low-energy indices, we allow a maximum 1σ uncertainty value of 0.4 in order for the parameters to be *good*. The value was selected so as to adequately constrain the parameters and still preserve more than 90% of all low-energy indices regardless of models.

High-Energy Indices. In order for the BAND β to be well determined, E_0 needs to be less than the upper energy threshold of 1.5 MeV. For SBPL λ_2, similar to the low-energy index case above, the maximum break scale energy has to be less than 1.5 MeV. In addition, we allow a maximum uncertainty of 1.0 for the high-energy indices, again determined from the error distributions. More than 80% of all β and λ_2 provided uncertainties smaller than this value.

$\boldsymbol{E_{\mathrm{peak}}}$**.** For BAND and COMP, E_{peak} is the value fitted, whereas for SBPL, it is a calculated value (see Appendix A for calculation). By definition, the parameter needs to represent the actual peak of the νF_ν spectrum. When the high-energy

power-law index is -2 or larger, the fitted $E_{\rm peak}$ value is just a break and not the peak of $\nu F_\nu = E^2 f(E)$. Another case in which the fitted $E_{\rm peak}$ value is not the νF_ν peak is when the spectrum has a shape that is concave up. This could occur only in the COMP fits when $\alpha < -2$ and the SBPL fits when $\lambda_1 < \lambda_2$. The BAND model presumes $\alpha > \beta$. Therefore, to obtain final $E_{\rm peak}$ distributions, BAND model fits with $\beta \geq -2$ and COMP fits with $\alpha \leq -2$ are excluded (for SBPL with $\lambda_1 < \lambda_2$, the $E_{\rm peak}$ was not calculated). The maximum uncertainty allowed was 40% of the parameter value for BAND and COMP, and 60% for SBPL.

Break Energy. Break energy includes a calculated $E_{\rm b}$ of BAND (Appendix B) and a fitted $E_{\rm b}$ value of SBPL. Unlike the case for the $E_{\rm peak}$, the break energy does not need to be the peak of the spectrum. Therefore, the only requirement is that the parameter is within the data energy range, i.e., between 30 keV and 2 MeV. This is justified by the fact that all BAND and SBPL fits with $E_{\rm b}$ values below 30 keV and above 2 MeV are associated with very large uncertainties in low-energy and high-energy indices, respectively, as well as in $E_{\rm b}$. The maximum allowed uncertainty of 70% of the parameter value was set in order to include 85 - 90% of all break energies.

With these in mind, we can now examine the spectral parameter distributions for each model. We first compare the spectral parameters obtained by fitting all spectra with all models, in order to explore the internal characteristics of the models. In Figures 4.9 – 4.12, we present distributions of the time-integrated spectral parameters, followed by the distributions of the time-resolved spectral parameters in Figures 4.14 – 4.18, comparing all parameters and *good* parameters obtained with each model. In addition, the most probable values and width (Half-Width at Half-Maximum; HWHM) of each distribution are listed in Table 4.6. The PWRL indices are included in both low-energy and high-energy index distributions because

we cannot judge which power law the model represents. They are found to cluster around ~ -1.7 by themselves, which is in between the typical values of low-energy and high-energy indices.

As seen in these plots and the table, the corresponding parameters of different models are consistent with each other within one HWHM. The low-energy indices (Figures 4.9 and 4.14) determined by the COMP and SBPL models tend to be softer than those determined by the BAND model, consistent with what was found with the simulation in §4.3. As for the high-energy indices (Figures 4.10 and 4.15), the SBPL fits result in slightly lower values than those of the BAND fits. This

Table 4.6 The most probable *good* parameter values and the widths of the distributions determined by fitting all spectra, both time-integrated and time-resolved, separately with four models.

	Time-Integrated Parameters				
	Low Index	High Index	$E_{\rm peak}$ (keV)	$E_{\rm b}$ (keV)	ΔS
PWRL	$-1.70\ ^{+0.30}_{-0.10}$	$-1.70\ ^{+0.30}_{-0.10}$	—	—	—
COMP	$-1.30\ ^{+0.70}_{-0.30}$	—	$266\ ^{+198}_{-119}$	—	—
BAND	$-1.10\ ^{+0.50}_{-0.30}$	$-2.30\ ^{+0.30}_{-0.50}$	$266\ ^{+198}_{-119}$	$181\ ^{+283}_{-\ 81}$	$1.40\ ^{+0.60}_{-0.60}$
SBPL	$-1.30\ ^{+0.50}_{-0.10}$	$-2.30\ ^{+0.30}_{-0.50}$	$266\ ^{+198}_{-119}$	$181\ ^{+283}_{-\ 34}$	$1.30\ ^{+0.70}_{-0.50}$

	Time-Resolved Parameters				
	Low Index	High Index	$E_{\rm peak}$ (keV)	$E_{\rm b}$ (keV)	ΔS
PWRL	$-1.85\ ^{+0.45}_{-0.15}$	$-1.85\ ^{+0.45}_{-0.15}$	—	—	—
COMP	$-0.95\ ^{+0.35}_{-0.55}$	—	$424\ ^{+402}_{-279}$	—	—
BAND	$-0.85\ ^{+0.35}_{-0.45}$	$-2.25\ ^{+0.45}_{-0.55}$	$350\ ^{+213}_{-229}$	$178\ ^{+205}_{-\ 78}$	$1.40\ ^{+0.80}_{-0.60}$
SBPL	$-0.95\ ^{+0.35}_{-0.55}$	$-2.45\ ^{+0.55}_{-0.35}$	$215\ ^{+347}_{-\ 94}$	$238\ ^{+145}_{-117}$	$1.30\ ^{+0.90}_{-0.50}$

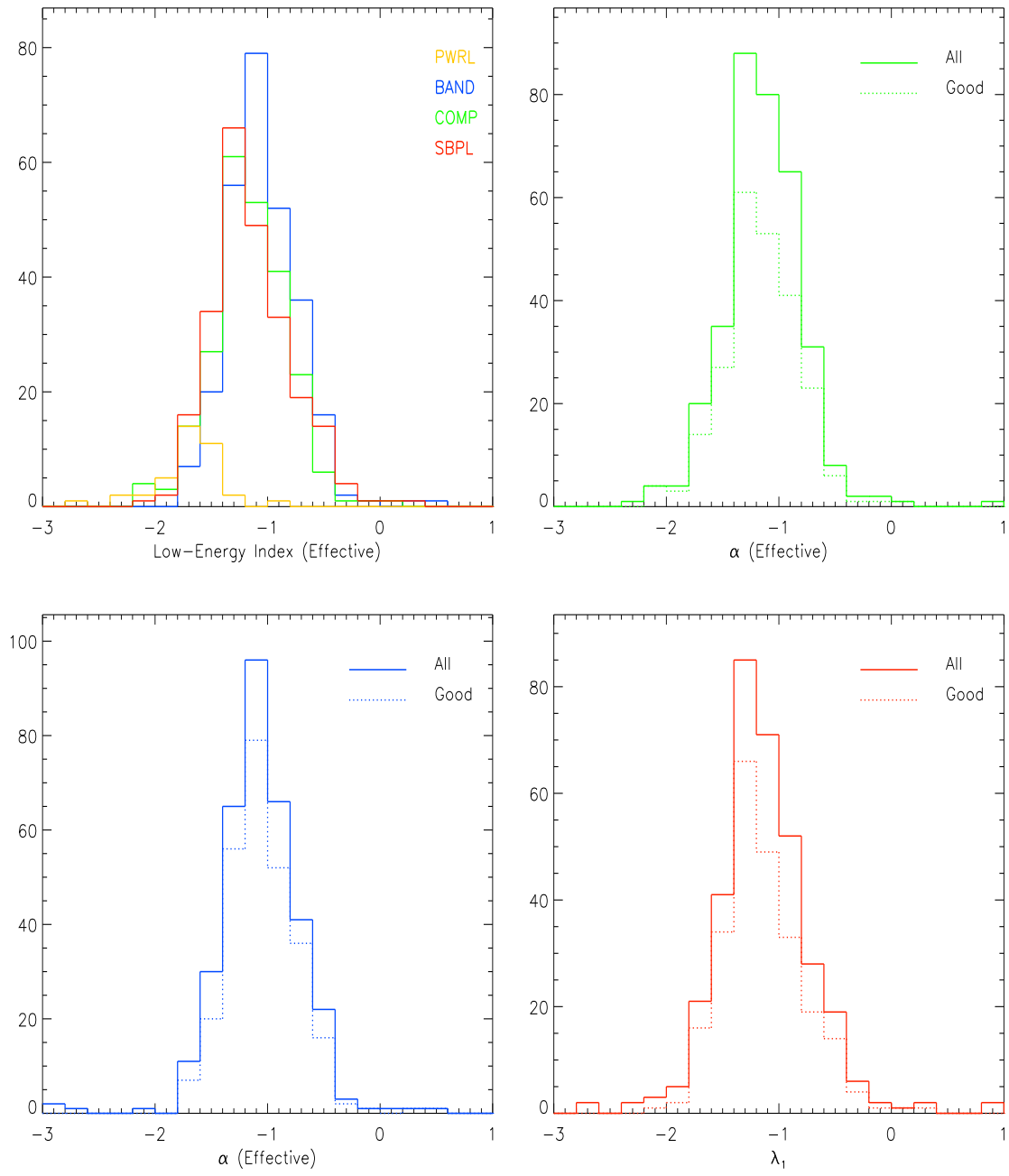

Figure 4.9 Low-energy index distribution of 342 time-integrated spectra. [*Top Left*] *Good* parameters of all models. Numbers of parameters included are 38 PWRL, 235 COMP, 271 BAND, and 241 SBPL. The other plots show all (solid line) and *good* (dotted line) parameters of COMP (green), BAND (blue), and SBPL (red). The lowest (highest) bin includes values lower (higher) than the edge values.

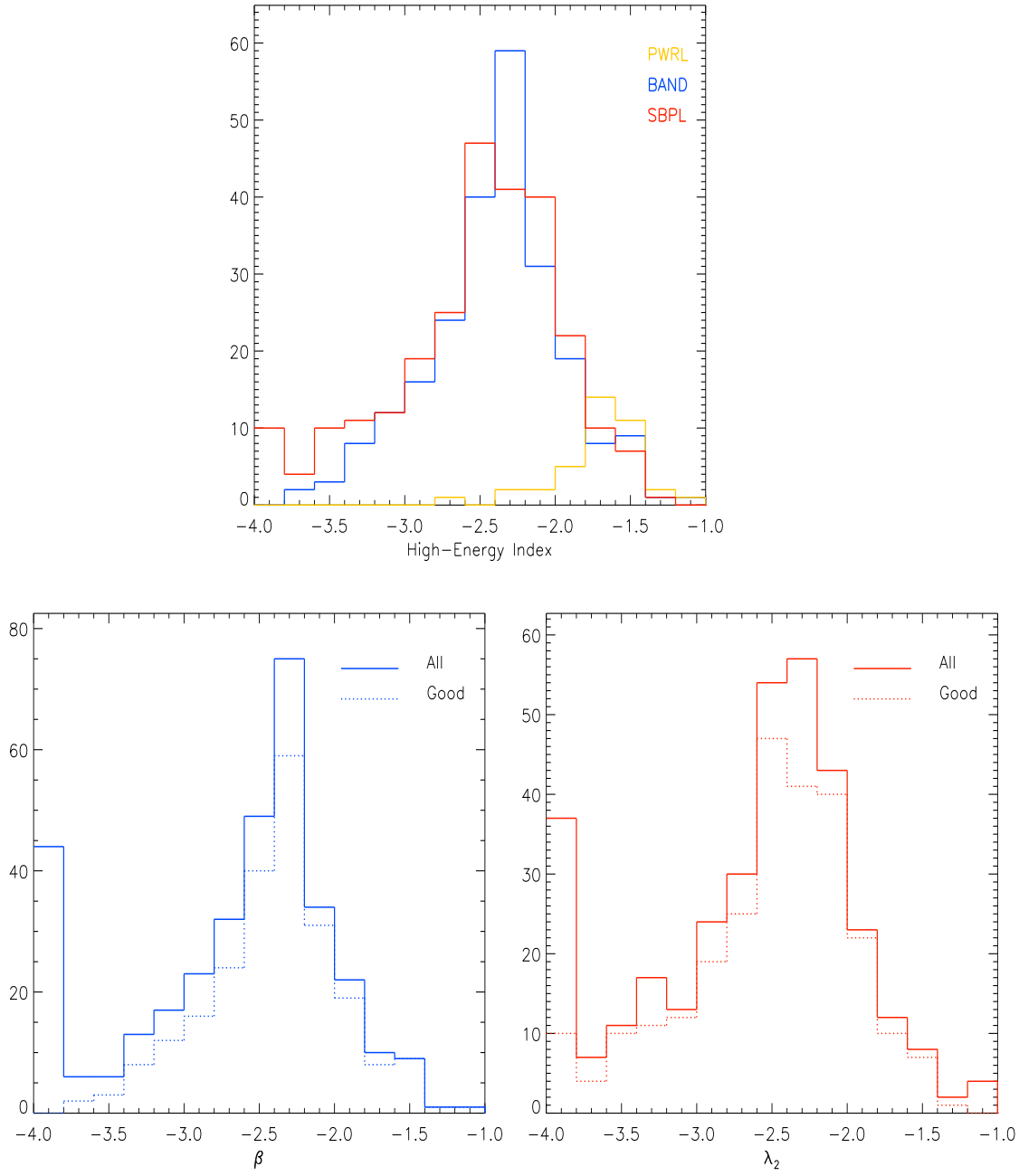

Figure 4.10 High-energy index distribution of 342 time-integrated spectra. [*Top*] *Good* parameters of all models. Numbers of parameters included are 38 PWRL, 233 BAND, and 259 SBPL. The other plots show all (solid line) and *good* (dotted line) parameters of BAND (blue) and SBPL (red). The lowest (highest) bin includes values lower (higher) than the edge values.

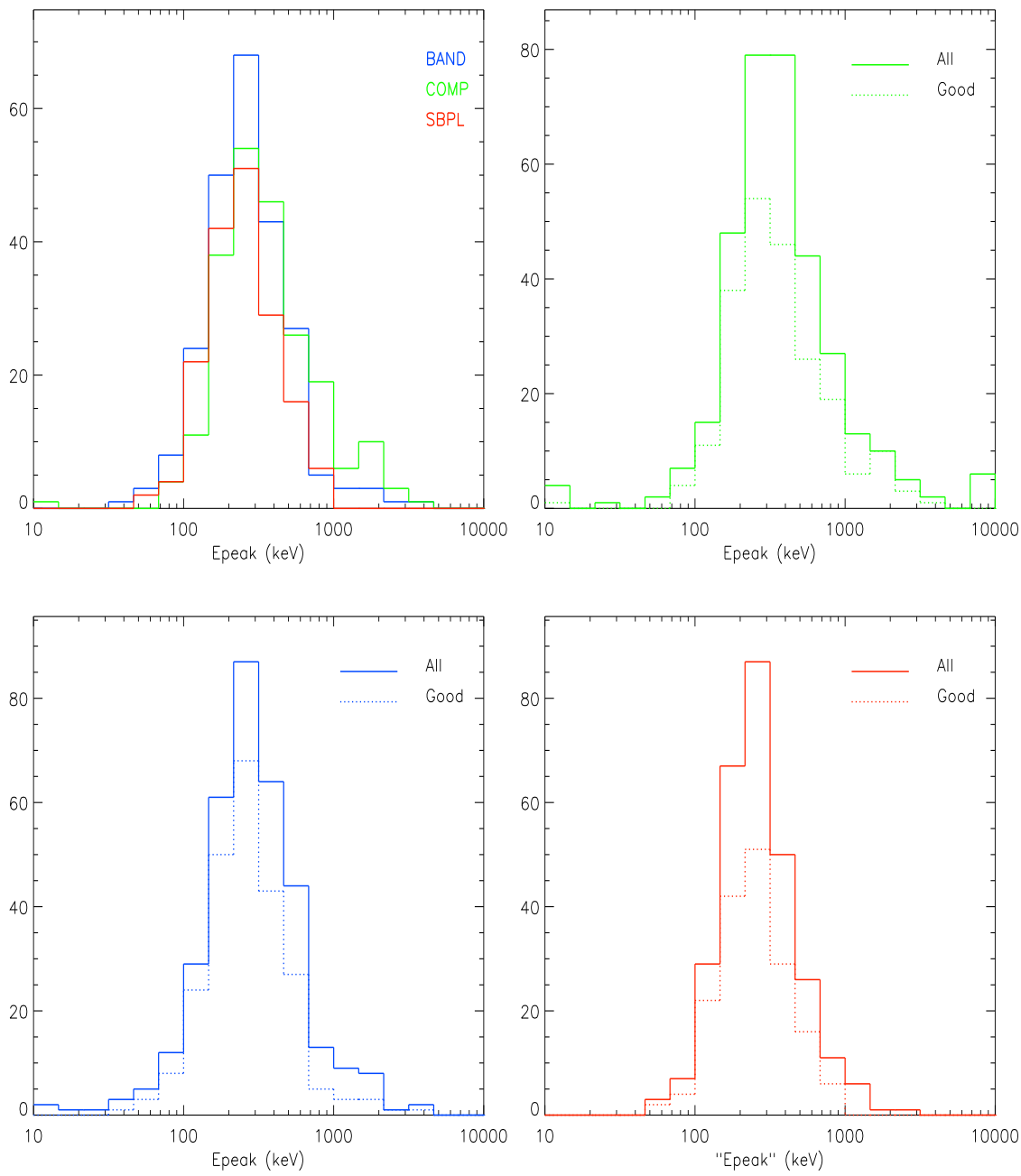

Figure 4.11 $E_{\rm peak}$ distribution of 342 time-integrated spectra. [*Top Left*] *Good* parameters of all models. Numbers of parameters included are 219 COMP, 237 BAND, and 172 SBPL. The other plots show all (solid line) and *good* (dotted line) parameters of COMP (green), BAND (blue), and SBPL (red). The lowest (highest) bin includes values lower (higher) than the edge values.

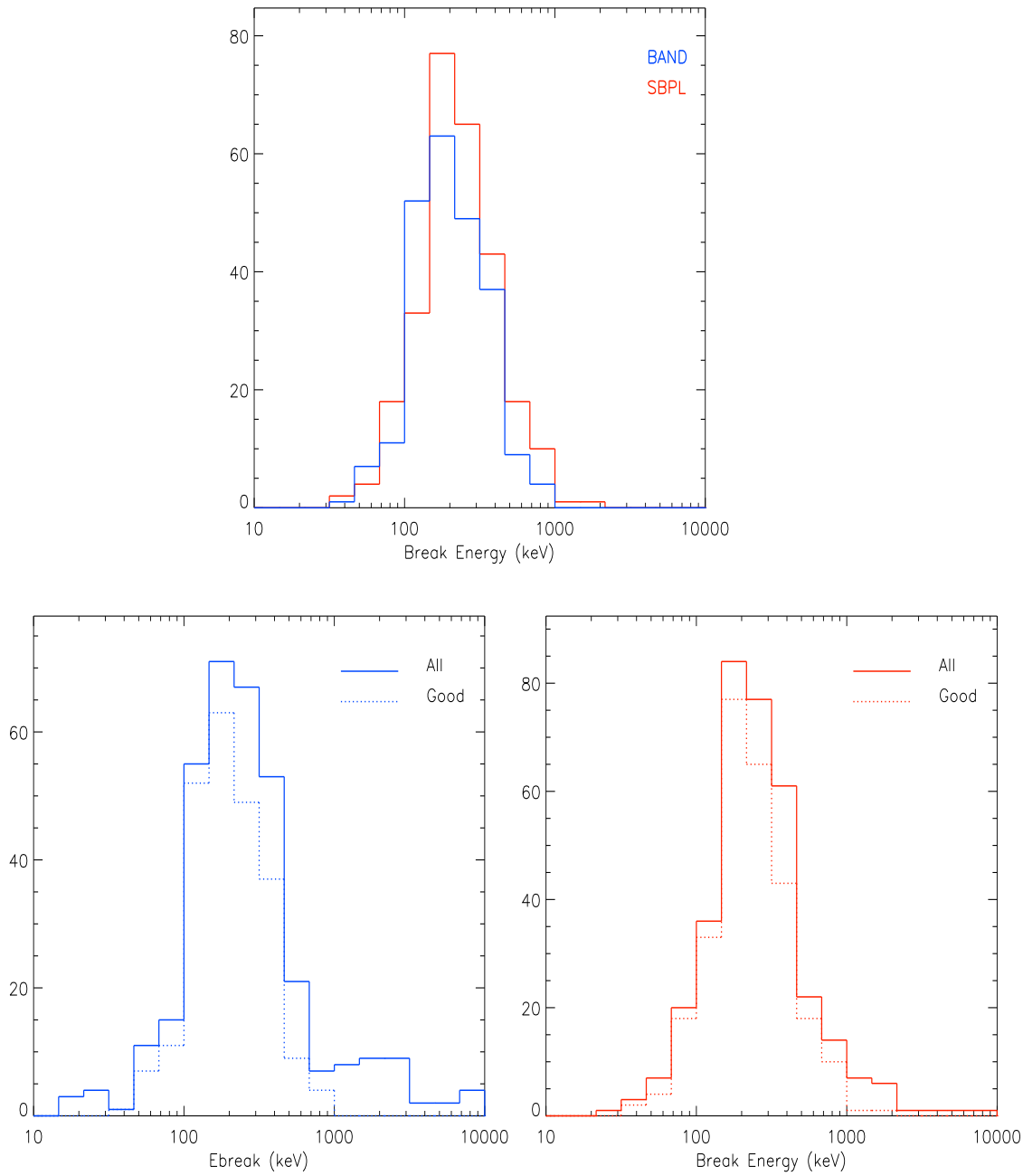

Figure 4.12 Break Energy distribution of 342 time-integrated spectra. [*Top*] *Good* parameters of all models. Numbers of parameters included are 233 BAND and 272 SBPL. The other plots show all (solid line) and *good* (dotted line) parameters of BAND (blue) and SBPL (red). The lowest (highest) bin includes values lower (higher) than the edge values.

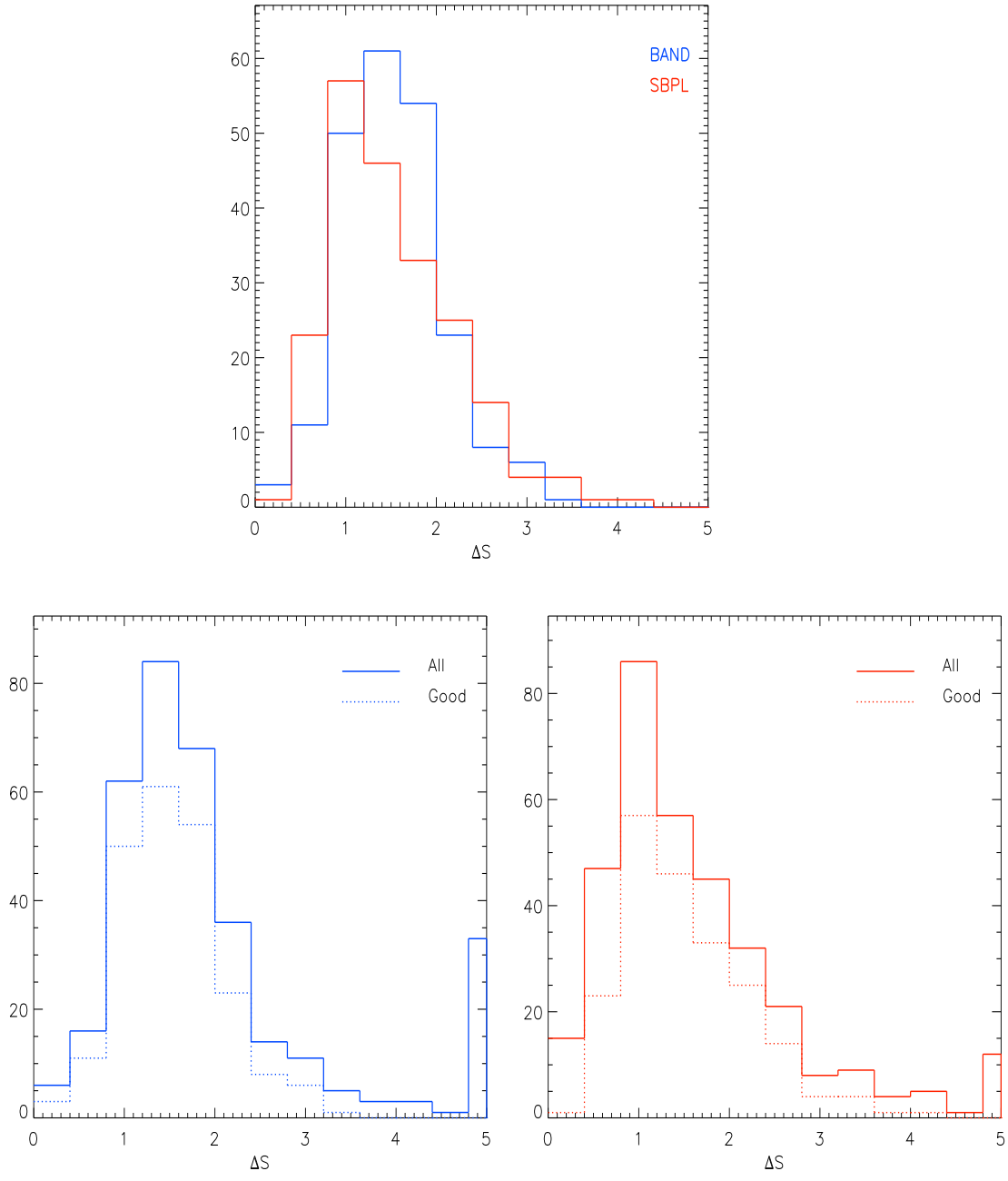

Figure 4.13 ΔS distribution of 342 time-integrated spectra. ΔS is the difference between low-energy and high-energy indices. [*Top*] *Good* parameters of all models. Numbers of parameters included are 217 BAND and 209 SBPL. The other plots show all (solid line) and *good* (dotted line) parameters of BAND (blue) and SBPL (red). The lowest (highest) bin includes values lower (higher) than the edge values.

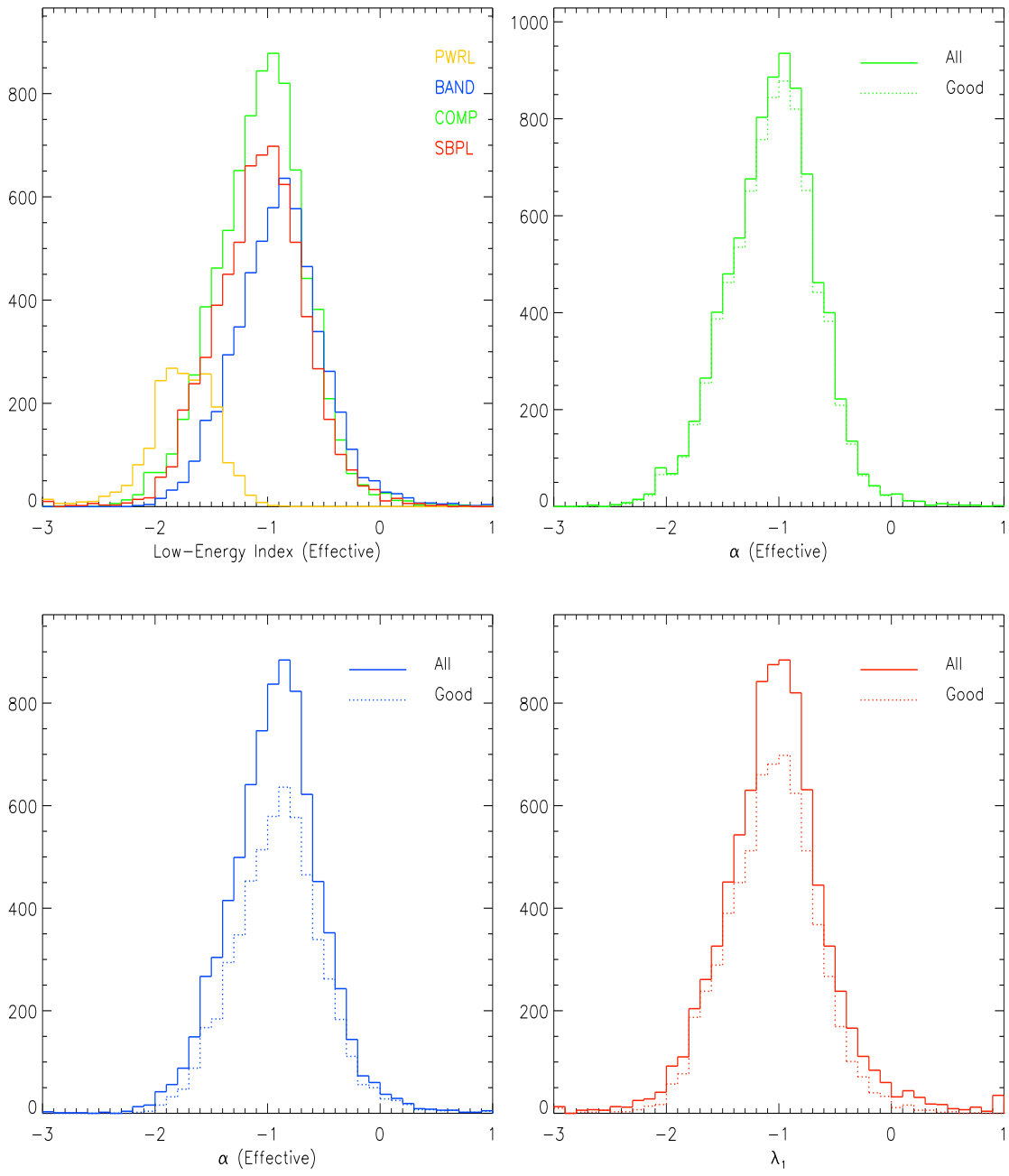

Figure 4.14 Low-energy spectral index distribution of 8459 time-resolved spectra. [*Top Left*] *Good* parameters of all models. Numbers of parameters included are 1971 PWRL, 8050 COMP, 5510 BAND, and 6533 SBPL. The other plots show all (solid line) and *good* (dotted line) parameters of COMP (green), BAND (blue), and SBPL (red). The lowest (highest) bin includes values lower (higher) than the edge values.

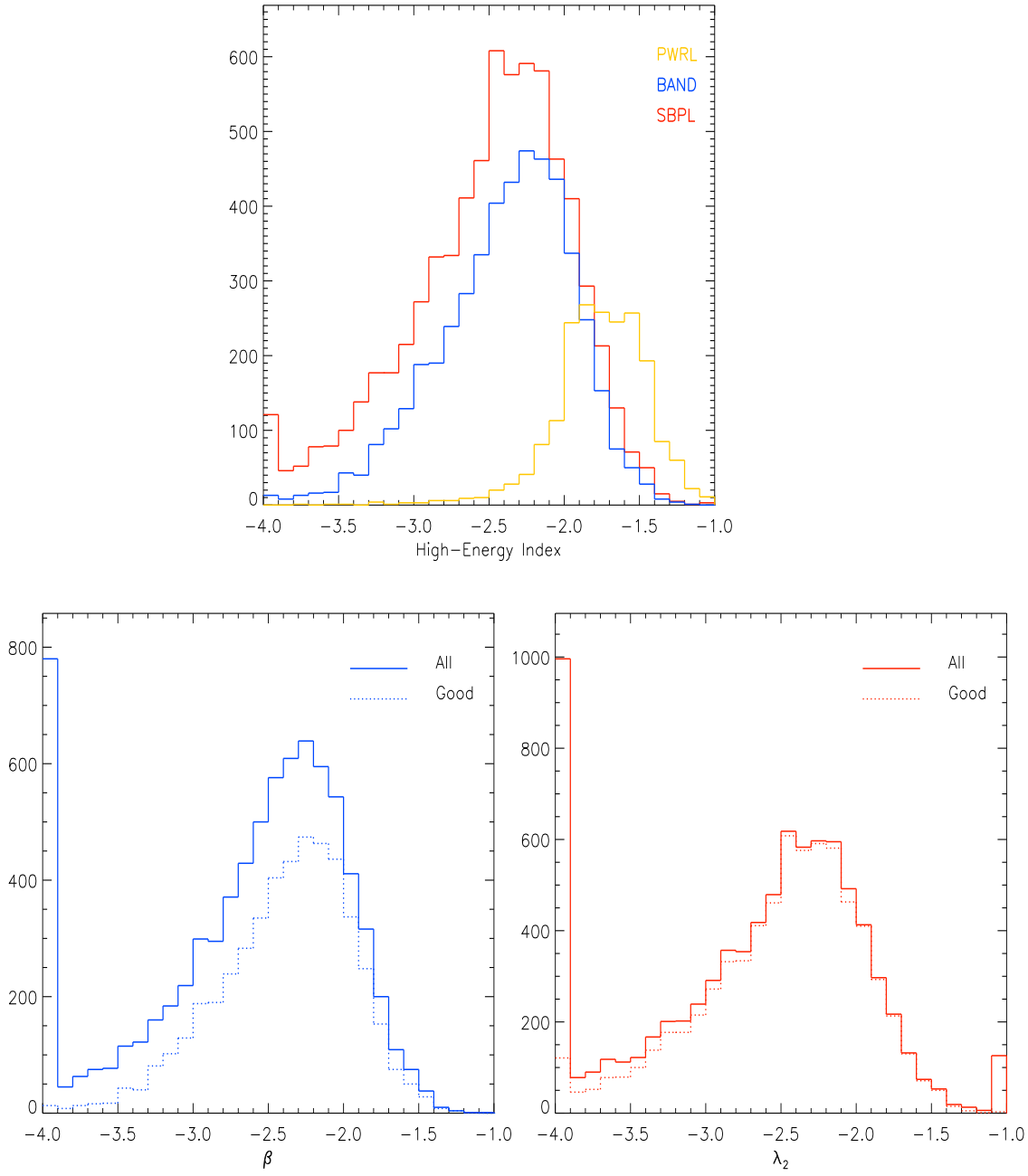

Figure 4.15 High-energy spectral index distribution of 8459 time-resolved spectra. [*Top*] *Good* parameters of all models. Numbers of parameters included are 1971 PWRL, 4810 BAND, and 7003 SBPL. The other plots show all (solid line) and *good* (dotted line) parameters of BAND (blue) and SBPL (red). The lowest (highest) bin includes values lower (higher) than the edge values.

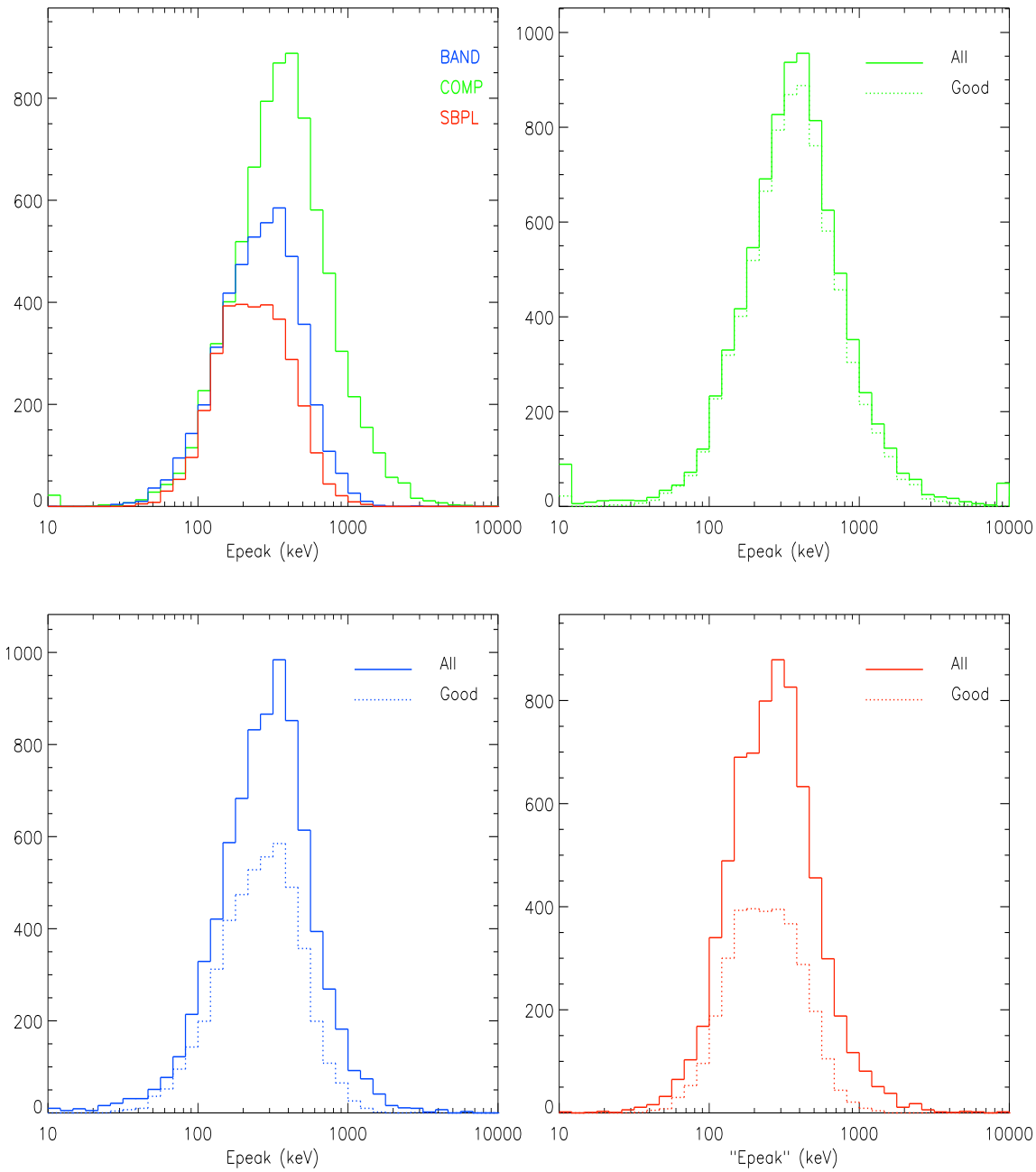

Figure 4.16 $E_{\rm peak}$ distribution of 8459 time-resolved spectra. [*Top Left*] *Good* parameters of all models. Numbers of parameters included are 7702 COMP, 4677 BAND, and 3291 SBPL. The other plots show all (solid line) and *good* (dotted line) parameters of COMP (green), BAND (blue), and SBPL (red). The lowest (highest) bin includes values lower (higher) than the edge values.

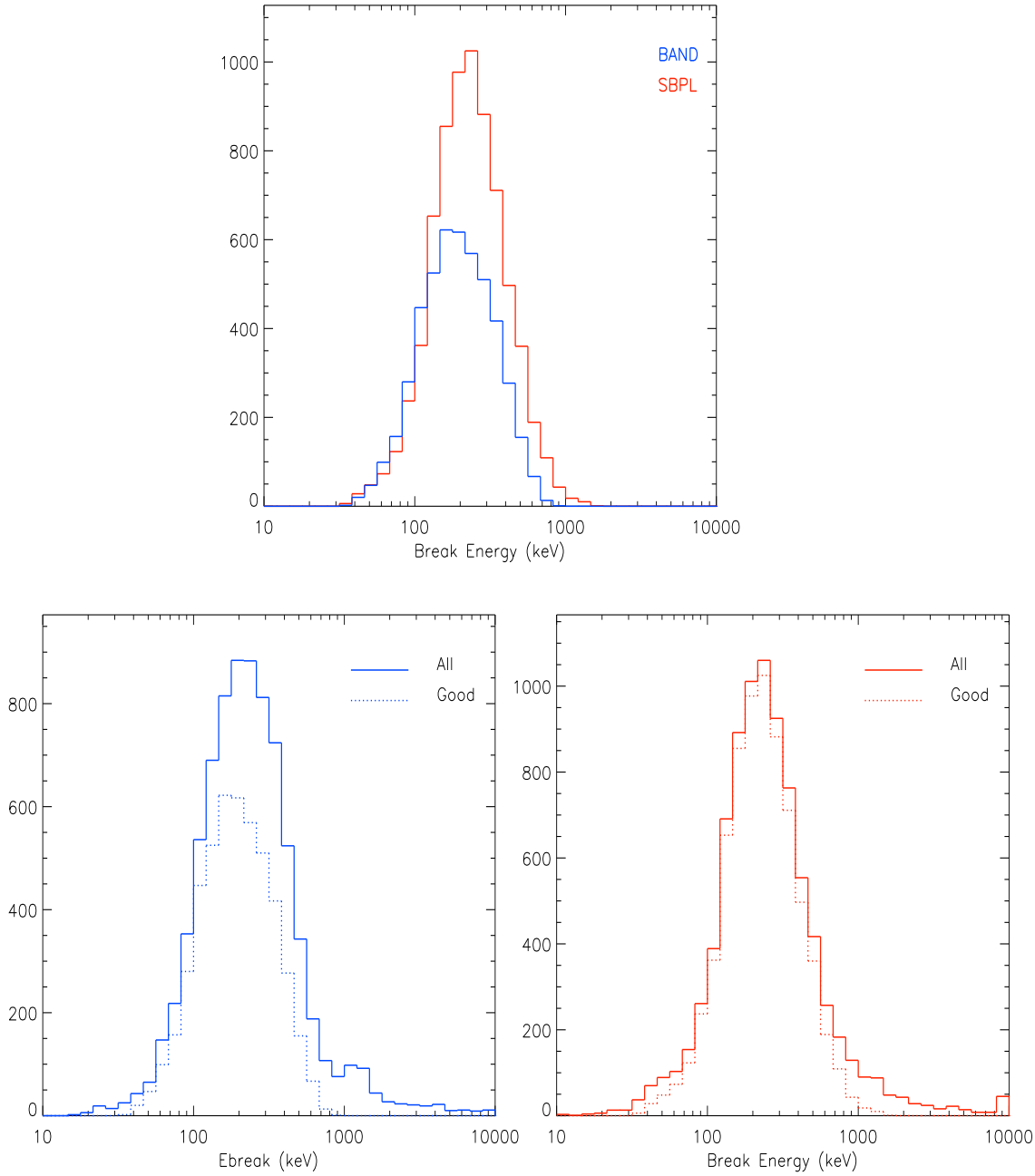

Figure 4.17 Break energy distribution of 8459 time-resolved spectra. [*Top*] *Good* parameters of all models. Numbers of parameters included are 4825 BAND and 7207 SBPL. The other plots show all (solid line) and *good* (dotted line) parameters of BAND (blue) and SBPL (red). The lowest (highest) bin includes values lower (higher) than the edge values.

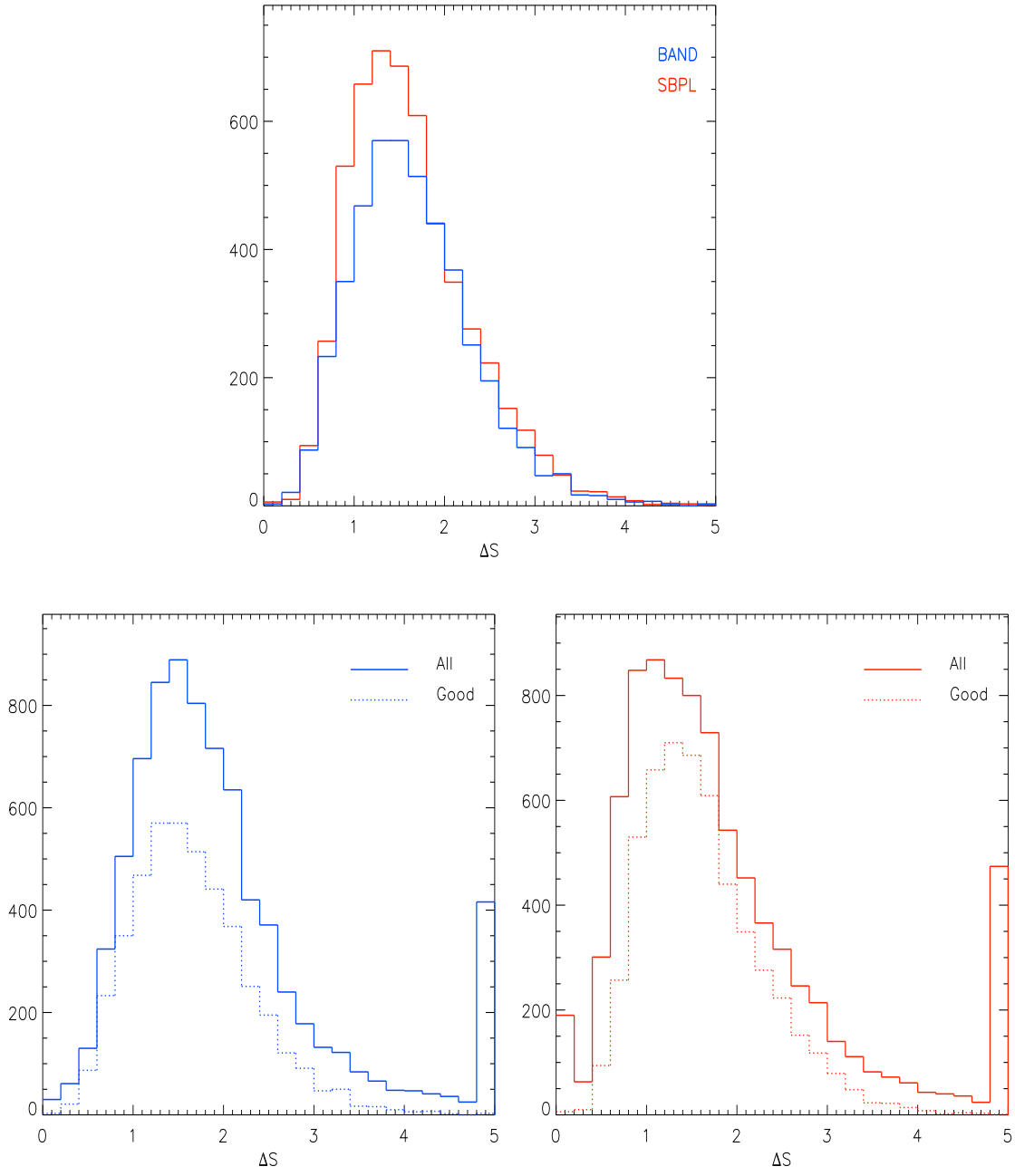

Figure 4.18 ΔS distribution of 8459 time-resolved spectra. ΔS is the difference between low-energy and high-energy indices. [*Top*] *Good* parameters of all models. Numbers of parameters included are 5322 BAND and 4441 SBPL. The other plots show all (solid line) and *good* (dotted line) parameters of BAND (blue) and SBPL (red). The lowest (highest) bin includes values lower (higher) than the edge values.

is more evident in the time-resolved parameters. In the $E_{\rm peak}$ distribution of the time-resolved spectra (Figure 4.16), we find that the COMP fits result in higher $E_{\rm peak}$ values and broader distribution than the BAND and SBPL ones, while they are all similar in time-integrated spectra. Finally, the time-resolved break energy distributions seen in Figure 4.17 indicate that the typical break energies found by the BAND fits are softer than the $E_{\rm peak}$ of the same model, due to the curvature in the spectra. In the time-integrated spectra, better agreements of $E_{\rm peak}$ values of the BAND and SBPL models are due to the fact that they are fitted mostly by smooth-break-scale SBPL models. The high-energy tail populations are more noticeable than the $E_{\rm peak}$ case, although they are not constrained. We also present in Figures 4.13 and 4.18, the change in the spectral indices: $\Delta{\rm S} \equiv \alpha_{\rm eff} - \beta$ (BAND), $\lambda_1 - \lambda_2$ (SBPL). This parameter has been previously examined by Preece et al. (2002) using the results of SP1, in order to probe the GRB emission process. The distributions of ΔS of the BAND and SBPL agree well.

In terms of comparisons between the time-integrated and time-resolved spectral parameters, the most obvious difference is seen in the low-energy index distributions. The indices of time-integrated spectra are found to be softer than the time-resolved ones, regardless of the model fitted. Peak energies ($E_{\rm peak}$) are also softer in the time-integrated spectra. The differences are probably due to the fact that α and $E_{\rm peak}$ are very often found to strongly evolve during a burst (e.g., Ford et al. 1995; Liang & Kargatis 1996; Band 1997; Crider et al. 1997; Ryde 1999; Crider et al. 1999; Preece et al. 1998a). No significant differences in high-energy index distributions as well as in ΔS distributions are seen.

4.4.2 Model Comparison within Each Spectrum

Since we have fitted four models to all spectra, it is possible to statistically compare models and determine the best-fitted model to each individual spectrum. The comparison is, however, not straightforward because each model provides a different dof. A model that consists of a lower number of parameters is always preferred statistically over more complex models for the same χ^2. However, the data may require an extra parameter for a better fit, in which case it should result in a significant improvement in χ^2 when the extra parameter is fitted. Therefore, we look at the χ^2 improvements in adding N parameters ($\Delta\text{dof} = N$), starting from the simplest model (i.e., PWRL) to determine the best-fitted models.

The four models employed, namely PWRL, COMP, BAND, and SBPL, consist of 2, 3, 4, and 5 parameters, respectively. For each spectrum, we take the χ^2 of the PWRL fit as a reference. We first compare the PWRL fit χ^2 to the COMP fit χ^2 for $\Delta\text{dof} = 1$, and find the confidence level in χ^2 improvement. If the confidence level is greater than 99.9%, the COMP fit is significantly better than the PWRL fit; whereas, for confidence levels between $80.0 - 99.9\%$, we cannot statistically determine the better model between the two. The best-fit model in such a case is classified as PWRL/COMP. A confidence level lower than 80.0% suggests that the PWRL is preferred. The threshold values for the confidence levels were determined by the simulated spectra of each model fitted with other models, as described above in Section §4.3. Likewise, comparisons were made for all possible combinations of four models, with corresponding Δdof. The confidence intervals of 99.9% and 80.0% were used for all comparisons involving PWRL, while 99.9% and 68.3% were used for the comparisons among the other models, according to the simulation results.

In most cases, the χ^2 probability was an adequate measure of the best fit determination; however, we found some cases where the best-fitted model found by

χ^2 probability was actually not better than the other models in terms of parameter constraints. Therefore, in addition to the χ^2 probabilities, the spectral parameters were also checked, according to the *good* parameter criteria described in the previous section (§4.4.1). If the best-fit model parameters are not constrained, the next statistically best-fit model was preferred. Finally, in case a preferred model could not be determined solely by changes in χ^2, such as the PWRL/COMP case above, again their parameters were compared and a model with more constrained parameter set was designated as the best-fit model. The results of the best-fit model determination are shown in Table 4.7. It is seen that for many spectra, the COMP, BAND, and SBPL models all resulted in comparably good fits (C/B/S case in the Table 4.7). In most of these cases, the additional parameters were still well constrained, and the more complex models were meaningful. Consequently, the SBPL fits were selected as the BEST models, despite the complexity of the model, in many of the C/B/S

Table 4.7 Model comparison summary. The best-fit models were first determined statistically by χ^2 probabilities (Column 1) and finalized by fitted parameter constraints (Columns 3 – 6, 8 – 11).

Best-Fit	Time Integrated					Time Resolved				
Model	Total	**PWRL**	**COMP**	**BAND**	**SBPL**	Total	**PWRL**	**COMP**	**BAND**	**SBPL**
PWRL	8	8	–	–	–	186	186	–	–	–
COMP	45	–	45	–	–	1855	–	1855	–	–
BAND	46	–	–	46	–	801	–	–	801	–
SBPL	46	–	–	–	46	52	–	–	–	52
P/B/C/S	2	0	0	0	2	24	2	3	0	19
C/B/S	53	–	2	6	45	1559	–	88	192	1279
P/C/B	4	1	3	0	–	149	40	101	8	–
P/C/S	1	1	0	–	0	19	9	6	–	4
P/B/S	0	0	–	0	0	4	2	–	0	2
P/C	6	5	1	–	–	182	86	96	–	–
P/B	1	1	–	0	–	43	37	–	6	–
P/S	2	1	–	–	1	21	12	–	–	9
C/B	26	–	3	23	–	2300	–	621	1679	–
C/S	29	–	16	–	13	704	–	394	–	310
B/S	73	–	–	44	29	560	–	–	142	418
TOTAL	**342**	**17**	**70**	**118**	**137**	**8459**	**374**	**3164**	**2828**	**2093**
%		5.0	20.5	34.5	40.1		4.4	37.4	33.4	24.7

case. To illustrate the goodness of fits of each model, a count spectrum of one C/B/S event with all four model counts is plotted in Figure 4.19. Moreover, for the time-resolved spectra, in almost 30% of the cases, the COMP and BAND fits were both found to be acceptable (i.e., C/B). The more complex BAND model was able to provide adequate parameter constraints, similar to the SBPL model in the C/B/S case above. In these cases, low-energy indices from all models were usually found in agreement within 1σ uncertainties (if $\alpha_{\rm eff}$ is used). We also find that COMP tends to be preferable in fitting time-resolved spectra, because of the existence of more spectra without high-energy component, as well as the lower S/N in each spectrum compared with the time-integrated spectra. In addition, those fitted by PWRL ($\sim$ 5% of all spectra) were indeed among the dimmer, low S/N spectra. In the case of SBPL fitted spectra, a larger number of spectra provided small break scales, i.e., sharper breaks.

Henceforth, we refer to this set of models as the "BEST" models, consisting of PWRL, COMP, BAND, and SBPL, each with numbers presented in the **TOTAL** row of Table 4.7. A collection of parameters obtained with the BEST models can be thought as a well-constrained, model-unbiased set of parameters best describing each spectrum in our sample. The time-integrated spectral fit results obtained with the BEST models are presented in Table 4.8, for each event. Additionally, we show the spectral parameter distributions of the BEST models in Figures 4.20 – 4.23, for both the time-integrated and time-resolved cases. In these figures, the distributions of each parameter of the BEST model and the contribution of each model that consists the BEST model are shown in color. Also, the most probable values and the widths of these distributions are summarized in Table 4.9.

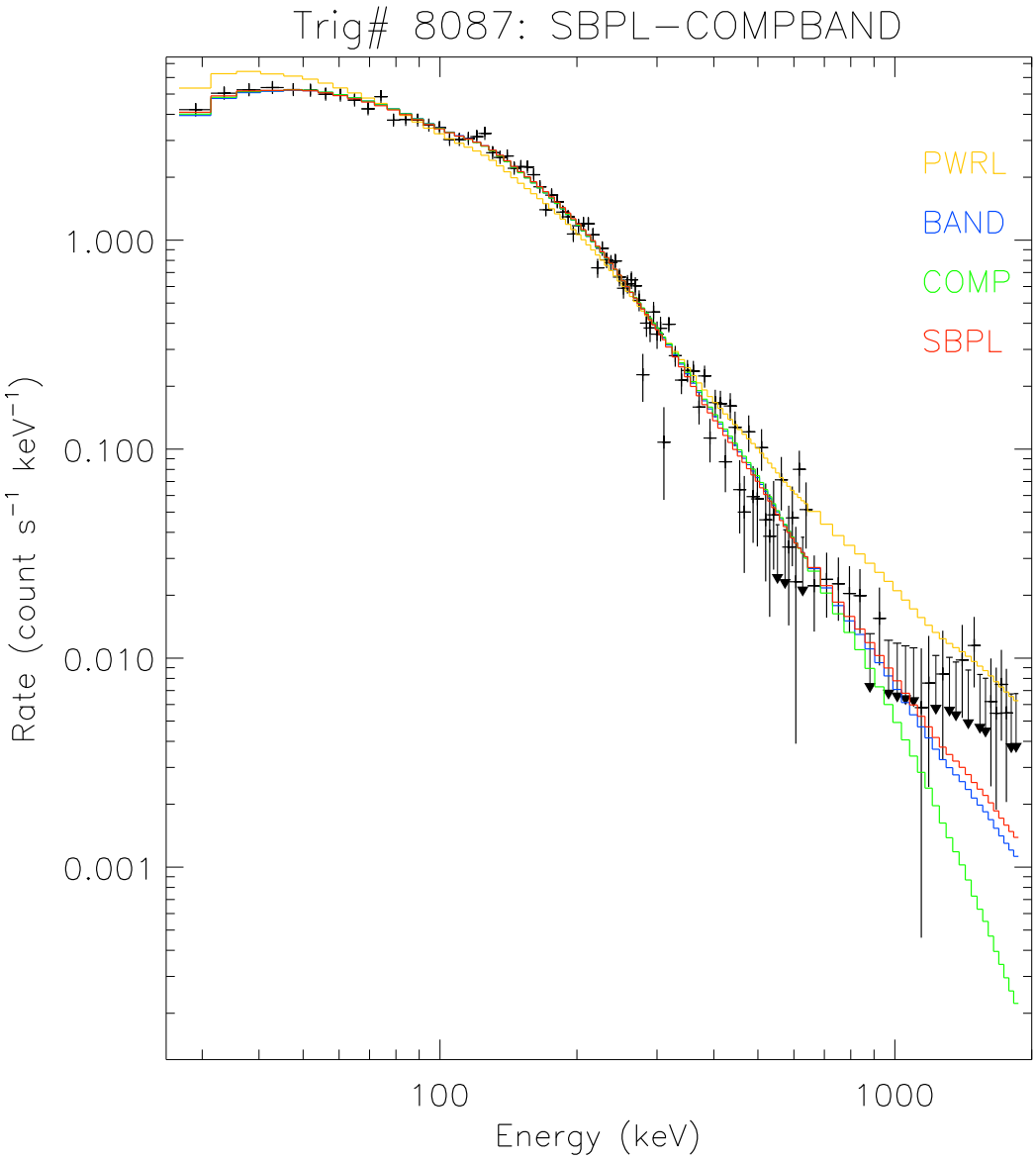

Figure 4.19 Count spectra of GRB 000429 (trigger number 8087). Data points are shown as crosses and the color lines are convolved model counts. COMP, BAND, and SBPL all fit statistically as good as each other. The BEST model determined by parameter constraints in this case is SBPL.

Table 4.8 Summary of time-integrated spectral fit results of 342 GRBs. 1σ uncertainties are shown in parentheses.

		Spectral Fit Parameters						
BATSE Trig #	BEST Model	A (ph s^{-1} cm^{-2})	$E_{\rm peak}$[1] (keV)	α, λ_1[2]	β, λ_2[3]	$E_{\rm b}$[4] (keV)	Λ	χ^2/dof
105	SBPL	0.0328 (0.0003)	130 (17)	–0.97 (0.08)	–2.96 (0.13)	126 (14)	0.40	125.0/112
109	COMP	0.0081 (0.0004)	523 (87)	–1.24 (0.06)	—	—	—	10.6/11
130	BAND	0.0110 (0.0015)	180 (23)	–1.23 (0.13)	–2.33 (0.22)	141 (31)	—	6.5/10
143	SBPL	0.0482 (0.0001)	586 (28)	–1.06 (0.01)	–2.22 (0.03)	420 (13)	0.20	190.6/112
219	SBPL	0.0198 (0.0001)	240 (12)	–1.23 (0.02)	–2.28 (0.03)	191 (8)	0.20	7.9/10
226	COMP	0.0037 (0.0003)	404 (63)	–1.05 (0.10)	—	—	—	8.8/11
249	SBPL	0.0355 (0.0001)	446 (22)	–1.06 (0.01)	–3.30 (0.07)	537 (21)	0.50	8.6/9
257	PWRL	0.0064 (0.0001)	—	–1.54 (0.01)	—	—	—	136.8/116
298	SBPL	0.0131 (0.0003)	389 (67)	–1.24 (0.04)	–2.40 (0.28)	387 (66)	0.01	10.6/9
351	COMP	0.0039 (0.0003)	174 (12)	–1.42 (0.08)	—	—	—	141.8/113
394	BAND	0.0172 (0.0005)	315 (13)	–0.91 (0.03)	–2.03 (0.04)	175 (9)	—	111.9/109
444	BAND	0.5183 (0.5078)	91 (13)	0.18 (0.65)	–2.11 (0.07)	60 (7)	—	124.1/114
451	BAND	0.0332 (0.0019)	143 (8)	–1.47 (0.05)	–2.41 (0.10)	139 (16)	—	106.6/113
543	COMP	0.0376 (0.0011)	263 (8)	–0.97 (0.03)	—	—	—	108.1/113
647	BAND	0.0499 (0.0021)	190 (3)	–0.19 (0.05)	–3.34 (0.17)	178 (9)	—	122.6/113
676	BAND	0.0071 (0.0008)	315 (36)	–0.52 (0.14)	–2.33 (0.25)	204 (35)	—	5.3/9
678	SBPL	0.0152 (0.0001)	—	–0.99 (0.01)	–1.85 (0.05)	580 (41)	0.20	124.3/112
761	SBPL	0.0063 (0.0000)	285 (25)	–1.24 (0.02)	–2.43 (0.10)	250 (17)	0.20	113.5/115
973	SBPL	0.0149 (0.0001)	251 (27)	–1.35 (0.03)	–2.08 (0.03)	156 (10)	0.20	128.7/108
999	BAND	0.0273 (0.0029)	265 (26)	–0.60 (0.11)	–1.95 (0.06)	140 (14)	—	126.0/113
1025	SBPL	0.0466 (0.0008)	131 (6)	–1.12 (0.05)	–2.59 (0.06)	125 (6)	0.10	120.1/112
1121	SBPL	0.0137 (0.0001)	250 (16)	–1.46 (0.01)	–2.13 (0.04)	213 (11)	0.10	145.6/112
1122	BAND	0.0455 (0.0016)	157 (3)	–0.93 (0.03)	–2.48 (0.04)	127 (4)	—	119.3/109
1156	COMP	0.0017 (0.0003)	383 (174)	–1.25 (0.24)	—	—	—	10.7/10
1157	BAND	0.0219 (0.0011)	203 (9)	–1.00 (0.05)	–2.21 (0.05)	135 (8)	—	101.2/109
1288	SBPL	0.0070 (0.0001)	233 (22)	–1.27 (0.04)	–2.31 (0.11)	211 (18)	0.10	4.2/9
1385	SBPL	0.0097 (0.0001)	417 (52)	–0.88 (0.02)	–3.57 (0.28)	488 (46)	0.40	141.2/112
1419	COMP	0.0048 (0.0002)	213 (17)	–1.65 (0.04)	—	—	—	8.5/10
1440	SBPL	0.0090 (0.0001)	248 (25)	–1.07 (0.03)	–2.57 (0.10)	209 (16)	0.30	111.5/110
1468	COMP	0.0034 (0.0001)	811 (54)	–0.55 (0.05)	—	—	—	106.0/113
1480	BAND	0.0090 (0.0029)	246 (66)	–0.50 (0.33)	–1.76 (0.09)	116 (29)	—	135.5/111
1484	SBPL	0.0358 (0.0004)	162 (9)	–1.50 (0.02)	–2.63 (0.08)	166 (9)	0.10	134.6/110
1503	SBPL	0.0170 (0.0002)	104 (8)	–1.54 (0.04)	–3.22 (0.14)	131 (9)	0.20	89.7/113
1519	PWRL	0.0071 (0.0001)	—	–1.64 (0.02)	—	—	—	94.8/110
1525	SBPL	0.0265 (0.0005)	536 (119)	–0.76 (0.06)	–2.44 (0.20)	375 (59)	0.30	12.7/9
1538	BAND	0.0408 (0.0024)	226 (15)	–1.07 (0.05)	–2.20 (0.07)	150 (13)	—	118.3/109
1541	SBPL	0.0125 (0.0001)	290 (27)	–1.25 (0.02)	–2.58 (0.09)	266 (20)	0.30	11.7/9
1553	SBPL	0.0371 (0.0005)	—	–0.88 (0.03)	–1.74 (0.04)	225 (16)	0.01	119.0/110
1571	COMP	0.0059 (0.0003)	297 (42)	–1.58 (0.06)	—	—	—	8.7/10
1601	COMP	0.0048 (0.0001)	872 (68)	–0.67 (0.05)	—	—	—	132.2/110
1606	SBPL	0.0115 (0.0001)	189 (30)	–1.41 (0.04)	–2.80 (0.19)	209 (28)	0.30	7.8/9
1609	BAND	0.0406 (0.0008)	262 (7)	–1.03 (0.02)	–2.51 (0.07)	213 (11)	—	12.4/9
1623	BAND	0.0055 (0.0002)	522 (47)	–0.87 (0.05)	–2.53 (0.39)	396 (97)	—	133.4/110
1625	SBPL	0.0326 (0.0001)	383 (15)	–1.07 (0.01)	–2.30 (0.03)	295 (9)	0.20	151.8/112
1652	BAND	0.0141 (0.0014)	129 (6)	–1.13 (0.09)	–2.73 (0.22)	131 (18)	—	6.1/9
1663	SBPL	0.0418 (0.0001)	409 (13)	–1.12 (0.01)	–2.30 (0.03)	319 (8)	0.20	225.9/112
1676	BAND	0.0173 (0.0005)	206 (7)	–1.25 (0.03)	–2.85 (0.22)	233 (32)	—	13.0/9
1695	BAND	0.0343 (0.0007)	421 (15)	–0.73 (0.03)	–2.38 (0.08)	286 (17)	—	9.1/9
1698	SBPL	0.0201 (0.0002)	182 (9)	–1.14 (0.02)	–2.55 (0.07)	164 (7)	0.20	124.5/112
1709	BAND	0.0545 (0.0017)	192 (5)	–1.09 (0.03)	–3.06 (0.23)	221 (26)	—	118.3/111
1711	SBPL	0.0307 (0.0002)	284 (20)	–1.14 (0.02)	–3.26 (0.19)	311 (19)	0.20	12.3/9
1712	SBPL	0.0048 (0.0001)	178 (13)	–1.37 (0.04)	–2.53 (0.10)	175 (12)	0.10	2.7/9
1721	SBPL	0.0215 (0.0003)	182 (27)	–1.61 (0.03)	–2.61 (0.17)	201 (27)	0.20	105.1/110
1733	SBPL	0.0066 (0.0001)	—	–1.23 (0.03)	–1.91 (0.10)	260 (37)	0.10	8.2/9
1872	SBPL	0.0109 (0.0001)	—	–0.97 (0.02)	–1.91 (0.04)	284 (16)	0.20	13.8/9
1886	SBPL	0.0285 (0.0002)	560 (47)	–0.43 (0.03)	–2.58 (0.06)	315 (18)	0.50	132.6/113
1982	SBPL	0.0052 (0.0002)	—	–0.88 (0.08)	–1.95 (0.09)	147 (15)	0.10	118.0/113
1989	COMP	0.0045 (0.0006)	99 (8)	–1.58 (0.11)	—	—	—	14.0/10
1997	BAND	0.0294 (0.0184)	66 (8)	–1.08 (0.37)	–2.06 (0.02)	48 (4)	—	116.1/112

Table 4.8 (continued)

BATSE	BEST	Spectral Fit Parameters						
Trig #	Model	A	$E_{\rm peak}$ [1]	α, λ_1 [2]	β, λ_2 [3]	$E_{\rm b}$ [4]	Λ	χ^2/dof
2061	COMP	0.0053 (0.0005)	294 (26)	–0.65 (0.13)	—	—	—	16.8/10
2080	BAND	0.0136 (0.0005)	303 (18)	–1.12 (0.04)	–2.39 (0.14)	231 (28)	—	90.0/112
2090	BAND	0.0113 (0.0007)	183 (9)	–1.05 (0.06)	–2.40 (0.10)	143 (12)	—	101.9/109
2110	BAND	0.0120 (0.0002)	459 (16)	–0.66 (0.03)	–3.00 (0.29)	415 (51)	—	20.7/9
2112	PWRL	0.0004 (0.0001)	—	–1.89 (0.62)	—	—	—	5.3/11
2122	COMP	0.0047 (0.0002)	393 (84)	–1.58 (0.06)	—	—	—	91.8/112
2127	SBPL	0.0123 (0.0001)	467 (72)	–1.29 (0.02)	–2.23 (0.11)	359 (38)	0.20	99.1/115
2138	SBPL	0.0091 (0.0001)	161 (13)	–1.65 (0.02)	–2.73 (0.10)	191 (14)	0.20	10.6/9
2151	COMP	0.0721 (0.0025)	534 (86)	–1.46 (0.06)	—	—	—	108.9/110
2156	SBPL	0.0129 (0.0001)	281 (33)	–1.45 (0.02)	–2.30 (0.06)	228 (21)	0.30	8.4/9
2193	BAND	0.0140 (0.0006)	282 (7)	0.47 (0.07)	–2.89 (0.15)	204 (10)	—	111.9/108
2228	BAND	0.0137 (0.0007)	204 (8)	–0.92 (0.05)	–2.45 (0.09)	156 (11)	—	140.5/111
2276	PWRL	0.0023 (0.0001)	—	–2.65 (0.07)	—	—	—	115.1/110
2286	COMP	0.0265 (0.0008)	299 (11)	–0.97 (0.04)	—	—	—	83.8/112
2287	COMP	0.0060 (0.0002)	331 (16)	–1.03 (0.04)	—	—	—	96.6/113
2316	BAND	0.0226 (0.0007)	157 (6)	–1.57 (0.03)	–2.57 (0.11)	195 (23)	—	108.6/108
2329	SBPL	0.0501 (0.0001)	—	–1.26 (0.00)	–1.79 (0.02)	331 (13)	0.20	30.7/9
2383	SBPL	0.0032 (0.0001)	—	–0.81 (0.05)	–1.81 (0.09)	272 (30)	0.10	106.5/111
2387	SBPL	0.0117 (0.0001)	135 (21)	0.07 (0.28)	–2.48 (0.06)	69 (9)	0.40	125.8/112
2389	SBPL	0.0131 (0.0001)	142 (11)	–1.19 (0.03)	–5.03 (0.39)	224 (15)	0.30	163.1/114
2431	BAND	0.1730 (0.0078)	199 (8)	–0.99 (0.04)	–2.19 (0.03)	131 (6)	—	16.5/8
2450	COMP	0.0091 (0.0004)	227 (9)	–1.11 (0.04)	—	—	—	4.3/10
2486	COMP	0.0082 (0.0003)	195 (7)	–1.28 (0.04)	—	—	—	75.1/115
2514	SBPL	0.0853 (0.0017)	208 (22)	–1.34 (0.04)	–2.76 (0.20)	212 (21)	0.10	106.1/111
2522	BAND	0.0112 (0.0023)	200 (11)	0.91 (0.23)	–2.00 (0.06)	112 (6)	—	122.0/111
2533	BAND	0.0269 (0.0003)	413 (8)	–0.87 (0.01)	–2.32 (0.04)	278 (9)	—	9.4/10
2537	BAND	0.1376 (0.0050)	94 (1)	–1.40 (0.03)	–2.88 (0.07)	129 (6)	—	115.1/110
2571	PWRL	0.0049 (0.0000)	—	–1.55 (0.01)	—	—	—	89.5/114
2606	COMP	0.0053 (0.0008)	281 (56)	–1.01 (0.18)	—	—	—	4.8/10
2611	SBPL	0.0552 (0.0004)	511 (73)	–1.21 (0.02)	–2.83 (0.20)	519 (59)	0.30	175.0/113
2617	BAND	0.0225 (0.0004)	458 (19)	–0.88 (0.03)	–2.62 (0.17)	369 (38)	—	164.8/111
2619	PWRL	0.0014 (0.0001)	—	–2.14 (0.07)	—	—	—	13.6/11
2661	BAND	0.1040 (0.0037)	177 (3)	–0.78 (0.04)	–2.80 (0.08)	160 (7)	—	128.6/109
2676	SBPL	0.0414 (0.0001)	310 (13)	–1.14 (0.01)	–2.86 (0.06)	311 (11)	0.30	33.8/9
2679	SBPL	0.0241 (0.0009)	792 (212)	–0.54 (0.05)	–2.13 (0.24)	599 (94)	0.10	127.8/114
2700	SBPL	0.0044 (0.0001)	177 (26)	–1.23 (0.07)	–2.72 (0.21)	175 (22)	0.20	92.7/110
2703	SBPL	0.0039 (0.0000)	282 (29)	–1.36 (0.02)	–2.53 (0.18)	276 (26)	0.10	114.0/114
2770	PWRL	0.0024 (0.0000)	—	–1.45 (0.02)	—	—	—	117.7/115
2790	SBPL	0.0081 (0.0001)	188 (8)	–1.59 (0.02)	–2.60 (0.08)	189 (8)	0.01	135.7/114
2797	SBPL	0.0330 (0.0003)	255 (26)	–1.00 (0.03)	–2.57 (0.11)	210 (17)	0.30	97.6/110
2798	SBPL	0.0269 (0.0001)	379 (31)	–1.13 (0.02)	–2.25 (0.04)	245 (13)	0.30	26.7/9
2812	BAND	0.0175 (0.0005)	242 (8)	–1.10 (0.03)	–3.03 (0.35)	273 (49)	—	94.9/111
2831	SBPL	0.0178 (0.0000)	503 (24)	–1.29 (0.00)	–2.21 (0.03)	382 (14)	0.20	49.9/9
2833	SBPL	0.0331 (0.0002)	211 (9)	–1.53 (0.01)	–2.35 (0.04)	203 (8)	0.10	118.9/114
2852	SBPL	0.0171 (0.0001)	307 (25)	–1.05 (0.02)	–3.14 (0.16)	327 (21)	0.30	126.9/112
2855	SBPL	0.0184 (0.0001)	360 (19)	–0.61 (0.03)	–2.43 (0.05)	241 (9)	0.30	159.1/114
2856	SBPL	0.0182 (0.0001)	299 (30)	–1.24 (0.02)	–2.32 (0.09)	245 (19)	0.20	19.4/10
2863	SBPL	0.0058 (0.0001)	243 (46)	–1.05 (0.06)	–2.49 (0.25)	208 (31)	0.20	6.8/10
2889	SBPL	0.0055 (0.0001)	218 (13)	–0.93 (0.04)	–2.11 (0.08)	212 (12)	0.01	117.4/113
2890	SBPL	0.0040 (0.0001)	—	–1.09 (0.03)	–2.00 (0.11)	414 (48)	0.01	118.4/111
2891	COMP	0.0090 (0.0001)	1116 (60)	–0.94 (0.02)	—	—	—	148.8/115
2895	BAND	0.0512 (0.0027)	225 (10)	–0.75 (0.05)	–2.50 (0.12)	170 (13)	—	111.0/112
2919	BAND	0.0167 (0.0009)	359 (53)	–1.32 (0.05)	–2.09 (0.13)	216 (45)	—	97.4/111
2929	SBPL	0.0105 (0.0001)	—	–1.14 (0.01)	–1.98 (0.04)	280 (16)	0.20	131.3/114
2940	BAND	0.0099 (0.0002)	432 (21)	–1.10 (0.02)	–2.75 (0.30)	409 (76)	—	12.3/10
2984	SBPL	0.0069 (0.0001)	—	–1.19 (0.02)	–1.89 (0.07)	294 (39)	0.20	145.9/114
2993	COMP	0.0057 (0.0001)	2036 (219)	–1.02 (0.02)	—	—	—	103.9/111
2994	COMP	0.0116 (0.0001)	1099 (55)	–1.13 (0.01)	—	—	—	112.6/112
3002	COMP	0.0079 (0.0004)	205 (11)	–1.28 (0.06)	—	—	—	8.8/10
3003	SBPL	0.0084 (0.0001)	—	–1.29 (0.02)	–1.93 (0.05)	231 (19)	0.10	84.1/114
3035	COMP	0.0109 (0.0003)	263 (12)	–1.30 (0.03)	—	—	—	10.7/9

Table 4.8 (continued)

BATSE	BEST	Spectral Fit Parameters						
Trig #	Model	A	$E_{\rm peak}$ [1]	α, λ_1 [2]	β, λ_2 [3]	$E_{\rm b}$ [4]	Λ	χ^2/dof
3042	BAND	0.0112 (0.0004)	250 (11)	–1.07 (0.03)	–2.47 (0.13)	200 (20)	—	105.9/111
3044	PWRL	0.0018 (0.0001)	—	–2.20 (0.14)	—	—	—	125.8/114
3057	SBPL	0.0366 (0.0001)	620 (35)	–1.08 (0.01)	–2.39 (0.04)	417 (15)	0.40	87.3/9
3067	BAND	0.0493 (0.0010)	388 (18)	–1.15 (0.02)	–2.32 (0.08)	279 (22)	—	131.5/112
3071	COMP	0.0043 (0.0006)	241 (35)	–1.17 (0.15)	—	—	—	7.1/10
3087	BAND	0.2097 (0.0431)	182 (20)	–0.59 (0.19)	–2.22 (0.10)	118 (13)	—	139.3/114
3110	COMP	0.0098 (0.0003)	567 (22)	–0.08 (0.06)	—	—	—	114.0/115
3115	SBPL	0.0092 (0.0001)	255 (20)	–0.97 (0.03)	–2.29 (0.07)	190 (11)	0.20	102.3/109
3128	BAND	0.0249 (0.0005)	363 (9)	–0.54 (0.03)	–2.32 (0.05)	234 (9)	—	157.0/112
3138	COMP	0.0215 (0.0007)	177 (5)	–1.38 (0.04)	—	—	—	126.6/112
3152	SBPL	0.0089 (0.0002)	—	–0.99 (0.04)	–1.79 (0.16)	490 (110)	0.01	138.7/114
3178	SBPL	0.0096 (0.0001)	—	–1.23 (0.01)	–1.99 (0.05)	298 (21)	0.20	131.0/114
3227	SBPL	0.0094 (0.0001)	257 (20)	–1.33 (0.02)	–2.30 (0.06)	213 (13)	0.20	5.8/9
3245	SBPL	0.0247 (0.0001)	291 (8)	–1.07 (0.01)	–2.30 (0.02)	225 (5)	0.20	37.2/9
3247	COMP	0.0020 (0.0002)	358 (53)	–0.75 (0.14)	—	—	—	6.5/10
3253	SBPL	0.0258 (0.0001)	213 (14)	–1.31 (0.01)	–3.39 (0.11)	294 (15)	0.40	23.4/9
3255	COMP	0.0124 (0.0002)	5 (2)	–1.99 (0.00)	—	—	—	108.4/112
3287	SBPL	0.0084 (0.0001)	168 (16)	–1.46 (0.04)	–2.48 (0.12)	165 (15)	0.10	114.5/113
3290	SBPL	0.0085 (0.0001)	127 (18)	–1.77 (0.03)	–2.80 (0.18)	169 (21)	0.20	99.4/115
3298	SBPL	0.0083 (0.0002)	246 (45)	–1.33 (0.06)	–2.47 (0.36)	245 (45)	0.01	7.2/9
3301	BAND	0.0076 (0.0004)	427 (48)	–0.85 (0.06)	–1.98 (0.11)	222 (31)	—	126.7/113
3330	SBPL	0.0040 (0.0001)	536 (281)	–1.00 (0.04)	–2.05 (0.11)	271 (32)	0.20	95.9/109
3345	SBPL	0.0205 (0.0003)	166 (16)	–1.46 (0.03)	–2.16 (0.06)	145 (12)	0.10	104.7/111
3352	BAND	0.0175 (0.0009)	143 (4)	–1.14 (0.05)	–2.57 (0.09)	132 (8)	—	105.6/111
3360	BAND	0.0031 (0.0003)	565 (176)	–1.00 (0.09)	–1.55 (0.06)	169 (53)	—	119.0/111
3408	BAND	0.0298 (0.0003)	308 (5)	–1.04 (0.01)	–2.70 (0.08)	279 (14)	—	2.7/9
3410	COMP	0.0662 (0.0204)	120 (9)	–0.78 (0.29)	—	—	—	122.4/112
3412	PWRL	0.0155 (0.0005)	—	–2.13 (0.06)	—	—	—	115.5/112
3415	SBPL	0.0097 (0.0001)	168 (27)	–1.51 (0.04)	–2.81 (0.19)	199 (28)	0.30	109.6/112
3448	PWRL	0.0014 (0.0001)	—	–1.71 (0.05)	—	—	—	14.4/11
3458	BAND	0.0344 (0.0008)	257 (5)	–0.49 (0.03)	–2.62 (0.06)	193 (6)	—	13.1/8
3464	COMP	0.0062 (0.0003)	321 (27)	–1.14 (0.06)	—	—	—	144.2/110
3480	BAND	0.0293 (0.0010)	341 (14)	–0.56 (0.04)	–2.64 (0.16)	258 (21)	—	102.2/109
3481	BAND	0.0146 (0.0005)	347 (24)	–1.08 (0.04)	–2.07 (0.07)	200 (19)	—	131.7/112
3489	BAND	0.0308 (0.0008)	314 (9)	–0.70 (0.04)	–3.33 (0.34)	329 (42)	—	127.8/111
3491	SBPL	0.0451 (0.0002)	186 (9)	–1.65 (0.01)	–2.31 (0.03)	180 (8)	0.20	228.6/109
3492	SBPL	0.0207 (0.0001)	373 (63)	–1.50 (0.01)	–2.75 (0.18)	453 (59)	0.40	249.3/112
3523	SBPL	0.0301 (0.0001)	—	–0.97 (0.01)	–1.85 (0.02)	345 (12)	0.20	125.0/113
3537	SBPL	0.0092 (0.0001)	220 (20)	–1.75 (0.01)	–2.32 (0.08)	227 (20)	0.10	136.7/113
3567	PWRL	0.0003 (0.0001)	—	–0.95 (0.20)	—	—	—	12.6/11
3571	COMP	0.0129 (0.0003)	307 (11)	–1.11 (0.03)	—	—	—	136.9/113
3593	COMP	0.0063 (0.0001)	1243 (114)	–1.16 (0.02)	—	—	—	163.9/114
3634	BAND	0.0048 (0.0008)	229 (26)	–0.55 (0.17)	–2.25 (0.19)	146 (21)	—	133.1/110
3657	SBPL	0.0110 (0.0001)	279 (51)	–1.26 (0.04)	–2.55 (0.18)	252 (36)	0.30	91.0/113
3658	BAND	0.0536 (0.0019)	221 (6)	–0.66 (0.03)	–2.31 (0.05)	148 (5)	—	134.7/114
3662	SBPL	0.0045 (0.0001)	—	–1.23 (0.03)	–1.68 (0.05)	170 (20)	0.01	85.7/113
3663	COMP	0.0018 (0.0001)	505 (158)	–1.51 (0.07)	—	—	—	122.7/111
3734	SBPL	0.0915 (0.0005)	339 (30)	–0.84 (0.02)	–4.04 (0.25)	440 (31)	0.40	137.5/110
3736	COMP	0.0102 (0.0004)	920 (159)	–0.89 (0.08)	—	—	—	10.3/10
3765	BAND	0.0158 (0.0005)	220 (6)	–0.97 (0.03)	–2.58 (0.10)	185 (12)	—	85.4/111
3767	COMP	0.0465 (0.0006)	459 (13)	–1.00 (0.02)	—	—	—	148.3/109
3788	BAND	0.0334 (0.0020)	175 (5)	–0.48 (0.06)	–2.24 (0.04)	114 (4)	—	118.3/109
3860	BAND	0.0108 (0.0002)	535 (24)	–0.57 (0.03)	–2.33 (0.11)	341 (26)	—	132.6/112
3870	BAND	0.0242 (0.0033)	118 (19)	–1.61 (0.10)	–2.03 (0.03)	76 (11)	—	168.3/112
3891	BAND	0.0129 (0.0025)	145 (13)	–0.69 (0.16)	–2.05 (0.06)	88 (8)	—	133.6/112
3917	BAND	0.0061 (0.0008)	393 (82)	–0.69 (0.17)	–2.45 (0.66)	276 (114)	—	102.5/111
3918	BAND	0.0090 (0.0009)	319 (38)	–0.52 (0.12)	–1.80 (0.07)	150 (18)	—	103.8/111
3929	SBPL	0.0118 (0.0001)	351 (50)	–1.39 (0.02)	–2.48 (0.16)	332 (39)	0.20	105.0/114
3930	SBPL	0.0137 (0.0001)	430 (28)	–1.16 (0.01)	–2.48 (0.08)	377 (19)	0.20	201.6/113
3937	COMP	0.0096 (0.0011)	164 (7)	–0.72 (0.11)	—	—	—	108.7/114
3954	BAND	0.0231 (0.0014)	262 (24)	–1.06 (0.06)	–1.91 (0.04)	131 (12)	—	136.7/113

Table 4.8 (continued)

BATSE	BEST	Spectral Fit Parameters						
Trig #	Model	A	$E_{\rm peak}$ [1]	α, λ_1 [2]	β, λ_2 [3]	$E_{\rm b}$ [4]	Λ	χ^2/dof
4039	COMP	0.0071 (0.0001)	1316 (119)	–1.12 (0.02)	—	—	—	157.1/112
4368	SBPL	0.0700 (0.0003)	112 (20)	–0.77 (0.19)	–2.48 (0.03)	66 (9)	0.50	30.0/10
4556	BAND	0.0719 (0.0023)	235 (7)	–0.85 (0.03)	–2.26 (0.05)	157 (7)	—	152.2/113
4701	COMP	0.0121 (0.0004)	232 (6)	–1.00 (0.04)	—	—	—	128.5/112
4898	BAND	1.0609 (0.2503)	58 (1)	–0.62 (0.17)	–3.31 (0.06)	69 (4)	—	140.8/110
5299	SBPL	0.0395 (0.0001)	142 (4)	–1.93 (0.01)	–2.89 (0.05)	189 (5)	0.10	61.3/9
5304	BAND	0.0611 (0.0009)	285 (4)	–0.63 (0.02)	–2.41 (0.03)	198 (5)	—	8.2/9
5470	BAND	0.0149 (0.0006)	940 (159)	–0.65 (0.07)	–1.72 (0.11)	384 (75)	—	94.6/112
5473	COMP	0.0048 (0.0003)	354 (32)	–0.98 (0.07)	—	—	—	103.4/113
5477	SBPL	0.0094 (0.0001)	—	–1.11 (0.01)	–1.65 (0.10)	696 (132)	0.01	144.0/110
5486	BAND	0.0177 (0.0026)	184 (27)	–0.96 (0.11)	–1.67 (0.01)	76 (10)	—	221.3/112
5489	SBPL	0.0083 (0.0001)	219 (19)	–1.31 (0.02)	–2.34 (0.08)	186 (13)	0.20	106.2/110
5512	SBPL	0.0092 (0.0001)	174 (11)	–1.30 (0.03)	–2.08 (0.06)	170 (11)	0.01	82.3/113
5526	COMP	0.0044 (0.0002)	270 (19)	–1.32 (0.04)	—	—	—	147.5/112
5563	BAND	0.0763 (0.0061)	171 (9)	–1.00 (0.07)	–2.36 (0.08)	129 (9)	—	120.6/112
5567	SBPL	0.0233 (0.0001)	268 (14)	–1.50 (0.01)	–2.38 (0.06)	260 (12)	0.10	198.5/114
5568	BAND	0.0391 (0.0012)	527 (32)	–0.51 (0.05)	–2.33 (0.13)	335 (30)	—	118.3/111
5585	PWRL	0.0012 (0.0001)	—	–1.83 (0.15)	—	—	—	8.3/11
5591	COMP	0.0065 (0.0005)	435 (122)	–1.40 (0.11)	—	—	—	11.1/10
5606	BAND	0.0036 (0.0008)	203 (48)	–1.15 (0.19)	–2.13 (0.23)	130 (39)	—	5.2/9
5609	SBPL	0.0163 (0.0001)	145 (14)	–1.43 (0.03)	–2.96 (0.13)	173 (14)	0.30	137.2/112
5621	BAND	0.0794 (0.0056)	213 (13)	–0.90 (0.07)	–2.06 (0.04)	125 (8)	—	120.9/112
5624	BAND	0.0118 (0.0025)	227 (32)	–0.31 (0.21)	–1.88 (0.09)	118 (16)	—	116.9/112
5629	BAND	0.0325 (0.0010)	232 (6)	–0.88 (0.03)	–3.00 (0.24)	233 (26)	—	150.3/112
5632	COMP	0.0031 (0.0001)	1205 (243)	–1.04 (0.06)	—	—	—	122.1/113
5649	SBPL	0.0419 (0.0001)	220 (15)	–1.48 (0.01)	–2.80 (0.06)	268 (15)	0.40	52.3/9
5654	SBPL	0.0175 (0.0001)	242 (11)	–0.70 (0.02)	–2.47 (0.04)	171 (6)	0.30	180.2/113
5697	BAND	0.4029 (0.0664)	54 (2)	–0.97 (0.12)	–3.60 (0.12)	82 (6)	—	158.0/111
5701	SBPL	0.0169 (0.0002)	—	–0.99 (0.02)	–1.79 (0.07)	426 (55)	0.20	129.4/113
5704	BAND	0.0705 (0.0047)	151 (7)	–1.29 (0.06)	–2.57 (0.14)	149 (17)	—	118.4/113
5711	SBPL	0.0399 (0.0003)	—	–1.22 (0.02)	–1.89 (0.05)	247 (19)	0.10	109.9/112
5731	SBPL	0.0058 (0.0001)	171 (58)	–1.69 (0.05)	–2.05 (0.10)	139 (34)	0.10	113.5/109
5773	SBPL	0.0488 (0.0002)	177 (6)	–0.87 (0.01)	–4.37 (0.13)	228 (6)	0.30	146.9/113
5989	SBPL	0.0114 (0.0001)	—	–2.75 (0.02)	–2.47 (0.20)	191 (106)	0.30	233.8/110
5995	SBPL	0.0298 (0.0001)	755 (80)	–0.79 (0.01)	–2.39 (0.06)	391 (24)	0.50	210.0/111
6100	BAND	0.0208 (0.0003)	560 (32)	–1.06 (0.02)	–2.32 (0.14)	389 (48)	—	101.5/111
6115	COMP	0.0048 (0.0001)	487 (22)	–0.75 (0.03)	—	—	—	88.6/113
6124	BAND	0.0673 (0.0006)	402 (7)	–0.89 (0.01)	–2.70 (0.09)	340 (17)	—	16.5/8
6157	SBPL	0.0224 (0.0002)	321 (25)	–1.18 (0.02)	–2.42 (0.08)	275 (17)	0.20	125.2/114
6168	SBPL	0.0129 (0.0001)	—	–1.24 (0.02)	–1.71 (0.02)	172 (10)	0.01	8.3/8
6198	BAND	0.1037 (0.0012)	338 (8)	–1.20 (0.01)	–2.48 (0.06)	282 (14)	—	158.6/111
6235	SBPL	0.0506 (0.0005)	321 (33)	–0.98 (0.03)	–3.01 (0.18)	320 (27)	0.30	121.1/113
6240	COMP	0.0048 (0.0005)	365 (71)	–1.15 (0.12)	—	—	—	97.1/111
6249	SBPL	0.0029 (0.0000)	223 (25)	–1.36 (0.03)	–2.13 (0.13)	218 (24)	0.01	96.6/115
6266	SBPL	0.0072 (0.0001)	280 (24)	–1.04 (0.02)	–2.57 (0.13)	249 (16)	0.20	100.4/113
6274	BAND	0.0097 (0.0012)	126 (10)	–1.34 (0.10)	–2.35 (0.12)	109 (15)	—	93.9/110
6293	PWRL	0.1817 (0.0026)	—	–1.25 (0.01)	—	—	—	137.2/115
6329	SBPL	0.0140 (0.0001)	202 (19)	–1.27 (0.02)	–2.70 (0.11)	199 (15)	0.30	93.8/113
6336	BAND	0.0196 (0.0004)	805 (89)	–1.03 (0.03)	–2.03 (0.15)	429 (77)	—	223.9/111
6349	SBPL	0.0035 (0.0001)	—	–1.35 (0.05)	–1.84 (0.06)	150 (20)	0.01	99.9/112
6350	BAND	0.0185 (0.0004)	325 (10)	–0.70 (0.03)	–2.26 (0.06)	207 (10)	—	150.7/113
6353	SBPL	0.0068 (0.0001)	135 (11)	–1.72 (0.02)	–2.12 (0.04)	134 (10)	0.01	104.6/113
6380	SBPL	0.0042 (0.0001)	226 (33)	–1.35 (0.03)	–2.15 (0.12)	190 (22)	0.10	108.2/110
6389	BAND	0.0236 (0.0018)	203 (17)	–1.12 (0.07)	–2.06 (0.06)	120 (12)	—	16.5/9
6390	SBPL	0.0036 (0.0001)	—	–0.68 (0.06)	–1.31 (0.07)	330 (68)	0.01	119.4/110
6397	BAND	0.0246 (0.0013)	186 (6)	–0.73 (0.05)	–2.54 (0.12)	145 (10)	—	132.1/111
6404	SBPL	0.0103 (0.0002)	150 (14)	–1.50 (0.04)	–2.59 (0.14)	153 (13)	0.10	103.3/111
6414	SBPL	0.0070 (0.0001)	171 (21)	–1.42 (0.03)	–2.11 (0.08)	141 (13)	0.10	123.0/109
6453	BAND	0.0223 (0.0013)	102 (2)	–1.26 (0.05)	–2.62 (0.07)	107 (6)	—	147.7/110
6454	COMP	0.0020 (0.0003)	381 (153)	–1.33 (0.16)	—	—	—	7.1/10
6472	BAND	0.0146 (0.0004)	298 (13)	–0.92 (0.03)	–2.21 (0.07)	191 (12)	—	15.2/9

Table 4.8 (continued)

BATSE	BEST	Spectral Fit Parameters						
Trig #	Model	A	$E_{\rm peak}$ [1]	α, λ_1 [2]	β, λ_2 [3]	$E_{\rm b}$ [4]	Λ	χ^2/dof
6476	PWRL	0.0037 (0.0000)	—	–1.47 (0.01)	—	—	—	124.6/117
6525	SBPL	0.0091 (0.0001)	183 (13)	–1.07 (0.03)	–2.42 (0.13)	168 (10)	0.10	94.6/110
6526	COMP	0.0097 (0.0030)	128 (17)	–1.22 (0.29)	—	—	—	3.4/10
6539	COMP	0.0049 (0.0001)	2039 (251)	–0.58 (0.05)	—	—	—	103.2/112
6560	BAND	0.0211 (0.0011)	177 (5)	–0.61 (0.05)	–2.90 (0.21)	158 (14)	—	130.8/111
6570	BAND	0.0190 (0.0053)	89 (6)	–1.10 (0.19)	–2.20 (0.04)	67 (5)	—	108.7/112
6576	BAND	0.0152 (0.0003)	602 (56)	–1.28 (0.03)	–2.31 (0.22)	444 (100)	—	130.6/111
6581	SBPL	0.0077 (0.0001)	193 (15)	–1.57 (0.02)	–2.12 (0.07)	190 (15)	0.01	116.5/114
6587	BAND	0.0828 (0.0009)	311 (5)	–0.90 (0.01)	–2.38 (0.03)	222 (6)	—	232.0/110
6593	SBPL	0.0202 (0.0001)	218 (13)	–1.23 (0.02)	–2.30 (0.05)	176 (8)	0.20	129.9/110
6609	BAND	0.0161 (0.0017)	204 (17)	–0.71 (0.09)	–1.90 (0.05)	107 (9)	—	109.3/112
6615	BAND	0.0061 (0.0004)	336 (25)	–0.51 (0.07)	–2.26 (0.20)	209 (27)	—	97.4/112
6617	SBPL	0.1325 (0.0013)	259 (32)	–1.13 (0.02)	–3.46 (0.31)	309 (31)	0.30	117.7/114
6618	SBPL	0.0053 (0.0001)	315 (47)	–1.10 (0.03)	–2.20 (0.11)	224 (20)	0.20	104.1/113
6629	SBPL	0.0028 (0.0000)	239 (34)	–1.39 (0.03)	–2.14 (0.10)	202 (23)	0.10	79.0/114
6630	COMP	0.0193 (0.0005)	270 (13)	–1.45 (0.03)	—	—	—	159.6/110
6642	COMP	0.0043 (0.0002)	289 (14)	–0.57 (0.07)	—	—	—	81.9/112
6665	SBPL	0.0413 (0.0002)	224 (7)	–1.21 (0.01)	–2.33 (0.03)	183 (5)	0.20	164.9/114
6668	SBPL	0.0166 (0.0010)	—	–1.22 (0.14)	–1.98 (0.19)	149 (37)	0.01	123.0/112
6694	BAND	0.0043 (0.0002)	422 (30)	–0.23 (0.08)	–2.31 (0.19)	261 (29)	—	112.6/113
6744	BAND	0.1301 (0.0156)	119 (4)	–0.80 (0.10)	–2.64 (0.10)	104 (6)	—	116.4/113
6763	BAND	0.0175 (0.0048)	122 (15)	–0.86 (0.20)	–2.00 (0.05)	73 (8)	—	102.8/112
6891	COMP	0.0050 (0.0003)	434 (99)	–1.38 (0.08)	—	—	—	105.9/110
6892	COMP	0.0028 (0.0002)	308 (41)	–1.22 (0.08)	—	—	—	71.2/112
6904	SBPL	0.0076 (0.0001)	939 (180)	–0.99 (0.02)	–2.08 (0.29)	912 (171)	0.01	122.2/112
6944	BAND	0.0340 (0.0030)	105 (2)	–0.87 (0.07)	–2.71 (0.07)	98 (4)	—	136.9/111
6963	BAND	0.0527 (0.0012)	214 (3)	–0.64 (0.02)	–2.79 (0.08)	182 (7)	—	43.9/9
6985	SBPL	0.0359 (0.0001)	340 (25)	–1.00 (0.01)	–2.67 (0.07)	284 (15)	0.40	216.1/109
7012	SBPL	0.0196 (0.0001)	255 (16)	–1.40 (0.01)	–2.50 (0.08)	245 (13)	0.20	144.8/114
7028	BAND	0.0620 (0.0100)	223 (20)	–0.25 (0.18)	–2.08 (0.07)	129 (11)	—	103.0/111
7113	SBPL	0.0693 (0.0001)	339 (7)	–0.93 (0.00)	–2.74 (0.03)	298 (4)	0.30	123.7/8
7170	COMP	0.0061 (0.0001)	1861 (279)	–1.23 (0.02)	—	—	—	73.6/111
7236	COMP	0.0056 (0.0003)	239 (13)	–0.94 (0.06)	—	—	—	88.2/110
7240	BAND	0.0150 (0.0007)	649 (73)	–0.54 (0.07)	–2.26 (0.29)	395 (77)	—	114.6/111
7247	SBPL	0.0045 (0.0000)	—	–1.07 (0.03)	–1.52 (0.02)	186 (15)	0.01	113.4/110
7248	SBPL	0.0081 (0.0001)	382 (204)	–0.95 (0.13)	–2.14 (0.11)	120 (32)	0.50	175.5/112
7270	PWRL	0.0009 (0.0000)	—	–1.50 (0.04)	—	—	—	86.2/113
7277	BAND	0.0541 (0.0095)	113 (4)	–0.64 (0.14)	–2.45 (0.05)	88 (4)	—	119.7/112
7281	BAND	0.2143 (0.0345)	140 (6)	–0.23 (0.14)	–2.54 (0.10)	103 (6)	—	125.2/113
7285	COMP	0.0053 (0.0008)	107 (7)	–1.42 (0.13)	—	—	—	142.4/113
7295	COMP	0.0108 (0.0007)	330 (19)	–0.32 (0.09)	—	—	—	118.4/111
7301	SBPL	0.0208 (0.0001)	386 (33)	–1.40 (0.01)	–2.21 (0.06)	303 (18)	0.20	12.0/8
7310	COMP	0.0065 (0.0002)	319 (15)	–0.79 (0.04)	—	—	—	89.0/111
7318	COMP	0.0127 (0.0002)	694 (30)	–0.62 (0.03)	—	—	—	118.2/113
7343	SBPL	0.0275 (0.0000)	444 (9)	–0.98 (0.00)	–2.29 (0.02)	331 (4)	0.20	173.8/8
7360	COMP	0.0147 (0.0005)	259 (11)	–1.13 (0.04)	—	—	—	8.1/9
7446	BAND	0.0338 (0.0027)	178 (17)	–1.46 (0.08)	–2.67 (0.42)	214 (74)	—	103.1/114
7457	COMP	0.0041 (0.0004)	737 (332)	–1.07 (0.15)	—	—	—	97.4/112
7464	SBPL	0.0089 (0.0001)	326 (26)	–1.09 (0.02)	–2.50 (0.11)	284 (18)	0.20	130.1/110
7475	BAND	0.0242 (0.0012)	138 (5)	–1.31 (0.04)	–2.36 (0.06)	118 (8)	—	209.6/112
7477	SBPL	0.0079 (0.0001)	216 (20)	–1.26 (0.03)	–2.11 (0.06)	174 (12)	0.10	118.8/112
7491	BAND	0.0511 (0.0003)	442 (7)	–0.91 (0.01)	–2.36 (0.04)	306 (9)	—	14.8/9
7503	SBPL	0.0055 (0.0001)	154 (22)	–1.73 (0.03)	–2.36 (0.12)	159 (22)	0.10	80.3/112
7515	BAND	0.0209 (0.0028)	187 (12)	–0.32 (0.12)	–2.20 (0.08)	117 (8)	—	117.0/110
7527	BAND	0.0448 (0.0011)	316 (8)	–0.44 (0.03)	–2.51 (0.09)	222 (10)	—	174.7/110
7530	BAND	0.2131 (0.0215)	147 (4)	–0.17 (0.09)	–2.73 (0.12)	115 (6)	—	111.0/112
7549	BAND	0.0262 (0.0005)	269 (8)	–1.07 (0.02)	–2.08 (0.03)	159 (6)	—	26.6/8
7560	BAND	0.0127 (0.0009)	136 (6)	–1.24 (0.05)	–2.41 (0.09)	117 (10)	—	124.2/113
7569	PWRL	0.0040 (0.0001)	—	–1.65 (0.02)	—	—	—	108.2/113
7575	COMP	0.0109 (0.0003)	478 (33)	–0.83 (0.04)	—	—	—	17.7/10
7578	SBPL	0.0112 (0.0002)	215 (45)	–1.31 (0.05)	–2.57 (0.20)	202 (34)	0.30	129.6/112

Table 4.8 (continued)

BATSE	BEST	Spectral Fit Parameters						
Trig #	Model	A	$E_{\rm peak}$ [1]	α, λ_1 [2]	β, λ_2 [3]	$E_{\rm b}$ [4]	Λ	χ^2/dof
7586	BAND	0.0162 (0.0029)	195 (20)	–0.52 (0.17)	–2.24 (0.16)	126 (16)	—	4.7/9
7592	SBPL	0.0197 (0.0002)	183 (10)	–1.38 (0.02)	–2.19 (0.04)	159 (8)	0.10	131.3/112
7610	COMP	0.0121 (0.0016)	185 (17)	–1.06 (0.13)	—	—	—	95.0/112
7647	COMP	0.0030 (0.0001)	2559(1056)	–1.33 (0.05)	—	—	—	106.0/110
7660	COMP	0.0038 (0.0002)	498 (53)	–0.99 (0.06)	—	—	—	111.2/112
7678	SBPL	0.0224 (0.0001)	285 (14)	–1.04 (0.02)	–2.33 (0.04)	222 (9)	0.20	130.6/111
7688	SBPL	0.0039 (0.0001)	207 (37)	–1.13 (0.07)	–2.22 (0.20)	177 (25)	0.10	4.4/9
7695	SBPL	0.0218 (0.0001)	725 (95)	–0.90 (0.01)	–4.17 (0.41)	991 (96)	0.40	16.3/8
7703	COMP	0.0082 (0.0012)	231 (38)	–1.15 (0.15)	—	—	—	115.4/114
7760	SBPL	0.0129 (0.0001)	149 (28)	–0.48 (0.19)	–2.39 (0.06)	68 (10)	0.50	188.7/111
7766	SBPL	0.0114 (0.0001)	—	–0.83 (0.02)	–1.87 (0.16)	591 (104)	0.20	129.4/114
7788	BAND	0.0123 (0.0019)	127 (9)	–0.85 (0.11)	–2.03 (0.04)	78 (5)	—	122.1/113
7794	BAND	0.0055 (0.0004)	220 (27)	–1.28 (0.07)	–2.25 (0.20)	161 (36)	—	102.4/110
7810	BAND	0.0091 (0.0003)	622 (47)	–0.35 (0.07)	–2.76 (0.49)	467 (99)	—	12.8/9
7854	SBPL	0.0086 (0.0001)	150 (9)	–1.36 (0.02)	–2.95 (0.12)	165 (8)	0.20	124.6/112
7868	BAND	0.0134 (0.0013)	144 (5)	–0.50 (0.08)	–2.52 (0.09)	110 (6)	—	99.5/112
7884	COMP	0.0063 (0.0003)	636 (129)	–1.23 (0.06)	—	—	—	105.0/112
7898	BAND	0.0541 (0.0037)	246 (18)	–0.86 (0.06)	–2.09 (0.07)	145 (12)	—	128.1/112
7906	BAND	0.0917 (0.0007)	394 (7)	–1.12 (0.01)	–2.30 (0.03)	278 (8)	—	443.2/112
7925	SBPL	0.0069 (0.0001)	—	–1.05 (0.02)	–1.51 (0.04)	298 (36)	0.01	94.9/111
7929	SBPL	0.0082 (0.0000)	343 (22)	–1.36 (0.01)	–2.10 (0.06)	336 (22)	0.01	117.3/112
7932	BAND	0.0148 (0.0020)	135 (9)	–1.13 (0.12)	–2.51 (0.14)	120 (14)	—	141.5/109
7938	COMP	0.0070 (0.0009)	145 (8)	–1.07 (0.13)	—	—	—	129.2/114
7941	PWRL	0.0074 (0.0001)	—	–1.43 (0.01)	—	—	—	63.3/115
7948	COMP	0.0095 (0.0023)	68 (4)	–1.07 (0.18)	—	—	—	93.7/111
7954	BAND	0.0671 (0.0014)	220 (4)	–0.83 (0.02)	–2.70 (0.08)	189 (8)	—	208.6/112
7971	BAND	0.0123 (0.0006)	237 (15)	–1.18 (0.04)	–2.42 (0.17)	192 (27)	—	101.1/111
7975	BAND	0.0181 (0.0040)	132 (11)	–0.69 (0.17)	–2.05 (0.05)	81 (6)	—	92.8/112
7976	COMP	0.0062 (0.0002)	311 (16)	–1.07 (0.04)	—	—	—	125.0/112
7986	COMP	0.0667 (0.0033)	216 (5)	–0.45 (0.06)	—	—	—	126.7/109
7994	SBPL	0.0142 (0.0001)	254 (16)	–0.60 (0.03)	–3.22 (0.13)	242 (12)	0.30	156.8/113
8005	BAND	0.0114 (0.0008)	428 (52)	–0.67 (0.08)	–2.14 (0.20)	249 (43)	—	119.6/112
8008	BAND	0.0234 (0.0004)	497 (15)	–0.64 (0.02)	–2.46 (0.10)	346 (20)	—	137.5/109
8053	BAND	0.4870 (0.0423)	90 (1)	–0.50 (0.07)	–3.68 (0.18)	108 (6)	—	122.0/112
8069	SBPL	0.0564 (0.0003)	221 (21)	–1.34 (0.02)	–3.11 (0.13)	280 (22)	0.40	139.7/110
8081	BAND	0.0188 (0.0048)	155 (27)	–1.19 (0.23)	–2.11 (0.07)	100 (17)	—	9.9/8
8087	SBPL	0.0021 (0.0000)	329 (75)	–1.15 (0.04)	–2.22 (0.16)	240 (35)	0.20	113.5/112
8098	BAND	0.0248 (0.0041)	146 (10)	–0.75 (0.14)	–2.43 (0.13)	111 (11)	—	103.5/113
8101	COMP	0.0071 (0.0002)	306 (9)	–0.64 (0.04)	—	—	—	92.2/111

[1] *Fitted* $E_{\rm peak}$ for BAND or COMP, and *calculated* $E_{\rm peak}$ for SBPL.
[2] λ for PWRL, α for BAND, or COMP and λ_1 for SBPL.
[3] β for BAND and λ_2 for SBPL.
[4] *Fitted* $E_{\rm b}$ for SBPL, and *calculated* $E_{\rm b}$ for BAND.

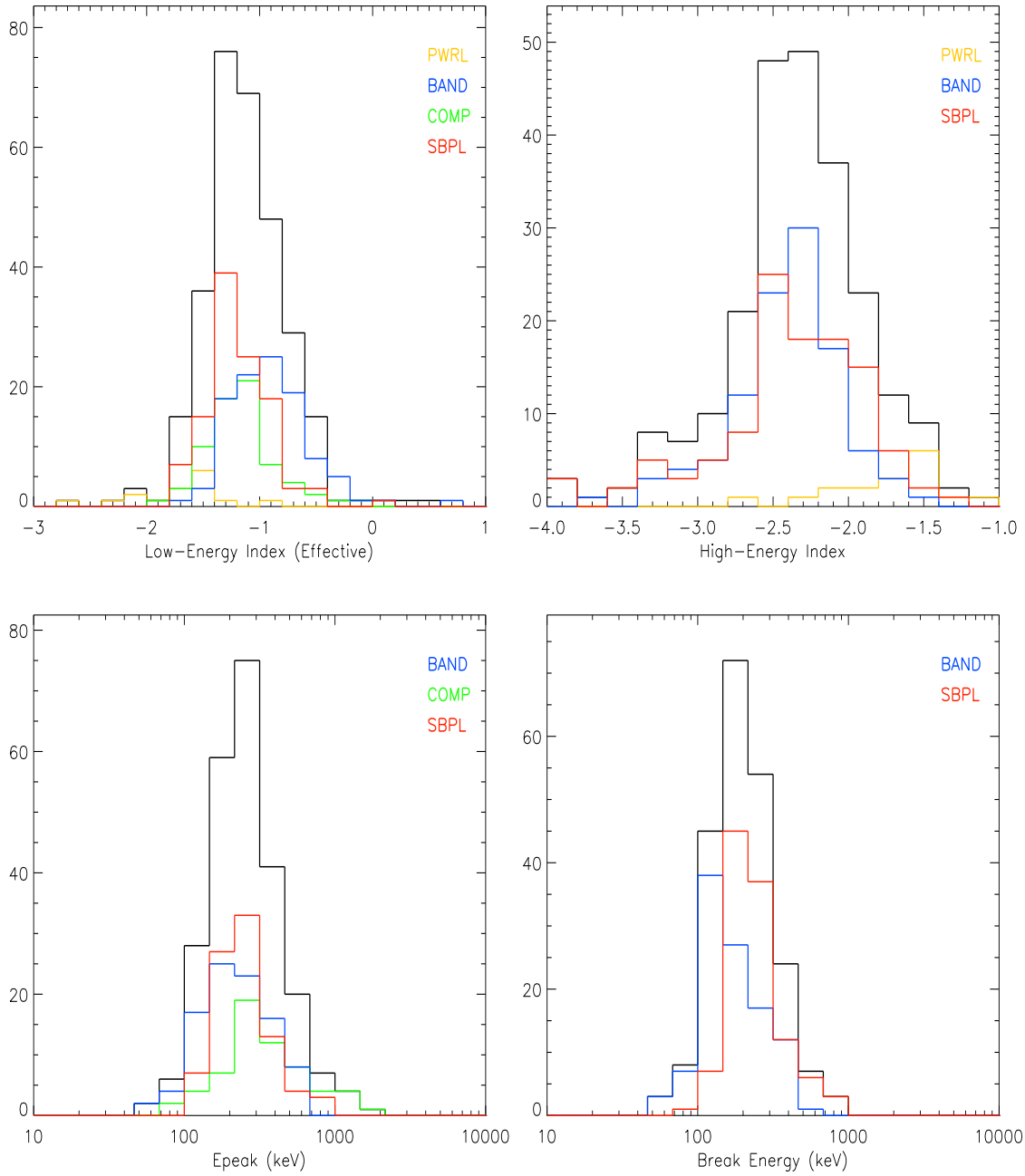

Figure 4.20 BEST model parameter distributions of the time-integrated spectra. The black lines show the total distributions, and the constituents are shown in colors. The lowest (highest) bin includes values lower (higher) than the edge values.

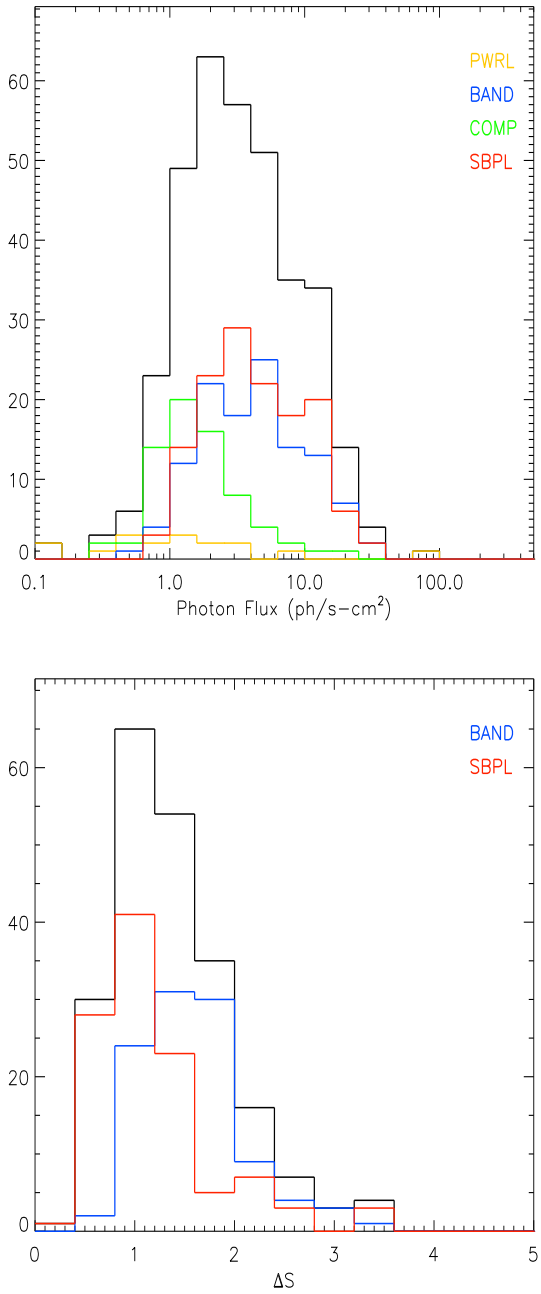

Figure 4.21 BEST model parameter distributions of the time-integrated spectra. The black lines show the total distributions, and the constituents are shown in colors. The lowest (highest) bin includes values lower (higher) than the edge values.

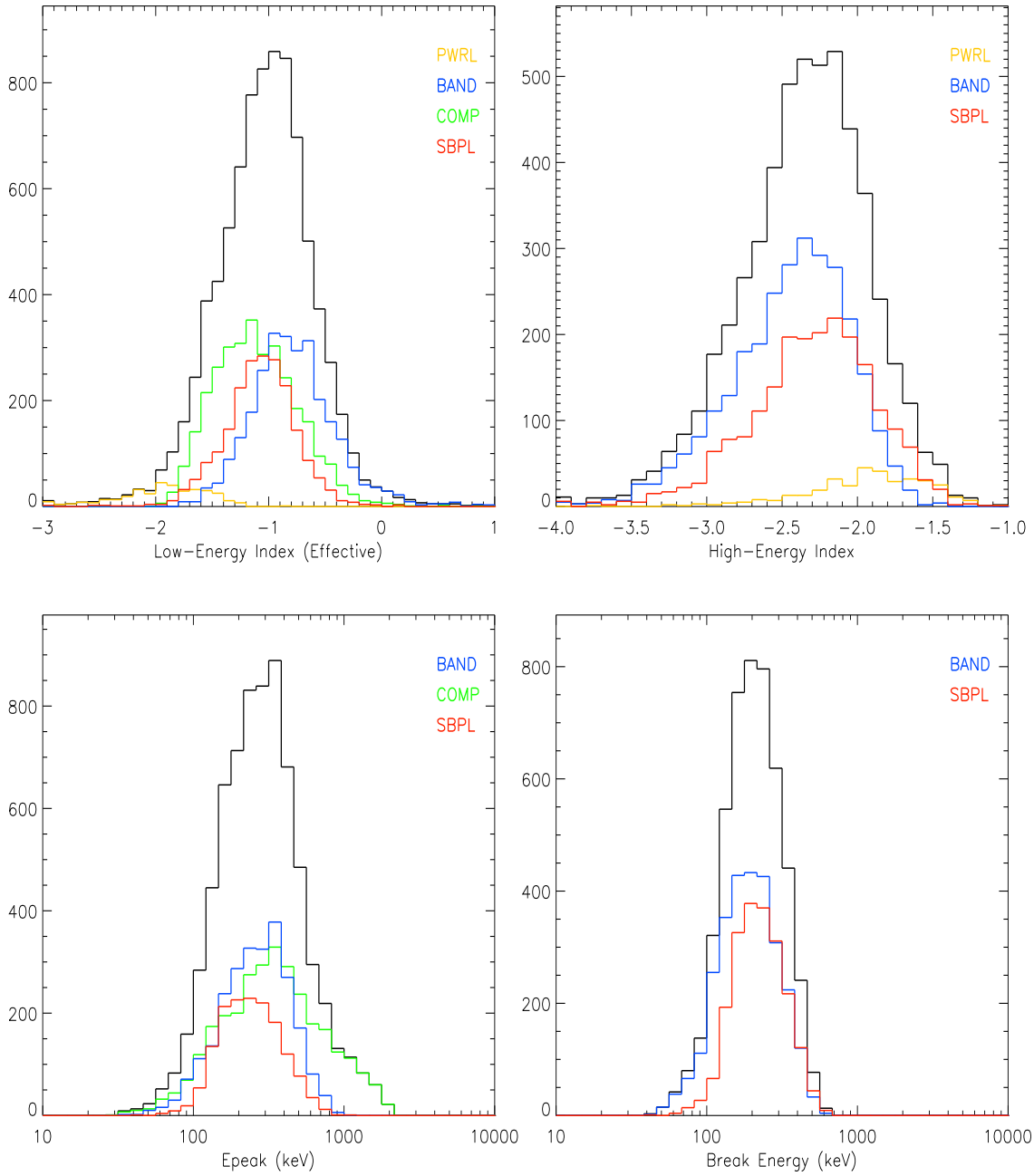

Figure 4.22 BEST model parameter distributions of the time-resolved spectra. The black lines show the total distributions, and the constituents are shown in colors. The lowest (highest) bin includes values lower (higher) than the edge values.

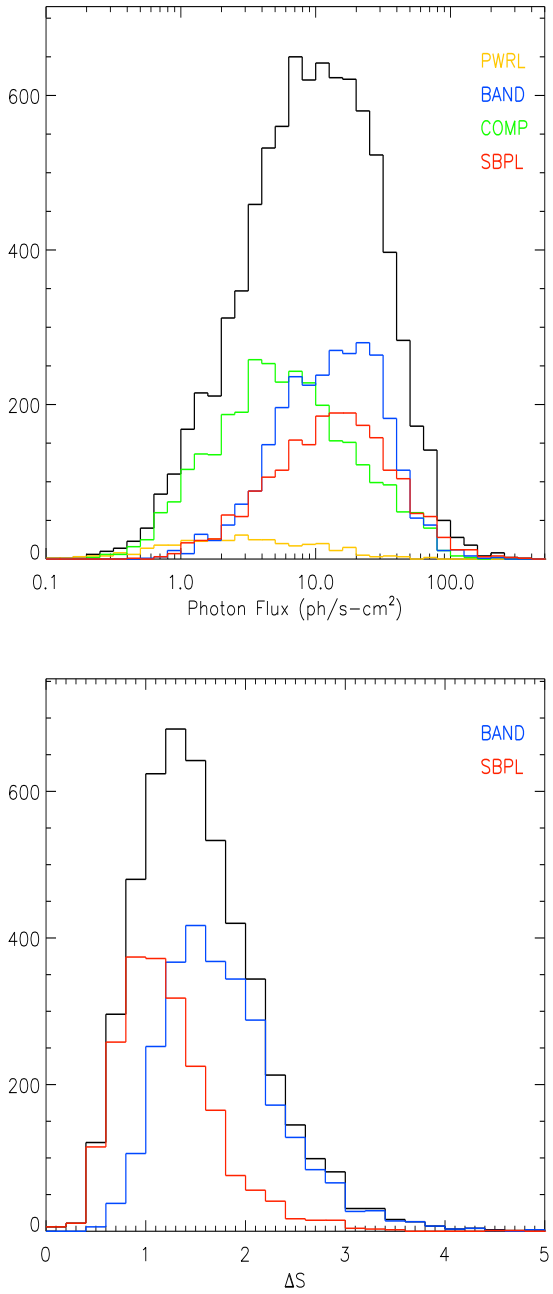

Figure 4.23 BEST model parameter distributions of the time-resolved spectra. The black lines show the total distributions, and the constituents are shown in colors. The lowest (highest) bin includes values lower (higher) than the edge values.

Table 4.9 Most probable parameter values and HWHM determined by the BEST model fits. The BEST model set consists of 17 (374) PWRL, 70 (3164) COMP, 118 (2828) BAND, and 137 (2093) SBPL time-integrated (time-resolved) spectra. The constituent parameter distribution values are also shown.

	Time-Integrated Parameters				
	Low Index	High Index	$E_{\rm peak}$ (keV)	$E_{\rm b}$ (keV)	ΔS
BEST	$-1.25\ ^{+0.35}_{-0.25}$	$-2.45\ ^{+0.55}_{-0.25}$	$238\ ^{+145}_{-117}$	$197\ ^{+120}_{-\ 97}$	$1.10\ ^{+0.70}_{-0.30}$
PWRL	$-1.50\ ^{+0.01}_{-0.01}$	—	—	—	—
COMP	$-1.10\ ^{+0.10}_{-0.30}$	—	$266\ ^{+198}_{-119}$	—	—
BAND	$-0.90\ ^{+0.50}_{-0.50}$	$-2.30\ ^{+0.30}_{-0.30}$	$215\ ^{+249}_{-115}$	$123\ ^{+\ 92}_{-\ 23}$	$1.60\ ^{+0.40}_{-0.80}$
SBPL	$-1.30\ ^{+0.30}_{-0.30}$	$-2.50\ ^{+0.70}_{-0.10}$	$266\ ^{+\ 50}_{-119}$	$181\ ^{+135}_{-\ 34}$	$1.00\ ^{+0.60}_{-0.60}$

	Time-Resolved Parameters				
	Low Index	High Index	$E_{\rm peak}$ (keV)	$E_{\rm b}$ (keV)	ΔS
BEST	$-0.95\ ^{+0.55}_{-0.50}$	$-2.25\ ^{+0.35}_{-0.55}$	$350\ ^{+213}_{-229}$	$197\ ^{+186}_{-\ 75}$	$1.30\ ^{+0.90}_{-0.50}$
PWRL	$-1.95\ ^{+0.55}_{-0.25}$	—	—	—	—
COMP	$-1.15\ ^{+0.45}_{-0.45}$	—	$350\ ^{+476}_{-229}$	—	—
BAND	$-0.80\ ^{+0.40}_{-0.40}$	$-2.35\ ^{+0.45}_{-0.45}$	$350\ ^{+114}_{-202}$	$197\ ^{+268}_{-\ 97}$	$1.50\ ^{+0.70}_{-0.50}$
SBPL	$-1.05\ ^{+0.25}_{-0.35}$	$-2.15\ ^{+0.35}_{-0.55}$	$215\ ^{+250}_{-\ 94}$	$197\ ^{+268}_{-\ 75}$	$1.00\ ^{+0.60}_{-0.40}$

In the time-resolved spectra, we find the BAND model tends to fit spectra with harder low-energy indices, while the COMP model seems to fit those with much softer indices. The spectra with positive low-energy indices are dominated by the BAND model fits. Most of the time-resolved COMP spectra with low-energy indices less than -1.5 were found to have low $E_{\rm peak} \lesssim 300$ keV. The value of low-energy index -1.5 corresponds to the fast-cooling case of the synchrotron emission spectrum. Meanwhile, for the high-energy spectral index distribution of time-resolved spectra, it seems those with harder high-energy indices are better fitted by the SBPL model, while those with softer indices are better fitted by the BAND model. We also find that the majority of SBPL with high-energy indices larger than -2.0 have small differences in low-energy and high-energy spectral indices (i.e., $\Delta \mathrm{S} < 1$). The majority of those spectra with small differences in indices ΔS, have sharp breaks (i.e., $\Lambda \leq 0.1$).

In the distributions of $E_{\rm peak}$ and break energy, we observe no secondary populations at energy below 100 keV, which was previously indicated by the break energy distribution of time-resolved spectra in SP1. The distributions of $E_{\rm peak}$ and break energy are different mainly due to the contribution of $E_{\rm peak} \gtrsim 1$ MeV that is dominated by COMP spectra. These represent very hard spectra with the actual $E_{\rm peak}$ values lying very close to or higher than the upper energy bound of our datasets (i.e., $\gtrsim 1$ MeV). For such spectra, BAND or SBPL do not provide well-constrained high-energy spectral indices, and PWRL does not accommodate well the curvature of the spectra; therefore, the COMP model fits were preferred. Finally, from the photon flux plots (top panels in Figures 4.21 and 4.23), it is also found that the simpler models (PWRL and COMP) are best fit to weaker spectra, compared with more complex models (BAND and SBPL), as expected.

Using the set of BEST models determined for each time-resolved spectrum, we can also examine which parts of the burst are well fitted by which models. This

in turn reveals the evolution of spectral shapes within bursts. In Figures 4.24 and 4.25, we present the BEST models as a function of time for two events that exhibit the hard-to-soft and the "tracking" behaviors. Both behaviors are defined by $E_{\rm peak}$ and low-energy index evolution, which are commonly observed in GRBs (Ford et al. 1995; Crider et al. 1997). The evolution of the low-energy index and $E_{\rm peak}$ are also shown along with the BEST model histories.In the hard-to-soft burst (Figure 4.24), the first half is best-fitted by BAND, SBPL, or the COMP with high $E_{\rm peak}$. The softer tail spectra of the burst are well fitted by either PWRL with index less than -2 (indicating $E_{\rm peak} \lesssim 30$ keV) or COMP with low $E_{\rm peak}$. On the other hand, in the tracking burst (Figure 4.25), the rise and fall of each peak are well fitted by the low-$E_{\rm peak}$ COMP or PWRL.

4.4.3 Time-Integrated and Time-Resolved Spectra

For the comparison between the time-integrated and the time-resolved spectral parameters of the BEST models, we plot the total distributions of time-integrated and resolved parameters in Figure 4.26. These are the total distributions presented in Figures 4.20 – 4.22, but are now plotted on top of each other. Also the most probable values of each parameter are summarized in Table 4.10, along with the HWHM of the distributions. It must be noted that these distributions are initially un-binned, so the binning of the data affects to some extent the most likely values observed in the probability distributions. Therefore, these values presented in Table 4.10 should be taken only as approximate, rather than exact. In order to determine if the distributions of the time-integrated and time-resolved spectral parameters are consistent, we employed the Kolmogorov-Smirnov (K-S) test (Press et al. 1992). The K-S test determines the parameter $D_{\rm KS}$ that measures the maximum difference in the cumulative probability distributions over all parameter space,

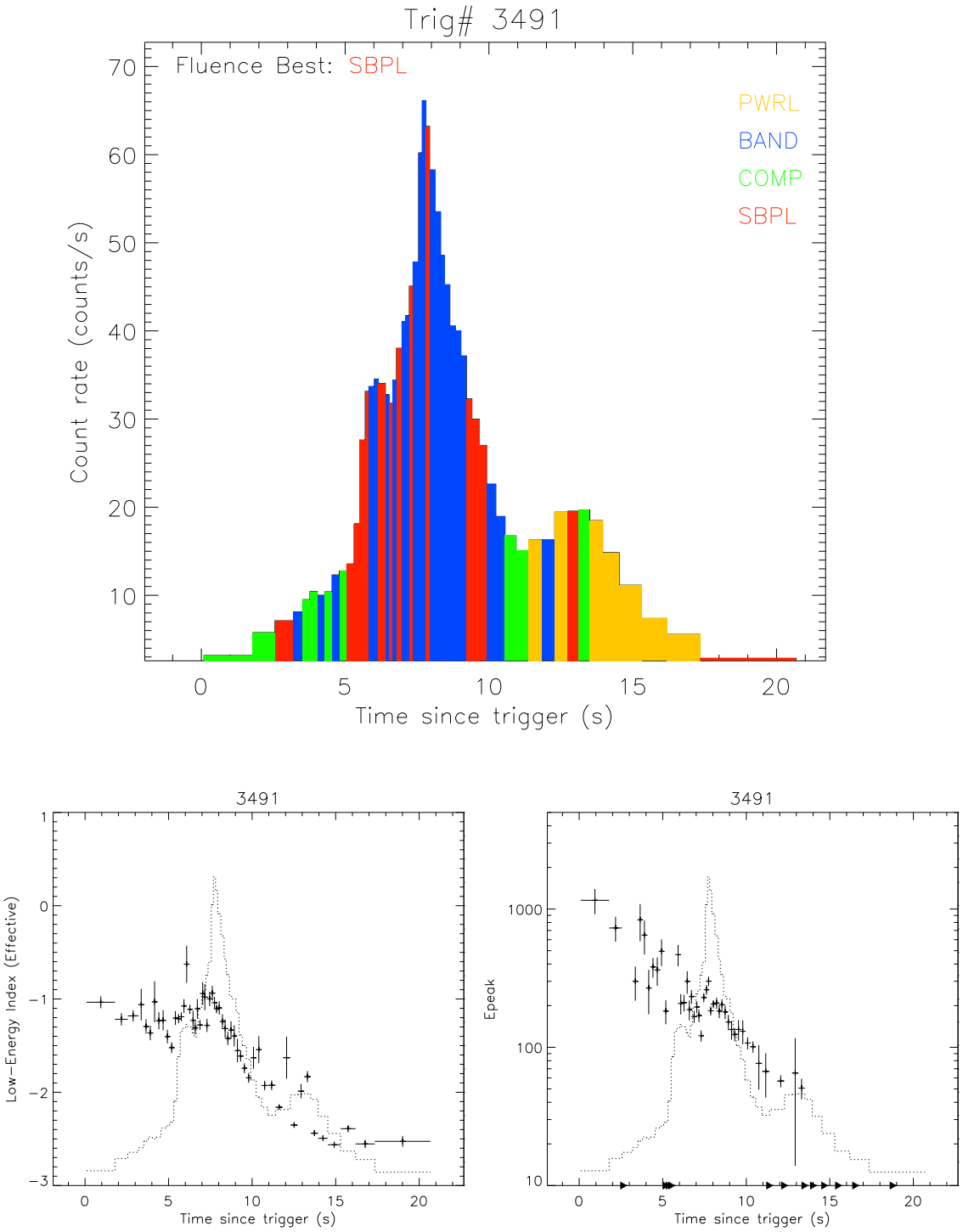

Figure 4.24 [*Top*] BEST model history of GRB 950403 (BATSE trigger number 3491). The BEST model of the time-integrated for this burst is SBPL. [*Bottom*] Evolutions of the low-energy index (effective) and $E_{\rm peak}$ for the same event. The arrowheads in $E_{\rm peak}$ plot indicate where the $E_{\rm peak}$ values cannot be determined.

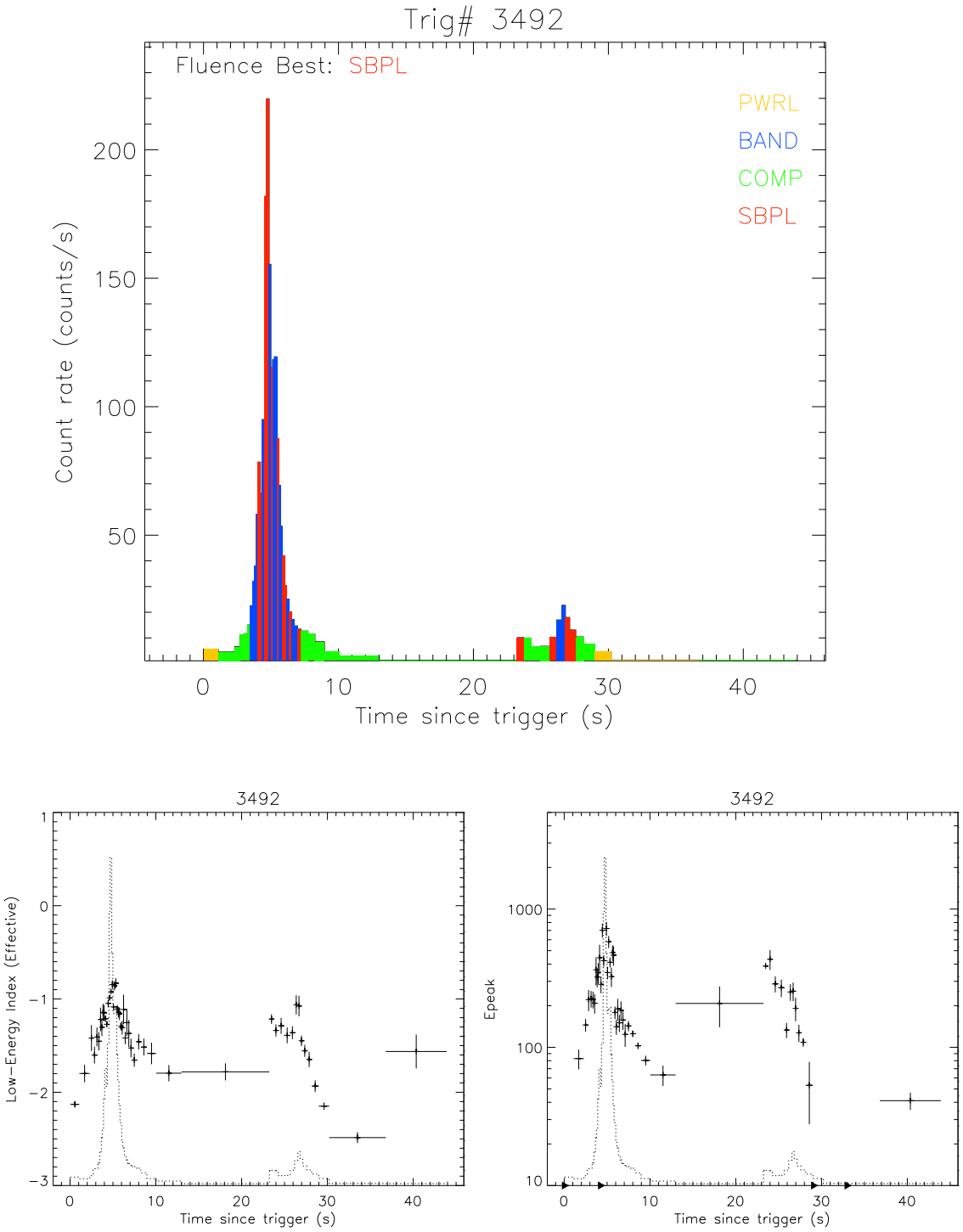

Figure 4.25 [*Top*] BEST model history of GRB 950403 (BATSE trigger number 3492). The BEST model of the time-integrated for this burst is SBPL. [*Bottom*] Evolutions of the low-energy index (effective) and $E_{\rm peak}$ for the same event. The arrowheads in $E_{\rm peak}$ plot indicate where the $E_{\rm peak}$ values cannot be determined.

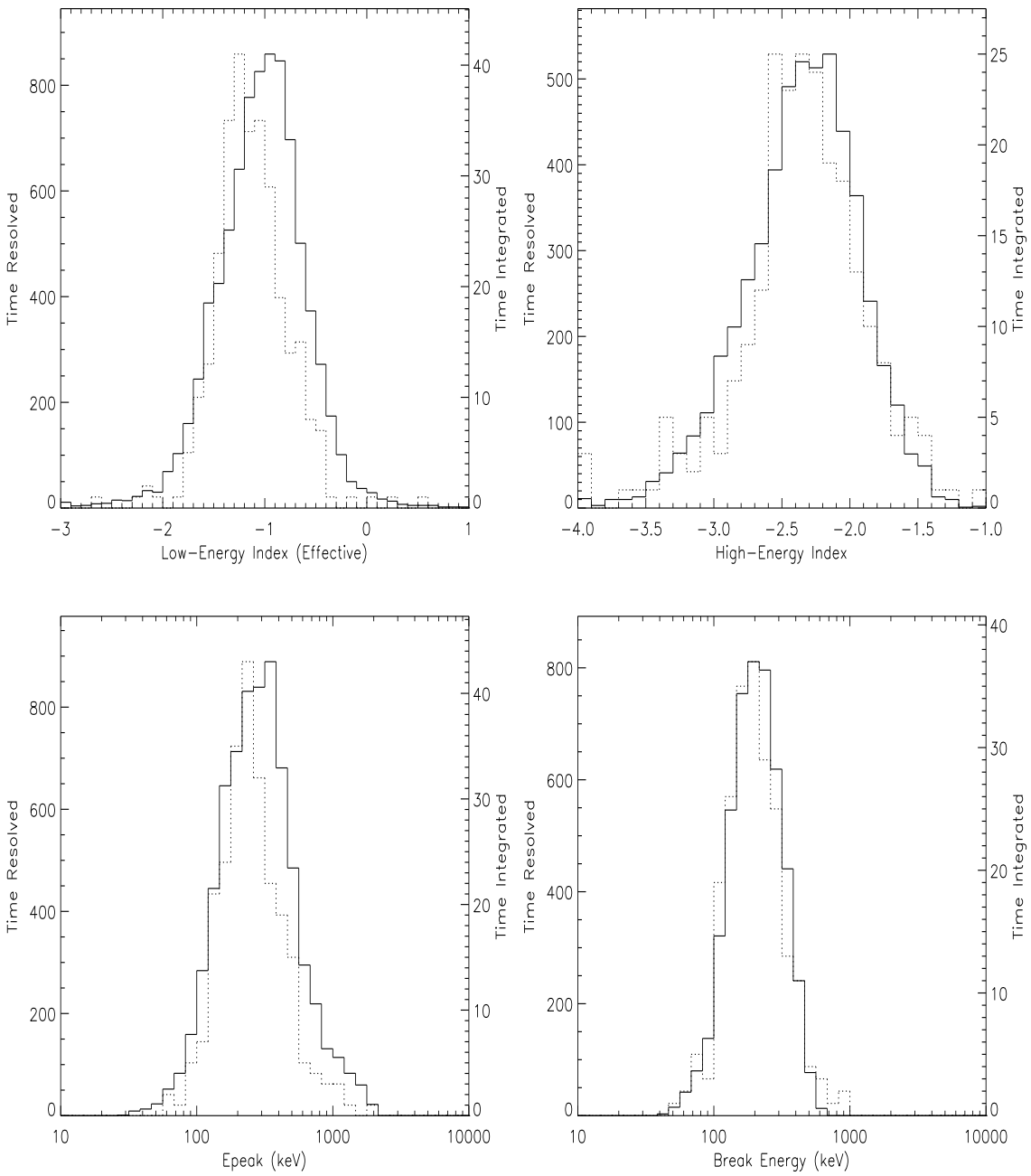

Figure 4.26 Comparisons of the BEST model parameter distributions of time-integrated (dotted; right axis) and time-resolved spectra (solid; left axis). The lowest (highest) bin includes values lower (higher) than the edge values.

Table 4.10 Comparison of the most probable values for time-integrated and time-resolved spectra. HWHM of each distribution is shown in parentheses. K-S probabilities and the corresponding parameters for two distributions are also shown.

Spectrum Type	Low Index	High Index	$E_{\rm peak}$ (keV)	$E_{\rm b}$ (keV)	ΔS
Time Integrated	$-1.25\ ^{+0.35}_{-0.25}$	$-2.45\ ^{+0.55}_{-0.25}$	$238\ ^{+145}_{-117}$	$197\ ^{+120}_{-\ 97}$	$1.10\ ^{+0.70}_{-0.30}$
Time Resolved	$-0.95\ ^{+0.35}_{-0.50}$	$-2.25\ ^{+0.35}_{-0.55}$	$350\ ^{+213}_{-229}$	$197\ ^{+186}_{-\ 75}$	$1.30\ ^{+0.90}_{-0.50}$
$P_{\rm KS}$	1.53×10^{-7}	0.75	1.40×10^{-3}	0.87	1.95×10^{-3}
$D_{\rm KS}$	0.17	0.04	0.12	0.04	0.12

and the significance probability $P_{\rm KS}$ for the value of $D_{\rm KS}$. The null hypothesis is that the two datasets are drawn from the same parent distributions; therefore, a small $P_{\rm KS}$ rejects the hypothesis and indicates that the datasets are likely to be different. Determined by the K-S statistics, we find a significant difference in the low-energy spectral index distributions of time-integrated and time-resolved spectra, with $P_{\rm KS}$ of 10^{-7} ($D_{\rm KS} = 0.17$). Also, a less significant difference was found between the $E_{\rm peak}$ distributions with $P_{\rm KS}$ of 10^{-3} ($D_{\rm KS} = 0.12$). The distributions of the high-energy index and the break energy were consistent. This is in agreement with what we observed in the parameter distributions of individual model fits earlier (Figures 4.9 – 4.17 and Table 4.6), and is, again, most likely due to the spectral evolution within each event.

We also compare the time-integrated and time-resolved distributions of SBPL break scales and ΔS in Figure 4.27. It can be seen from the break scale comparison that the time-integrated SBPL spectra are smoother (larger break scales) than the time-resolved ones. This is naturally expected because the integrated spectra are summations of resolved spectra with possibly various $E_{\rm b}$ values, and therefore, any

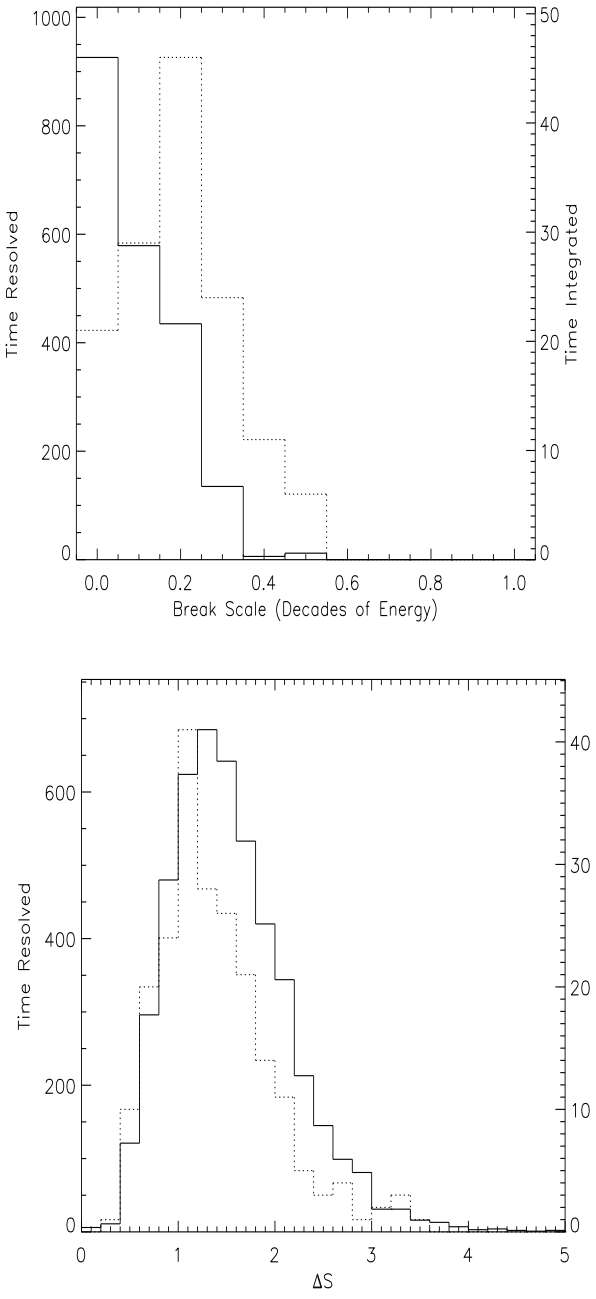

Figure 4.27 Comparisons of the BEST model break scale and ΔS distributions of time-integrated (dotted; right axis) and time-resolved spectra (solid; left axis). The break scale values are for spectra fitted with SBPL only, while ΔS values are for those fitted with BAND and SBPL.

sharp break features may be smeared over. For the same reason, the tendency of smaller ΔS observed in integrated spectra is expected as well.

It has been a common practice to fit the same broken-power law model (BAND in particular) to both time-integrated and time-resolved spectra. The model usually yields sufficiently good fits to both types of spectra; however, if the time-integrated spectrum consists of a set of broken-power law spectra with evolving break energy and indices, it is possible that the time-integrated spectra deviates from a broken-power law shape. Often, we do observe some indication of such deviations in the residual patterns obtained from time-integrated spectral fits to broken-power law models. To probe this, we explored how each time-resolved spectrum contributes to the time-integrated spectrum. The time-integrated spectra are usually considered as "average" spectra; however, averaging (whether error/intensity-weighted or not) the best-fitted spectral parameters from each time-resolved spectrum does not yield the best-fitted time-integrated spectral parameters. This is because the time-integrated spectra are averaged over count space rather than parameter space. Consequently, if each of the fitted time-resolved spectral models are indeed accurately representing the observed spectral data, summing over the model photon counts should reveal the *true* time-integrated photon spectrum.

Therefore, for each burst, we obtained the *true* time-integrated photon flux by summing the BEST model photon counts in the time-resolved spectra and dividing by their total durations;

$$\bar{\mathcal{F}}_{flnc}(E) = \frac{\sum_i f_i(E)\Delta t_i}{\sum_i \Delta t_i}. \tag{4.5}$$

Here, $f_i(E)$ is the model photon flux of each time-resolved spectrum as a function of photon energy, and Δt_i is the accumulation time of each spectrum. The initial visual comparisons of $\bar{\mathcal{F}}_{flnc}$ plotted against the best-fitted time-integrated spectral

models suggested that they agree remarkably well for most of the GRBs in our sample. For quantitative comparisons of $\bar{\mathcal{F}}_{flnc}$ to the actual BEST model photon flux, we employed the χ^2 statistic (Press et al. 1992):

$$\chi^2 = \sum_{j=1}^{N} \frac{(\bar{\mathcal{F}}_j - \mathcal{F}_j)^2}{{\sigma_j}^2}, \tag{4.6}$$

where N is a number of energy bins, $\bar{\mathcal{F}}_j$ denotes $\bar{\mathcal{F}}_{flnc}$ per energy bin, $\mathcal{F}_j$ is the actual time-integrated BEST model flux per energy bin, and ${\sigma_j}^2$ is the variance associated with $\mathcal{F}_j$ obtained from the fits. For each event, the χ^2 statistics and the corresponding significance probability, P_{χ^2}, were determined. We note that P_{χ^2} is the chance probability of χ^2 exceeding the calculated value for a given dof, and therefore, a small P_{χ^2} rejects the hypothesis of two distributions being the same. The number of dof was equal to N. According to the statistics, $\bar{\mathcal{F}}$ and $\mathcal{F}$ were found to be consistent for about 73% of 325 bursts, providing P_{χ^2} values greater than 1%. An example of such events is shown in Figure 4.28. We found that the other 27% of the bursts with very small P_{χ^2} values were of the brightest of the burst sample in terms of peak photon flux (Figure 4.29). The events with extremely high peak flux ($\gtrsim 70$ photons s^{-1} cm^{-2}) resulted in large χ^2 because the brightest spectrum within the event tends to dominate in the summation process. This caused $\bar{\mathcal{F}}$ to consistently have larger flux than the BEST model photon flux. The time-integrated spectral fits for most of these events also resulted in statistically poor fits, with χ^2 confidence level $> 3\sigma$, even with the BEST models. In very bright events, the contribution of systematic uncertainties in the data is generally expected to be more evident (see Figure 4.1). As a result, the best-fitted photon models may not represent the true spectral shapes for these events. We also found that the majority of the events for which MER data were used fall into the group of small P_{χ^2}. This is likely because there are more systematic uncertainties present in the multiple-detector MER data

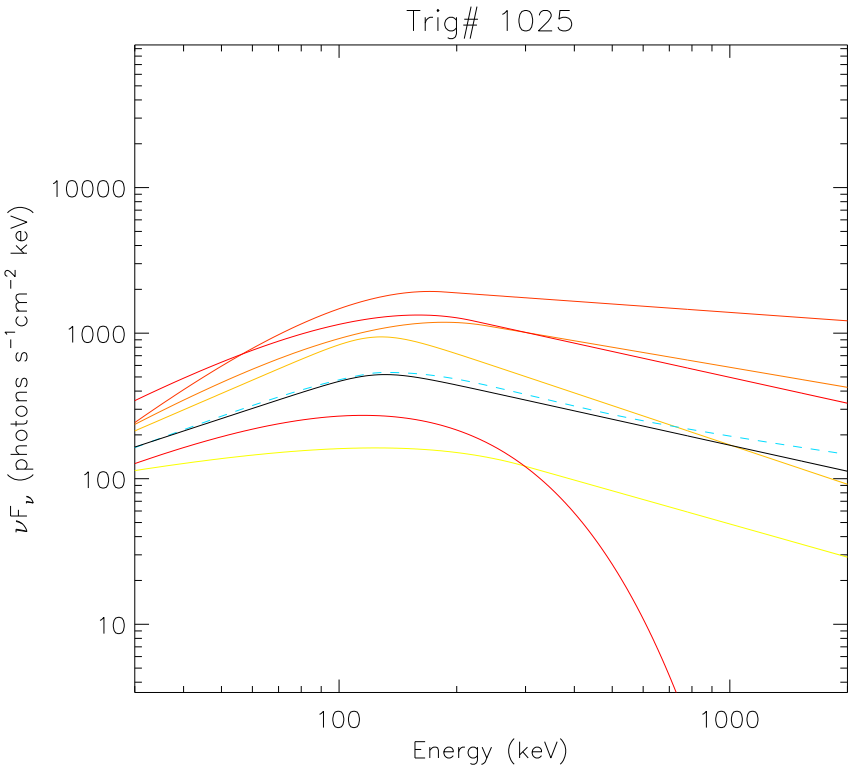

Figure 4.28 Spectral evolution of GRB 911109 (BATSE trigger number 1025). Time-resolved BEST models are color-coded by time from yellow to red, earlier to later. Time-integrated BEST model is plotted in black solid curve. The blue-dashed curve shows the $\bar{\mathcal{F}}_{flnc}$ spectrum, which is consistent with the BEST model.

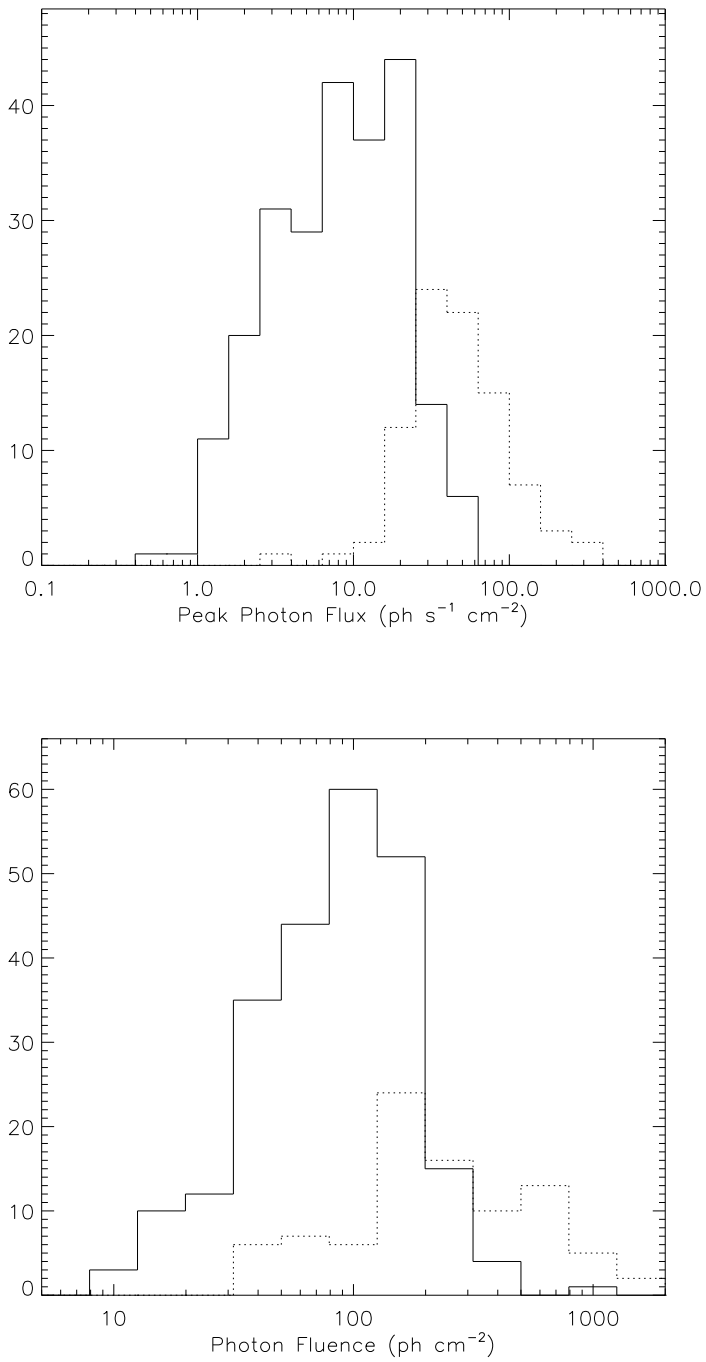

Figure 4.29 Distribution of peak (maximum) photon flux (*top*) and total photon fluence values (*bottom*) of 325 bursts. The bursts with $P_{\chi^2} > 1\%$ (solid line) have lower peak flux than those with $P_{\chi^2} < 1\%$ (dotted line).

than the single-detector HERB or CONT data. In addition, the MER bursts in this group tend to consist of a larger number of spectra. This is because the MER data type was used when the corresponding HERB data were incomplete, which occurs frequently in the case of very bright bursts.

Furthermore, among the small-P_{χ^2} group, there are some bursts where the constructed photon flux $\bar{\mathcal{F}}$ seems to follow the actual deconvolved photon data points very well. One such example is shown in the Figure 4.30, for GRB 980306 (BATSE Trigger number 6630). Although there seems be a slight offset in amplitude, it is remarkable that the shape of constructed photon flux (dashed line) traces the actual deconvolved data points of the time-integrated spectrum. The time-integrated spectral fit for this event is still acceptable ($\chi^2/\mathrm{dof} = 126.7/109$; see Table 4.8); however, the deviations of the real spectral shape from a smoothly-broken power-law model are evident.

From these, we infer that the true time-integrated spectrum can be constructed by summing over the photon model counts of each time-resolved spectra within the event (Equation 4.5), provided that the BEST model in each time-resolved spectrum is an accurate representation of the observed spectral shape. The true spectrum may not be as simple as the BEST models, possibly due to spectral evolution. The events with peak photon flux larger than ~ 30 photons s^{-1} cm^{-2} will likely suffer from large systematic uncertainties, with the results that the constructed spectrum does not represent the true spectral shape, nor has a shape that differs greatly from the best-fitted model. Therefore, the fitted spectral parameters of the time-integrated spectra may only represent the best parameter possibly fitted by our simple models that are limited in their spectral shapes, and the spectral parameter distributions should be interpreted with this in mind. This may also be applicable to the time-resolved spectra given that the cooling timescales (both radiative and dynamical) can be much shorter than the integration times of each spectrum.

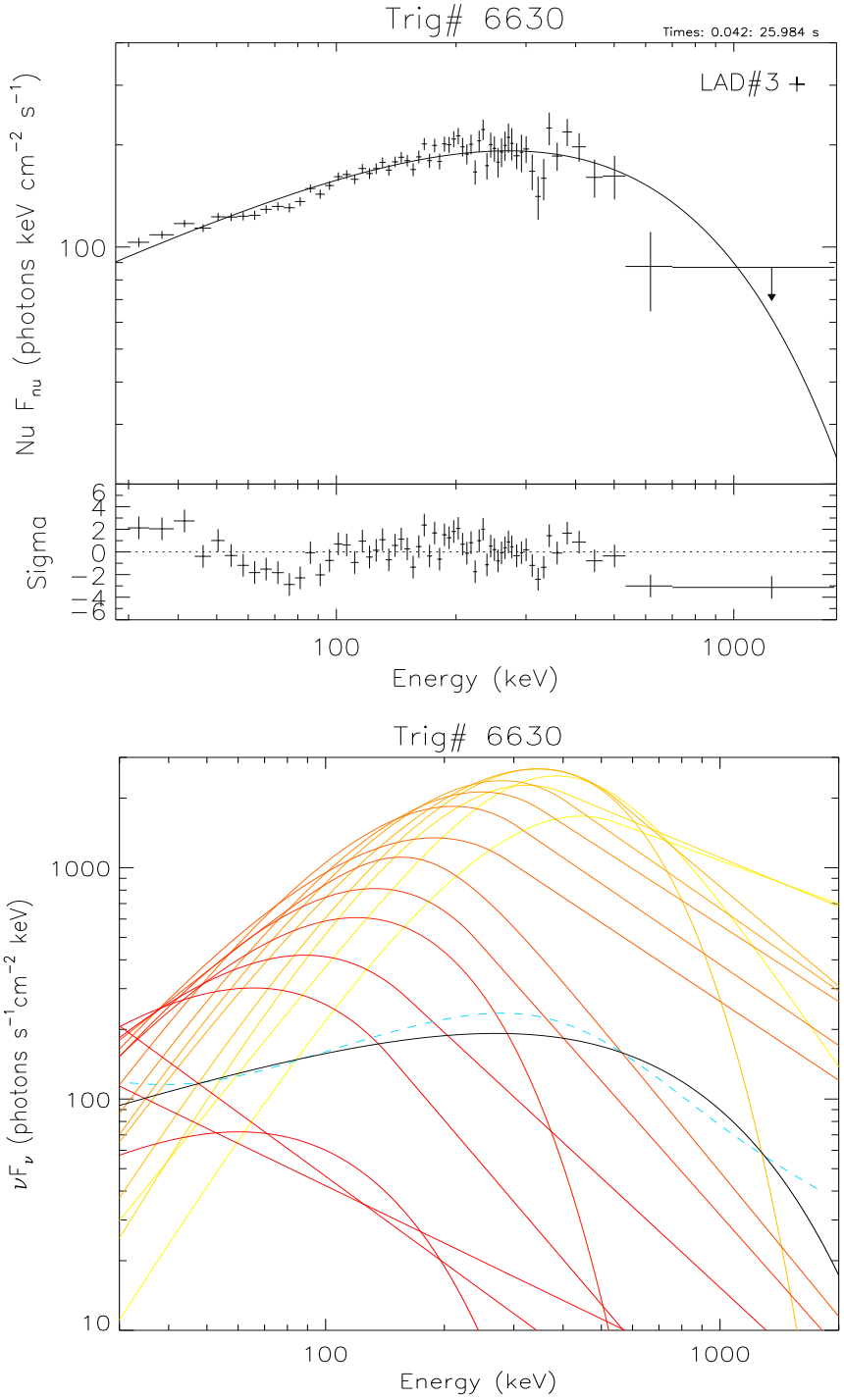

Figure 4.30 [*Top*] The actual deconvolved time-integrated photon data and model of GRB 980306. [*Bottom*] The spectral evolution of GRB 980306 (yellow to red, earlier to later) blue dashed curve is the constructed photon flux $\bar{\mathcal{F}}$. In both plots, the best-fitted model (SBPL with $\Lambda = 0.2$) is plotted with black solid curves.

4.4.4 Correlations Among Spectral Parameters

Some empirical correlations among GRB spectral parameters, such as between $E_{\rm peak}$ and low-energy index, have been reported with smaller samples (e.g., Crider et al. 1997; Lloyd-Ronning & Petrosian 2002). The correlations were found either within individual bursts or for a collection of time-resolved parameters. To probe the existence of correlations among the spectral parameters derived from our sample, we calculated the Spearman rank-order correlation coefficients (Press et al. 1992) and the associated significance probabilities for several combinations of spectral parameters. Given N pairs of data points, x and y, the rank correlation assigns ranks from 1 to N in ascending order, R_i and S_i for each x_i and y_i. It then looks for a linear correlation between the uniform sets of integers. The correlation coefficient is

$$r_s = \frac{\sum_i (R_i - \bar{R})(S_i - \bar{S})}{\sqrt{\sum_i (R_i - \bar{R})^2}\sqrt{\sum_i (S_i - \bar{S})^2}} \ , \tag{4.7}$$

and the significance probability (P_{rs}) of a nonzero value of r_s is found based on the t parameter,

$$t = r_s \sqrt{\frac{N-2}{1-{r_s}^2}} \ , \tag{4.8}$$

which is approximately normally distributed around zero. The null hypothesis is that no correlation exists; therefore, a small P_{rs} indicates a significant correlation.

We have found no indication of global correlations among the time-integrated spectral parameters. Among the time-resolved spectral parameters, on the other hand, broad positive trends between $E_{\rm peak}-$low-energy index, $E_{\rm b}-$low-energy index, and $E_{\rm peak}-$high-energy index, were visible in scatter plots. To eliminate the possible effects of a dispersion of $E_{\rm peak}$ and $E_{\rm b}$ due to the cosmological redshift that varies from burst to burst, it is best to look for parameter correlations within individual bursts. For each event with a sufficient number of data points ($N \geq 10$) in our

sample, we examined correlations between combinations of low-energy and high-energy indices, $E_{\rm peak}$, and $E_{\rm b}$, by determining r_s and P_{rs}. We use the BEST model parameters of each time-resolved spectrum within events, and also, for simplicity, we denote the low-energy and high-energy indices of the BEST model as α and β respectively, in this section. The number of parameter pairs (N) in each event was less than or equal to the number of time-resolved spectra; however, this varied according to which pair was considered since we used the BEST model parameters and certain parameters are not obtainable for certain spectra. For example, it is possible that for an $E_{\rm peak}-\alpha$ correlation, $N = 20$ pairs were available, but for $E_{\rm b}-\alpha$ only $N = 15$ were available. For most of the cases, N is $\gtrsim 80\%$ of the number of spectra and is always more than 10. We note that the P_{rs} values take into account the actual number N in the calculation that determines each correlation significance. The resulting numbers of events considered for each correlation were summarized in Table 4.11 along with percentages of events with significant correlations between each pair of parameters. We considered the correlation significant if $P_{rs} < 10^{-3}$ ($> 3\sigma$). The coefficient r_s and the associated P_{rs} of the events that showed significant correlations in at least one of the parameter pairs are listed in Table 4.12.

Table 4.11 Summary of total numbers of events considered for each correlation and percentages of events with high significance.

	$E_{\rm peak}-\alpha$	$E_{\rm b}-\alpha$	$E_{\rm peak}-\beta$	$E_{\rm b}-\beta$	$\alpha-\beta$
Total Number of Events	199	139	106	139	153
Significant Correlation (%)	27.6	14.4	4.7	12.9	4.6

Table 4.12 Events with strong spectral parameter correlations. Spearman rank correlation coefficients (r_s) and associated significance probabilities (P_{rs}) are listed. α and β denote low-energy and high-energy indices.

BATSE	Number of	$E_{\rm peak} - \alpha$		$E_{\rm b} - \alpha$		$E_{\rm peak} - \beta$		$E_{\rm b} - \beta$		$\alpha - \beta$	
Trig #	Spectra	r_s	P_{rs}	r_s	P_{rs}	r_s	P_{rs}	r_s	P_{rs}	r_s	P_{rs}
109	26	0.70	8.85E–4	———		———		———		———	
143	46	———		———		———		–0.60	1.51E–4	———	
219	13	0.80	9.69E–4	———		———		———		———	
249	68	0.50	1.55E–5	———		———		–0.59	3.60E–6	———	
1085	60	0.84	4.00E–16	0.73	2.11E–10	0.64	2.03E–7	0.60	1.31E–6	0.47	3.00E–4
1141	42	———		———		———		–0.57	5.92E–4	———	
1288	28	0.63	4.73E–4	———		———		———		———	
1541	15	0.84	1.60E–4	———		———		———		———	
1625	37	———		0.63	1.19E–4	———		———		———	
1652	18	0.84	2.65E–5	———		———		———		———	
1663	61	0.51	2.97E–4	0.61	2.02E–6	———		–0.60	5.05E–6	———	
1676	30	0.74	2.65E–6	0.84	9.14E–5	———		———		———	
1695	142	0.44	8.25E–8	———		———		–0.38	2.60E–5	———	
1698	32	0.79	1.03E–7	———		———		———		———	
1712	11	0.87	4.55E–4	———		———		———		———	
1983	54	———		———		———		–0.70	6.17E–6	———	
1872	110	———		0.45	4.06E–5	———		———		–0.53	5.23E–7
2067	45	0.64	2.08E–6	———		———		–0.68	1.08E–6	———	
2083	45	0.89	4.76E–15	0.72	2.60E–5	———		———		———	
2138	39	———		———		———		–0.77	5.00E–7	———	
2156	97	0.64	6.77E–11	0.47	5.57E–5	———		———		———	
2329	100	———		0.65	3.02E–8	———		———		———	
2533	70	———		———		———		–0.56	3.52E–5	———	
2661	29	0.64	1.80E–4	———		———		———		———	
2676	122	0.70	1.43E–18	0.58	1.45E–9	———		–0.40	8.56E–5	–0.43	2.45E–5
2790	19	0.80	6.78E–5	———		———		———		———	
2798	95	0.62	2.96E–10	0.37	8.90E–4	———		———		———	
2831	112	0.48	1.90E–7	———		———		———		———	
2833	35	0.82	1.19E–6	———		———		———		———	
2855	35	———		———		———		–0.56	6.16E–4	———	
2856	114	0.68	6.51E–15	0.46	6.64E–5	———		———		———	
3002	19	0.74	2.75E–4	———		———		———		———	
3035	28	0.60	6.70E–4	———		———		———		———	
3057	165	———		0.43	9.38E–6	–0.44	3.19E–4	———		———	
3128	44	———		———		———		–0.68	1.81E–5	———	
3227	50	0.62	1.25E–6	0.60	8.65E–5	———		———		———	
3241	44	0.60	1.40E–4	———		———		———		———	
3245	116	0.70	8.02E–17	0.60	9.03E–12	———		———		———	
3253	94	0.73	3.40E–17	0.60	4.07E–6	———		———		–0.48	4.07E–4
3298	20	0.73	4.09E–4	———		———		———		———	
3492	49	0.80	5.27E–11	0.65	1.17E–4	———		———		———	
3571	22	0.73	1.03E–4	———		———		———		———	
3658	30	0.68	8.78E–5	———		———		———		———	
3765	33	0.69	1.16E–5	———		———		———		———	
3767	20	0.92	1.49E–8	———		———		———		———	
5299	50	0.60	5.87E–5	———		———		———		———	
5304	48	0.81	6.06E–12	0.67	8.77E–7	———		———		———	
5486	32	———		———		———		———		–0.84	1.04E–4
5649	155	0.46	1.60E–9	———		———		———		———	
5773	57	0.72	3.84E–10	———		———		———		———	
5995	61	0.64	4.41E–7	———		———		———		———	
6124	60	———		———		———		–0.71	5.00E–8	———	
6266	18	———		———		–0.88	3.30E–4	———		———	
6329	31	0.59	4.94E–4	———		———		———		———	
6350	44	0.55	4.88E–4	———		———		–0.52	8.52E–4	———	
6576	21	0.76	1.53E–4	———		———		———		———	
6587	60	———		———		———		–0.72	8.90E–9	———	
6630	17	0.85	5.17E–5	———		———		———		———	
6665	38	———		———		———		–0.58	2.85E–4	———	

Table 4.12 (continued)

BATSE	Number of	$E_{\rm peak}-\alpha$		$E_{\rm b}-\alpha$		$E_{\rm peak}-\beta$		$E_{\rm b}-\beta$		$\alpha-\beta$	
Trig #	Spectra	r_s	P_{rs}	r_s	P_{rs}	r_s	P_{rs}	r_s	P_{rs}	r_s	P_{rs}
7113	243	0.42	4.47E–11	———		–0.58	1.33E–11	———		–0.30	5.94E–4
7170	30	0.78	3.66E–4	———		———		———		———	
7301	56	0.76	6.12E–9	0.57	1.35E–5	0.64	9.29E–4	———		0.47	5.10E–4
7343	134	0.59	7.51E–13	0.59	7.93E–9	———		———		———	
7360	32	0.77	2.19E–7	———		———		———		———	
7575	21	0.85	1.71E–5	———		———		———		———	
7678	37	———		———		———		–0.70	3.05E–5	———	
7695	29	0.70	2.51E–5	———		———		———		———	
7906	59	0.72	9.26E–10	———		———		———		———	
7954	27	0.62	5.85E–4	———		———		———		———	
7976	17	0.87	1.19E–4	———		———		———		———	
7994	25	0.68	1.60E–4	———		———		———		———	
8008	27	0.72	3.87E–5	———		———		———		———	

To illustrate some of the strong correlations, we show example scatter plots of each type of parameter pairs in Figures 4.31 – 4.33. The strongest positive correlation is found between $E_{\rm peak}$ and α, in 28% of the bursts. The chance probabilities of these correlations are extremely low in many cases. Positive correlations between $E_{\rm b}-\alpha$ are also evident, although only in half of the fraction of the $E_{\rm peak}$ cases. The $E_{\rm b}$ value is equal to the $E_{\rm peak}$ value only when a spectrum has a sharp break. Otherwise, a break scale or curvature determines the relation between them. Therefore, the same degree of correlation is not expected for $E_{\rm b}$ and $E_{\rm peak}$. On the contrary, the $E_{\rm peak}-\beta$, $E_{\rm b}-\beta$ and $\alpha-\beta$ correlations are found in a much lower fraction of events than the $E_{\rm b}/E_{\rm peak}$ and α cases, and are mostly negative. It must be noted, however, that the uncertainty associated with each parameter is not taken into account in determining the rank-order correlation, and β is usually associated with relatively larger uncertainties than the other parameters. This can be seen in the scatter plots in Figures 4.31 – 4.33. The actual significance of the correlations, therefore, may differ. We have also found significant positive correlations between $E_{\rm peak}$ and the photon flux in 27% of GRBs, and between α and photon flux (41%), indicating the tracking behavior. About 15% of GRBs belong to both groups, and therefore show

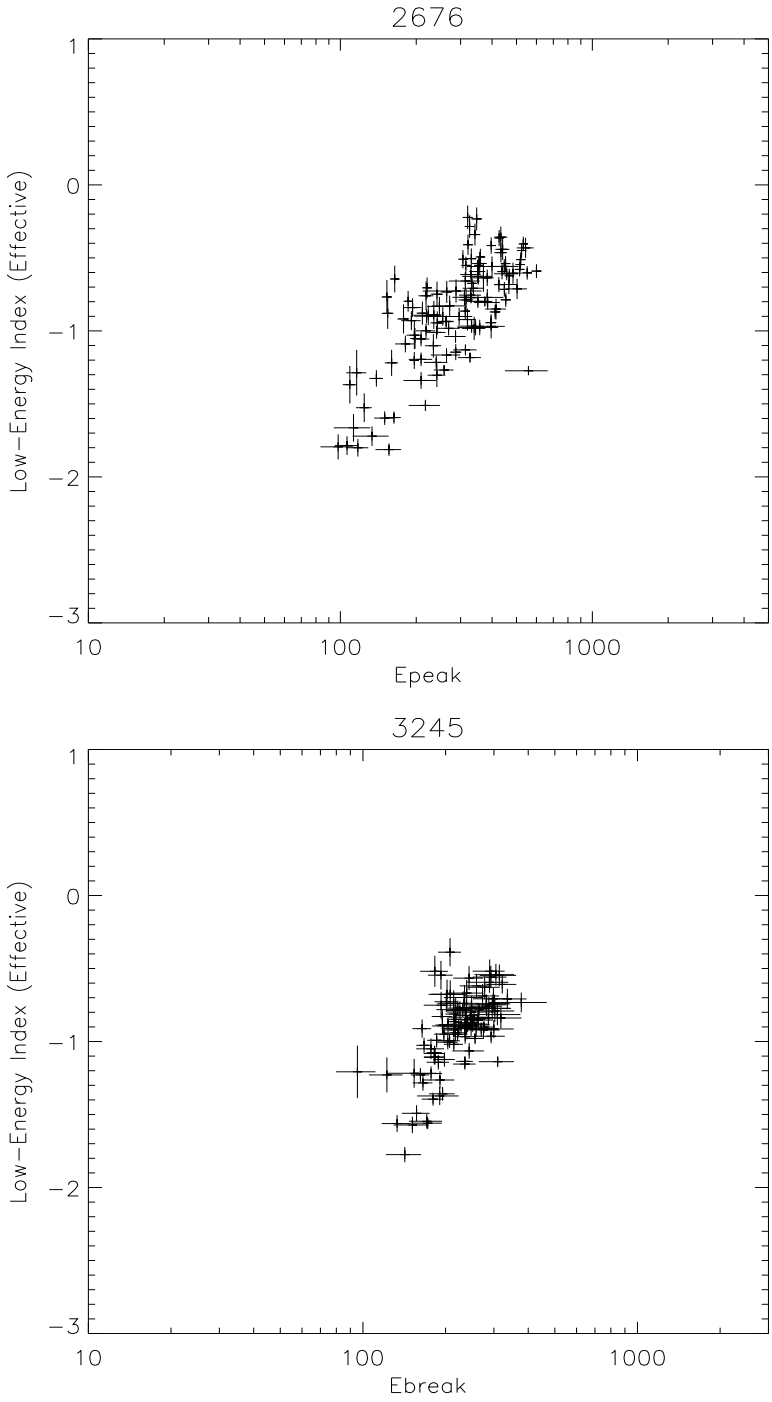

Figure 4.31 Example scatter plots of $E_{\rm peak} - \alpha$ of GRB 931204 (trigger number 2676; *top*) and $E_{\rm b} - \alpha$ of GRB 941017 (3245; *bottom*). Both show strong correlations.

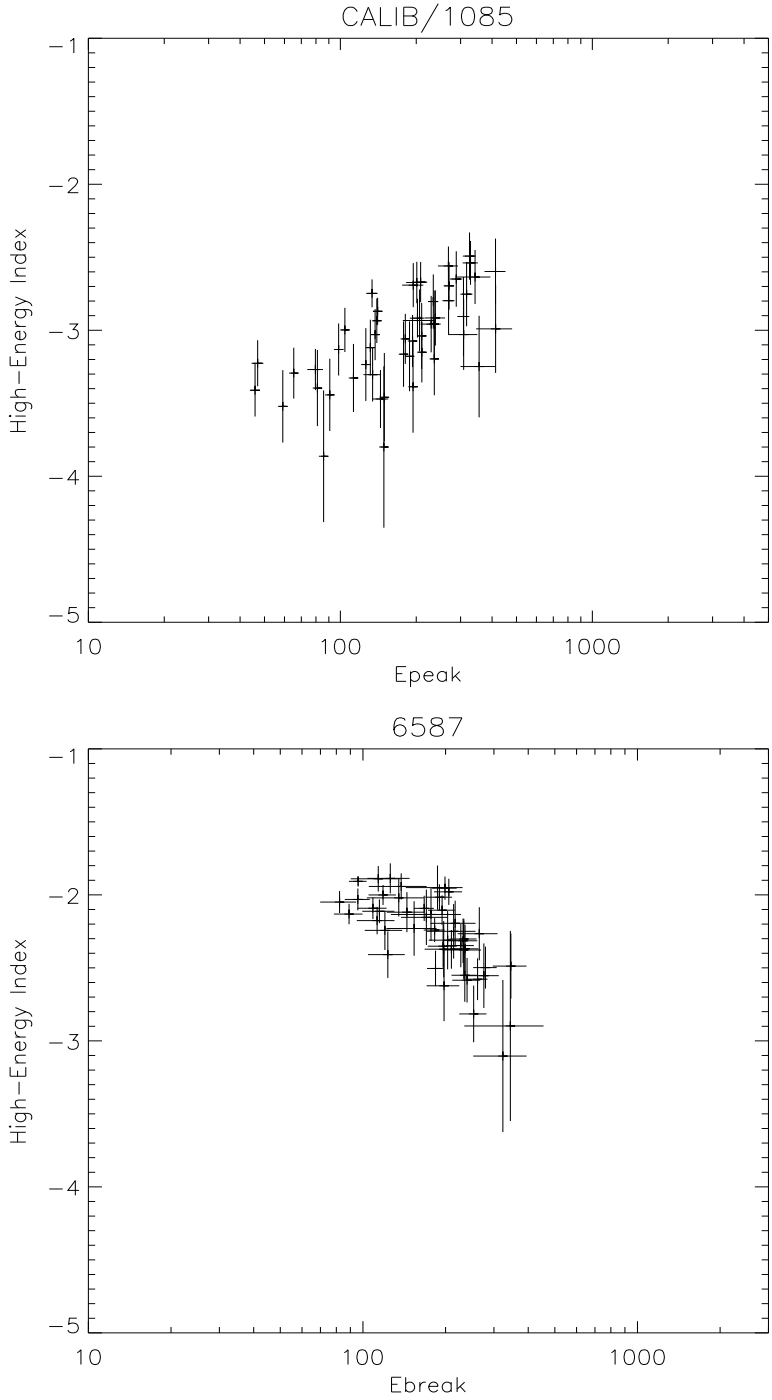

Figure 4.32 Example scatter plots of $E_{\rm peak} - \beta$ of GRB 911118 (trigger number 1085; *top*) and $E_{\rm b} - \beta$ of GRB 980203 (6587; *bottom*). Positive (*top*) and negative (*bottom*) correlations are seen.

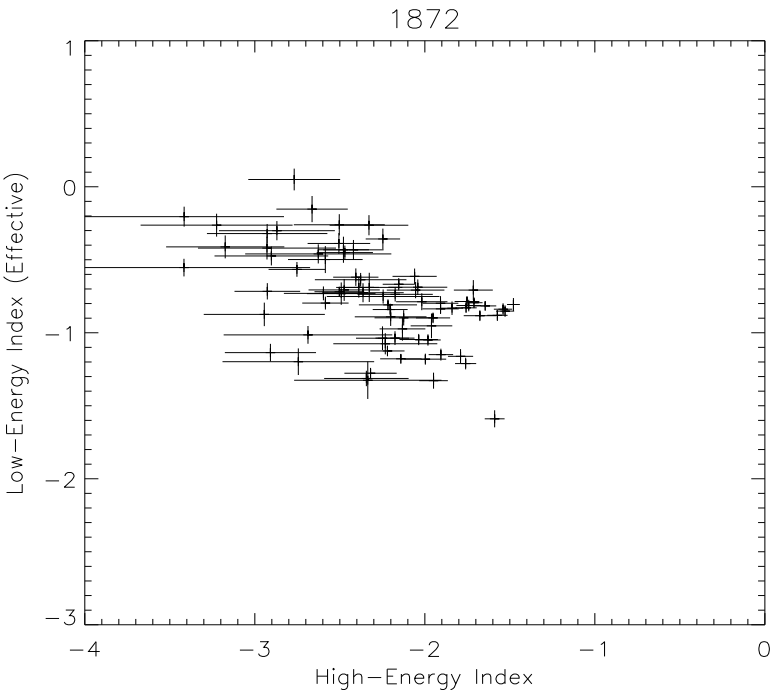

Figure 4.33 Example scatter plot of $\alpha - \beta$ of GRB 920824 (trigger number 1872). Negative correlation is evident.

strong tracking behavior in both $E_{\rm peak}$ and α. Some of these also display overall hard-to-soft behavior, indicated by strong correlations of the parameters with time.

These correlations among the spectral parameters should be accounted for within an emission model. The observed correlations between fitted model parameters indicate possible correlations between physical parameters at the GRB emitting region. For example, according to the synchrotron shock model, $E_{\rm peak}$ should be related to the magnetic field strength and the minimum energy of accelerated electrons (Tavani 1996b), whereas the low-energy index may depend on the electron pitch-angle distribution or density of the absorbing medium (Lloyd-Ronning & Petrosian 2002).

Finally, global correlations between the time-integrated $E_{\rm peak}$, α, β, and energy or photon flux/fluence values (including peak photon flux) were also investigated. We found only one relatively significant correlation, between $E_{\rm peak}$ and total energy fluence, with $r_s = 0.24$ and $P_{rs} = 1.4 \times 10^{-4}$. One of the most highly cited empirical correlations is the $E_{\rm peak} - E_{\rm iso}$ correlation found by Amati et al. (2002). The Amati relation is $E_{\rm p,0} \propto E_{\rm iso}^{0.5}$, where $E_{\rm p,0}$ is the peak energy in the source rest frame, namely, $(1+z)E_{\rm peak}$, and $E_{\rm iso}$ is an isotropic equivalent total emitted energy for a given distance. The relation was found by using a dozen GRBs observed with *BeppoSAX* with known redshift values z. If true, such a correlation can provide strong constraints on the GRB emission mechanism and the fundamental nature of GRBs. It has recently been shown, however, that the Amati relation suffers from a strong selection effect and is greatly inconsistent with a larger set of GRB data obtained with BATSE (Nakar & Piran 2005b; Band & Preece 2005). This was indicated by a limit in observed $E_{\rm peak}$ and energy fluence values (and therefore independent of redshift) that is implied by the Amati relation. Responding to the results, Ghirlanda et al. (2005) reported that if the actual scatter existed in the correlation when it was found, the BATSE events may still be consistent. This claim, however, has been also challenged (Nakar & Piran 2005c). To show how $E_{\rm peak}$ and

energy fluence values in our sample are correlated, we plot $E_{\rm peak}$ vs. energy fluence and number of events in three different energy fluence groups in Figure 4.34. On the scatter plot, we also show the limit on the Amati relation and the maximum 3σ limit derived by Ghirlanda et al. (2005). The events below these lines are inconsistent with the relation. Note that the GRB sample used to test the consistency in Band & Preece (2005) includes many more dimmer events than bursts in our sample. Despite the fact that our sample only consists of bright GRBs, we confirm that most of our events are significantly inconsistent with the Amati limit with good statistics. Even for the 3σ Ghirlanda limit, we observe more inconsistent events than they found in their work. Our well-constrained parameters strongly indicate that the Amati relation is only valid for a small sample of selected events.

4.4.5 BETA Model Fit Results

Since the BETA model is a variation of the BAND model, we did not include the BETA model in obtaining the overall model statistics above. The purpose of this model is to test whether the high-energy power-law index, β, stays constant for the entire duration of a burst, which is expected in the simplest shock acceleration and the GRB emission scenario. Earlier work by Preece et al. (1998a) found that 34% of 122 GRBs investigated were not consistent with the constant-β hypothesis. We note that most GRBs in their sample overlaps with the sample presented herein. In Preece et al. (1998a), the β values that are taken to be constant were the error-weighted average of β obtained from fits to each of time-resolved spectra within bursts. They are different from those obtained by the time-integrated fits, due to the following reasons. Spectra with higher S/N usually have smaller error associated with their fits. Therefore, they have more weight in determining the error-weighted average of β. These spectra, however, may have much shorter integration times,

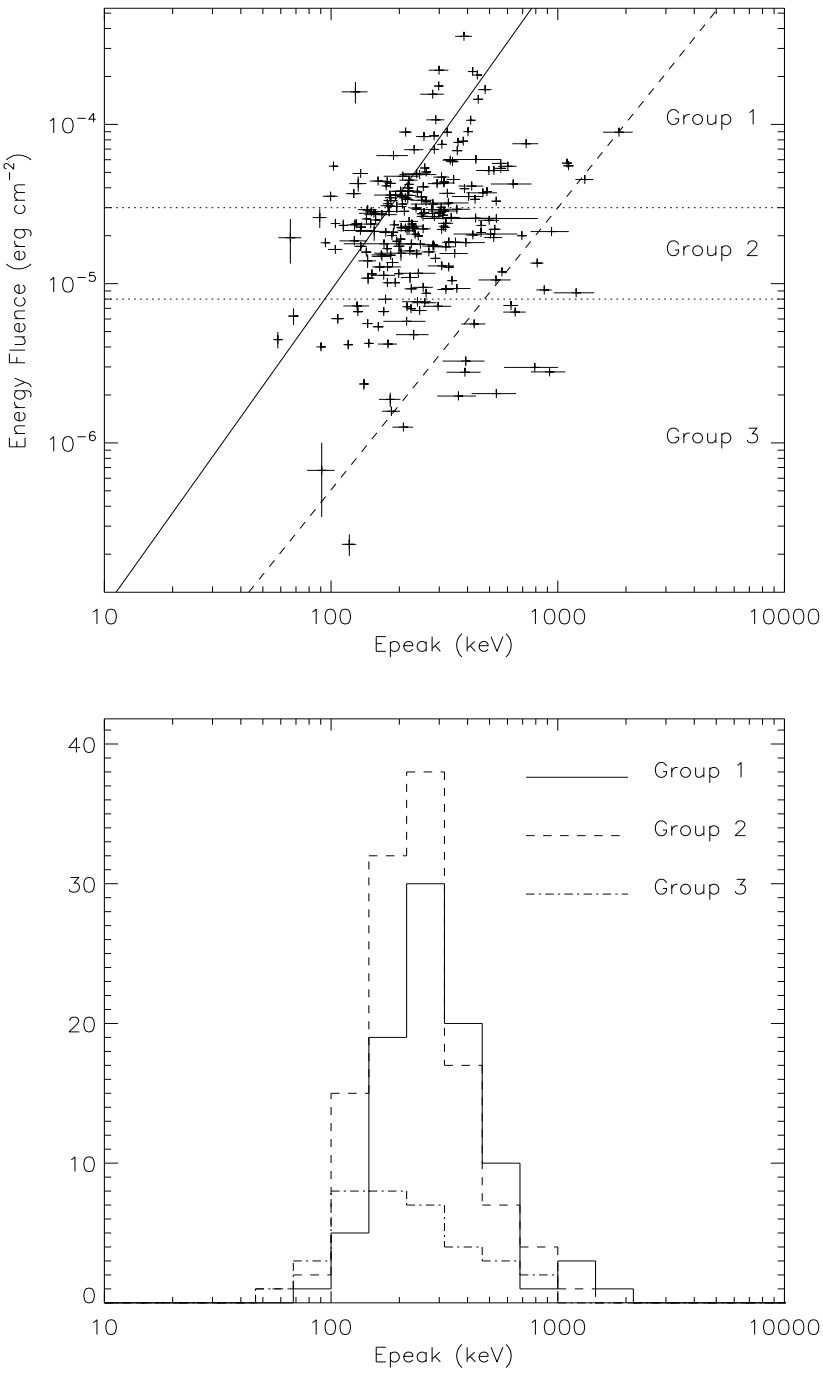

Figure 4.34 [*Top*]Energy fluence in 20 – 2000 keV vs. $E_{\rm peak}$ plot. The Amati relation limit is shown as a solid line and Ghirlanda 3σ limit is shown as a dashed line. Bursts below these lines are inconsistent with the relation. The uncertainties are 1σ. [*bottom*]$E_{\rm peak}$ distributions of three different intensity groups.

because of the binning by S/N as well as the characteristics of HERB data. Despite their large photon flux values, they may not provide large photon fluence counts due to the short time intervals. As discussed in the previous section, the time-integrated spectrum can be obtained by summing over the photon counts (not count rate) rather than error-weighted averaging of parameters. This resulted in the values used to test the constancy of the index in Preece et al. (1998a) to be higher than those obtained from fits to the time-integrated spectra, which are used in this work.

In order to obtain a satisfactory statistic for the time evolution of β, as well as to be consistent with the Preece et al. (1998a) analysis, our sample was limited to events that consist of at least 8 spectra. Additionally, there were some cases in which the time-integrated β values were less than -5 by more than 1σ, and thus lacking the high-energy power-law component (i.e., COMP-like spectra). In these cases, fitting the time-resolved spectra with these small values is not meaningful for our purpose here, and therefore, those events were also excluded. The remaining total number of events in the sample was 210.

To determine whether β is consistent with being constant throughout a burst, we checked the resulting χ^2 of the BETA model fit to each time-resolved spectrum and calculated the corresponding confidence level. The maximum confidence level allowed was set to an equivalent chance probability of one per number-of-spectra in each burst: in other words, one spectrum in each burst was statistically expected not to give an acceptable BETA fit. Consequently, the confidence level was always at least 87.5% (corresponding to a minimum number of spectra of 8). Then, if all but one spectrum within a burst resulted in χ^2 probabilities less than the given maximum confidence level, the burst was considered to be consistent with a constant β. We call these events "constant-β GRBs" and the others "varying-β GRBs" hereafter.

We found that nearly a half of the sample (108 out of 210 GRBs) are varying-β GRBs. The result differs from the result of 34% that was obtained by Preece et al.

(1998a). The time-integrated spectra of the varying-β GRBs are more likely to be best fitted with the COMP model, which has a high-energy cutoff. In Figure 4.35, the distributions of the BAND fit β values (i.e., fit with β as a free parameter) for the time-resolved spectra within the varying-β and constant-β GRBs are compared. A larger number of the varying-β spectra are fitted by smaller β values than the constant-β spectra. It may be the case that the varying-β GRBs contain high-energy cutoff spectra where β is essentially less than -5, which in turn fails the BETA fits with $\beta > -5$. No differences in the $E_{\rm peak}$ and the α distributions are evident between the constant and varying β bursts. In both cases, the most likely

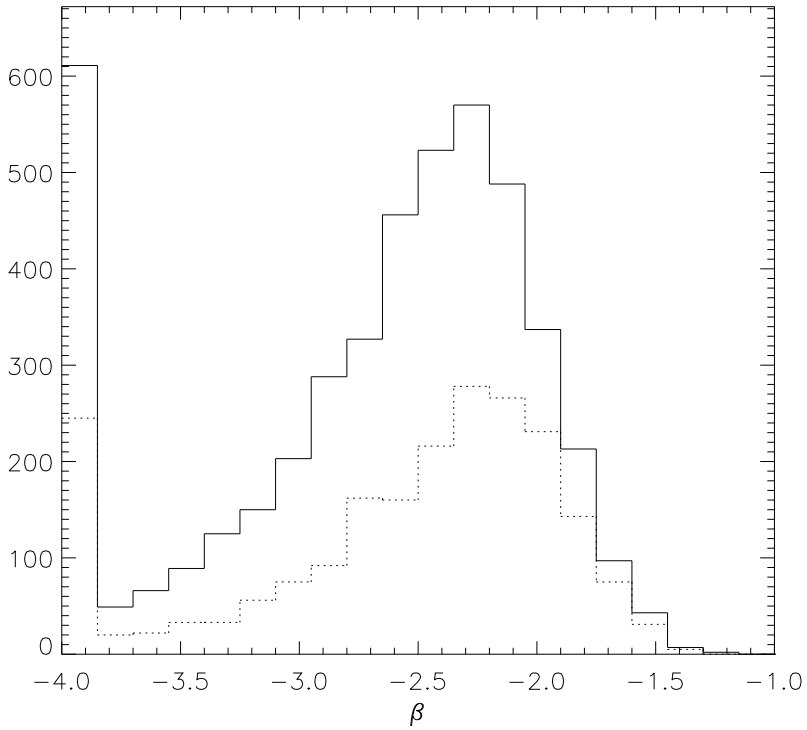

Figure 4.35 The distributions of the BAND fit β values of time-resolved spectra within varying-β (solid line) and constant-β (dotted line) GRBs. The lowest bin includes values lower than –4.

value of β is -2.3 ± 0.3, which agrees with the value found by the BEST model fits. More detailed discussion on the high-energy indices can be found in a later chapter, in §6.3.

4.4.6 Short GRBs

Our sample includes 17 short bursts ($T_{90} \lesssim 2$ s), which are listed in Table 4.13. Short GRBs were previously shown to be spectrally harder than long bursts in terms of the spectral hardness ratio (Dezalay et al. 1992; Kouveliotou et al. 1993) and spectral parameters (Paciesas et al. 2003). The parameter comparison of short GRBs and long GRBs is summarized in Table 4.14. There is no significant difference between the spectral parameters of the short bursts and the rest (long bursts), in

Table 4.13 Summary of time-integrated spectral fit results for 17 short GRBs. 1σ uncertainties are shown in parentheses.

BATSE Trig #	# of spec	BEST Model	A (ph s^{-1} cm^{-2})	$E_{\rm peak}$ [1] (keV)	α, λ_1 [2]	β, λ_2 [3]	$E_{\rm b}$ [4] (keV)	Λ	χ^2/dof
298	1	SBPL	0.0131 (0.0003)	389 (66)	–1.24 (0.04)	–2.40 (0.28)	387 (66)	0.01	10.6/9
444	1	BAND	0.5183 (0.5078)	90 (12)	0.18 (0.65)	–2.11 (0.07)	60 (7)	—	124.1/114
1525	1	SBPL	0.0265 (0.0005)	535 (118)	–0.76 (0.06)	–2.44 (0.20)	375 (59)	0.30	12.7/9
1553	3	SBPL	0.0371 (0.0005)	—	–0.88 (0.03)	–1.74 (0.04)	225 (16)	0.01	119.0/110
2514	1	SBPL	0.0853 (0.0017)	208 (21)	–1.34 (0.04)	–2.76 (0.20)	212 (21)	0.10	106.1/111
2679	1	SBPL	0.0241 (0.0009)	791 (211)	–0.54 (0.05)	–2.13 (0.24)	599 (94)	0.10	127.8/114
3044	1	PWRL	0.0018 (0.0001)	—	–2.20 (0.14)	— (0.00)	—	—	125.8/114
3087	1	BAND	0.2097 (0.0431)	182 (19)	–0.59 (0.19)	–2.22 (0.10)	—	—	125.8/114
3152	2	SBPL	0.0089 (0.0002)	—	–0.99 (0.04)	–1.79 (0.16)	118 (13)	—	139.3/114
3410	1	COMP	0.0662 (0.0204)	120 (8)	–0.78 (0.29)	—	490 (110)	0.01	138.7/114
3412	1	PWRL	0.0155 (0.0005)	—	–2.13 (0.06)	—	—	—	122.4/112
3736	1	COMP	0.0102 (0.0004)	920 (159)	–0.89 (0.08)	—	—	—	115.5/112
6293	1	PWRL	0.1817 (0.0026)	—	–1.25 (0.01)	—	—	—	10.3/10
6617	3	SBPL	0.1325 (0.0013)	259 (32)	–1.13 (0.02)	–3.46 (0.31)	309 (31)	0.30	117.7/114
6668	1	SBPL	0.0166 (0.0010)	—	–1.22 (0.14)	–1.98 (0.19)	149 (37)	0.01	123.0/112
7281	2	BAND	0.2143 (0.0345)	139 (6)	–0.23 (0.14)	–2.54 (0.10)	103 (6)	—	125.2/113
8053	5	BAND	0.4870 (0.0423)	90 (1)	–0.50 (0.07)	–3.68 (0.18)	108 (6)	—	122.0/112

[1] *Fitted* $E_{\rm peak}$ for BAND or COMP, and *calculated* $E_{\rm peak}$ for SBPL.
[2] λ for PWRL, α for BAND, or COMP and λ_1 for SBPL.
[3] β for BAND and λ_2 for SBPL.
[4] *Fitted* $E_{\rm b}$ for SBPL, and *calculated* $E_{\rm b}$ for BAND.

Table 4.14 Median values of the BEST spectral parameters for short and long GRBs. K-S probabilities and the corresponding K-S parameters for two distributions are also shown.

	Low Index		High Index		$E_{\rm peak}$ (keV)		$E_{\rm b}$ (keV)	
	Short	Long	Short	Long	Short	Long	Short	Long
Time Integrated	–0.89	–1.09	–2.22	–2.36	209	255	225	202
$P_{\rm KS}$	0.07		0.42		0.45		0.20	
$D_{\rm KS}$	0.31		0.25		0.26		0.31	
Time Resolved	–0.78	–0.95	–2.38	–2.34	183	284	204	203
$P_{\rm KS}$	0.05		0.54		0.07		0.31	
$D_{\rm KS}$	0.26		0.19		0.28		0.23	

both time-integrated and time-resolved spectra. This may be expected since our sample is limited to the brightest bursts, whereas the sample used in Paciesas et al. (2003) did not have such selection effects. Mallozzi et al. (1995) have found that brighter bursts tend to be harder, and our sample here belongs to the brightest of the five groups defined by Mallozzi et al. (1995). Besides, we used mostly HERB data for the short events as well, which may be missing a substantial portion of the short events due to the accumulation start time of the HERB data. We note that three short events, GRBs 920414, 980228, and 000326 (BATSE trigger numbers 1553, 6617, and 8053), were bright enough to provide 3 – 5 time-resolved spectra and clearly exhibited spectral evolutions. The spectral evolution of GRB 000326 is shown in Figure 4.36, as an example. In two cases (GRBs 920414 and 980228), the spectra evolved hard to soft in all low-energy & high-energy indices and $E_{\rm peak}$, whereas in the other case (GRB 000326; Figure 4.36) we observed tracking behavior in $E_{\rm peak}$ while both indices monotonically decayed. If short GRBs generally evolve hard to soft, the HERB data of short events lacks a coverage of the hardest portions of the events.

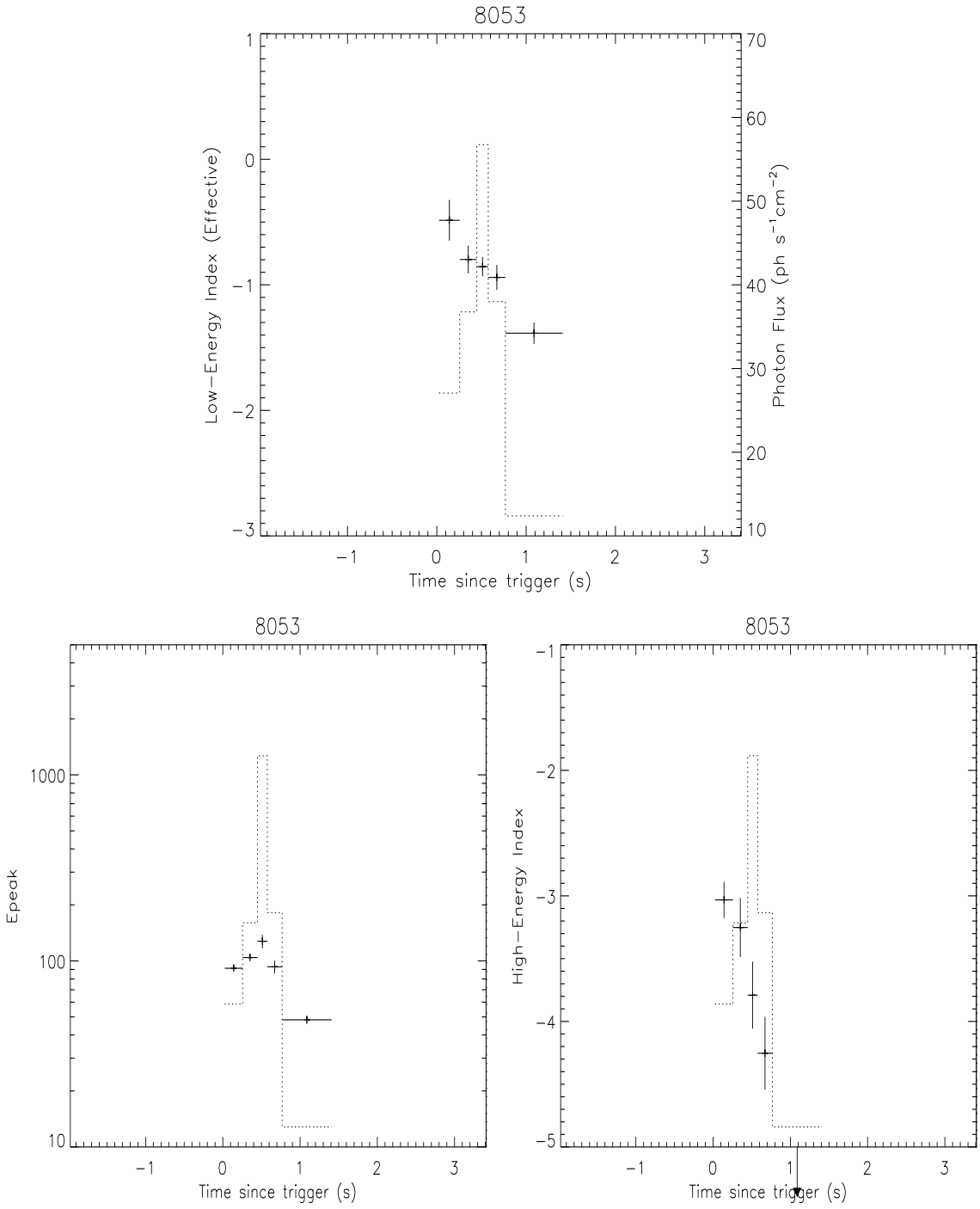

Figure 4.36 Parameter evolution of a short event, GRB 000326 (trigger number 8053). The photon flux histories are over-plotted with dotted lines (top panel, right axis). $E_{\rm peak}$ tracks the photon flux while the indices evolve from hard to soft.

4.5 Summary and Discussion

We have analyzed the large sample of bright BATSE GRBs with high-energy resolution and high-time resolution, using five different photon models. For both time-integrated and time-resolved spectra, we have presented the distributions of each spectral parameter: low-energy and high-energy power law indices, $E_{\rm peak}$, and break energy, determined with the best-fit model to each spectrum, with good statistics.

We confirmed, using a much larger sample, that the most common value for the low-energy index is ~ -1 (SP1; Ghirlanda et al. 2002), and the overall distribution of this parameter shows no clustering or distinct features at the values expected from various emission models, such as –2/3 for synchrotron (Katz 1994; Tavani 1996b), 0 for jitter radiation (Medvedev 2000), or –3/2 for cooling synchrotron (Ghisellini & Celotti 1999), as will be discussed in a later chapter (Chapter 6). The most probable value for the high-energy indices is found to be ~ -2.3 and the parameter can be constrained only if the value is larger than -5. The dispersions in the low-energy and high-energy index distributions were found to be comparable, $\sigma \sim 0.4$.

For the first time, $E_{\rm peak}$ and break energy, at which the two power laws are joined, have been made distinct. We presented the $E_{\rm peak}$ and break energy distributions separately, and found that $E_{\rm peak}$ tends to be harder than the break energy. This is because of the existence of curvature in spectra. $E_{\rm peak}$ becomes break energy only in a sharply broken spectrum. The $E_{\rm peak}$ distribution peaks at $\sim$ 300 keV while that of the break energy peaks at $\sim$ 200 keV, both with very narrow half-width of $100 - 200$ keV. The narrowness of the distributions that we confirmed implies an extremely narrow intrinsic distribution of these parameters, and poses a challenge for the internal shock model (Zhang & Mészáros 2002). There are small populations of GRBs (7% of time-resolved spectra) that have high-energy indices above –2 by

more than 3σ. This indicates that there may be a small tail population of spectra with $E_{\rm peak} \gtrsim 2$ MeV.

It must be noted that the time-resolved spectral analysis results obtained here may be biased by the brighter (higher photon flux) portions of each event because the HERB data type was designed to sample more frequently during the intense episodes. Since the $E_{\rm peak}$ values tend to be correlated with the photon flux in general (Mallozzi et al. 1995), the spectra with higher $E_{\rm peak}$ might be oversampled whereas those with lower $E_{\rm peak}$ are likely to be under-sampled. This may explain the differences observed in the $E_{\rm peak}$ distributions of time-integrated and resolved spectra. Similarly, the low-energy indices also tend to correlate with $E_{\rm peak}$; therefore, the same type of bias may exist in the low-energy index distribution as well.

We have also explored time-integrated spectra by reconstructing them from the time-resolved spectra, and identified cases where the true integrated spectra deviate from the simple broken power-law model, due to spectral evolution within the integration time. Therefore, fine time resolution data are crucial to more accurately represent the spectral shape using a relatively simple model. Significant correlations among parameters are also observed in some GRBs. The most evident positive correlation is found between $E_{\rm peak}$ and the low-energy index, in 27% of GRBs considered. Since our parameter sets are well constrained and unbiased by photon models, the correlations found are more likely to reflect intrinsic properties of GRBs, rather than the instrumental or any other systematic effects, as has been pointed out (e.g., Lloyd-Ronning & Petrosian 2002). In addition, a mild global correlation between $E_{\rm peak}$ and energy fluence in our sample was found. The significance of the correlation is much lower than what was found previously by Lloyd et al. (2000). Finally, we found no significant difference between the spectral parameters of 17 short bursts and long bursts in our sample. In addition, spectral evolutions, hard-to-soft or tracking, were found in three of the short events with enough number

of time-resolved spectra. These evolution patterns are often observed in individual peaks of long GRBs. With the use of our results, the existing models of the GRB acceleration and emission mechanisms can be tested in a photon model-independent manner. The spectral database obtained here also allows for the spectral evolutions within each event to be taken into consideration when constraining such models. In Chapter 6, we use our spectral database to examine some of the proposed GRB acceleration and emission models.

CHAPTER 5

BROADBAND SPECTRAL STUDY OF HIGH-ENERGY GRBs

High-energy spectra of GRB prompt emission observed with *SMM* (Harris & Share 1998) or with other experiments aboard the *CGRO*, such as EGRET (Hurley et al. 1994; Catelli et al. 1998; Dingus et al. 1998) and COMPTEL (Hanlon et al. 1994; Kippen et al. 1998), have indicated that GRB continuum spectra extend up to MeV – GeV energies. However, in order for bursts to be observed at high energies, they must produce sufficiently high photon counts in the high energy range, and they must be in the field of view of a high-energy detector. Consequently, the number of GRBs observed in the energy band above the BATSE energy cut-off of $\sim$ 2 MeV is very small, compared with the lower energy observations. EGRET and COMPTEL observed a few dozen BATSE-triggered GRBs, most of which are included in the sample of the bright BATSE bursts presented in Chapter 4. GRB spectra in the MeV to GeV range are usually well-described by a single power law with an index in the approximate range of -1 to -4 (Schneid et al. 1992; Kwok et al. 1993; Hurley et al. 1994; Hanlon et al. 1994; Schneid et al. 1995; Catelli et al. 1998; Kippen et al. 1998; Briggs et al. 1999; Wren et al. 2002). This range is in agreement with the distributions of the high-energy power-law indices observed with BATSE (Figure 4.26).

Previously, we showed in Chapter 4 that there are many BATSE spectra in which $E_{\rm peak}$ lies very close to or above the upper energy bound of the LAD energy range

($\gtrsim$ 2 MeV). For such cases, the LAD data alone cannot adequately determine either $E_{\rm peak}$ or the high-energy power law index. Moreover, the ability to identify the high-energy power law component using LAD data alone is limited, since the LAD sensitivity decreases significantly toward the upper energy bound (see Figure 2.5). Therefore, observations of spectra extending to much higher energies with reasonable sensitivity are needed in order for these parameters to be well determined. Combining BATSE data with multi-MeV observations by another high-energy detector enables such a broadband study.

Broadband spectral analyses of a few BATSE GRBs have been presented in the literature, using the data obtained with the *CGRO* instruments (Schaefer et al. 1998; Briggs et al. 1999). However, those broadband spectra were superpositions of the deconvolved photon spectra that were obtained by analyzing each dataset separately with various photon models. Deconvolved photon counts are model dependent, and a spectrum constructed by combining individually deconvolved spectra can be quite different from that obtained properly by simultaneously fitting a common model to all datasets.

The EGRET Total Absorption Shower Counter (TASC) was one of the few instruments capable of observing GRBs in the > 1 MeV energy band with high energy resolution, as described in Chapter 2. Some BATSE-triggered GRBs were also observed with the TASC in its BURST mode (initiated by the BATSE trigger), as well as the continuous SOLAR mode, independently from the EGRET spark chamber events. Unlike the spark chamber, TASC was sensitive to all directions and, therefore, observed many more events than the spark chamber. Since the TASC provides spectra in the range $\sim 1 - 200$ MeV, broadband GRB spectra spanning four decades of energy can be obtained by combining LAD and TASC data. Such spectra, in at least one case, resulted in the discovery of a distinct multi-MeV spectral component apart from the extrapolated sub-MeV BATSE component (González et al. 2003, see

§5.4). In this chapter, we first present the time-integrated broadband spectral analysis of 15 bright BATSE GRBs using LAD and TASC data in §5.1 – §5.3. Then in §5.4, we discuss the analysis of GRB 941017, the GRB with the distinct high-energy component mentioned above, using the COMPTEL data in addition to the LAD and TASC data. We will show that the COMPTEL observation of the event is in accordance with the MeV spectra observed with TASC.

5.1 Selection Methodology

The TASC data were searched for the trigger times of 43 bright BATSE GRBs with peak photon flux of at least 10 photons cm^{-2} s^{-1} in the 1024 ms timescale and with BATSE channel 4 energy fluence (> 300 keV) of at least 5.0×10^{-5} ergs cm^{-2}. The flux and fluence values were taken from the 4B (Paciesas et al. 1999) and the current[1] BATSE catalog. Among those, only 15 GRBs were identified to have significant detections in the TASC data, and therefore, TASC DRMs were calculated for these bursts. The properties of these events are listed in Table 5.1 along with the selected time and energy intervals described below.

For this analysis, we use TASC SOLAR data, which provides 32.768 second time resolution. Since all of the 15 events are very strong and most have durations (T_{90}) longer than 33 seconds, the time resolution is adequate for time-integrated spectral analysis. As for the selection of corresponding BATSE data, we use the LAD CONT data, with 2.048 second time resolution. The CONT time intervals can provide a sufficient match to the SOLAR data time intervals, which often begin before the BATSE trigger time. The time intervals chosen for the analysis were determined based upon the detection significance above background for either the LAD or TASC lightcurves. Each of the 15 events is also included in the LAD spectral analysis

[1]Available online at http://gammaray.nsstc.nasa.gov/batse/grb/catalog/current/

Table 5.1 General properties of GRBs included in the LAD–TASC joint spectral analysis.

				Time Interval		LAD Energy		TASC Energy	
GRB Name	BATSE Trig #	Trig SOD (UT,s)	LAD #	Start (s)	End (s)	Start (keV)	End (MeV)	Start (MeV)	End (MeV)
910503	143	25452	6	–9.8	88.5	36.6	1.81	1.29	201
910601	249	69734	2	15.9	48.6	37.0	1.82	1.32	198
920525	1625	12421	5	–18.4	47.1	32.6	1.85	1.30	195
920622	1663	25504	4	–30.9	34.6	31.9	1.81	1.32	195
920902	1886	1736	5	–10.2	120.8	32.7	1.85	1.39	196
930506	2329	53571	3	–33.1	32.5	44.2	1.85	1.18	167
940217	2831	82962	2	–8.2	188.4	37.1	1.82	1.25	187
940703	3057	16846	1	–1.0	97.2	33.3	1.88	1.28	139
940921	3178	18493	2	–25.6	72.6	28.1	1.82	1.31	178
941017	3245	37173	4	–51.2	210.9	31.8	1.81	1.25	199
950425	3523	919	6	–23.6	107.5	36.3	1.80	1.57	197
970315	6124	56454	2	–15.8	82.5	37.1	1.82	1.51	189
980923	7113	72647	7	–20.0	78.7	33.4	1.92	1.44	131
990104	7301	57753	7	–4.5	257.7	29.3	1.96	1.45	202
990123	7343	35216	0	–0.1	98.3	33.1	1.81	1.40	128

presented in Chapter 4, although the data type used here (hence the time and the energy intervals) may be different. In Figure 5.1, we present examples of LAD and TASC lightcurves, in which the background model and the time interval used are also shown. The background models were determined by fitting a low-order polynomial function to the spectra accumulated for several hundreds of seconds before and after the burst interval. The time interval for each event is listed in columns 5 and 6 of Table 5.1.

Energy interval selection for LAD CONT data are described in §4.1.5, and the intervals are also shown in Table 5.1 (columns 7 & 8). For the TASC SOLAR data, the lowest 6 – 7 channels are always excluded to assure the exclusion of an electronic cutoff. This translates into a lowest energy of $\sim$ 1.3 MeV (Table 5.1, column 9). In addition, the uppermost 10 – 20 channels are also excluded, depending upon the gain of the detector at the time of the event. The resulting upper bound for the TASC energy range was $\sim$ 130 – 200 MeV (Table 5.1, column 10). Note that overlap in energy between the LAD and TASC datasets of a few hundred keV exists in each event.

5.2 Spectral Analysis

The TASC data were converted into the BATSE BFITS format, and the BATSE spectral analysis tool RMFIT (see §4.2.1) was used also for this analysis. For consistency, the same set of photon models used to analyze the BATSE GRBs in Chapter 4, namely, the power law (PWRL; §4.2.2.1), the empirical GRB function with and without the high-energy power law (BAND and COMP, respectively; §4.2.2.2 and 4.2.2.4), and the smoothly-broken power-law (SBPL; §4.2.2.5) with its subsets were fitted to the joint LAD–TASC dataset as well. Since we are only analyzing the time-integrated spectra, the GRB function with fixed β, the BETA model (§4.2.2.3),

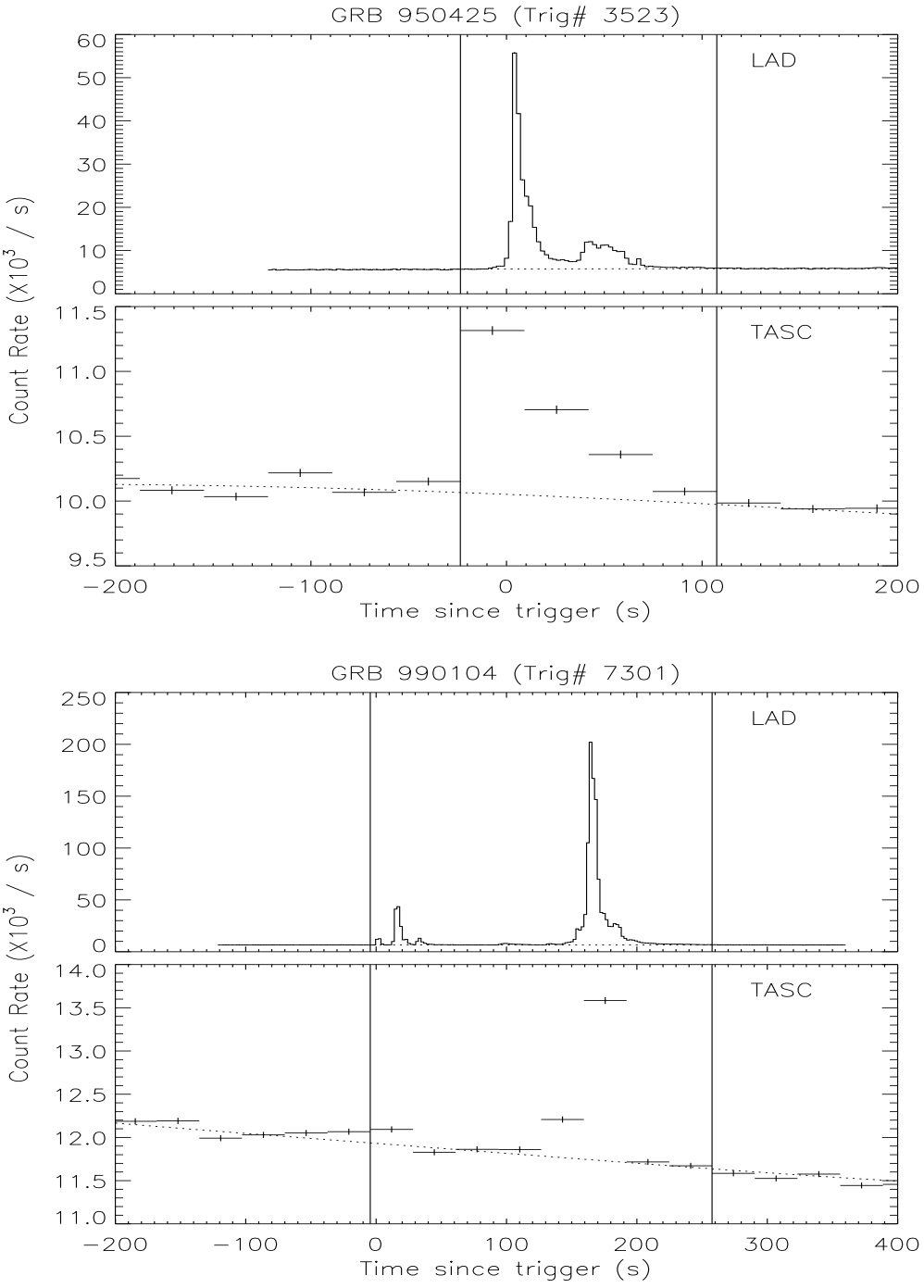

Figure 5.1 LAD and TASC lightcurves of GRBs 950425 and 990104. The dotted lines show background models and the vertical solid lines indicate the selected integration time intervals.

is not used. The PWRL is expected to result in very poor fits to the joint spectra, because of the broad energy coverage, as well as the fact that our sample contains the very brightest of all BATSE GRBs, which have been shown to have a smoothly broken power law behavior (their BEST models in the LAD analysis are SBPL or BAND).

In order to account for uncertainties in the effective areas of the two detectors, we add an effective area correction (EAC) term to each fit: this is a multiplicative factor, to normalize the data of the second detector to those of the first detector. In our case, the EAC factor always normalizes the TASC data to the LAD data. The EAC values vary from event to event and are determined by simultaneously fitting the BAND model to both datasets with the EAC term as a free parameter. Once the EAC factor is found, it is kept fixed in the subsequent final fits. Between the LAD and the TASC datasets, they are always found to be unusually large (~ 0.5). We investigate this issue further in §5.3.1.

5.3 Analysis Results

As we presumed, the PWRL and COMP models resulted mostly in poor fits due to the wide energy range and brightness of the bursts. Following the LAD GRB analysis in Chapter 4, we determined the best-fitted (BEST) models for the 15 joint spectra as well. The method of determining the BEST models is described in §4.4.2. The spectral parameters of the BEST models are presented in Table 5.2. It should be noted that due to the high photon counts of these events, uncertainties in the data are dominated by systematics, which can be large, especially at lower energies in the LAD data.

To compare these parameters with the parameter distributions of the larger sample of bright BATSE bursts presented in the previous chapter, we over-plot in

Table 5.2 Summary of LAD–TASC joint fit results for time-integrated spectra. 1σ uncertainties are shown in parentheses.

		Spectral Fit Parameters							
BATSE Trig #	BEST Model	A (ph s^{-1} cm^{-2})	$E_{\rm peak}$ [1] (keV)	α, λ_1 [2]	β, λ_2 [3]	$E_{\rm b}$ [4] (keV)	Λ	EAC	χ^2/dof
143	SBPL	0.0116 (0.0000)	612 (28)	–1.18 (0.01)	–2.25 (0.03)	467 (17)	0.20	0.63	204.4/224
249	BAND	0.0567 (0.0003)	515 (8)	–1.04 (0.01)	–3.08 (0.10)	562 (26)	—	0.71	288.0/221
1625	BAND	0.0151 (0.0003)	427 (18)	–0.88 (0.03)	–2.45 (0.10)	311 (23)	—	0.19	250.1/221
1663	SBPL	0.0174 (0.0001)	386 (20)	–1.11 (0.01)	–2.24 (0.04)	286 (11)	0.20	0.73	228.9/220
1886	BAND	0.0043 (0.0001)	469 (26)	–0.41 (0.05)	–2.25 (0.11)	284 (21)	—	0.70	110.8/219
2329	SBPL	0.0220 (0.0001)	>167000	–1.26 (0.01)	–1.85 (0.02)	349 (22)	0.30	0.50	226.6/208
2831	BAND	0.0203 (0.0001)	553 (12)	–1.17 (0.01)	–2.88 (0.10)	580 (35)	—	0.49	257.7/222
3057	SBPL	0.0315 (0.0001)	585 (29)	–1.15 (0.01)	–2.27 (0.03)	393 (13)	0.30	0.33	211.8/206
3178	BAND	0.0067 (0.0002)	684 (65)	–1.17 (0.03)	–2.30 (0.13)	478 (74)	—	0.73	218.6/217
3245	SBPL	0.0086 (0.0001)	250 (17)	–1.07 (0.02)	–2.07 (0.03)	185 (7)	0.10	0.44	183.4/215
3523	SBPL	0.0095 (0.0001)	2150 (1568)	–1.03 (0.02)	–2.01 (0.03)	479 (30)	0.30	0.69	203.8/215
6124	BAND	0.0143 (0.0004)	392 (19)	–0.90 (0.03)	–2.77 (0.29)	345 (55)	—	0.63	207.3/215
7113	BAND	0.0639 (0.0005)	379 (5)	–0.66 (0.01)	–2.65 (0.05)	294 (8)	—	0.37	267.7/198
7301	BAND	0.0190 (0.0006)	696 (119)	–1.31 (0.05)	–2.40 (0.09)	560 (104)	—	0.35	202.5/217
7343	SBPL	0.0256 (0.0001)	517 (16)	–1.04 (0.01)	–2.58 (0.03)	436 (10)	0.30	0.68	400.4/200

[1] *Fitted* $E_{\rm peak}$ for BAND, and *calculated* $E_{\rm peak}$ for SBPL.
[2] α for BAND and λ_1 for SBPL.
[3] β for BAND and λ_2 for SBPL.
[4] *Fitted* $E_{\rm b}$ for SBPL, and *calculated* $E_{\rm b}$ for BAND.

Figures 5.2 and 5.3 the BEST model parameters of the jointly-analyzed events on top of the time-integrated LAD spectral parameter distributions. It is evident in terms of the photon fluence (Figure 5.2, top panel) that these 15 events are in the very brightest group of all BATSE GRBs. No bias or tendency is seen in the distributions of spectral indices (Figure 5.2, bottom panels). It is clear, however, that the fitted values of the $E_{\rm peak}$ and break energy for the 15 events belong to the higher end of the BATSE distributions (Figure 5.3). A likely reason for this is because our sample selection was based on the high fluence above 300 keV. The photon fluence and the energy fluence determined with the joint spectra were consistent with the values found by extrapolating the LAD-only spectra up to $\sim$ 200 MeV. We also note that we do not find significant correlation between photon fluence and $E_{\rm peak}$ or break energy within our sample.

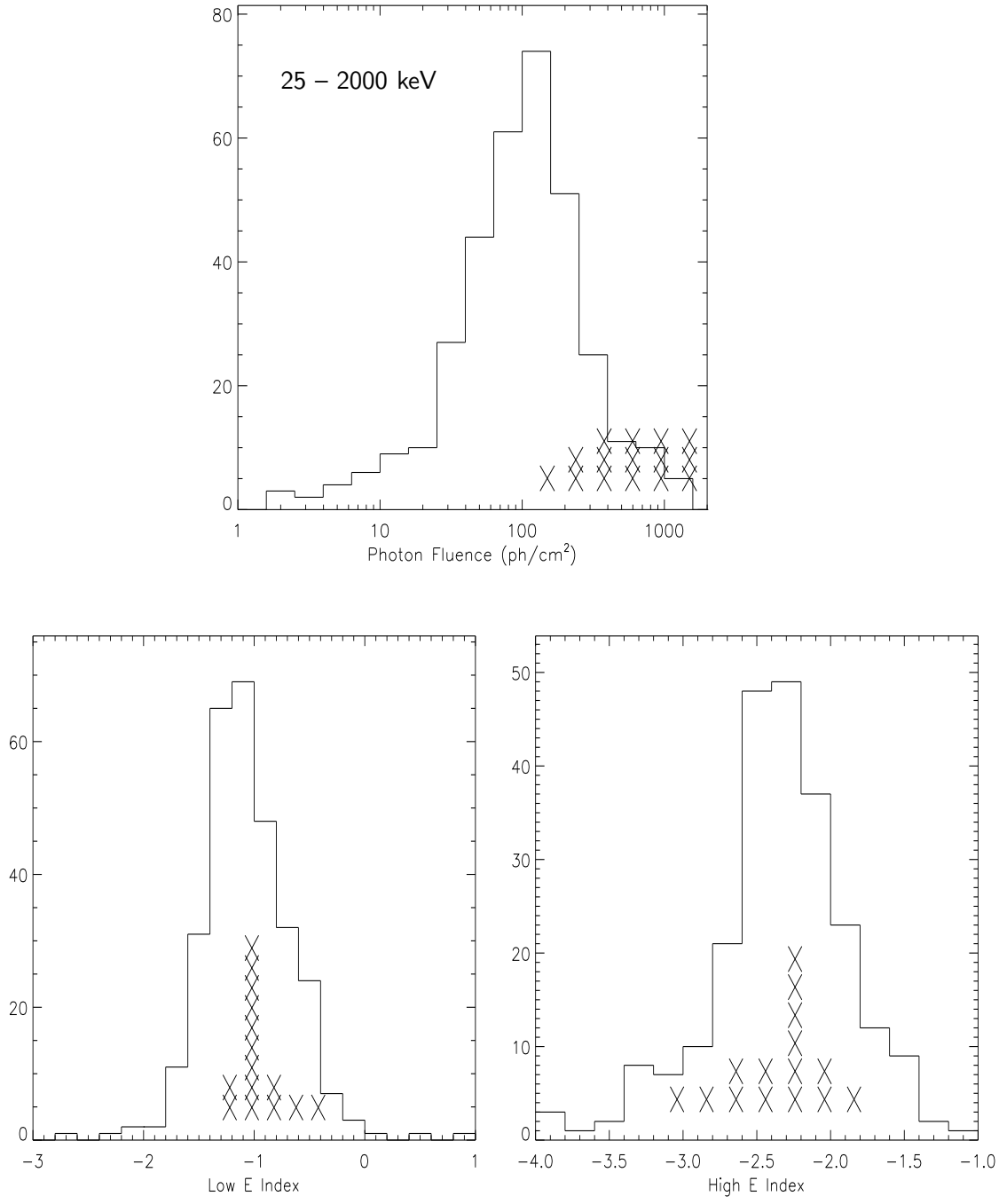

Figure 5.2 Parameter distribution comparisons of 15 joint events with 342 bright BATSE GRBs. The crosses represent photon fluence (*top*) and spectral indices (*bottom*) of jointly analyzed events, and histogram shows the distribution of LAD events.

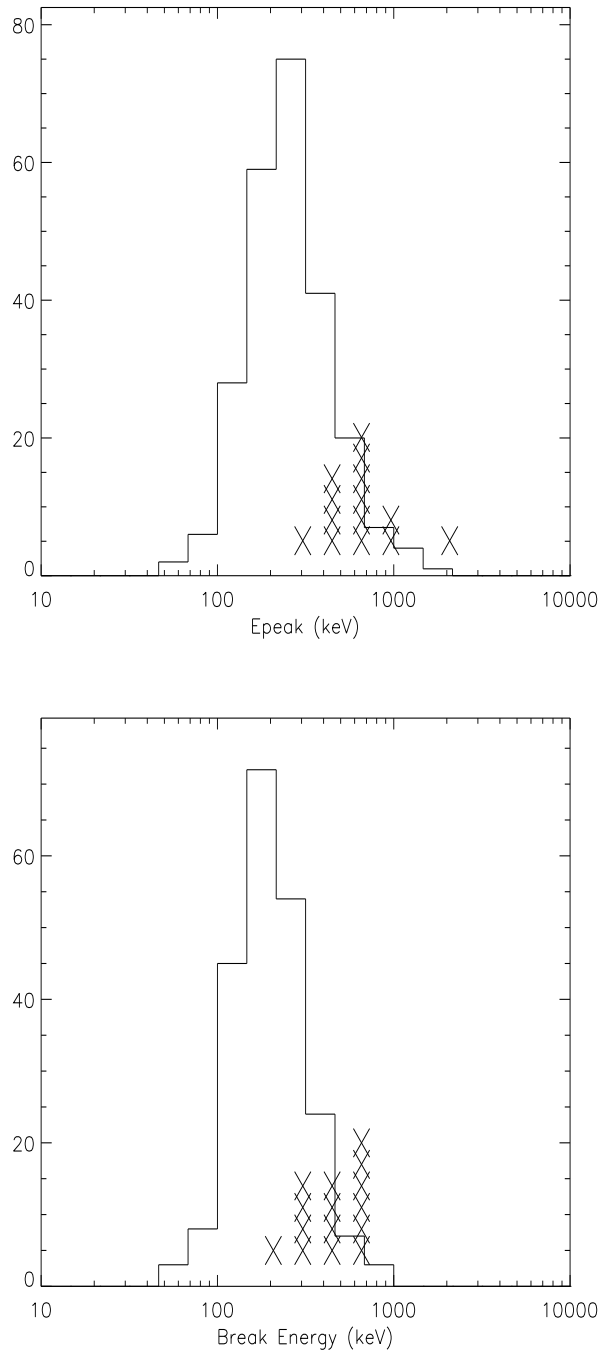

Figure 5.3 Parameter distribution comparisons of 15 joint events with 342 bright BATSE GRBs. The crosses represent $E_{\rm peak}$ (*top*) and break energy (*bottom*) values of jointly analyzed events, and histogram shows the distribution of LAD events.

To illustrate the improvements in parameter constraints as a result of the joint analysis, in comparison with the single-detector analysis, we show the spectral parameters determined by the joint fits and the individual detector fits in Figures 5.4 and 5.5. In the single-detector analysis, the LAD data were fitted with the BEST model listed in Table 5.2 while the TASC data were fitted with PWRL with pivot energy ($E_{\rm piv}$) of 10 MeV. The PWRL indices of TASC are compared with the high-energy indices of the BEST models in Figure 5.4 (bottom panel). In most bursts, the parameters are determined much better with the joint analysis than with the individual cases.

As seen in Figure 5.4, the low-energy spectral indices are already well constrained by the LAD data alone and are the least affected by the addition of TASC data. On the other hand, the high-energy indices are much more constrained by the joint analysis, as expected. The values determined by the joint analysis are nearly always found between the values derived from the LAD-only and TASC-only analyses. In cases where the LAD-determined index differs from the jointly determined index by more than a few σ (i.e., trigger numbers 249 and 2831), the spectral break energy was also found to change significantly (Figure 5.5, bottom panel). The $E_{\rm peak}$ values found by the joint analysis are consistent with those found by the LAD-only fits, although in many cases it seems to settle in the higher ends of the values determined by LAD. We observed one case, trigger number 3523, in which the value of $E_{\rm peak}$ determined with the joint fit was less constrained than the one found with the LAD-only fit. This is due to the high-energy index being very close to -2 (-2.01 ± 0.03), making the constraint of $E_{\rm peak}$ very difficult, by definition. There was one event (trigger number 2329) for which the $E_{\rm peak}$ could not be determined even with the joint spectra because the high-energy index was above -2 by 7.5σ (see Table 5.2) and therefore, the νF_ν spectrum did not peak within the energy range. This indicates

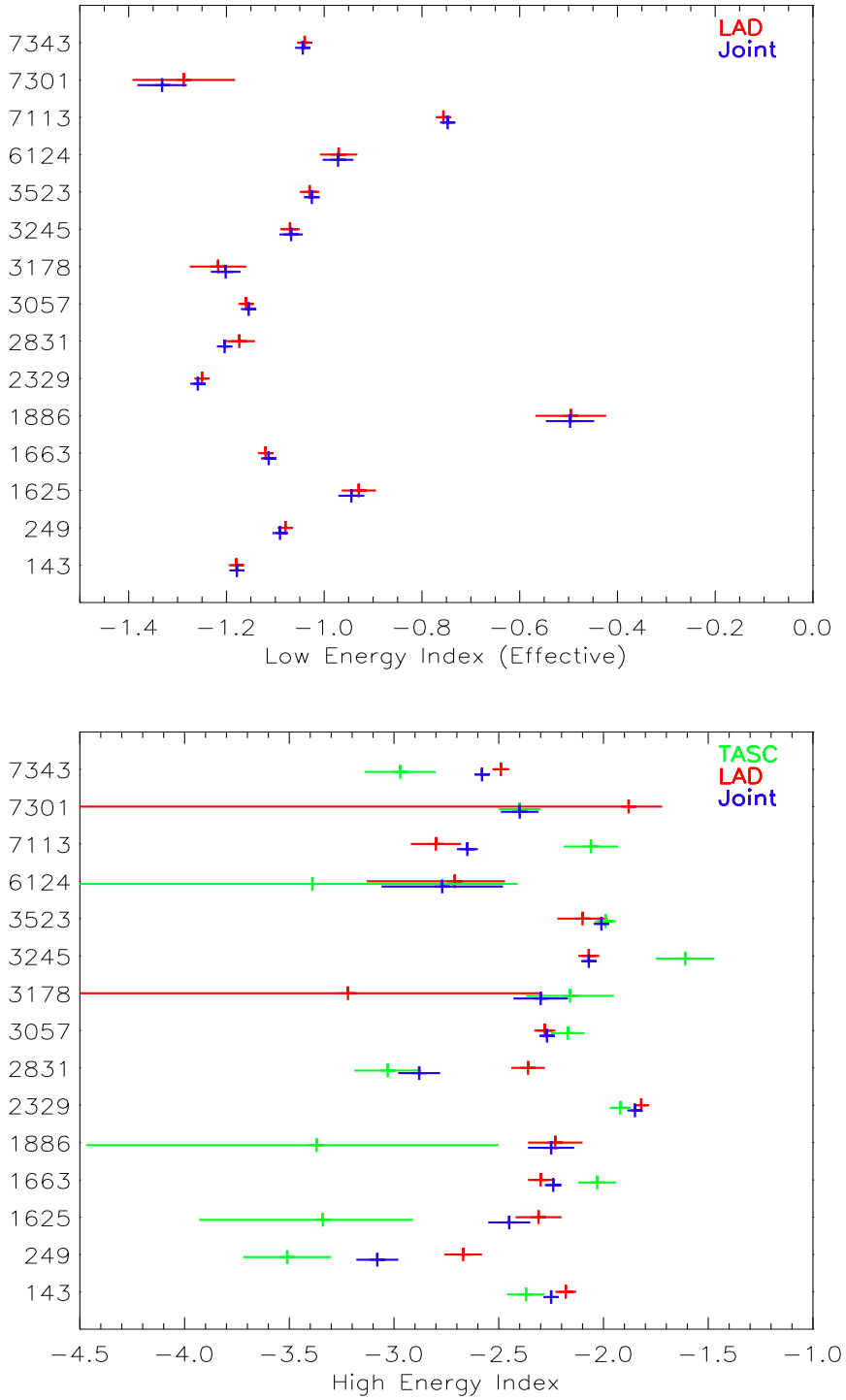

Figure 5.4 Effective low-energy indices (*top*) and high-energy indices (*bottom*) determined by joint analysis and individual analysis of LAD and TASC. Left axis shows the event trigger numbers.

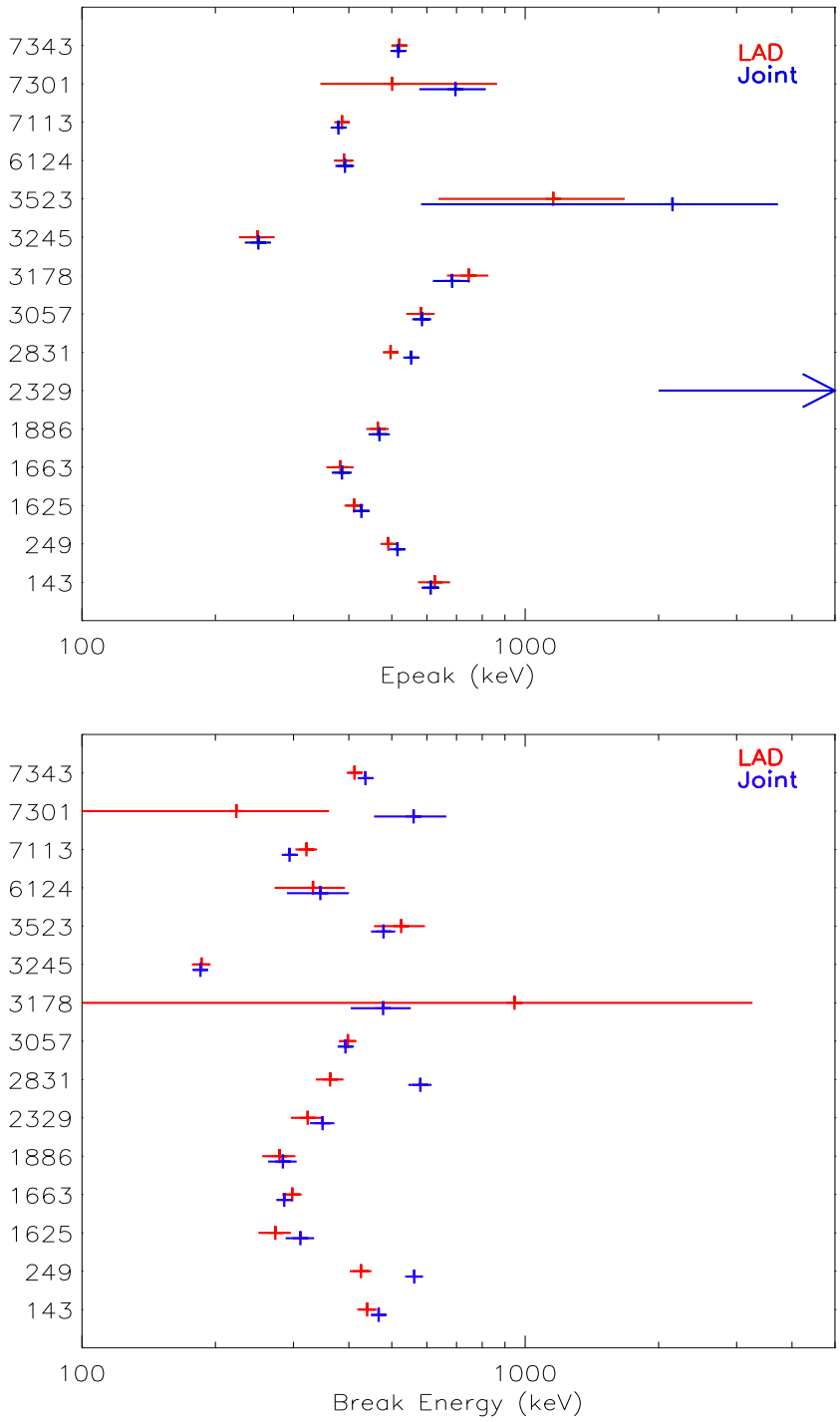

Figure 5.5 $E_{\rm peak}$ (*top*) and break energy (*bottom*) values determined by joint analysis and individual analysis of LAD and TASC. Left axis shows the event trigger numbers. For 2329, $E_{\rm peak} > 167$ MeV.

a lower limit in $E_{\rm peak}$ of 167 MeV for this event. It should be noted that the time-resolved joint analysis for this event in a time interval of 1 – 23 seconds also found that the high-energy indices were always above -2 by at least 1σ (González et al. 2004; Kaneko et al. 2005).

Although the spectral fits presented in Table 5.2 were all sufficiently good (large χ^2 were due to systematics in LAD), indications of a high-energy excess were found in the residual patterns of at least two spectra (trigger numbers 1886 and 3245). This was much more evident in the spectrum of 3245; the lightcurves and the νF_ν spectral fit of this event are shown in Figure 5.6. The high-energy excess above 10 MeV is seen in sigma residuals of the spectrum and is also evident from the lightcurve. For this event, fitting an additional high-energy PWRL together with the BEST model resulted in an improvement in χ^2 of 18 (for Δdof = 2), corresponding to a chance probability of 10^{-4}. In the case of the other burst, 1886, the corresponding χ^2 improvement is only about 4, which translates into a chance probability of 0.03. However, in either case, the additional high-energy PWRL indices could not be well determined (1σ uncertainties > 1). The time-resolved analysis of 3245, in fact, revealed a high-energy spectral component that deviates from the extrapolated keV LAD component, with much higher significance (González et al. 2003). The distinct high-energy component of 3245 (GRB 941017) is discussed in detail in §5.4.

5.3.1 Effective Area Correction Issue

When simultaneously analyzing spectra from multiple detectors, normalization factors between detectors may be required, due to uncertainties in the effective area of each detector. Usually only about 10% difference between datasets is expected (Briggs et al. 1999). In our joint analysis, however, we find the discrepancy between the LAD and TASC data to be relatively large, $\sim$ 30 – 80%, as indicated by the

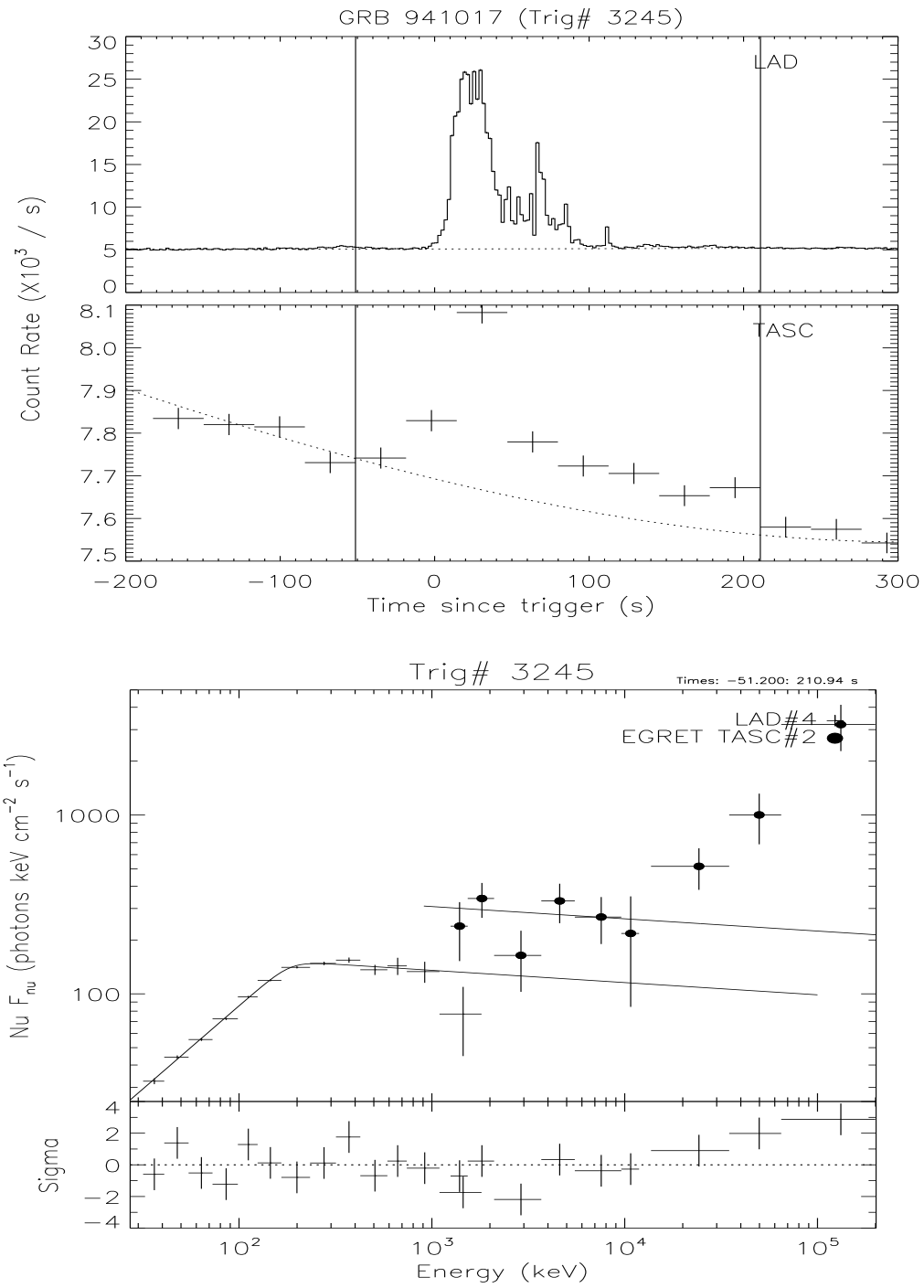

Figure 5.6 Lightcurves (*top*) and time-integrated νF_ν spectrum (*bottom*) of LAD and TASC of GRB 941017 (trigger number 3245). Dotted lines in the lightcurves are background models. The spectra were fitted with the BEST model shown in solid line in the spectrum (Table 5.2). The normalization

EAC factors (see column 9 of Table 5.2). Disagreements between LAD and TASC data were also previously found in some of the composed spectra (Schaefer et al. 1998; Briggs et al. 1999), although the DRMs used here have been newly calculated. As mentioned earlier, the TASC effective area depends highly upon the incident angles of events, because of the geometric area of the NaI crystal as well as varying amount of intervening spacecraft material (see Figure 2.8). Therefore, we investigated the EAC factors in our sample in terms of the incident angles, as well as other potential contributing factors, such as the TASC live time, event brightness, energy range, and spectral parameters. No apparent correlation was found in any of those; however, we noticed a striking resemblance between the patterns in a plot of EAC as a function of incident zenith angle (shown in Figure 5.7) and in the effective area plot (Figure 2.8). This indicates that the discrepancy is more severe when the

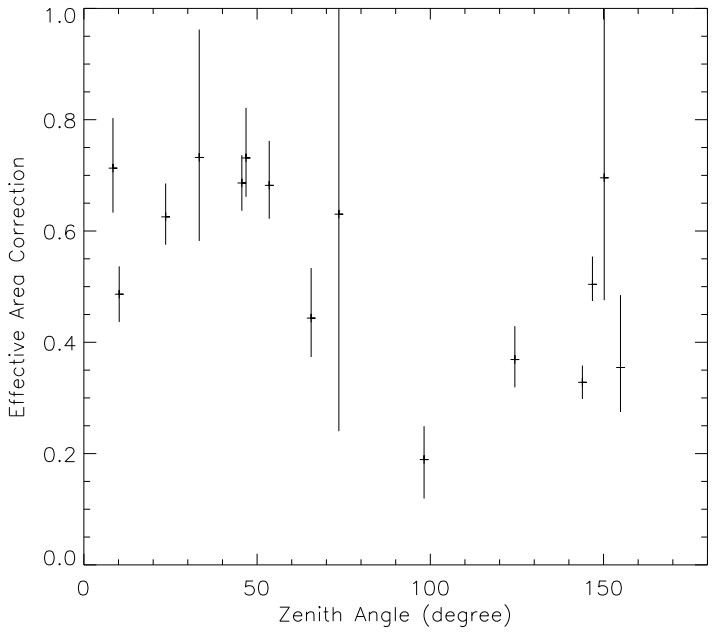

Figure 5.7 Effective area correction values of 15 events as a function of incident zenith angle.

effective area is smaller. As a matter of fact, a disagreement between the calculated effective area and the actual experimental value was found at the time of the TASC instrument calibration, which was attributed to the *CGRO* mass model underestimating the intervening material (Thompson et al. 1993). The EAC factors in our analysis were always found to be less than 1, meaning count rates in the TASC data are overestimated. The count overestimation becomes more apparent when there is larger amount of intervening material, namely, when the effective area is smaller. Consequently, we conclude that the *CGRO* mass model used to determine the effective area indeed underestimates the intervening material, at each zenith angle, resulting in overestimation of the photon counts observed with TASC.

5.4 GRB 941017: A Distinct MeV Spectral Component

For one event (GRB 941017; trigger number 3245) out of our sample of 15 bursts, a distinct multi-MeV spectral component has been identified with time-resolved joint spectral analysis of LAD and TASC (González et al. 2003). The component was delayed with respect to the keV component and found to last much longer than the low-energy component. The νF_ν spectral evolution of the event is shown in Figure 5.8, in which the spectra were fitted with the BAND model, plus an additional high-energy PWRL (with $E_{\rm piv} = 30$ MeV). Fitting the additional high-energy PWRL resulted in a significant improvement in χ^2, with a chance probability of $10^{-7} - 10^{-4}$ in each time interval. Very interestingly, the high-energy component remained constant with index $\lambda \sim -1$ while the brightness of the keV component decayed a few orders of magnitude. The keV component evolved from hard to soft, with $E_{\rm peak}$ and α changing from 500 to 10 keV and from –0.8 to –1.5, respectively. The total energy fluence (< 200 MeV) was 6.5×10^{-4} erg cm^{-2}, which is more than three times larger than the value estimated from the LAD data alone.

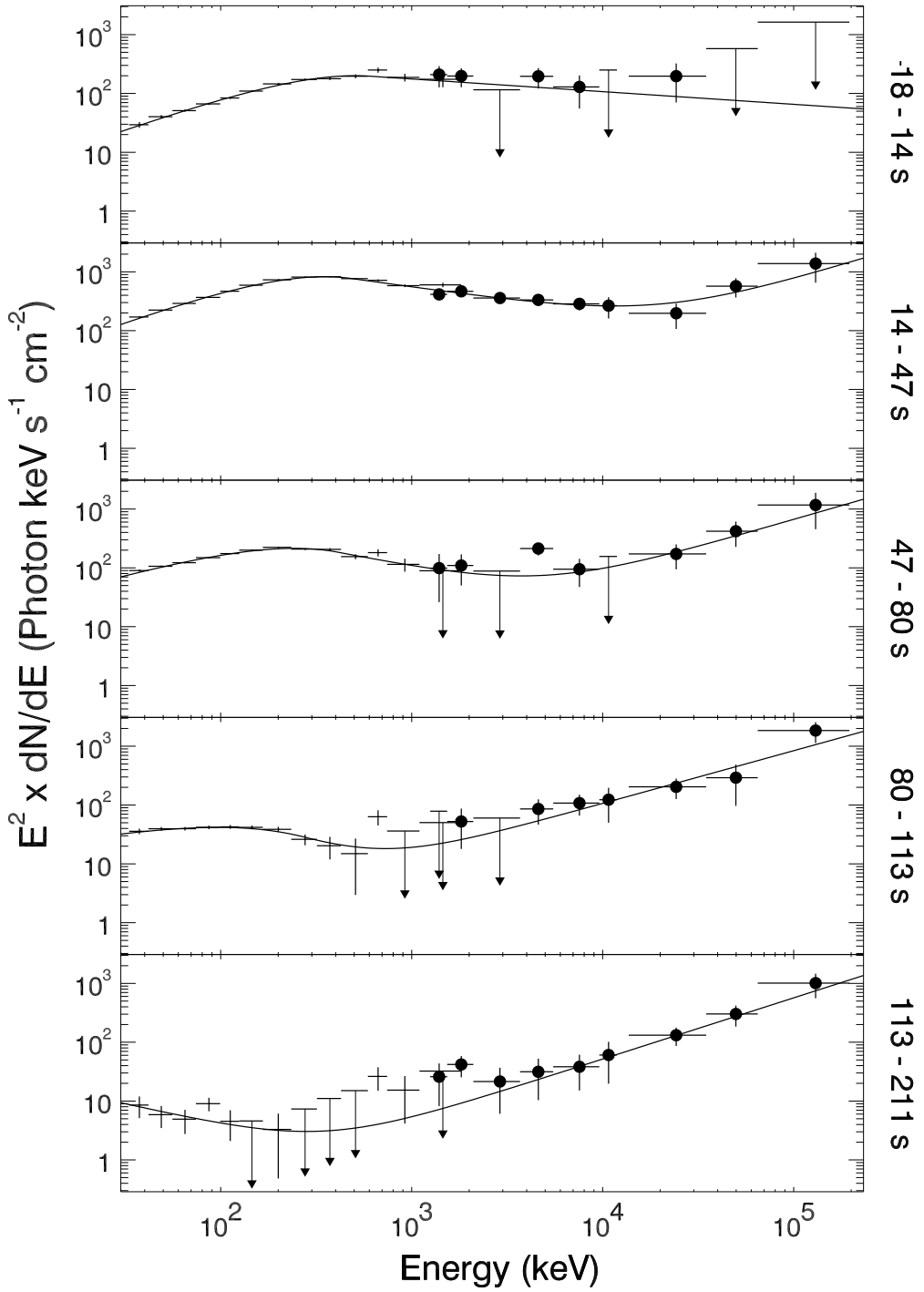

Figure 5.8 Spectral evolution of GRB 941017, shown in νF_ν spectra. LAD data (plus sign) and TASC data (filled circle) are fitted with BAND and additional power law with index ~ -1.

5.4.1 COMPTEL Observation of GRB 941017

Apart from the LAD and the TASC observations, COMPTEL BSA data were also available for this event (see §2.4 for instrument and data description). BSA data are provided in the energy ranges of 300 keV – 1.3 MeV ("Low") and 800 keV – 10.6 MeV ("High"). The COMPTEL BSA spectra nicely provide a bridge between the energy ranges of LAD and TASC, and thus would be expected to supply an excellent confirmation and/or constraint to the joint analysis with LAD and TASC. Accordingly, we jointly analyzed the spectra of GRB 941017 using the data from all three instruments.

For this event, the early burst-mode data from the BSA did not show significant signal above background. In addition, the BSA signal faded roughly 80 seconds after the BATSE trigger, leaving 12 tail-mode spectra from 6 to 78 s with useful data. Due to the large incident angle of the event (zenith angle = 66°), some photons were detected through the side of the COMPTEL module. This caused the normalization factor (EAC) between the Low data and High data to be rather large.

The joint analysis was performed using four datasets: LAD, TASC, COMPTEL Low, and COMPTEL High. The LAD data and the TASC data, as well as their response matrices and the spectral models used here, are identical to those used by González et al. (2003). The COMPTEL data were available only in the second and third of the five time intervals, namely, 14 to 47 seconds and 47 to 80 seconds (see Figure 5.8). The COMPTEL accumulation intervals that best match these two intervals were 12 to 48 seconds and 48 to 78 seconds. For each time interval, the data from all detectors were jointly fitted to a single photon model. The EAC factors were applied to all combinations of four datasets but kept constant for both time intervals. The photon index of the highest energy PWRL was fixed at –1 for the 14 to 47 second time interval, as was done by González et al. (2003), due to the

weak constraint on this parameter by the data. The deconvolved νF_ν spectra of the two time intervals for which the analysis was performed are shown in Figure 5.9, and the best fit parameters are presented in Table 5.3.

For comparison, the spectral parameters determined without the COMPTEL data are also listed. We found that the joint analysis using the four datasets improved the significance for the interval of 47 to 80 seconds, in which the high-energy component is more evident in the COMPTEL passband. The best-fit parameters were still consistent with those found with the LAD–TASC joint analysis. Therefore, having the COMPTEL spectra, along with the TASC spectra, strengthens the evidence for the extra high-energy component described by a power law.

In addition to the fits presented here, the joint spectra of COMPTEL High and Low as well as COMPTEL and LAD data were also fitted with the BAND model. In the case of COMPTEL-only fits, the $E_{\rm peak}$ and the α were not well constrained, due to the fact that the peak energy lies very close to the lower bound of the COMPTEL energy range. The β values were consistent with those found by fitting the LAD data alone. Joint spectra of COMPTEL and LAD data provide better constraints on all of the spectral parameters. Although there is a slight indication of a possible high-energy excess, at least for the later time interval (47 to 80 s) in the COMPTEL High data, an additional high-energy power law did not improve the fits.

Similarly, in the energy range of 1 to 10 MeV, the COMPTEL High data and the TASC data were fitted separately with a single power law, to test the consistency of the two datasets. This was only possible for the first time interval, in which the COMPTEL High data contained enough signal to produce an acceptable fit. The spectral indices agreed to within 1σ, and thus the two datasets were confirmed to be consistent within the overlapping energy range. These analysis results, obtained by jointly analyzing the data of three independent instruments, provide strong evidence for the prompt high-energy spectral component.

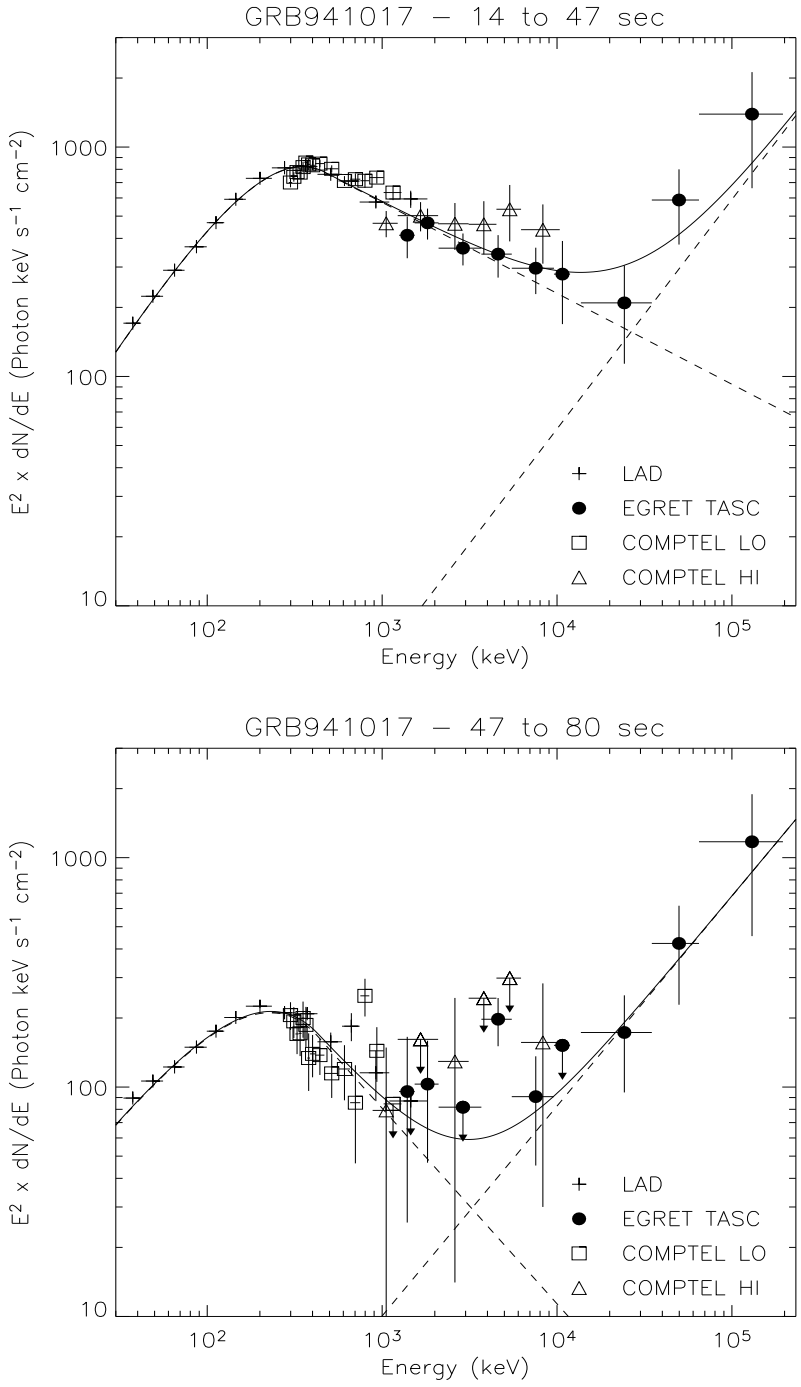

Figure 5.9 νF_ν spectra corresponding to the second and third time intervals of Figure 5.8, with the data from LAD, TASC, and COMPTEL. The BAND model and the additional high-energy PWRL model are shown separately with dashed lines.

Table 5.3 Best fit parameters for the two time intervals, with only LAD and TASC data ("**LAD+TASC**"), and with data from all three instruments ("**+COMPTEL**"). The uncertainties are 1σ.

	14 – 47 s		**47 – 80 s**	
	LAD+TASC	**+COMPTEL**	**LAD+TASC**	**+COMPTEL**
BAND				
A [1]	0.061 (0.001)	0.060 (0.001)	0.024 (0.001)	0.025 (0.001)
$E_{\rm peak}$ (keV)	350 (8)	350 (7)	240 (14)	229 (9)
α	–0.79 (0.02)	–0.79 (0.02)	–1.08 (0.06)	–1.03 (0.05)
β	–2.46 (0.05)	–2.40 (0.03)	$-2.65\ ^{+0.22}_{-0.85}$	$-2.85\ ^{+0.20}_{-0.40}$
PWRL ($E_{\rm piv}$ = 30 MeV)				
A [1] $/10^{-7}$	2.40 (0.63)	1.97 (0.60)	2.36 (0.93)	2.51 (0.76)
λ	–1.00 fixed	–1.00 fixed	$-1.06\ ^{+0.70}_{-0.44}$	–1.09 (0.37)
EAC (Fixed)				
TASC/LAD	0.45	0.45	0.45	0.45
Low/LAD	—	1.15	—	1.15
High/LAD	—	2.30	—	2.30
χ^2/dof	259.3/214	485.4/400	235.2/213	388.1/399
$\Delta\chi^2$ [2]	14.5	10.4	15.8	20.1
Probability [3]	1.4E–4	1.3E–3	3.7E–4	4.3E–5

[1] In photons s^{-1} cm^{-2} keV^{-1}

[2] Change in χ^2 with and without the high-energy power law (Δdof = 1 for the 1st time interval and Δdof = 2 for the 2nd time interval)

[3] Chance probability for improvement in χ^2 by adding the high-energy power-law, determined by χ^2 probability function.

5.5 Summary and Discussion

Broadband spectra in the energy range of $\sim$ 30 keV – 200 MeV indeed constrain the high-energy spectral indices and break energies of strong GRBs that have significant MeV emission much better than single detector analysis. We identified one case (trigger number 2329) in which the $E_{\rm peak}$ is extremely high, with a lower limit of 167 MeV. This, combined with the fact that in some cases the $E_{\rm peak}$ values were found to be slightly higher than those determined by LAD data only, may indicate that there exists a tail population of $E_{\rm peak}$ values extending to a few hundred MeV. In addition, while the broadband spectra were mostly consistent with broken power laws (BAND or SBPL), indications of high-energy excess were also found in two events (trigger numbers 1886 and 3245). For one of them (GRB 941017, 3245), the distinct MeV component has been potentially identified with time-resolved spectral analysis (González et al. 2003, §5.4), with much stronger significance than with the time-integrated spectrum.

Possible explanations that have been proposed for such a high-energy component are the Compton upscattering of synchrotron photons in the reverse shock by the synchrotron-emitting relativistic electrons (Granot & Guetta 2003), and the electromagnetic cascade emission of ultra-relativistic baryons through photo-pion interactions and subsequent pion decay (Dermer & Atoyan 2004). It is particularly interesting if the component is indeed due to the relativistic baryons, since the observed component may be direct evidence of baryonic acceleration, namely, cosmic rays. The high-energy power-law component observed in GRB 941017 requires that there exists another break energy (and $E_{\rm peak}$) above 200 MeV, in order to avoid the energy divergence. Although the redshift for this event is unknown, a rough upper limit energy for such a break could be placed at $\sim$ 1 TeV, solely by the total

(isotropic equivalent) energy constraint of $\sim 10^{53}$ ergs, and by assuming the burst originated nearby ($z \ll 1$).

It is possible that the time-resolved spectral analysis of broadband spectra would reveal such high-energy spectral components in many more GRBs. Unfortunately, the TASC data is only available for the brightest of BATSE GRBs due to its sensitivity limitation. Future observations by *GLAST*[2] with much higher sensitivity extending to GeV will certainly help clarify the high-energy spectral properties of GRB prompt emission.

[2]http://glast.gsfc.nasa.gov/

CHAPTER 6

EXAMINING GRB PROMPT EMISSION MODELS

Observed non-thermal spectra of GRBs imply that energy of the particles emitting the gamma-rays are distributed non-thermally (i.e., a power law). Also, the emission process must be very efficient in order to release a large amount of energy in a flash. Synchrotron radiation naturally arises as a strong candidate because the radiation process is very efficient and it seems to successfully explain many other astrophysical systems associated with non-thermal spectra, such as supernova remnants or active galactic nuclei. In the standard synchrotron shock model of GRB (SSM, Tavani 1996a,b), described briefly in §3.2.3 as the currently most favored GRB emission model, electrons are assumed to be accelerated at the shock by the Fermi mechanism. In the Fermi-type (or diffusive) shock acceleration, electrons are scattered back and forth across the shock due to non-uniformity of the magnetic field behind and ahead of the shock. The electrons gain energy rapidly as they are much more likely to go through "head-on collisions" with the turbulence at each shock crossing. The resulting energy distribution of the accelerated electrons is a power law of index p; $N(\gamma_e) \propto \gamma_e^{-p}$ $(\gamma_e > \gamma_m)$ with $p \approx 2.2$ for relativistic shocks (Gallant 2002, and references therein). The minimum energy γ_m depends on the amount of energy that is converted into the internal energy of the electrons whereas the maximum energy is determined by balancing the acceleration time and the cooling time. The post-shock particle distribution is therefore represented by a thermal component with the non-thermal "tail." Other assumptions in the SSM include a

random magnetic field with no preferred direction, an isotropic electron pitch angle distribution, and no inverse Compton scattering or absorption of the synchrotron photons. The asymptotic low-energy index expected in the SSM spectrum is $\leq -2/3$ (Katz 1994; Tavani 1996b; Preece et al. 1998b). The high-energy index is expected to be $-p/2-1$ with fast cooling (Sari et al. 1998). The fast-cooling SSM spectrum is shown in Figure 3.11 and is given by

$$f(\nu) \propto \begin{cases} \nu^{-2/3} & \nu < \nu_c \\ \nu^{-3/2} & \nu_c < \nu < \nu_m \\ \nu^{-p/2-1} & \nu_m < \nu, \end{cases} \tag{6.1}$$

where ν_c corresponds to an electron whose radiative cooling timescale equal to the dynamical cooling timescale, and ν_m is the minimum energy of power-law distributed electrons. This is a three-component spectrum, while the photon models that we employed in our analysis consisted of at most two power-law components. Therefore, it is possible that the fitted low-energy index lies in the range of $-3/2$ and $-2/3$ or high-energy index in between $-p/2-1$ and $-2/3$, but not flatter than the upper limits (e.g., Preece et al. 2002). The νF_ν peak energy ($E_{\rm peak}$) should be near ν_c or ν_m, which is determined by the magnetic field strength at the shock. The SSM has been supported by the fact that the curvature of the expected spectrum at $E_{\rm peak}$ agrees well with that of the empirical BAND model (§4.2.2.2), and the agreement with afterglow observations (Waxman 1997).

However, there has been compelling observational evidence that the simple SSM is not adequate to explain the GRB prompt emission (Preece et al. 1998b, 2000; Ghirlanda et al. 2002; Lloyd-Ronning & Petrosian 2002; González et al. 2003; Baring & Braby 2004). In particular, a significant fraction of GRB spectra exhibit low-energy indices harder than $-2/3$ that cannot be reconciled with the model. The shock acceleration mechanism assumed in the SSM has been recently challenged as well, in terms of the post-shock electron distribution. It was found that in order

for synchrotron or inverse Compton emission to account for observed broadband spectra, the post-shock distribution must be dominated by a non-thermal component, rather than the thermal component with a non-thermal tail, presumed in the SSM (Baring & Braby 2004; Baring 2005). Some alternative emission models to the standard SSM have been suggested to account for the observations.

6.1 Alternative Emission Models

Alternative emission models are mainly motivated by the observed low-energy spectral indices being harder than that expected by the SSM spectrum, namely $> -2/3$. Since the SSM is a simple model that assumes the least complicated case, modifying some of the assumptions for possibly more realistic conditions could alter the predicted spectral shape. Harder low-energy indices can naturally be obtained if one assumes an optically thick scenario or anisotropic electron pitch-angle distribution (Lloyd-Ronning & Petrosian 2002; Medvedev 2004). Other emission models that can accommodate the hard low-energy indices include the fireball photospheric model (Mészáros & Rees 2000), the saturated Comptonization model (Liang et al. 1997), and the jitter radiation model (Medvedev 2000). The photospheric model and the saturated Comptonization model, both involving thermal spectrum characteristics, can result in quite complicated spectral shapes in the gamma-ray energy band, depending on the parameters. Therefore, we only consider the modified SSMs and the jitter radiation model here, which can be compared to our spectral analysis results. These models and their predicted limits on spectral parameters are reviewed below. Note that the spectral indices in each model are asymptotic power law indices.

Synchrotron Self Absorption. The optically-thick scenario can arise in high density or strong magnetic field cases, in which the synchrotron photons are absorbed by synchrotron-emitting electrons in the magnetic field. The low-energy index can be as hard as +1 below an absorption energy ν_a (with low-energy cutoff in the power-law electron distribution; Lloyd-Ronning & Petrosian 2002), and the spectrum expected is

$$f(\nu) \propto \begin{cases} \nu^{1} & \nu < \nu_a \\ \nu^{-2/3} & \nu_a < \nu < \nu_m \\ \nu^{-(p+1)/2} & \nu_m < \nu. \end{cases} \tag{6.2}$$

However, in order for the absorption energy to be within the gamma-ray (i.e., BATSE) energy band, a magnetic field of the order of $\gtrsim 10^7$ G is required (Crider & Liang 1999; Medvedev 2004). This is a few orders of magnitude larger than what is typically assumed in the GRB source environment, and it would be difficult to sustain such a strong magnetic field in an expanding fireball.

Small Pitch Angle Distribution. In a low-density environment, assumed for the GRB emission region, pitch angles of the accelerated electrons with respect to the local magnetic field can be highly anisotropic (Lloyd-Ronning & Petrosian 2002, and references therein). In such a scenario, the spectrum would have a shape described by

$$f(\nu) \propto \begin{cases} \nu^{0} & \nu < \nu_s \\ \nu^{-2/3} & \nu_s < \nu < \nu_m \\ \nu^{-(p+1)/2} & \nu_m < \nu, \end{cases} \tag{6.3}$$

where ν_s is determined by the synchrotron characteristic energy ($eB/\gamma m_e c$) and the mean pitch angle. In general, the break at ν_m should be more pronounced than at ν_s, and therefore, when fitted with a model consisting of two power laws, the low-energy index is expected to be between $-2/3$ and 0 (Lloyd-Ronning & Petrosian 2002).

Jitter Radiation. It has been recently shown in simulations that a small scale, inhomogeneous magnetic field is generated at the shock by the Weibel instability (Medvedev & Loeb 1999; Nishikawa et al. 2005). When the inhomogeneity of the magnetic field is much smaller than the gyroradius of the shock electrons, the deflection angle (α) due to the small-scale magnetic field is smaller than the beaming angle ($\Delta\theta \sim 1/\gamma$) of the synchrotron emission, and so-called "jitter" radiation is observed (Figure 6.1; Medvedev 2000). This is a special case of the small pitch angle mechanism of the previous section. The jitter spectrum is

$$f(\nu) \propto \begin{cases} \nu^0 & \nu < \nu_{\rm jm} \\ \nu^{-(p+1)/2} & \nu_{\rm jm} \lesssim \nu, \end{cases} \tag{6.4}$$

where $\nu_{\rm jm}$ is proportional to electron plasma frequency ($\omega_{\rm pe} = \sqrt{4\pi e^2 n/m_e}$); therefore, the spectral break energy (or $E_{\rm peak}$) of jitter spectrum is independent of the magnetic field strength, but depends on the number density, n, of electrons in the expanding shell instead. The spectral shape is determined by the configuration of the small-scale magnetic field, as well as the ratio of angles ($\alpha/\Delta\theta$); however,

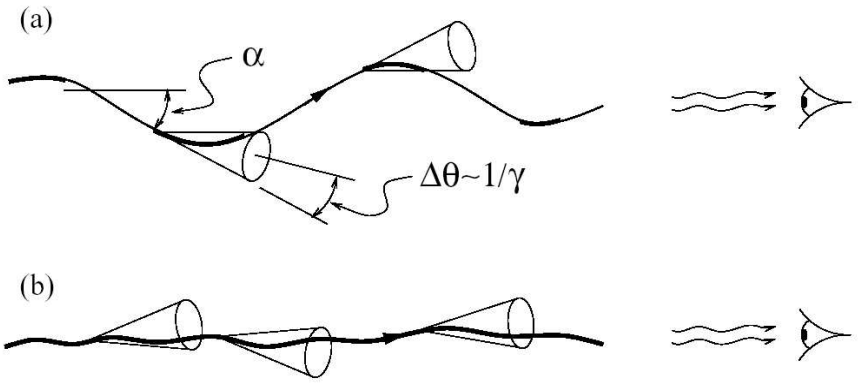

Figure 6.1 (a) Regular synchrotron emission case where only parts of trajectory is observed and (b) jitter radiation case where the entire trajectory is observed (from Medvedev 2000).

the shape is found to be very distinct from the SSM spectrum, characterized by a much sharper spectral break. Therefore, a sharply broken power law should fit well to the jitter spectrum. In the GRB emission picture, perhaps a more likely scenario is that both small-scale and large-scale magnetic fields exist at the shock. The emerging spectrum in that case is a composite of a jitter component due to the small-scale fluctuation in the field and synchrotron component due to the large-scale field. Such a composite spectrum is shown in Figure 6.2. The relative strength of each component is determined by the ratio of the energy densities of the small-scale and large-scale magnetic field. The jitter–synchrotron spectrum can accommodate the low-energy indices ≤ 0 and can have sharp or smooth spectral break scale. An advantage of the jitter model is that it is a natural outcome of collisionless shock physics and it is not proposed to solely explain observed GRB spectra. Observations

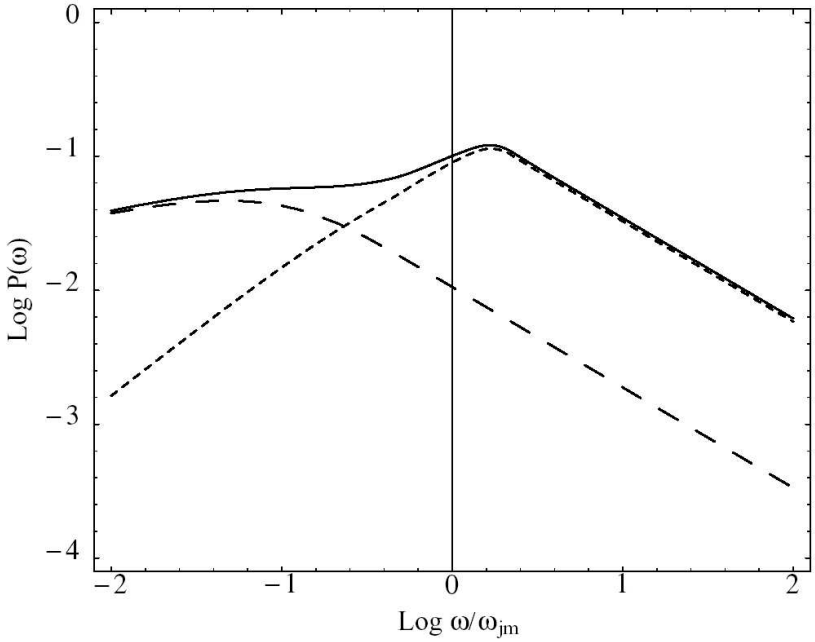

Figure 6.2 A composite F_ν spectrum of jitter (short dashed) + synchrotron (long dashed; from Medvedev 2000).

of the jitter radiation component will be a direct confirmation of the magnetic field generation at the shock due to the instability.

Using the large set of spectral analysis results obtained in Chapters 4 and 5, we can explore the compatibilities of the existing GRB acceleration and emission mechanisms with the observations, with much better constraints than any previously available spectral database. We only examine spectral indices here because they are unaffected by either the cosmological redshift z, which is unknown for most BATSE GRBs, or the bulk Lorentz factor Γ of the relativistic shell. The break energy or $E_{\rm peak}$ values in observed GRB spectra are shifted from the source frame values, due to the cosmological redshift and Lorentz boosting. It should be mentioned, however, that the narrow distributions of the break energy or $E_{\rm peak}$ may be indicative of very narrow intrinsic distributions of the parameters.

6.2 Low-Energy Spectral Index

We start by comparing our time-resolved spectral analysis results to those predicted by the above-mentioned emission models in terms of the low-energy spectral index, of which various limits are imposed by various emission models. In Figure 6.3, we show the overall distribution of the time-resolved low-energy indices that are well determined, with critical indices in the emission models highlighted. As mentioned in Chapter 4, no clustering at these critical indices is observed. In addition, deviations in units of σ of the time-resolved low-energy indices from these critical values, 0, –2/3, and –3/2, are shown in Figure 6.4. The σ deviations were determined by taking differences between fitted indices and the critical values, divided by 1σ uncertainties associated with the fitted values. Any fitted indices that deviate from

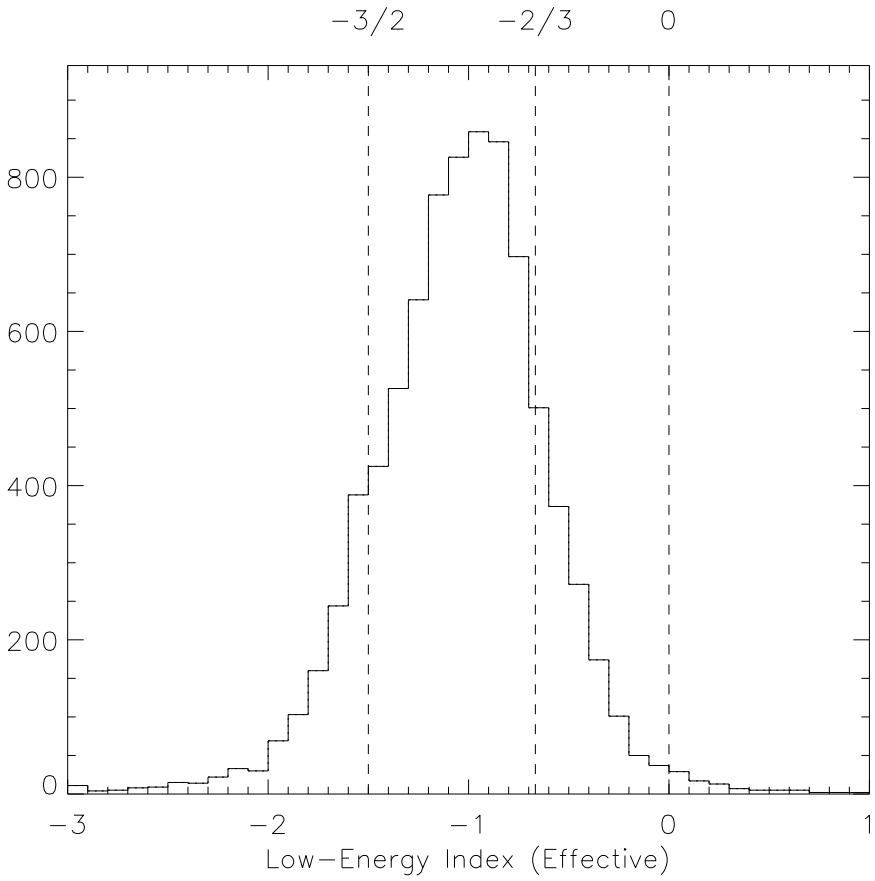

Figure 6.3 *Good* time-resolved low-energy index distribution (same as Figure 4.22, top left panel), with three critical values indicated.

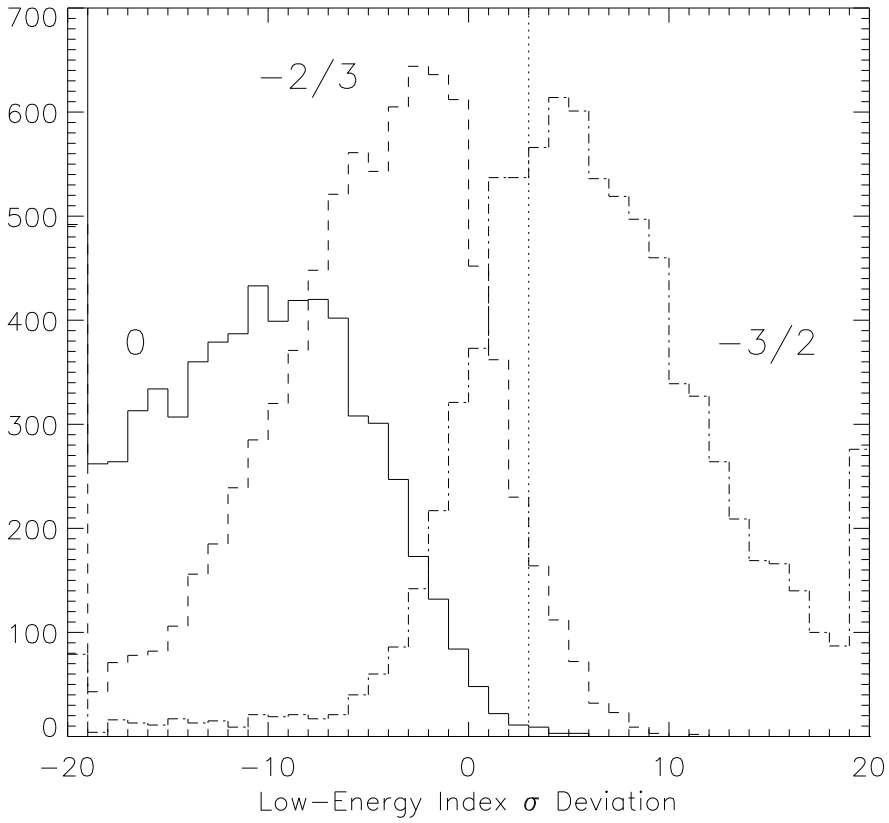

Figure 6.4 Distribution of deviations (in units of σ) of time-resolved low-energy indices from values predicted by the emission models; 0 (solid line), –2/3 (dashed line), and –3/2 (dash-dot line). Positive 3σ deviation is marked by the dotted line.

the critical values by more than 3σ (to the right of 3σ line in Figure 6.4) are inconsistent with the model predictions. The 3σ chosen here was based upon the earlier simulation work by Preece et al. (1998b) that suggested 2.4σ deviations from any given index value are expected statistically. The numbers and percentages of the indices that are inconsistent with each critical value are listed in Table 6.1. They are all consistent with being less than 1, with only 0.2% of the fitted indices found to be inconsistent with the small pitch-angle and jitter limit of 0. We have found that all of those spectra were fitted equally well with BAND, COMP, and SBPL with break scale, $\Lambda \geq 0.2$. In other words, these are all spectra with a smooth break similar to the SSM spectrum. All sharp-break spectra (SBPL with $\Lambda < 0.2$) have low-energy indices less than 0, consistent with the jitter–synchrotron case. Note that about 20% of all time-resolved spectra (except PWRL-fitted spectra) have sharp break scales. We also observe that very few spectra have indices consistent with 0 within a few σ, expected for pure jitter case. Many of the hard spectra with positive indices are found to constitute the early part of a burst's emission. Examples of such bursts are shown in Figure 6.5. In the case of GRB 930214 (trigger number 2193), a weak tail portion of the burst is excluded in the analysis and the actual duration of the burst (T_{90} = 135 s) is much longer than the duration used for the analysis (36 s);

Table 6.1 Numbers and percentages of 8459 time-resolved spectra providing low-energy indices inconsistent with 1, 0, –2/3, and –3/2 (by 1σ and 3σ).

	$> 1\sigma$		$> 3\sigma$	
Index	Number of Spectra	%	Number of Spectra	%
1	0	0	0	0
0	48	0.6	15	0.2
–2/3	1009	11.9	417	4.9
–3/2	6944	82.1	5870	69.4

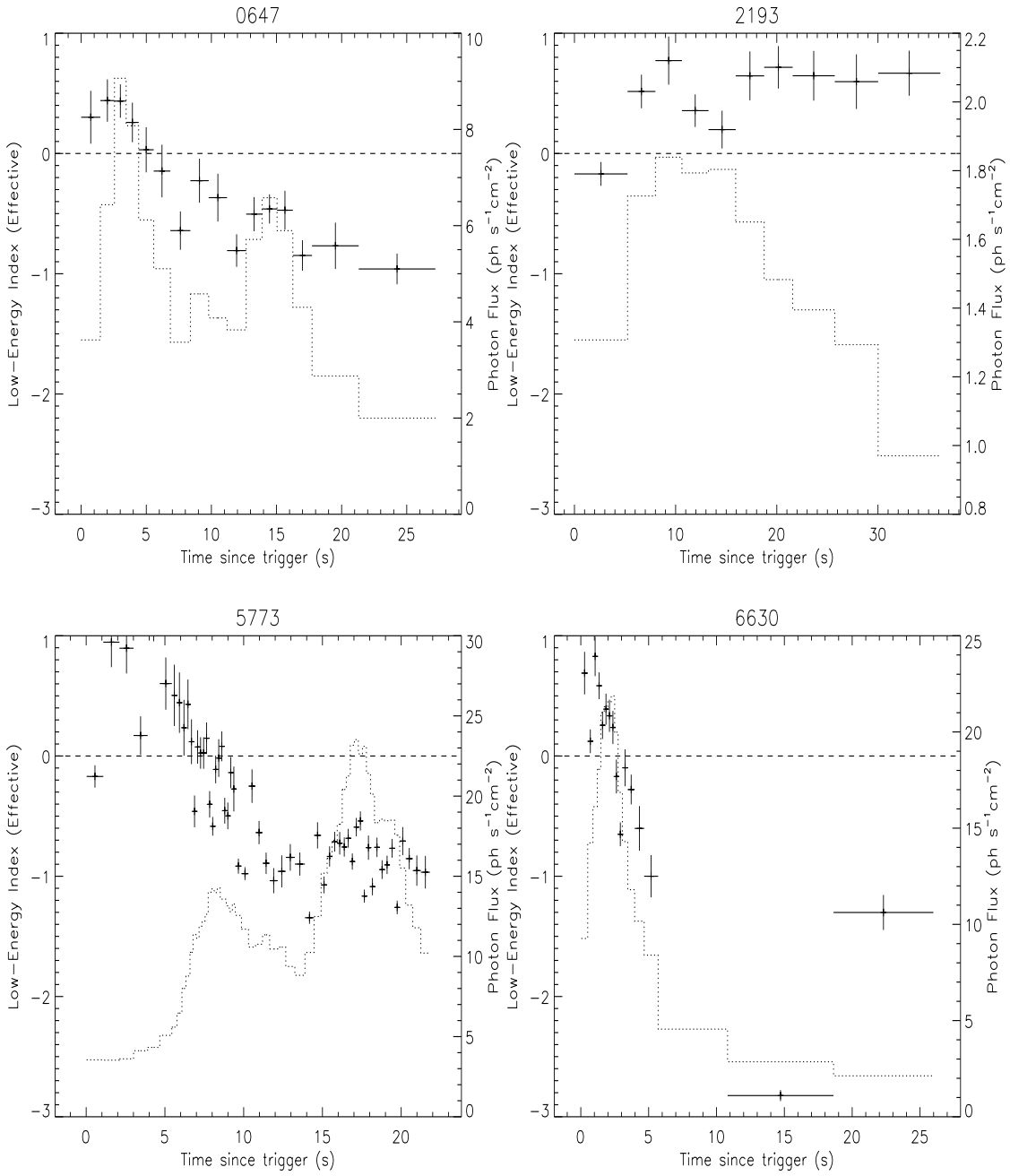

Figure 6.5 Examples of hard low-energy index events. Clockwise from top left: GRB 910807 (trigger number 647), GRB 930214 (2193), GRB 980306 (6630), and GRB 970111 (5773). The photon flux histories are over-plotted with dotted lines (right axes) and index = 0 is indicated by dashed lines.

therefore, the hard spectra are indeed in the early part of the event. Similar results were also obtained by Ghirlanda et al. (2003) and Ryde (2004), who fitted a thermal blackbody model to the hard spectra and observed that the blackbody temperature cooled down during the hard period. This, in our case, is seen as a softening of $E_{\rm peak}$ in all of the hard time intervals of the events presented in Figure 6.5.

As for the SSM spectrum limit of –2/3, $\sim 5\%$ of the spectra were not consistent. This is still a significant number of spectra, given the large sample size, although it is a smaller fraction than those found previously with smaller samples: 8% (Preece et al. 1998b) and $> 30\%$ (1σ, Lloyd-Ronning & Petrosian 2002). We also observe that fewer than 11% of all spectra belong to the small pitch-angle distribution model regime of –2/3 to 0 within 1σ, reduced considerably from 29% (1σ) obtained by Lloyd-Ronning & Petrosian (2002). Similar to the spectra with indices > 0 described above, many of these spectra with indices within the small pitch-angle model region are also found in the early time but lasting much longer. However, that is not the only pattern observed, and a considerable number of the spectra with indices in this region are found later in burst episodes. The low-energy index evolution of two such events are shown in Figure 6.6. In these events, the low-energy indices do not follow the commonly observed tracking pattern but vary independent of photon flux. We also note that only 16 out of 417 spectra violating the SSM limit are the sharp-break spectra.

Finally, the majority of the spectra have indices contradicting the cooling limit of –3/2. The cooling limit is imposed in the context of the standard SSM where no re-acceleration of the electrons takes place and equipartition of magnetic and particle energies is usually assumed (Ghisellini et al. 2000, also Equation 6.1). In an attempt to account for the discrepancy between the observation and the prediction, Ghisellini et al. (2000) explored several possibilities, such as constant re-heating of the relativistic electrons, deviation from equipartition, a strongly variable magnetic

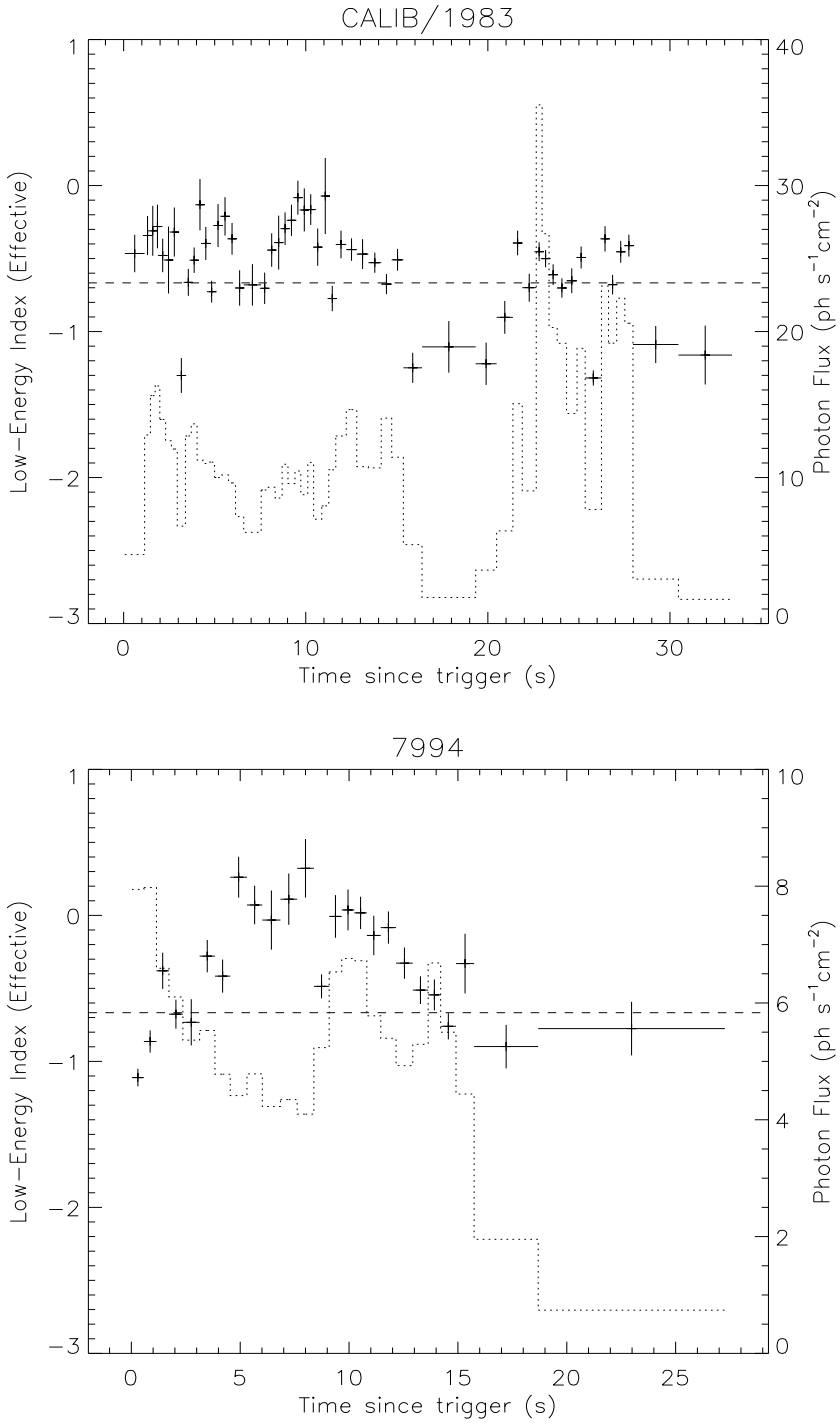

Figure 6.6 Examples of hard low-energy index events; GRB 921009 (trigger number 1983; *top*) and GRB 000221 (7994; *bottom*). The photon flux histories are over-plotted with dotted lines (right axes) and index = –2/3 is indicated by dashed lines.

field, and the inverse Compton process. However, it was found that they could not account for the observed hard indices, and that the index could even be softer than –3/2 in some cases. In our burst sample, we observed that the spectra in quiescent periods or tails of peak emission episodes provide indices consistent with the cooling limit ($< -3/2$) for many events. Good examples can be seen in Figures 4.24 and 4.25 in Chapter 4. There are also several cases in which the indices are always above or always below –3/2 during the entire duration of bursts, regardless of their time profiles or brightness.

It must be remarked, however, that we found in Chapter 4 (§4.4.3) that the time-integrated low-energy indices tend to be softer than the time-resolved ones. The longer integration time may obscure possibly underlying hard spectra. The integration times of our time-resolved spectra are still much longer than the timescales involved in the emission and acceleration processes, which are usually orders of magnitude shorter than a millisecond. Each emission pulse in a GRB lightcurve presumably corresponds to an internal shock episode and physical parameters can vary from pulse to pulse. It is very likely that a larger number of harder low-index spectra may be found with finer time-resolution analysis.

6.2.1 Constant Low-Energy Index Case

The low-energy index has been well known to evolve during a burst episode; however, there are some events during which the index stays constant. Two such events are shown in Figure 6.7 as examples. Although there seems to be no preferred values for constant indices, in these two cases, very interestingly, we observe the constant values of –2/3 and –3/2 that are expected from the SSM with and without cooling, respectively. In the case of GRB 000511 (trigger number 8101, top panel),

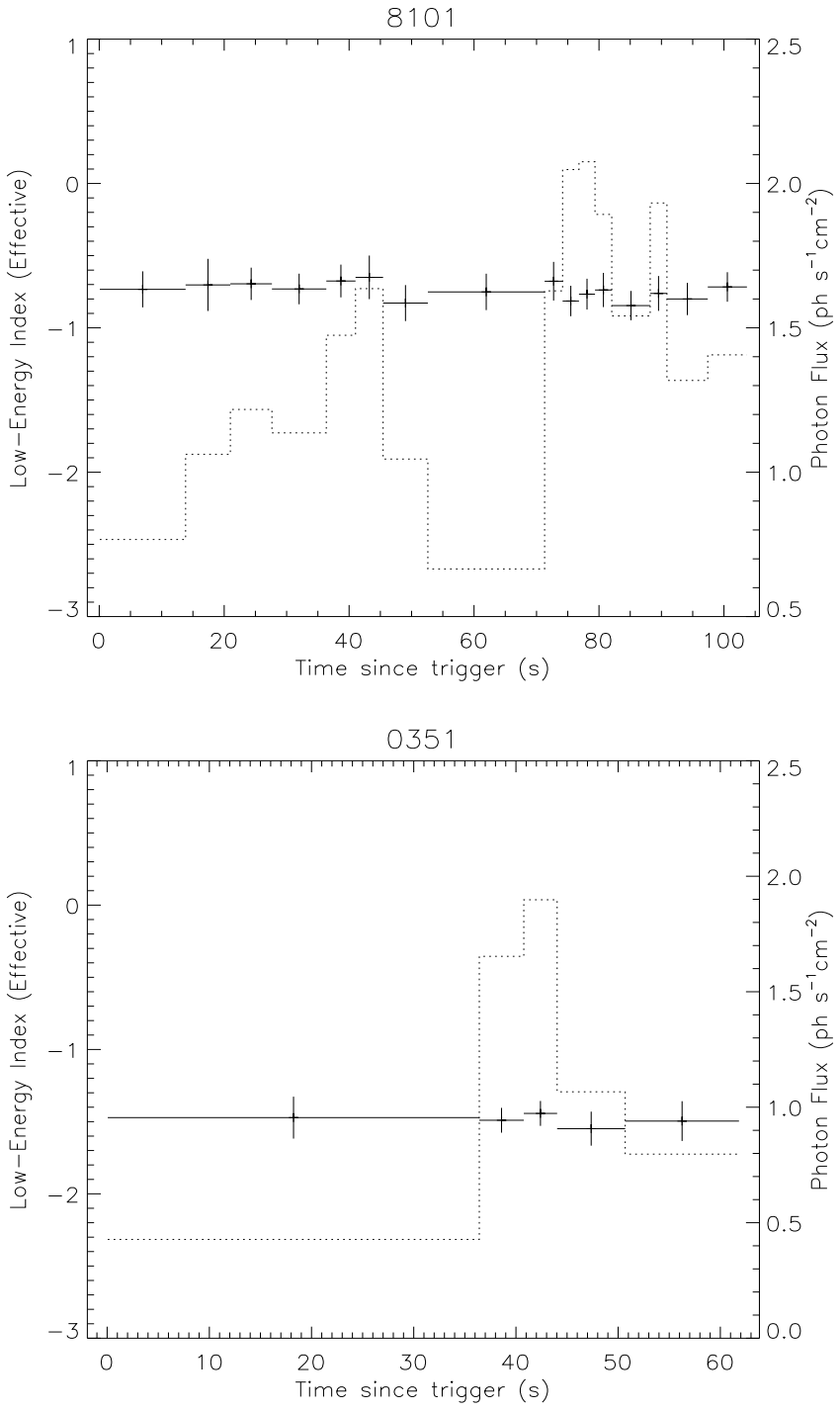

Figure 6.7 Examples of constant low-energy index events: GRB 000511 (trigger number 8101, *top*) and GRB 910614 (351, *bottom*). The photon flux histories are over-plotted with dotted lines (right axes).

$E_{\rm peak}$ values do not evolve much ($\sim$ 300 keV) for the entire duration. In fact, the spectral shape and amplitude do not vary much for all 16 time-resolved spectra that are mostly best-fitted with the COMP model. Most spectra of the other events characterized by constant low-energy indices are best-fitted with the COMP model with $E_{\rm peak} \lesssim 300$ keV. The $E_{\rm peak}$ values, however, usually evolve during these bursts.

6.3 High-Energy Spectral Index

The standard SSM, the small pitch-angle model, the self-absorption model, and the jitter radiation model, all produce spectra having a high-energy power law with a common index: $-(p+1)/2$, without cooling, or $-(p+2)/2$, with cooling. The distribution of observed time-resolved high-energy indices (Figure 4.26, top right panel) ranges from –4 to –1, with the most probable range of ~ -2.8 to -1.9 (Table 4.10). The indices translate into $2.8 \leq p \leq 4.6$, for the non-cooling case, and $1.8 \leq p \leq 3.6$, for the cooling case. As mentioned earlier, simulation studies of relativistic shock Fermi acceleration show much narrower range for $p = 2.2 - 2.3$ (Gallant 2002), and obviously the non-cooling case is out of this range. Even with the cooling case, the observed range of indices suggests that the Fermi-type relativistic shock acceleration is not sufficient to account for the observed spectra. Nor is the index expected to change; see next section.

6.3.1 Varying High-Energy Index Case

The constant β hypothesis was tested in §4.4.5 using the BETA model, and half of the GRBs in our sample are found to be consistent with a constant value for β. The values of the constant β did not differ from the distribution of the entire spectra, with the likely value of -2.3 ± 0.3. In most of the other half of the events

(the varying-β events), however, we do not observe any explicit pattern for the high-energy index evolution, such as hard-to-soft linear decay or the tracking behavior that is often observed with the low-energy index and $E_{\rm peak}$.

As we found in §4.4.4, the high-energy index is negatively correlated with $E_{\rm b}$ in 13% of GRBs, although uncertainty was not taken into account to find the correlations. However, very few events showed significant correlations between high-energy index and other parameters, such as $E_{\rm peak}$, low-energy index, or photon flux. This supports the conclusion of earlier work by Preece et al. (1998a) that the high-energy indices tend to behave independently of the other parameters within bursts, although their uncertainties are relatively large. We have found that in 14% of events high-energy index is negatively correlated with time (with $P_{\rm rs} > 10^{-3}$), indicating overall hard-to-soft evolution observable in high-energy index. For most of these events, $E_{\rm peak}$ was also negatively correlated with time (but not necessarily low-energy index and time). Also, among the varying-β events, two events that failed the BETA fits most severely showed significant variations in their high-energy index during the emission episodes. The index evolutions for these events are shown in Figure 6.8. In both cases, the change in index is about 1, corresponding to a change in electron distribution index of $\Delta p \sim 2$, within the bursts. The change of ~ 1 in indices within a burst seems to be the maximum value that we observe in our sample, since the COMP model fits better to a spectrum with very small high-energy index. In addition, the index seems to be harder at the onset of every peak.

In the Fermi-type shock acceleration, the timescale of acceleration is much shorter than the synchrotron cooling timescale, in an environment typically assumed in the GRB emission region. Such an evolution of p is therefore, not expected in the framework of the SSM. Moreover, a recent study by Baring & Braby (2004) showed that particle distributions must be dominated by a non-thermal component

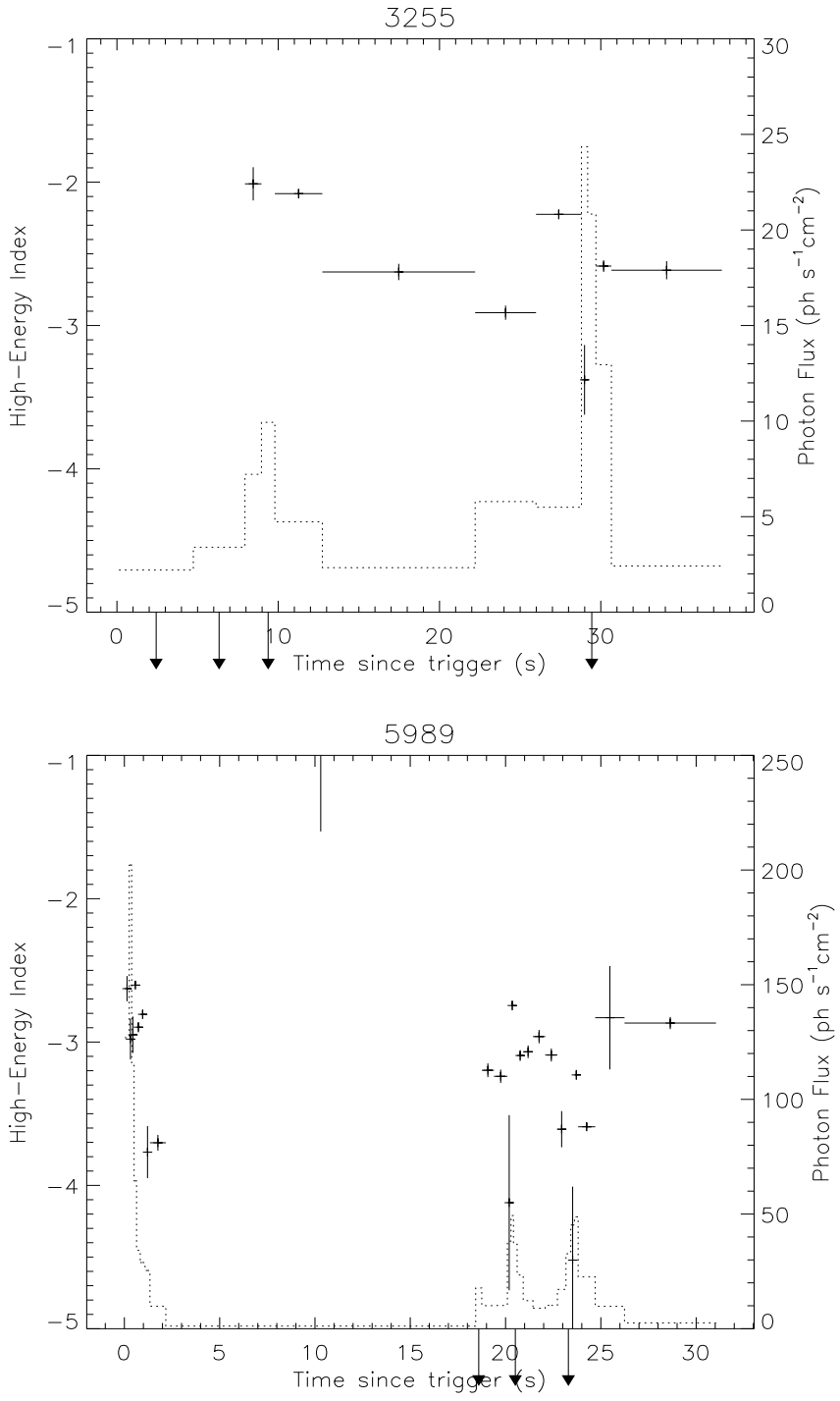

Figure 6.8 Examples of variable high-energy index events, GRB 941023 (trigger number 3255, *top*) and GRB 970201 (5989, *bottom*). The photon flux histories are over-plotted with dotted lines (right axes). Arrows indicate COMP model fits where no high-energy component is evident.

over a thermal component, if observed GRB (broadband) spectra are due to either synchrotron radiation or inverse Compton. This conflicts with the SSM, in which the accelerated electrons are assumed to be drawn from a thermal electron distribution and the resulting post-shock distribution is the thermal component with a non-thermal tail.

All the spectra within these two bursts shown here have break energy values that are low enough ($\lesssim$ 100 keV) to ensure good constraints on the high-energy index determinations using the LAD data alone. Some of the constant-β spectra are associated with large uncertainties. As we showed in the previous chapter (Chapter 5), broadband spectra that extend to much higher energies can certainly provide better constraints on the high-energy spectral indices. High-energy broadband analysis is urged in order to confidently relate the observed spectral indices to the post-shock particle distributions at the GRB source.

CHAPTER 7

CONCLUSIONS

In this dissertation, the spectral properties of a large sample of bright GRBs have been explored in great detail. The analysis results presented here provide the most detailed perspective of spectral aspects of the GRB prompt emission to date. Our main results are summarized below.

In Chapter 4, we presented a spectral analysis of 350 bright BATSE GRBs using high- and medium-energy resolution LAD data with moderate time resolution. Sets of well-constrained, model-unbiased spectral parameters were obtained and presented for both time-integrated and time-resolved spectra. Internal characteristics of the photon models employed were also investigated. We found the following.

- GRB spectra are described, in general, by two power laws joined at a break energy $E_{\rm b}$ with various curvature scales. They are not always adequately described by the BAND model, which is widely used. $E_{\rm b}$ is equal to the νF_ν peak energy $E_{\rm peak}$ only when the spectrum has a sharp break.

- We showed that the low-energy power law index, α, determined with the BAND and COMP models, is often overestimated. This is because α is fitted to an asymptotic power law that the data do not usually match within the BATSE energy range. Instead, an effective α (Appendix C) better represents the low-energy power law that is actually reached by the data. The resulting

number of hard spectra, which often pose a challenge to GRB emission models, is smaller than the number previously found (SP1).

- Low-energy index distributions are smooth, both for time-integrated and time-resolved spectra. The most likely values and the width of the distributions are $-1.25\pm^{0.35}_{0.25}$ and $-0.95\pm^{0.35}_{0.55}$ respectively.

- High-energy indices are more asymmetrically distributed than the low-energy indices. Time-integrated and time-resolved values are consistent with one another, with the most probable values (and the widths) $-2.45\pm^{0.55}_{0.25}$ and $-2.25\pm^{0.35}_{0.55}$, respectively. Both low-energy and high-energy indices are generally consistent with what was previously found with smaller samples (SP1; Ghirlanda et al. 2002) although our results have much better statistics and, more importantly, are unbiased by photon models.

- Distributions of $E_{\rm peak}$ and $E_{\rm b}$ are smooth and single-peaked, with no indication of secondary populations as was indicated previously in SP1. We confirm the narrowness of the distribution of $E_{\rm peak}$, and find that $E_{\rm b}$ values are distributed in an even narrower energy range. The most probable $E_{\rm peak}$ values and the distribution width for time-integrated and time-resolved parameters are $238\pm^{145}_{117}$ keV and $350\pm^{213}_{229}$ keV, respectively, while for $E_{\rm b}$, they are $197\pm^{120}_{97}$ keV and $197\pm^{186}_{75}$ keV. $E_{\rm peak}$ tends to be harder than $E_{\rm b}$ due to the curvature in spectra. The intrinsic $E_{\rm peak}$ distributions are even narrower because the observed spectra are cosmologically redshifted, with the redshift values possibly extending to $z \gtrsim 5$ (Bromm & Loeb 2002). These extremely narrow intrinsic distributions are difficult to account for in the internal shock model, since $E_{\rm peak}$ depends on the bulk Lorentz factor Γ as Γ^{-2}, which is variable in each shock episode. On the other hand, a Poynting-flux dominated fireball, dissipating energy through magnetic reconnection or a plasma instability, could

generate a narrower distribution than the shock cases, because of its linear dependence on Γ (Zhang & Mészáros 2002).

- Effects of longer integration times on the spectral parameter determination are significant, especially in determining the low-energy index and $E_{\rm peak}$. Larger percentages of hard low-energy index and hard $E_{\rm peak}$ spectra were identified with shorter integration times (time-resolved spectra). We also showed that the time-integrated spectra can be obtained by summing over the photon fluence of each time-resolved spectrum (and divided by total duration). In general, the harder spectra appear in relatively short time intervals with respect to the burst durations or have relatively low photon flux and so do not contribute much to the time-averaged, longer time interval spectra. This is consistent with hard-to-soft evolutions (harder spectrum when photon flux is low at the beginning of a burst) and tracking behavior (harder in short spikes) that has been observed.

- A significant positive correlation was seen between low-energy indices and $E_{\rm peak}$ in 28% of GRBs. Since our parameters are unbiased by photon models, the correlation is more likely to be intrinsic and not due to systematic effects, as suggested by Lloyd-Ronning & Petrosian (2002). Such positive correlations can be obtained with particular cases of the composite jitter–synchrotron emission model. The model predicts $E_{\rm peak} \propto \delta$ and low-energy index $\propto B_{\rm SS}^2/B_{\rm LS}^2$, where δ is a ratio of deflection and beaming angles of an electron, and $B_{\rm LS}$ and $B_{\rm SS}$ are the strength of large-scale and small-scale magnetic fields (Medvedev 2000). The positive correlation between low-energy index and $E_{\rm peak}$ then indicates a positive correlation between δ and $B_{\rm SS}^2/B_{\rm LS}^2$. This is naturally expected, since the deflection angle due to the Lorentz force is larger for larger $B_{\rm SS}$, if the fluctuation scale remains constant. In the anisotropic pitch angle model,

a negative correlation between these parameters is more likely to be expected (Lloyd-Ronning & Petrosian 2002).

- We verified a positive correlation between $E_{\rm peak}$ and energy fluence previously found by Lloyd et al. (2000), who suggested the correlation was intrinsic. However, distribution of our parameters indicates that the intrinsic correlation found by Amati et al. (2002) is mostly inconsistent with our data, as pointed out by Nakar & Piran (2005a) and Band & Preece (2005). We confirm, therefore, that the Amati correlation suffers from a strong selection bias.

- 50% of our sample of GRBs are inconsistent with the constant high-energy index. This cannot be explained within the SSM, since the acceleration mechanism presumed should be much more efficient than synchrotron cooling of electrons. Even for constant-β GRBs, the constant values were $-2.6 \gtrsim \beta \gtrsim -2.0$, which is much more dispersed than the expected electron distribution indices of $p = 2.2 - 2.3$.

- Three short GRBs containing multiple spectra, showed significant spectral evolution, mostly from hard to soft. This is in agreement with evolution frequently observed within individual peaks in long GRBs. The same emission mechanism may be responsible for creating some short GRBs and each peak within some long GRBs.

In Chapter 5, we extended the analysis to high-energy broadband spectra obtained by combining BATSE LAD data and EGRET TASC data. Time-integrated joint spectra of 15 hard BATSE GRBs were analyzed in order to probe high-energy spectral properties of prompt emission. We found the following.

- All 15 spectra are continuous up to ~ 200 MeV with no indications of attenuation due to pair production, suggesting a lower limit for the bulk Lorentz factor $\Gamma \gtrsim 150$, for a typical broadband spectrum (Baring 2000).

- High-energy indices were constrained much better with the joint analysis. In a few cases, the jointly-fitted indices differed significantly from those determined with the LAD data alone. This indicates the possibility that some high-energy indices obtained with BATSE alone may not reflect the intrinsic values. In most cases, $E_{\rm peak}$ and $E_{\rm b}$ values derived with LAD data alone and values found by joint analysis were consistent within 1σ uncertainty.

- In one case, GRB 930506, $E_{\rm peak}$ was found to be > 167 MeV. Also for some spectra, $E_{\rm peak}$ and $E_{\rm b}$ were higher than the values found with LAD data alone. These, combined with the existence of some BATSE spectra with high-energy indices > -2, suggest a small tail population of high $E_{\rm peak}$ and $E_{\rm b}$ extending to a few orders of magnitude higher energy range than the BATSE passband. However, the fact that we only found a fraction of events with significant signal among the entire TASC dataset indicates that these high $E_{\rm peak}$ events must be rare and not likely to significantly broaden the $E_{\rm peak}$ and $E_{\rm b}$ distributions found with BATSE data alone.

- Two events showed indications of high-energy excess. One of them was GRB 941017, for which a delayed, distinct MeV component has been identified with time-resolved LAD-TASC analysis with much higher significance than the time-integrated analysis (González et al. 2003). The brightness and delayed nature of the component are inconsistent with synchrotron-self Compton of the keV synchrotron component. Other possible sources of such a high-energy component include inverse Compton scattering of reverse shock photons (Granot & Guetta 2003) and baryonic cascade emission (Dermer & Atoyan 2004).

In Chapter 6, we examined some of the existing emission models using the model-unbiased spectral parameters with good constraints obtained in the analyses above. The following results were obtained:

- 5% of the time-resolved spectra violated the low-energy index upper limit of –2/3 predicted by the standard SSM and 0.2% were inconsistent with an upper limit of 0 allowed in both the small-pitch angle distribution model and the jitter radiation model. These are much lower fractions than the previously known values, yet still represent a considerable number of spectra. All sharp-break spectra, predicted by the jitter radiation model, have indices < 0 (with only 1% of them having $> -2/3$), consistent with the jitter–synchrotron composite case. In the jitter–synchrotron model, sharply-broken spectra can be expected when $\delta \sim 1$ and $B_{\rm LS}^2/B_{\rm SS}^2 \sim 1$. If there is no pre-existing magnetic field, the large scale field ($B_{\rm LS}$) is generated solely by an instability caused by protons; therefore, the condition ($B_{\rm LS} \sim B_{\rm SS}$) indicates equipartition between electrons and protons (Medvedev 2000).

- All spectra with low-energy index > 0 and many with $>$ –2/3 comprise early parts of bursts. Most of these events belong to the sample previously analyzed by Ghisellini et al. (2000) and Ryde (2004) with a thermal blackbody model. The hard component at early times may be interpreted as a thermal component involving the emission from the fireball (e.g., photospheric model, Mészáros & Rees 2000). In such a scenario, the hard-to-soft evolution is naturally explained by cooling as the fireball expands. However, many spectra with low-energy index $>$ –2/3 (but < 0) are also found in later portions of the emission episodes. These can be explained by transitions between isotropic and anisotropic pitch angle distributions in the SSM, or changes in $B_{\rm LS}^2/B_{\rm SS}^2$, in the context of the jitter–synchrotron model.

- Some bursts exhibit no evolution in low-energy indices while the $E_{\rm peak}$ evolves. The low-energy indices in such events are consistent with the SSM limit of $\leq -2/3$ and mostly fitted with the COMP model with $E_{\rm peak} \lesssim 300$ keV. In the SSM, $E_{\rm peak}$ can evolve as magnetic field strength and the minimum electron energy change, while the low-energy index remains constant (Tavani 1996b; Lloyd-Ronning & Petrosian 2002). Also, in the context of the jitter–synchrotron model, this suggests that $B^2_{\rm LS}/B^2_{\rm SS}$ remains unchanged while δ varies.

- High-energy indices can also vary significantly by ~ 1, indicating the change in electron distribution index $\Delta p \sim 2$ within bursts. As discussed earlier, this cannot be sufficiently explained with the simple SSM, in which a very efficient Fermi-type acceleration of electrons takes place, presumably at the same site where electrons emit synchrotron photons.

The existence of sharply-broken power law spectra and the positive correlation between $E_{\rm peak}$ and low-energy index can be explained with the jitter–synchrotron model, while these observations challenge the SSM. Jitter radiation could arise from the tangled magnetic field generated in a Weibel-like instability formed in collisionless shocks (Medvedev & Loeb 1999). It has recently been shown that electrons can be accelerated in such a situation by strong filamentation instabilities, to a power law distribution (Hededal et al. 2004; Nishikawa et al. 2005). Also, in another recent study, the small-scale magnetic field fluctuation scale was found to evolve (Medvedev et al. 2005), which in turn, may account for the spectral evolution we observed in our sample. Our results suggest that a combination of jitter and synchrotron radiation from non-Fermi accelerated electrons seems to be a more promising emission model than the SSM Fermi accelerated electrons. More simulation studies are needed in

order to probe whether such a mechanism can indeed account for observed properties of GRB prompt emission. We finally note that for any future models, our systematic analysis database presented here will provide a valuable test base.

7.1 Prospects for Future Work

Recent analyses of GRBs observed with *HETE-II*, which is sensitive in a lower energy band than that of BATSE, show that $E_{\rm peak}$ can be less than 10 keV for some bursts (Sakamoto et al. 2004b). Early observations with *Ginga* also found break energies lower than the BATSE passband. Additionally, *Ginga* observations showed positive low-energy indices in 40% of their sample (Strohmayer et al. 1998), greatly different from 0.2% in our sample. Therefore, the $E_{\rm peak}$ values that are below the BATSE energy band may represent a second spectral break separate from those found with BATSE data, with a harder low-energy power law, as GRB spectra are expected to have more than one break in a broad energy range (Figure 3.11). The *Swift* mission currently in orbit is detecting GRBs in the range 15 – 150 keV. The population of lower $E_{\rm peak}$ events may grow with the *Swift* and *HETE-II* observations.

The importance of broadband spectral analysis is evident in order to probe spectral properties at large. Identification of multiple spectral breaks or extra spectral components is only possible with joint analysis of multi-detector data providing a broad energy coverage, as we have demonstrated in Chapter 5. In determining the GRB emission mechanism, high-energy spectra can provide important clues. For example, in the SSM, the inverse Compton component of synchrotron photons (self-Compton) associated with the SSM synchrotron component that peaks in the keV band is expected to be observed in the MeV to TeV energy band depending on the electron Lorentz factor (Guetta & Granot 2003). Also, there should be a spectral cutoff at some energy above $\sim$ 1 MeV due to pair-production attenuation (Baring

2000). Such a cutoff energy would determine the bulk Lorentz factor Γ that is one of the main factors, along with the redshift z, preventing the determination of the intrinsic $E_{\rm peak}$ values in the rest frame of expanding matter (Zhang & Mészáros 2004). To extend the work presented here, the LAD-TASC broadband analysis with a larger sample is ongoing.

One of the main scientific purposes of the upcoming *GLAST* mission is to provide GRB spectra in an unprecedented broad energy band of 10 keV – $\sim$ 30 GeV. It is highly anticipated that *GLAST* will reveal broadband characteristics of GRBs. The main instrument on *GLAST* is the Large Area Telescope (LAT), capable of observing GRBs in 30 MeV to 30 GeV with much greater sensitivity than EGRET. A complementary instrument, the GLAST Burst Monitor[1] (GBM) will provide burst spectra in the range 10 keV – 30 MeV. Together, GBM and LAT provide very wide energy coverage with excellent temporal resolution of 2 μs.

The analysis of GRB prompt emission spectra presented in this dissertation is derived from the most sensitive and largest GRB database to date. Therefore, these results provide exceptional statistics to set a standard for spectral properties of GRB prompt emission, and will be a pivotal reference for both theorists and observers, for the *GLAST* era and for defining science criteria for future missions. The systematic analysis of BATSE spectra can be naturally extended to include GBM spectra because of their similar characteristics. Such an extended work will increase the size of the spectral database of GRB prompt emission even more and possibly include many more short GRBs. The nature of short GRBs is a main question still unanswered. In this work, we found that at least some short GRBs display significant spectral evolution. An analysis of short event spectra with much finer time-resolution and with a much larger sample is necessary to probe the nature of short GRBs. It is also very likely that many of events that will be detected

[1]http://gammaray.nsstc.nasa.gov/gbm/

with GBM will have their redshifts and jet opening angles measured with afterglow observations, which may give an insight into the redshift or jet angle distribution of BATSE bursts that are mostly unknown.

In addition, with improvements of rapid GRB follow-up network and instruments, prompt flashes in optical and IR band are actively sought after. This may further extend the prompt emission spectrum down to longer wavelength or probe reverse shock emission expected in the fireball-shock model (§3.1.3.2). Finally, other observable signatures, such as strong polarization of prompt emission photons, will also place firm constraints on the emission mechanism, if confirmed.

APPENDICES

APPENDIX A

SBPL MODEL $E_{\mathbf{peak}}$

The SBPL model is parameterized with $E_{\rm b}$, which is the energy at which the low-energy power law joins with the high-energy power law; this is clearly different from the $E_{\rm peak}$ parameters of the BAND and COMP models. Therefore, $E_{\rm b}$ and $E_{\rm peak}$ are not directly comparable with each other. However, it is easy to derive "$E_{\rm peak}$" (i.e., the peak in νF_ν spectrum) for a spectrum fitted with SBPL, which, in turn, can be compared to the $E_{\rm peak}$ of the other models directly.

A.1 Finding $E_{\rm peak}$

Starting from Equation 4.4, the νF_ν flux can be written as

$$\nu F_\nu \equiv E^2 f(E) = \frac{A}{E_{\rm piv}^b} E^{(b+2)} 10^{(a-a_{\rm piv})},$$

where

$$a = m\Lambda \ln\left(\frac{e^q + e^{-q}}{2}\right), \qquad a_{\rm piv} = m\Lambda \ln\left(\frac{e^{q_{\rm piv}} + e^{-q_{\rm piv}}}{2}\right),$$
$$q = \frac{\log\left(E/E_{\rm b}\right)}{\Lambda}, \qquad q_{\rm piv} = \frac{\log\left(E_{\rm piv}/E_{\rm b}\right)}{\Lambda},$$
$$m = \frac{\lambda_2 - \lambda_1}{2}, \quad \text{and} \quad b = \frac{\lambda_1 + \lambda_2}{2}.$$

To find the peak in the νF_ν spectrum, we need

$$\frac{d}{dE}(\nu F_\nu)\bigg|_{E_{\rm peak}} = 0,$$

and we find

$$\frac{d}{dE}(\nu F_\nu) = \frac{A}{E_{\rm piv}^b} E^{(b+1)} 10^{(a-a_{\rm piv})}(b+2+m\ \tanh(q)).$$

Set this equation to 0 at $E = E_{\rm peak}$, and we obtain

$$\tanh(q) = \frac{-(b+2)}{m}.$$

But $q(E_{\rm peak}) = \dfrac{\log\left(E_{\rm peak}/E_{\rm b}\right)}{\Lambda}$ so the equation becomes

$$\tanh\left(\frac{\log\left(E_{\rm peak}/E_{\rm b}\right)}{\Lambda}\right) = \frac{-(b+2)}{m},$$

and solving this for $E_{\rm peak}$, we obtain

$$E_{\rm peak} = \ E_{\rm b}\ 10^{\left[\Lambda \tanh^{-1}\left(\frac{\lambda_1+\lambda_2+4}{\lambda_1-\lambda_2}\right)\right]}. \tag{A.1}$$

We note here that since we must have $\left|\frac{\lambda_1+\lambda_2+4}{\lambda_1-\lambda_2}\right| < 1$, this is only valid for $\lambda_1 > -2$ and $\lambda_2 < -2$ in order for the νF_ν spectrum to have a peak within the spectral energy range.

A.2 Error Propagation ($\sigma_{E_{\rm peak}}$)

In order to calculate the uncertainties associated with the derived $E_{\rm peak}$ values, the errors associated with each parameter involved have to be propagated correctly.

Generally, the variance of a function, y, of N parameters (x_1, x_2,...,x_N) can be found by:

$$\mathrm{Var}(y) = \sum_{i=1}^{N}\left[\left(\frac{\partial y}{\partial x_i}\right)^2 \mathrm{Var}(x_i)\right] + 2\frac{\partial y}{\partial x_1}\frac{\partial y}{\partial x_2}\mathrm{Cov}(x_1,x_2) + 2\frac{\partial y}{\partial x_2}\frac{\partial y}{\partial x_3}\mathrm{Cov}(x_2,x_3) + ..., \tag{A.2}$$

where $\mathrm{Cov}(x_j, x_k) = R_{jk}\sigma_{x_j}\sigma_{x_k}$ and R_{jk} is the correlation coefficient between x_j and x_k. Unfortunately, the covariance matrices for individual fits were not stored in the parameter files in our analysis here, and therefore, we could only estimate the

uncertainties of the derived $E_{\rm peak}$ by neglecting the cross terms in Equation A.2. The general effect of excluding the terms may be tested by examining cross-correlations between each parameter involved.

For the SBPL $E_{\rm peak}$, we have Equation A.1 as a function of three parameters, $E_{\rm b}$, λ_1, and λ_2, with the uncertainties associated with each parameter, $\sigma_{E_{\rm b}}, \sigma_{\lambda_1}, \sigma_{\lambda_2}$. First, to make the equation simpler, define

$$s \equiv \Lambda \tanh^{-1} u \quad \text{and} \quad u \equiv \frac{\lambda_1 + \lambda_2 + 4}{\lambda_1 - \lambda_2}, \tag{A.3}$$

and rewrite Equation A.1 as

$$f(E_{\rm b}, \lambda_1, \lambda_2) = E_{\rm peak} = E_{\rm b}\ 10^s.$$

Then, the variance of "$E_{\rm peak}$" is

$$\sigma^2_{E_{\rm peak}} = \sigma^2_{E_{\rm b}} \left(\frac{\partial f}{\partial E_{\rm b}}\right)^2 + \sigma^2_{\lambda_1} \left(\frac{\partial f}{\partial \lambda_1}\right)^2 + \sigma^2_{\lambda_2} \left(\frac{\partial f}{\partial \lambda_2}\right)^2, \tag{A.4}$$

considering only the uncorrelated terms of Equation A.2.

Now, the derivatives are

$$\begin{aligned}
\frac{\partial f}{\partial E_{\rm b}} &= 10^s \\
\frac{\partial f}{\partial \lambda_1} &= E_{\rm b} 10^s\ \ln 10\ \frac{\Lambda}{(1+u)(\lambda_1 - \lambda_2)} \\
\frac{\partial f}{\partial \lambda_2} &= E_{\rm b} 10^s\ \ln 10\ \frac{\Lambda}{(1-u)(\lambda_1 - \lambda_2)}.
\end{aligned}$$

Therefore, Equation A.4 becomes

$$\sigma^2_{E_{\rm peak}} = \sigma^2_{E_{\rm b}} (10^s)^2 + \left(E_{\rm b} 10^s\ \ln 10\ \frac{\Lambda}{\lambda_1 - \lambda_2}\right)^2 \left(\frac{\sigma^2_{\lambda_1}}{(1+u)^2} + \frac{\sigma^2_{\lambda_2}}{(1-u)^2}\right),$$

and finally, the "$E_{\rm peak}$" uncertainty is

$$\sigma_{E_{\rm peak}} = 10^s \sqrt{\sigma^2_{E_{\rm b}} + \left(E_{\rm b}\ \ln 10\ \frac{\Lambda}{\lambda_1 - \lambda_2}\right)^2 \left(\frac{\sigma^2_{\lambda_1}}{(1+u)^2} + \frac{\sigma^2_{\lambda_2}}{(1-u)^2}\right)}, \tag{A.5}$$

where

$$s = \Lambda \tanh^{-1} u \quad \text{and} \quad u = \frac{\lambda_1 + \lambda_2 + 4}{\lambda_1 - \lambda_2}.$$

The covariance terms that were excluded are

$$2\left[\mathrm{Cov}(E_\mathrm{b}, \lambda_1)\frac{\partial f}{\partial E_\mathrm{b}}\frac{\partial f}{\partial \lambda_1} + \mathrm{Cov}(E_\mathrm{b}, \lambda_2)\frac{\partial f}{\partial E_\mathrm{b}}\frac{\partial f}{\partial \lambda_2} + \mathrm{Cov}(\lambda_1, \lambda_2)\frac{\partial f}{\partial \lambda_1}\frac{\partial f}{\partial \lambda_2}\right]$$

$$= \frac{2(10^{2x})E_\mathrm{b}\ln 10\Lambda}{\lambda_1 - \lambda_2}\left[\frac{R_{E_\mathrm{b},\lambda_1}\sigma_{E_\mathrm{b}}\sigma_{\lambda_1}}{1+u} + \frac{R_{E_\mathrm{b},\lambda_2}\sigma_{E_\mathrm{b}}\sigma_{\lambda_2}}{1-u} + R_{\lambda_1,\lambda_2}\sigma_{\lambda_1}\sigma_{\lambda_2}\frac{E_\mathrm{b}\ln 10\Lambda(2+\lambda_2)}{(1-u^2)(\lambda_1-\lambda_2)}\right], \tag{A.6}$$

where s and u are defined above. To understand the overall consequence of disregarding the covariance terms, we investigated the correlations between the parameters (i.e., E_b, λ_1, and λ_2, with Λ = fixed). This was done by using the results of 4-parameter SBPL fits to a set of simulated SBPL spectra with several different break scales described in §4.3.2. Although the correlation coefficients change slightly as a function of fixed Λ values, we found $E_\mathrm{b} - \lambda_1$ and $E_\mathrm{b} - \lambda_2$ are always strongly anti-correlated. The corresponding average correlation coefficients were $\langle R_{E_\mathrm{b},\lambda_1}\rangle \sim -0.8$ and $\langle R_{E_\mathrm{b},\lambda_2}\rangle \sim -0.9$. On the other hand, $\lambda_1 - \lambda_2$ was always positively correlated with $\langle R_{\lambda_1,\lambda_2}\rangle \sim 0.5$.

Using the real set of parameters in our analysis, along with the average correlation coefficients found from the simulation above, we found that the correlated terms (Equation A.6) are almost always negative, as long as two of the correlation coefficients are negative. Therefore, it is likely that the errors calculated using Equation A.4 is overestimated for many spectra.

APPENDIX B

BAND MODEL $E_{\rm b}$

Although a break energy is not parameterized in the BAND model, it represents a broken power-law model, and therefore, we should be able to find a break energy equivalent to the $E_{\rm b}$ of SBPL for a direct comparison. We stress again, as we did in §4.2.2.5, that this $E_{\rm b}$ is not the characteristic energy in Equation 4.2; $E_{\rm c} = (\alpha-\beta)E_{\rm peak}/(2+\alpha)$, which is often called the *break energy* (e.g., SP1; Sakamoto et al. 2004a), but it is not the energy where the power law changes. Rather, the energy $E_{\rm c}$ corresponds to where the low-energy power law with an exponential cutoff ends and the pure high-energy power law starts; therefore, it is always greater than the $E_{\rm b}$ we are trying to find here.

B.1 Finding $E_{\rm b}$

Since $E_{\rm b} < E_{\rm c}$ always, we only use the $E < E_{\rm c}$ case in Equation 4.2. To find $E_{\rm b}$, we consider the change in slope of logarithmic tangential lines from α to β, which is smooth and continuous. We start by writing Equation 4.2 in logarithmic scale;

$$\log f(E) = \log A + (10)\alpha + \alpha \log E - \frac{(2+\alpha)E}{E_{\rm peak}} \log e.$$

Then, the derivative with respect to $\log E$ is

$$\frac{d\log f(E)}{d\log E} = \alpha - \frac{(2+\alpha)E}{E_{\rm peak}}, \tag{B.1}$$

which is the equation for the slope as a function of E.

A break region can be defined as the energy range where the slope is between α and β. By definition of the model, the slope equals to α when $E = 0$ and β when $E = E_{\rm c}$; therefore, the break region is from 0 to $E_{\rm c}$ in keV. However, since the fitted α value is the tangential slope at $E = 0$ and does not exactly represent the low-energy spectral shape, the actual slopes at energies $E > 0$ is always less than α due to the exponential term in the model. In order to take this into account, we use "effective" low-energy power law index, $\alpha_{\rm eff}$, described in Appendix C. This is essentially the slope (Equation B.1) at a fixed energy of 25 keV. Accordingly, we use the $\alpha_{\rm eff}$ in calculating the $E_{\rm b}$, and the break region is from 25 keV to $E_{\rm c}$.

The $E_{\rm b}$ then should be at the center of the break region, namely, the energy at which the slope value differs from both α and β by the same amount, $(\alpha - \beta)/2$. In other words, the slope at $E_{\rm b}$ must equal $(\alpha + \beta)/2$. Since the slope is a linear function, this is just the center energy between 25 keV and $E_{\rm c}$, and is

$$E_{\rm b} = \frac{E_{\rm c} - 25}{2} + 25 = \frac{\alpha - \beta}{2}\frac{E_{\rm peak}}{2 + \alpha} + 12.5. \tag{B.2}$$

B.2 Error Propagation ($\sigma_{E_{\rm b}}$)

The general error propagation methodology was discussed in §A.2. For the same reason, we do not include the cross terms of Equation A.2 in the error calculation here. The BAND $E_{\rm b}$ (Equation B.2) is a function of three parameters, $E_{\rm peak}$, α, and β, with uncertainties, $\sigma_{E_{\rm peak}}$, σ_α, and σ_β, respectively. The $E_{\rm peak}$ is noted as $E_{\rm p}$ in the following equations for simplicity. Let $f(E_{\rm p}, \alpha, \beta) = E_{\rm b}$, then the variance of $E_{\rm b}$ can be written as

$$\sigma^2_{E_{\rm b}} = \sigma^2_{E_{\rm p}} \left(\frac{\partial f}{\partial E_{\rm p}}\right)^2 + \sigma^2_\alpha \left(\frac{\partial f}{\partial \alpha}\right)^2 + \sigma^2_\beta \left(\frac{\partial f}{\partial \beta}\right)^2, \tag{B.3}$$

without the covariance terms. The derivatives are

$$\frac{\partial f}{\partial E_{\rm p}} = \frac{\alpha - \beta}{2(2+\alpha)}$$

$$\frac{\partial f}{\partial \alpha} = \frac{E_{\rm p}(2+\beta)}{2(2+\alpha)^2}$$

$$\frac{\partial f}{\partial \beta} = -\frac{E_{\rm p}}{2(2+\alpha)}.$$

Therefore, Equation B.3 becomes

$$\sigma^2_{E_{\rm b}} = \sigma^2_{E_{\rm p}} \left(\frac{\alpha-\beta}{2(2+\alpha)}\right)^2 + \sigma^2_{\alpha} \left(\frac{E_{\rm p}(2+\beta)}{2(2+\alpha)^2}\right)^2 + \sigma^2_{\beta} \left(-\frac{E_{\rm p}}{2(2+\alpha)}\right)^2,$$

and we find the uncertainty

$$\sigma_{E_{\rm b}} = \frac{1}{2(2+\alpha)} \sqrt{(\alpha-\beta)^2 \sigma^2_{E_{\rm p}} + E^2_{\rm p} \left(\left(\frac{2+\beta}{2+\alpha}\right)^2 \sigma^2_{\alpha} + \sigma^2_{\beta}\right)}. \tag{B.4}$$

Similar to the SBPL $E_{\rm peak}$ case, the correlations between the parameters involved in Equation B.2 (i.e., $E_{\rm peak}$, α, and β) were investigated using the fits to the same set of the simulated SBPL spectra that was used to explore the SBPL parameter correlations in §A.2 for consistency, as well as the simulated BAND spectra. We found that both $E_{\rm peak} - \alpha$ and $E_{\rm peak} - \beta$ are always highly anti-correlated regardless of the $E_{\rm peak}$ values or the SBPL break scale, with correlation coefficients of $\langle R_{E_{\rm p},\alpha} \rangle \sim -0.9$ and $\langle R_{E_{\rm p},\beta} \rangle \sim -0.7$. The correlation between α and β tends to be weaker, though always positively correlated, with a correlation coefficient of $\langle R_{\alpha,\beta} \rangle \sim -0.5$.

The cross terms of $\sigma^2_{E_{\rm b}}$ are

$$2\left[{\rm Cov}(E_{\rm p},\alpha)\frac{\partial f}{\partial E_{\rm p}}\frac{\partial f}{\partial \alpha} + {\rm Cov}(E_{\rm p},\beta)\frac{\partial f}{\partial E_{\rm p}}\frac{\partial f}{\partial \beta} + {\rm Cov}(\alpha,\beta)\frac{\partial f}{\partial \alpha}\frac{\partial f}{\partial \beta}\right]$$

$$= \frac{2E_{\rm p}}{4(2+\alpha)^2}\left[R_{E_{\rm p},\alpha}\sigma_{E_{\rm p}}\sigma_{\alpha}\frac{(2+\beta)(\alpha-\beta)}{2+\alpha} + R_{E_{\rm p},\beta}\sigma_{E_{\rm p}}\sigma_{\beta}(\alpha-\beta) + R_{\alpha,\beta}\sigma_{\alpha}\sigma_{\beta}\frac{E_{\rm p}(2+\beta)}{2+\alpha}\right]. \tag{B.5}$$

Using the actual spectral parameters in our sample, with the average correlation coefficients found above, most of the time the cross term was found to be negative, as long as the parameters are more strongly anti-correlated. Therefore, we believe the uncertainties found in Equation B.3 without the covariance terms tend to be overestimated.

APPENDIX C

EFFECTIVE α

The discrepancy between the BAND (or COMP) α and the SBPL λ_1 can be especially severe when the e-folding energy, $E_0 = E_{\rm peak}/(2+\alpha)$, is close to the lower energy threshold and the actual low-energy power law component of the BAND or COMP is assumed to lie far below the lower energy bound of the data. As an example, we plot in Figure C.1, the BAND and the SBPL model with the same $E_{\rm peak}$, high-energy index, and $\alpha = \lambda_1 = -1$. The difference between the -1 power law and the actual BAND model behavior is obvious, whereas the SBPL low-energy component does follow the –1 power law.

To resolve this issue, we calculate the "effective" α of the BAND and COMP models, introduced by Preece et al. (2002). The effective α is simply the spectral slope in $\log f - \log E$ (Equations 4.2 and 4.3) determined at some fiducial energy, chosen to be 25 keV, and is given by

$$\alpha_{\rm eff} = \alpha - \frac{25\ {\rm keV}}{E_{\rm peak}}(2+\alpha) = \alpha - \frac{25\ {\rm keV}}{E_0}. \qquad \text{(C.1)}$$

By defining $\alpha_{\rm eff}$, we assume that at 25 keV the low-energy power law has already been reached. The energy of 25 keV was chosen because it is just outside the LAD energy range (Preece et al. 2002) and also the tangential slope at this energy seems to represent the data better than at other energies we tested, such as 10 keV, 50 keV, or certain fraction of $E_{\rm peak}$, $E_{\rm b}$, or E_0. The correction term is larger for lower E_0 values. In Figure C.2, we compare the BAND α and $\alpha_{\rm eff}$ of the time-resolved spectra

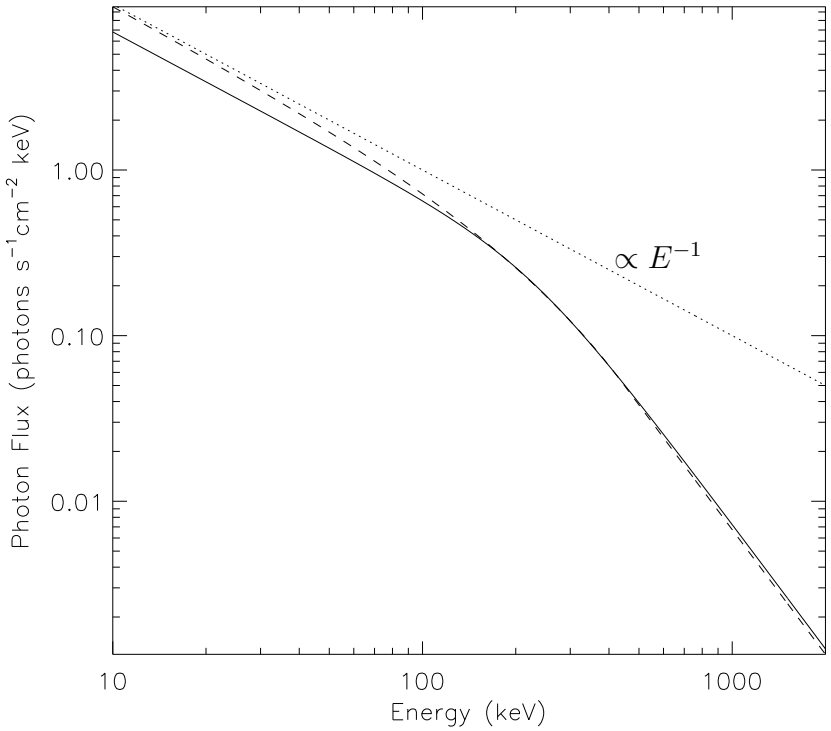

Figure C.1 The BAND model (dashed curve) and the SBPL model (solid curve) with the same low-energy index values of $\alpha = \lambda_1 = -1$. The other parameters are also kept the same ($E_{\rm peak} = 300$ keV and $\beta = \lambda_2 = -2.5$). A dotted line is a power law with index of –1. The difference in the low-energy behavior is evident.

in our sample. As seen in Figure C.2, $\alpha_{\rm eff}$ correction lowers the index values, making them more consistent with λ_1 of SBPL (Figure 4.14, bottom right panel).

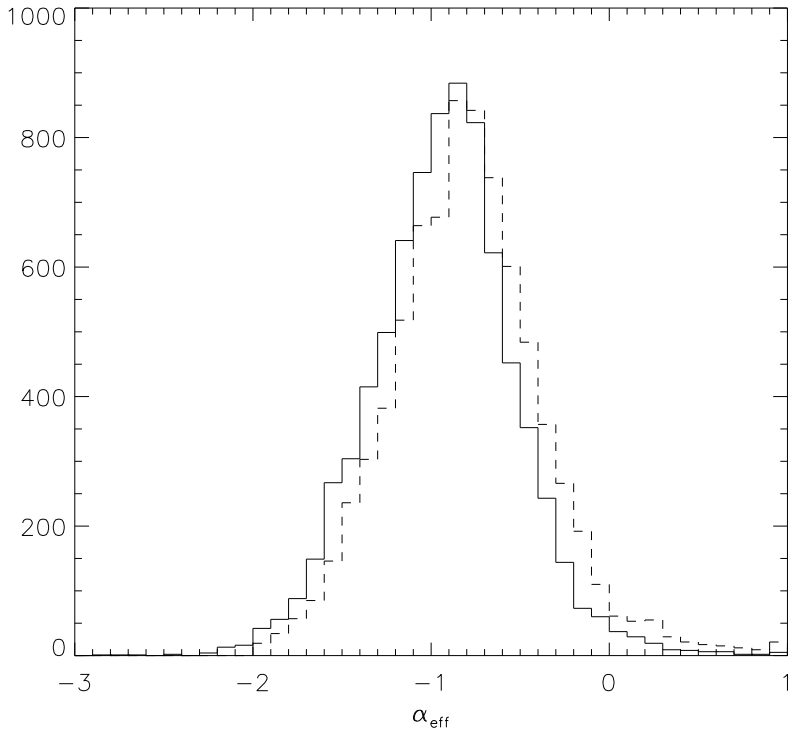

Figure C.2 The comparison of the effective α distribution (solid line) and the fitted α distribution (dashed line) of the BAND model fits to the 7861 time-resolved spectra.

C.1 Error Propagation ($\sigma_{\alpha_{\rm eff}}$)

The variance of $\alpha_{\rm eff}$, without the correlated terms, can be written as

$$\sigma^2_{\alpha_{\rm eff}} = \sigma^2_{E_{\rm peak}} \left(\frac{\partial f}{\partial E_{\rm peak}} \right)^2 + \sigma^2_{\alpha} \left(\frac{\partial f}{\partial \alpha} \right)^2 , \qquad \text{(C.2)}$$

where

$$\frac{\partial f}{\partial E_{\rm peak}} = \frac{25(2+\alpha)}{{E_{\rm peak}}^2}$$

$$\frac{\partial f}{\partial \alpha} = 1 - \frac{25}{E_{\rm peak}}.$$

Therefore, the $\alpha_{\rm eff}$ uncertainty is

$$\sigma_{\alpha_{\rm eff}} = \sqrt{\sigma^2_{E_{\rm peak}} \left(\frac{25(2+\alpha)}{{E_{\rm peak}}^2} \right)^2 + \sigma^2_{\alpha} \left(1 - \frac{25}{E_{\rm peak}} \right)^2}. \tag{C.3}$$

The correlation term neglected above is

$$2 \left[R_{E_{\rm peak},\alpha} \sigma_{E_{\rm peak}} \sigma_{\alpha} \frac{\partial f}{\partial E_{\rm peak}} \frac{\partial f}{\partial \alpha} \right],$$

where $R_{E_{\rm peak},\alpha}$ was found to be negative (see §B.2).

REFERENCES

Akerlof, C., et al. 1999, *Nature*, 398, 400

Amati, L., et al. 2002, *A&A*, 390, 81

Band, D.L., 1997, *ApJ*, 486, 928

Band, D.L. & Preece, R.D., 2005, *ApJ*, 627, 319

Band, D.L., et al. 1993, *ApJ*, 413, 281

Band, D.L., et al. 1994, *ApJ*, 434, 560

Band, D.L., et al. 1995, *ApJ*, 447, 289

Band, D.L., et al. 1996, *ApJ*, 458, 746

Band, D.L., et al. 1997, *ApJ*, 485, 747

Baring, M.G., 2000, in *GeV-TeV Gamma Ray Astrophysics Workshop: Towards a Major Atmospheric Cherenkov Detector VI*, ed. B. Dingus, et al. AIP, 515, 238

Baring, M.G., 2005, *Adv. Space Res.*, in press [astro-ph/0502156]

Baring, M.G. & Braby, M.L., 2004, *ApJ*, 613, 460

Bhat, P.N., et al. 1992, *Nature*, 359, 217

Blake, C.H., et al. 2005, *Nature*, 435, 181

Blandford, R.D. & Znajek, R.L., 1977, *MNRAS*, 179, 433

Bloom, J.S., et al. 2001, *ApJ*, 554, 678

Briggs, M.S., 1996, in *Gamma-Ray Bursts*, 3rd Huntsville Symposium, ed. C. Kouveliotou, M. Briggs & G. Fishman, AIP, 384, 133

Briggs, M.S., 1999, in *Gamma-Ray Bursts: The First Three Minutes*, ed. J. Poutanen & R. Svensson, ASP, 190, 133

Briggs, M.S., et al. 1996, *ApJ*, 459, 40

Briggs, M.S., et al. 1999, *ApJ*, 524, 82

Bromm, V. & Loeb, A., 2002, *ApJ*, 575, 111

Catelli, J.R., et al. 1998, in *Gamma-Ray Bursts*, 4th Huntsville Symposium, ed. C. Meegan, R. Preece and T. Koshut, AIP, 428, 309

Cobb, B.E., et al. 2004, *ApJ*, 608, L93

Colgate, S.A., 1974, *ApJ*, 187, 333

Connaughton, V., 2002, *ApJ*, 567, 1028

Costa, E., et al. 1997, *Nature*, 387, 783

Crider, A., & Liang, E.P., 1999, *A&AS*, 138, 405

Crider, A., et al. 1997, *ApJ*, 479, L39

Crider, A., et al. 1999, *A&AS*, 138, 401

Della Valle, M., et al. 2003, *A&A*, 406, L33

Dermer, C.D. & Atoyan, A., 2004, *A&A*, 418, L5

Dermer, C.D. & Mittman, K.E., 1999, *ApJ*, 513, L5

Dezalay, J-P., et al. 1992, in *Gamma-Ray Bursts*, 1st Huntsville Symposium, ed. W. Paciesas & G. Fishman, AIP, 265, 304

Dingus, B.L., et al. 1998, in *Gamma-Ray Bursts*, 4th Huntsville Symposium, ed. C. Meegan, R. Preece and T. Koshut, AIP, 428, 349

Djorgovski, S.G., et al., 1997, *Nature*, 387, 876

Eichler, D. & Waxman, E., 2005, *ApJ*, 627, 861

Eichler, D., et al. 1989, *Nature*, 340, 126

Fan, Y.Z., et al. 2005, *ApJ*, in press [astro-ph/0410060]

Fenimore, E.E., et al. 1993, *A&AS*, 97, 59

Fenimore, E.E., et al. 1993, in *Compton Gamma-Ray Observatory*, ed. M. Friedlander, N. Gehrels & D. Macomb, AIP, 280, 744

Fenimore, E.E., et al. 1996, *ApJ*, 473, 998

Fishman, G.J. & Meegan, C.A., 1995, *ARAA*, 33, 415

Fishman, G.J., et al. 1989, in *Proc. GRO Science Workshop*, GSFC, 2-39

Ford, L.A., et al. 1995, *ApJ*, 439, 307

Frail, D.A., et al. 1997, *Nature*, 389, 261

Frail, D.A., et al. 2001, *ApJ*, 562, L55

Frail, D.A., et al. 2003, *ApJ*, 125, 2299

Fynbo, J.P.U., et al. 2004, *ApJ*, 609, 962

Galama, T.J., et al. 1998, *Nature*, 395, 670

Gallant, Y.A., 2002, in *Relativistic Flows in Astrophysics*, ed. A. Guthmann et al., Lecture Notes in Physics (Springer-Verlag), 589, 24

Gallant, Y.A., et al. 1999, *AAPS*, 138, 549

Ghirlanda, G., et al. 2002, *A&A*, 393, 409

Ghirlanda, G., et al. 2003, *A&A*, 406, 879

Ghirlanda, G., et al. 2004, *ApJ*, 616, 331

Ghirlanda, G., et al. 2005, *MNRAS*, in press [astro-ph/0502186]

Ghisellini, G. & Celotti, A., *ApJ*, 511, L93

Ghisellini, G., et al. 2000, *MNRAS*, 313, L1

Giblin, T.W., et al. 2002, *ApJ*, 570, 573

González, M.M., et al. 2003, *Nature*, 424, 749

González, M.M., et al. 2004, in *Gamma-Ray Bursts: 30 Years of Discovery*, ed. E. Fenimore & M. Galassi, AIP, 727, 236

Goodman, J., 1986, *ApJ*, 308, L47

Goodman, J., 1997, *New Astronomy*, 2, 449

Granot, J. & Guetta, D., 2003, *ApJ*, 598, L11

Greiner, J., 2005, http://www.mpe.mpg.de/~jcg/grbgen.html

Greiner, J., et al. 2003, *Nature*, 426, 157

Guetta, D. & Granot, J., 2003, *ApJ*, 585, 885

Hanlon, L., et al. 1994, *A&A*, 285, 161

Harmon, B.A., et al. 2002, *ApJS*, 138, 149

Harris, M.J. & Share, G.H., 1998, *ApJ*, 494, 724

Harrison, F.A., et al. 1999, *ApJ*, 523, L121

Hededal, C.B., et al. 2004, *ApJ*, 617, L107

Heise, J., et al. 2001, in *Gamma-Ray Bursts in the Afterglow Era*, ed. E. Costa, F. Frontera, & J. Hjorth. (Berlin Heidelberg: Springer), 16

Hjorth, J., et al. 2003, *Nature*, 423, 847

Horack, J.M., 1991, *Development of the Burst and Transient Source Experiment (BATSE)*, NASA Reference Publication, 1268

Hurley, K., et al. 1994, *Nature*, 371, 652

Hurley, K., et al. 2005, *Nature*, 434, 1098

in't Zand, J.J.M., et al. 1999, *ApJ*, 516, L57

Kaneko, Y., et al. 2005, in *Astrophysical Particle Acceleration in Geospace and Beyond*, ed. D. Gallagher, et al. AGU, in press [astro-ph/0401285]

Katz, J.I., 1994, *ApJ*, 432, L107

Kippen, R.M., et al. 1998, *Adv. Space Res.*, 22, 1097

Kippen, R.M., et al. 2004, in *Gamma-Ray Bursts: 30 Years of Discovery*, ed. E. Fenimore & M. Galassi, AIP, 727, 119

Klebesadel, R.W., et al. 1973, *ApJ*, 182, L85

Kouveliotou, C., et al. 1993, *ApJ*, 413, L101

Kulkarni, S.R., et al. 1999, *Nature*, 398, 389

Kwok, P.W., et al. 1993, in *Compton Gamma-Ray Observatory*, ed. M. Friedlander, N. Gehrels & D. Macomb, AIP, 280, 855

Lamb, D.Q., et al. 2005, *ApJ*, 620, L355

Lazzati, D., et al. 2001, *A&A*, 422, 121

Lazzati, D., et al. 2004, *A&A*, 422, 121

Liang, E.P. & Kargatis, V.E., 1996, *Nature*, 381, 49

Liang, E.P., et al. 1997, *ApJ*, 479, L35

Lithwick, Y. & Sari, R., 2001, *ApJ*, 555, 540

Lloyd, N.M., et al. 2000, *ApJ*, 534, 227

Lloyd-Ronning, N.M. & Petrosian, V., *ApJ*, 565, 182

Lyutikov, M. & Blandford, R.D., 2003, astro-ph/0312347

MacFadyen, A.I. & Woosley, S.E., *ApJ*, 524, 262

Malesani, D., et al. 2004, *ApJ*, 609, L5

Mallozzi, R.S., et al. 1995, *ApJ*, 454, 597

Mallozzi, R.S., Preece, R.D. & Briggs, M.S., "RMFIT, A Lightcurve and Spectral Analysis Tool", ©2005 Robert D. Preece, University of Alabama in Huntsville

Matz, S.M., et al. 1985, *ApJ*, 288, L37

Mazets, E.P. & Golenetskii, S.V., 1981, *Ap&SS*, 75, 47

Mazets, E.P., et al. 1981, *Nature*, 290, 378

Mazets, E.P., et al. 1983, in *Positron-Electron Pairs in Astrophysics*, ed. M. Burns, A. Harding & R. Ramaty, AIP, 101, 36

Medvedev, M.V., 2000, *ApJ*, 540, 704

Medvedev, M.V., 2004, in *Gamma-Ray Bursts: 30 Years of Discovery*, ed. E. Fenimore & M. Galassi, AIP, 727, 25

Medvedev, M.V. & Loeb, A., 1999, *ApJ*, 526, 697

Medvedev, M.V., et al. 2005, *ApJ*, 618, L75

Meegan, C.A., et al. 1992, *Nature*, 355, 143

Mészáros, P., 2002, *ARAA*, 40, 137

Mészáros, P. & Rees, M.J., 1993, *ApJ*, 405, 278

Mészáros, P. & Rees, M.J., 1997, *ApJ*, 482, L29

Mészáros, P. & Rees, M.J., 1997, *ApJ*, 530, 292

Metzger, M.R., et al., 1997, *Nature*, 387, 878

Murakami, T., et al. 1988, *Nature*, 335, 234

Murakami, T., et al. 1991, *Nature*, 350, 592

Nakar, E. & Piran, T., 2005a, *ApJ*, 619, L147

Nakar, E. & Piran, T., 2005b, *MNRAS*, 360, L42

Nakar, E. & Piran, T., 2005c, astro-ph/0503517

Nelson, W.R., et al. 1985, *The EGS4 Code System*, SLAC Rep., 265

Nemiroff, R.J., 1994, in *Gamma-Ray Bursts*, 2nd Huntsville Workshop, ed. G. Fishman, J. Brainerd, & K. Hurley, AIP, 307, 730

Nishikawa, K.-I., et al. 2005, *ApJ*, 622, 927

Norris, J.P., et al. 1994, *ApJ*, 424, 540

Ogasaka, Y., et al. 1991, *ApJ*, 383, L61

Paciesas, W.S., et al. 1999, *ApJS*, 122, 465

Paciesas, W.S., et al. 2003, in *Gamma-Ray Bursts and Afterglow Astronomy*, ed. G. Ricker & R. Vanderspek, AIP, 662, 248

Paczyński, B., 1986, *ApJ*, 308, L43

Palmer, D.M., et al. 1994, *ApJ*, 433, L77

Palmer, D.M., et al. 2005, *Nature*, 434, 1107

Panaitescu, A. & Mészáros, P., 1998, *ApJ*, 492, 683

Pendleton, G.N., et al. 1995, *Nuclear Instruments and Methods*, Section A, 364, 567

Pendleton, G.N., et al. 1997, *ApJ*, 489, 175

Piran, T., 2005, *Rev. Mod. Phys.*, 76, 1143

Preece, R.D., et al. 1998a, *ApJ*, 496, 849

Preece, R.D., et al. 1998b, *ApJ*, 506, L23

Preece, R.D., et al. 2000, *ApJS*, 126, 19 (SP1)

Preece, R.D., et al. 2002, *ApJ*, 581, 1248

Press et al., 1992, *Numerical Recipes in FORTRAN*, 2nd Edition (New York: Cambridge University Press)

Price, P.A., et al. 2003, *Nature*, 423, 844

Rees, M.J. & Mészáros, P., 1992, *MNRAS*, 258, 41

Rees, M.J. & Mészáros, P., 1994, *ApJ*, 430, L93

Rhoads, J.E., 1999, *ApJ*, 525, 737

Rol, E., et al. 2003, *A&AS*, 405, L23

Rol, E., et al. 2005, *ApJ*, 624, 868

Rossi, E.M., et al. 2004, *MNRAS*, 354, 86

Rybicki, G.B. & Lightman, A.P., 1979, *Radiative Processes in Astrophysics* (New York: John Wiley & Sons)

Ryde, F., 1999, *ApL&C*, 39, 281

Ryde, F., 2004, *ApJ*, 614, 827

Sakamoto, T., et al. 2004a, *ApJ*, 602, 875

Sakamoto, T., et al, 2004b, *ApJ*, submitted [astro-ph/0409128]

Sari, R. & Piran, T., 1997, *ApJ*, 485, 270

Sari, R. & Piran, T., 1999, *ApJ*, 517, L109

Sari, R., et al. 1998, *ApJ*, 497, L17

Schaefer, B.E., et al. 1998, *ApJ*, 492, 696

Schneid, E.J., et al. 1992, *A&AL*, 255, 13

Schneid, E.J., et al. 1995, *ApJ*, 453, 95

Schönfelder, V. et al. 1993, *ApJS*, 86, 657

Share, G.H. & Matz, S.M., 1998, in *Gamma-Ray Bursts*, 4th Huntsville Symposium, ed. C. Meegan, R. Preece and T. Koshut, AIP, 428, 354.

Share, G.H., et al. 1993, *A&AS*, 97, 341

Soderberg, A.M., et al. 2004, *ApJ*, 606, 994

Soderberg, A.M., et al. 2005, *ApJ*, 627, 877

Stanek, K.Z., et al. 2003, *ApJ*, 59, L17

Strohmayer, T.E., et al. 1998, *ApJ*, 500, 873

Strong, I.B., et al. 1974, *ApJ*, 188, L1

Tavani, M., 1996a, *Phys. Rev. Lett.*, 76, 3478

Tavani, M., 1996b, *ApJ*, 466, 768

Thompson, D.J., et al. 1993, *ApJS*, 86, 629

Thomsen, B., et al. 2004, *A&A*, 419, L21

Uemura, M., et al. 2003, *Nature*, 423, 843

Vanderspek, R., et al. 2004, *ApJ*, 617, 1251

van Paradijs, J., et al. 1997, *Nature*, 386, 686

van Paradijs, J., et al. 2000, *ARAA*, 38, 379

Vestrand, W.T., et al. 2005, *Nature*, 435, 178

Vietri, M. & Stella, L., 1998, *ApJ*, 507, L45

Waxman, E., 1997, *ApJ*, 485, L5

Wiersema, K., et al. 2004, *GCN Circular*, 2800

Woosley, S., 1993, *ApJ*, 405, 273

Woosley, S. & MacFadyen, A.I., 1999, *A&AS*, 138, 499

Wren, D.N., et al. 2002, *ApJ*, 574, L47

Yamazaki, R., et al. 2004, *ApJ*, 606, L33

Zhang, B. & Mészáros, P., 2002, *ApJ*, 581, 1236

Zhang, B. & Mészáros, P., 2004, *Int. J. Mod. Phys. A.*, 19, 2385

Zhang, B., et al., 2004, *ApJ*, 601, L119

Zhang, W., Woosley, S.E., & Heger, A., 2004, *ApJ*, 608, 365